Synchronization and Formation Flying for Multistatic Synthetic Aperture Radar Systems

Zur Erlangung des akademischen Grades eines

DOKTORS DER INGENIEURWISSENSCHAFTEN (Dr.-Ing.)

von der KIT-Fakultät für
Elektrotechnik und Informationstechnik
des Karlsruher Instituts für Technologie (KIT)

genehmigte

DISSERTATION

von

M.Sc. Eduardo Rodrigues Silva Filho
geb. in Imperatriz, Maranhão, Brasilien

Tag der mündlichen Prüfung:	15.01.2026
Hauptreferent:	Prof. Dr.-Ing. habil. Alberto Moreira
Korreferent:	Prof. Dr. Alfredo Renga

Acknowledgements

First of all, I would like to thank my supervisor, Marc Rodriguez Cassola, for his valuable ideas and stimulating discussions. I would also like to thank Prof. Alberto Moreira for his support and motivation. I thank both for guiding me to continue improving and achieving the required methodological rigour in scientific work, and for giving me the opportunity to work at DLR's Microwaves and Radar Institute, where exceptional people and creative ideas are ubiquitous.

A special thank you to my colleagues for their technical and moral support throughout these years. To Jalal, for the comradeship and his key insights into mission design for SAR. To my fellow Reuben, with whom I had the opportunity of exchanging deep ideas on astrodynamics. To Felipe, for the uplifting attitude, and for always reminding me there is more to life than work. To Dominik, for the many fun times at the office and stimulating cross-field technical discussions. To Andy, for being a source of wisdom and relative stability. I'd also like to give an extra thank you to Thiago, Lucas, and Stephan for helping me polish my thesis.

I would like to thank Prof. Alfredo Renga from UNINA for taking the time to carefully evaluate my thesis, despite the tight schedule and busy end-of-the-year period. I'd like to thank Prof. Ulrich Lemmer, Prof. Christian Koos, and Prof. Marc Hiller from KIT for participating in the examination committee.

Finally, I would like to thank my family for their unconditional love and lifelong support. I thank my mother Mimorina, my late father Eduardo, Maria, who helped raise me, my brother Nikono, and my sisters Grazielle and Giselle. This achievement would not be possible without their influence, to which I attribute my best qualities. I also thank Mariusz for his patience and support during this difficult and demanding phase of my life.

Minor language editing and partial translation assistance were provided by AI-based tools (Grammarly, DeepL, Gemini). All content was subsequently reviewed and verified by the author.

Oberpfaffenhofen, January 2026

Eduardo Rodrigues Silva Filho

Kurzfassung

Synthetic Aperture Radar (SAR) ist ein zentrales Instrument in der Erdbeobachtung. Es liefert hochaufgelöste Bilder unabhängig von Tageszeit und Wetter und ermöglicht Anwendungen wie 2D- und 3D-Kartierung, sowie die Detektion von Veränderungen. Multistatisches SAR bezeichnet eine Konfiguration mit einem Radarsender und mehreren räumlich getrennten Empfängern auf unterschiedlichen Plattformen. Solche Systeme erlauben Einzelpass-Interferometrie und Tomographie und eignen sich damit besonders zur Höhenkartierung und der Charakterisierung von natürlichen Volumen, ohne zeitliche Dekorrelation und mit deutlich reduzierten atmosphärischen Effekten. Darüber hinaus eröffnet multistatisches SAR neue Möglichkeiten für flexible und effiziente verteilte SAR-Systeme, in denen sich hochaufgelöste Geoinformationsprodukte durch die kombinierte Auswertung der Daten mehrerer kleiner Satelliten erzeugen lassen. Diese Vorteile machen multistatisches SAR zu einem dynamischen Forschungsfeld und zu einer wichtigen technologischen Entwicklungsrichtung für zukünftige SAR-Missionen. Die praktische Umsetzung wird jedoch durch zwei wesentliche technische Herausforderungen erschwert: die Phasensynchronisation zwischen den Satelliten und die Einhaltung strenger geometrischer Randbedingungen im Formationsflug. Diese Arbeit stellt neuartige Lösungsansätze und Methoden für beide Aspekte vor.

Die Phasensynchronisation wird notwendig, wenn die Radarsignale mit verschiedenen Oszillatoren moduliert und demoduliert werden. Dadurch entstehen unterschiedliche Phasendrifts, die die Nutzbarkeit der SAR Daten beeinträchtigen. In dieser Arbeit wird eine neuartige GNSS-basierte Synchronisationstechnik vorgeschlagen, die auf differentiellen Trägerphasenmessungen und einer präzisen Bestimmung der Basislinien beruht. Dabei teilen sich Radarnutzlast und GNSS-Empfänger denselben Master Oszillator. Die Methode kommt ohne dedizierte Verbindungen zwischen den Satelliten aus und erfordert keine wesentlichen Änderungen in der Prozessierungskette des Bodensegments. Tests unter Laborbedingungen zeigen, dass eine Genauigkeit von unter 2° im X-Band erreicht werden kann.

Formationsflüge stellen eine weitere große Herausforderung für weltraumgestützte multistatische SAR-Systeme dar, da sie häufig strikte Anforderungen an die relative Position der Satelliten bei nur begrenzter Manövrierfähigkeit erfüllen müssen. In dieser Arbeit wird ein neues allgemeines Design-Framework für erdbezogene SAR-Formationen entwickelt, das sowohl Lösungen in geschlossener Form unter Verwendung eines vereinfachten Modells, als auch eine iterative Methode unter Verwendung eines Propagators umfasst. Die Algorithmen wurden verwendet, um neuartige, treibstoffeffiziente Lösungen für Along-Track-Formationen mit minimalen Abweichungen in der Cross-Track- und Radial-Richtung, sowie Konfigurationen mit nahezu konstanten Cross-Track-Basislinien über lange Orbitabschnitte zu identifizieren, die fast die Hälfte der Erdoberfläche abdecken.

Abstract

Synthetic Aperture Radar (SAR) is a fundamental Earth observation tool, offering high-resolution, day-and-night, and weather-independent images, enabling applications such as 2-D and 3-D mapping and change detection. Multistatic SAR is a configuration consisting of multiple radars deployed on separate platforms receiving the same signals. It enables single-pass interferometry and tomography, useful for elevation mapping and characterization of natural volumes without temporal decorrelation and reduced atmospheric distortions. It also offers the potential for flexible and efficient distributed SAR systems where data from multiple small satellites can be combined to deliver high-resolution imaging.

These advantages make multistatic SAR a highly active research area and a key direction for the future of SAR technology. However, its implementation is hindered by two critical technical challenges: phase synchronization between satellites and formation flying under strict geometric constraints. This thesis proposes solutions and methods to address both challenges.

The need for phase synchronization arises when the radar carrier is modulated and demodulated using different oscillators, which leads to differential phase drifts that compromise the usability of the SAR data. This thesis proposes a novel GNSS-based synchronization technique using differential carrier-phase measurements and precise baseline determination, with the radar payload and the GNSS receiver sharing the same master oscillator. The technique requires no dedicated inter-satellite links nor major modifications to the ground segment processing chain. The method was validated in a laboratory environment, achieving in X band precision below 2°.

Formation flying poses another major challenge for spaceborne multistatic SAR due to stringent relative positioning requirements and limited satellite maneuverability. This thesis develops a new general design framework for the Earth-referenced SAR formations, including both closed-form solutions using a simplified model and an iterative method with a propagator in the loop. The algorithms were used to identify novel, fuel-efficient solutions for along-track formations with minimal cross-track and radial deviations, and configurations maintaining near-constant cross-track baselines over large orbital arcs, covering nearly half the globe.

Contents

Acronyms and symbols

Acronyms

AASR	Azimuth Ambiguity-to-Signal Ratio
ADC	Analog-to-Digital Converter
ASI	*Agenzia Spaziale Italiana*
AT	Along-Track
BPSK	Binary Phase Shift Keying
BOC	Binary Offset Carrier
CHAMP	Challenging Minisatellite Payload
CNSA	China National Space Administration
CNES	*Centre National d'Études Spatiales*
CONAE	*Comisión Nacional de Actividades Espaciales*
CVXPY	Convex Optimization Python Library
DBF	Digital Beamforming
DCO	Digitally Controlled Oscillator
DD	Double Difference
DEM	Digital Elevation Model
DLL	Delay-Locked Loop
DLR	*Deutsches Zentrum für Luft- und Raumfahrt*
DMTD	Dual Mixer Time Difference
ECI	Earth-Centered Inertial
ECEF	Earth-Centered Earth-Fixed
ECOS	Embedded Conic Solver
ESA	European Space Agency
EUMETSAT	European Organisation for the Exploitation of Meteorological Satellites

GCRF	Geocentric Celestial Reference Frame
GLONASS	*Globalnaya Navigazionnaya Sputnikovaya Sistema*
GMAT	General Mission Analysis Tool
GNSS	Global Navigation Satellite System
GPS	Global Positioning System
GRACE	Gravity Recovery and Climate Experiment
GSOC	German Space Operations Center
HCW	Hill-Clohessy-Wiltshire
IGS	International GNSS Service
InSAR	Interferometric Synthetic Aperture Radar
LEO	Low Earth Orbit
LHLV	Local-Horizontal Local-Vertical
LQR	Linear Quadratic Regulator
MEO	Medium Earth Orbit
MGEX	Multi-GNSS Experiment
MILP	Mixed-Integer Linear Programming
MPC	Model Predictive Control
NAVSTAR	Navigation by Satellite Ranging and Timing
NCO	Numerically Controlled Oscillator
NESN	Noise Equivalent Sigma Nought
NRLMSISE00	Naval Research Laboratory Mass Spectrometer and Incoherent Scatter Radar Exosphere model
PBD	Precise Baseline Determination
PC	Proposed Concept
PLL	Phase-Locked Loop
POD	Precise Orbit Determination
PRF	Pulse Repetition Frequency
PRI	Pulse Repetition Interval
PRISMA	Prototype Research Instruments and Space Mission technology Advancement

PRN	Pseudorandom Noise
PPS	Pulse-Per-Second
PSD	Power Spectral Density
PVT	Position, Velocity, and Time
QZSS	Quasi-Zenith Satellite System
QPSK	Quadrature Phase Shift Keying
RAAN	Right Ascension of the Ascending Node
RASR	Range Ambiguity-to-Signal Ratio
ROE	Relative Orbital Element
SAR	Synthetic Aperture Radar
SOZB	Single-Oscillator Zero-Baseline
STM	State Transition Matrix
STK	Systems Tool Kit
SV	Space Vehicle
TEC	Total Electron Content
TECU	Total Electron Content Unit
TIR	Thermal Infrared
TLE	Two-Line Element
TOSB	Two-Oscillators Short-Baseline
TOZB	Two-Oscillators Zero-Baseline
USO	Ultra Stable Oscillator
VNA	Vector Network Analyzer
VTEC	Vertical Total Electron Content
XT	Cross-Track
ZD	Zero Doppler

Constants

π	Pi: 3.14159…
c	Speed of light in vacuum: 299,792,458 m/s

μ	Standard gravitational parameter of Earth: $3.986004418 \times 10^{14}$ m^3/s^2

Lower Case Letters

a	Semi-major axis
d_x, d_y, d_z	Relative disturbance acceleration components
f	Frequency
f_{uv}	Frequency offset between oscillators u and v
$\tilde{f}_{uv}$	Estimated frequency offset between oscillators u and v
i	Orbit inclination
n	Orbit mean motion
$n_\lambda^{(i)}$	Number of received GNSS frequencies from satellite i
q_{KF}	Process noise variance in the Kalman filter model
r	Magnitude of chief position vector
r_{KF}	Measurement noise variance in the Kalman filter model
t	Time
u	Argument of latitude
u_k	Argument of latitude at t_k
v_{g}	Ground-projected velocity of the platform
v_{s}	Platform velocity
v_{KF}	Kalman filter measurement noise
w_{KF}	Kalman filter process noise
x, y, z	Relative position components in the HCW frame
$\dot{x}, \dot{y}, \dot{z}$	Relative velocity components in HCW frame
x_{KF}	Kalman filter state
z_{KF}	Kalman filter measurement
$\hat{i}_{\mathrm{arr}}$	Array direction unit vector
$\hat{i}_{\mathrm{hcw}}, \hat{j}_{\mathrm{hcw}}, \hat{k}_{\mathrm{hcw}}$	HCW frame unit vectors
$\vec{h}$	Orbit angular momentum vector

$\vec{r}$	Satellite position vector
$\vec{v}_{\text{eci}}$	Satellite velocity in ECI frame

Capital Letters

A_{ant}	Antenna area
$A_u^{(i)}$	Carrier phase ambiguity term
$\mathcal{A}$	Set of actuated time intervals
A	Model matrix for linear estimation
A_{at}	Design matrix for along-track optimization
A_{xt}	Design matrix for cross-track optimization
B	Control input matrix
B_{az}	Azimuth bandwidth
$B_{\text{L}-\text{CA}}$	Tracking bandwidth of the GNSS receiver
$B_{\perp}$	Perpendicular baseline
B_{r}	Range bandwidth
B_{ψ}	Oscillator phase noise bandwidth
$\text{DD}_{kl}^{(ij)}$	Scaled and motion-compensated double difference between signals k and l, satellites i and j
E_{at}	Error vector for along-track optimization
E_{xt}	Error vector for cross-track optimization
$F(t)$	Time-varying system matrix
$I_{uv}^{(i)}(t)$	Difference in ionospheric delays between GNSS satellite i and receivers u and v
$\mathcal{I}$	Set of imaging instants
$\mathcal{J}$	Cost function
$\mathcal{J}_k$	Cost function for aperture element k
L_{a}	Antenna length in azimuth
L_{e}	Antenna length in elevation
L_{sa}	Synthetic aperture length

$L_{uv,k}^{(i)}$	Differential carrier phase measurement between receivers u and v, satellite i, carrier frequency k
$L_{u,k}^{(i)}$	Carrier phase GNSS observable for signal k, receiver u and GNSS satellite i
$M_{uv,k}^{(i)}(t)$	Differential systematic error components between receivers u and v, satellite i, carrier frequency k
$M_{\text{ext},k}^{(i)}(t)$	Differential systematic error components of external origin for GNSS satellite i, GNSS signal k
$M_{\text{int},k}(t)$	Differential systematic error components of internal origin for GNSS signal k
N	Number of GNSS satellites in view
P	Transmitted power
$P_{u,k}^{(i)}$	GNSS code-delay observable for signal k, receiver u and GNSS satellite i
$R(t)$	Time-dependent slant range
R_0	Reference slant range/Slant-range distance to target
R_{I}	Rotation matrix around the I-axis
R_{K}	Rotation matrix around the K-axis
S	Covariance matrix of the carrier phase random error
T_{sa}	Illumination time/Synthetic aperture time
T	Transformation matrix between frames or variables
T_k	Transformation matrix at time k
$\text{T}_{\text{zd}\rightarrow\text{hcw}}$	Transformation matrix from ZD to HCW frame
W	Weight matrix for least-squares estimation
W_{g}	Ground swath width
Y_k	Target geometry vector at time k

Greek Symbols and Variables

$\alpha_k^{(i)}$	Weight for the signal from satellite i and carrier k
β	Azimuthal thrust misalignment angle

β_1	First rotation angle (ZD to HCW)
β_2	Second rotation angle (ZD to HCW)
δa	Difference in semi-major axis between deputy and chief satellite
$\delta e_x, \delta e_y$	Relative eccentricity vector components (ROE elements)
δF_z	Thrust magnitude error
$\delta i_x, \delta i_y$	Relative inclination vector components (ROE elements)
δl	Relative mean longitude
$\delta \psi_{\mathrm{hw},k}$	Random common mode error at frequency k
$\delta t^{(i)}$	GNSS satellite clock error
$\delta t_{0,uv}$	Initialization time difference between receivers u and v
δt_u	Clock bias of receiver u
δt_{uv}	Differential time offset between clocks u and v
δt_v	Clock bias of receiver v
$\delta \vec{\alpha}$	Vector of relative orbit elements (ROEs)
$\delta \vec{\alpha}_0$	Initial ROE vector
$\delta \vec{X}$	Deputy state vector in HCW frame
$\delta \vec{X}_0$	Initial relative state
$\delta \vec{X}_k$	Relative state vector at time t_k
$\Delta \delta e_x$	Correction in relative eccentricity vector component x
$\Delta \delta e_y$	Correction in relative eccentricity vector component y
$\Delta \delta i_x$	Correction in relative inclination vector component x
$\Delta \delta i_y$	Correction in relative inclination vector component y
$\Delta \delta \lambda$	Correction in relative mean longitude
Δf_u	Frequency deviation of oscillator at receiver u
Δf_v	Frequency deviation of oscillator at receiver v
Δh	Topographic height difference
$\Delta \Omega$	Offset in the right ascension of the ascending node (RAAN)
ΔR	Range difference
$\Delta \vec{v}_k$	Control input (delta-V) vector at t_k

$\Delta\delta r_{\mathrm{e}}$	Array spacing in elevation
$\dot{\vec{\rho}}_{\mathrm{hcw}}$	Deputy velocity vector in HCW frame
$\epsilon_{uv,0}$	Differential phase estimation error at radar carrier
$\epsilon_{uv,k}^{(i)}$	Measurement error component on signal k for satellite i
η	Measurement noise
$\eta_{n,k}^{(i)}$	Noise term at GNSS signal k from satellite i
$\eta_{uv,k}^{(i)}(t)$	Zero-mean random noise in carrier phase measurement for satellite i, carrier k
Γ	Complex reflectivity constant
λ_0	Wavelength of radar carrier
λ_k	Wavelength of GNSS signal k
ω	Argument of perigee
ω_{e}	Earth's angular velocity
ν	True anomaly
$\phi^{(i)}$	Transmitted GNSS carrier phase
ϕ_0	Constant phase term
ϕ_u	Replica carrier phase at GNSS receiver
$\phi_{uv}(t)$	Time-dependent random phase error
$\Phi(t_0, t)$	State transition matrix
$\Phi(t_0, t_k)$	STM from time t_0 to t_k
$\psi_{u,0}$	Radar reference signal phase at receiver u
$\psi_{u,\mathrm{os}}$	Phase of master oscillator at receiver u
$\psi_{v,\mathrm{os}}$	Phase of master oscillator at receiver v
$\psi_{\mathrm{b}u,0}$	Phase bias at receiver u radar reference
$\psi_{uv,0}$	Differential radar carrier phase between receivers u and v
$\psi_{\mathrm{b}uv,0}$	Differential phase bias between receivers u and v
$\psi_{\mathrm{HW}uv,0}$	Residual hardware phase signature
$\psi_{uv,0}$	Differential radar carrier phase between receivers u and v
σ	Standard deviation

σ_ϵ	Standard deviation of phase estimator due to thermal noise
σ_ψ	Standard deviation of synchronization phase noise
θ_a	Azimuth beamwidth
θ_e	Elevation beamwidth
θ_i	Incident angle
θ_{arr}	Antenna look angle
$\tilde{\psi}_{0,k}^{(i)}$	Differential phase estimate at radar carrier derived from GNSS signal k, from satellite i
τ	Pulse delay
τ_pulse	Chirp duration
$\tau_u^{(i)}$	Signal travel time from GNSS satellite i to receiver u
φ_az	Phase of azimuth modulation
φ_{0u}	Constant phase offset at receiver u
φ_{0v}	Constant phase offset at receiver v
φ_gnss0	Initial GNSS carrier phase
$\varphi_u(t)$	Random phase noise process at receiver u
$\varphi_v(t)$	Random phase noise process at receiver v
$\rho_{uv}^{(i)}(t)$	Difference in distances from receivers u and v to satellite i
$\vec{\epsilon}_k$	Positioning error at instant k
$\vec{\rho}_\mathrm{hcw}$	Deputy position vector in HCW frame
$\vec{\rho}_\mathrm{zd}$	Relative position in zero-Doppler frame
ζ	Design factor for along-track reconstruction

Operators and Math Symbols

$<$	Less than
$>$	Greater than
$\lvert\cdot\rvert$	Absolute value
$\lvert\lvert\cdot\rvert\rvert$	Vector magnitude
arctan	Arctangent function

$\cdot$	Multiplication for scalars, dot product for vectors
$\dot{\cdot}$	Time derivative
δ_{ij}	Kronecker delta of indexes i and j
exp	Exponential operator
$\int$	Integral operator
$[\cdot]_{k\in\mathcal{I}}$	Vertically stack matrices over index set $\mathcal{I}$
$\mathrm{Cov}(\cdot,\cdot)$	Covariance operator
rect	Rectangular window function
$\mathrm{Var}(\cdot)$	Variance operator
$\sum$	Summation operator
$\times$	Cross product/Cross product operator
$\triangleq$	Equal by definition
$(\cdot)^{-1}$	Matrix inverse
$(\cdot)^{T}$	Transpose operator

General Deep Indexes

δei $\rightarrow$ hcw	Linear mapping from relative eccentricity and inclination vectors to HCW coordinates
δlei $\rightarrow$ hcw	Linear mapping from relative longitude, eccentricity and inclination vectors to HCW coordinates
at	Along-track
az	Azimuth
clock	Related to oscillator frequency/phase
ecef	Earth-Centered, Earth-Fixed frame
eci	Earth-Centered Inertial frame
hcw	Hill-Clohessy-Wiltshire frame
hcw $\rightarrow$ zd	Transformation from HCW to ZD frame
rng	Range
rx	Receive
tx	Transmit

u, v	Receiver indexes
xt	Cross-track
zd	Zero-Doppler frame

1 Introduction

1.1 Synthetic Aperture Radar Remote Sensing

RAdio Detection And Ranging (RADAR) is an active electromagnetic sensing technique used in the context of remote sensing for the mapping of Earth and planetary surfaces. A typical radar system consists of a pulsed microwave transmitter, an antenna, and a receiver and is often deployed aboard aircraft or spacecraft. The radar transmitter generates a signal and radiates it through the antenna. When the signal encounters a target, it is reflected and scattered. A portion of the scattered energy propagates back to the radar, where it is subsequently received by the antenna and the radar electronics. The delay between the signal transmission and reception is proportional to the distance to the target, while the intensity of the reflected pulse provides information about the target's reflectivity.

The principles of electromagnetic waves forming the basis of this remote sensing technique were first theorized by James Clerk Maxwell [1] and experimentally demonstrated by Heinrich Hertz in Karlsruhe [2] during the 19th century. The first radar device, designed for ship detection to prevent collisions in fog, was patented by Christian Hülsmeyer [3] in 1904. Subsequent advancements were made independently during World War II, leading to the widespread adoption of radar technology in aviation and other industries. In 1951, Carl Wiley achieved a breakthrough in radar remote sensing with the invention of the Synthetic Aperture Radar (SAR) principle [4, 5]. This technique makes it possible to achieve high resolution not only in the line-of-sight direction of the radar, but also in the movement direction of the radar platform by coherently combining Doppler information from echoes gathered along the platforms path [6]. The result is a high-resolution (e.g., metric) 2-D image of the illuminated scene, such as the example shown in Figure 1.1.

At first glance, SAR images resemble those obtained by optical remote sensing systems. However, SAR offers distinct advantages. It operates effectively day and night and is weather-independent, emitting its own radiation that is almost unaffected by cloud cover [7]. Moreover, SAR provides unique insights due to the specific ways microwaves interact with natural

Figure 1.1: SAR image of Brasilia, acquired by TerraSAR-X in October 2024.

or man-made scenes. Radar responds to the objects' structural (e.g., geometry, roughness) and dielectric properties (e.g., permittivity).

In 1978, NASA launched the first spaceborne Synthetic Aperture Radar (SAR) mission aboard the Seasat satellite. Seasat's SAR was used to image ocean surfaces, polar ice caps, and coastal regions [8]. Its success paved the way for many subsequent missions. Today, dozens of civil SAR satellites are in orbit, operated by space agencies and public institutions such as NASA, DLR, and ESA, as well as by private companies. Spaceborne SAR systems can collect data over large areas, up to hundreds of kilometers wide, with consistent, repeatable coverage on a global scale.

SAR also offers the distinctive capability of providing change detection and elevation information of an imaged scene through a technique called Interferometric SAR (InSAR) [9]. The technique is based on the comparison of two complex SAR images that have been acquired from slightly different positions or different times. InSAR allows for differential ranging with subwavelength accuracy (e.g., on the order of millimeters) over large areas and with high spatial resolution, capabilities that are unique in the field of remote sensing. Using multiple SAR images acquired from different positions with penetration capabilities enables a technique known as SAR tomography, which provides information on the structure of semi-transparent volumes such as glaciers, ice sheets, and forests [10]. SAR interferometry and tomography can be performed either by passing over a targeted scene at different times—referred to as repeat-pass interferometry and tomography—or by passing over the scene with two or more platforms simultaneously—referred to as single-pass interferometry and tomography.

Spaceborne SAR remote sensing has diverse applications, including geoscience and climate change research, environmental monitoring, Earth observation, 2-D and 3-D mapping, and change detection [9, 10, 11, 12], and constitutes one of the fundamental tools for understanding and monitoring our planet.

1.2 Bistatic and Multistatic SAR

A configuration with two satellites, where one transmits radar pulses, and the other receives them, is referred to as bistatic. When more than two satellites are involved, with one or several transmitting and several receiving the same transmitted pulses, the system is denominated multistatic. The traditional setup where the same satellite transmits and receives the pulses is denominated monostatic.

Bistatic and multistatic SAR offer the significant advantage of enabling single-pass interferometry, which provides many advantages compared to repeat-pass interferometry [13]. Most notably, it greatly reduces temporal decorrelation, i.e., loss of similarity (or coherence) between the two SAR images due to changes on ground and in the atmosphere. On ground, this decorrelation may result, for example, from changes in the vegetation cover (e.g., due to wind), changes in the snow cover, human activity, strong ground movement, etc. This makes single-pass better suited for monitoring dynamic environments such as forests, wetlands and urban environments. The reduced decorrelation makes it easier to isolate changes from topographic signatures, allowing the generation of more precise elevation models. Multistatic SAR further extends these capabilities by enabling single-pass tomography [14]. Bistatic and multistatic systems are also more energy-efficient since all satellites can make use of each transmitted pulse. Since the radar transmitter power is typically the primary driver of power consumption, sharing it among multiple satellites significantly reduces the total power required.

Additionally, multistatic SAR systems can enable system simplification by distributing antenna area, mass, and transmit power across multiple platforms through distributed SAR imaging. Conventional SAR systems are limited by the need for high transmit power and often large antennas to achieve acceptable image quality [15]. These requirements pose great challenges especially for small platforms, which typically lack the resources to support highly complex electronics with high power consumption. The issue becomes even more pronounced at lower frequency bands, since the required antenna size increases as operating frequency decreases.

Extensive research indicates that these limitations can be overcome using distributed SAR imaging based on digital beamforming (DBF) techniques, by coherently combining data from distributed platforms flying in close formation [16, 17, 18, 19, 20]. This approach could enable SAR imaging with multiple small, low-cost satellites operating cooperatively, offering benefits such as reduced development costs and time, improved performance, reconfigurability, and scalability [15].

Despite their great potential and wide range of applications, spaceborne bistatic and multistatic systems face several technical challenges, and only few of these systems have been put into operation. One key challenge is that bistatic and multistatic configurations use separate oscillators for the modulation and demodulation of the radar carrier. As a result, the low-frequency components of oscillator phase noise do not cancel out, unlike in monostatic systems [21, 22]. This phase noise can severely degrade performance in interferometric and tomographic applications [23]. This constitutes the so-called synchronization problem, which must be solved through accurate retrieval of the relative phase between platforms to enable these techniques.

Moreover, the performance of bistatic and multistatic systems is driven, among other factors, by the relative positions of the platforms, referred to as the baselines. Accommodating the stringent SAR positioning requirements with a formation flying satellite system is a complex problem that demands careful optimization [15]. For example, efficient distributed imaging may require positioning accuracy on the order of centimeters [24]. The natural orbital motion imposes restrictions that limit the coverage of spaceborne multistatic SAR systems. Deploying additional satellites to fill coverage gaps can mitigate this limitation, but at the expense of increased mission cost.

1.3 State-of-the-Art of Bistatic and Multistatic SAR

Table 1.1 highlights several notable current, proposed, and planned spaceborne bistatic and multistatic SAR systems, along with their primary applications. As shown in the table, one of the primary uses of such systems is the generation of Digital Elevation Models (DEMs). This focus reflects the critical importance of DEMs for a wide range of commercial and scientific applications. Fields such as hydrology, glaciology, forestry, geology, and land management rely on accurate and up-to-date information about the Earths surfaces and topography.

The German TanDEM-X mission, launched in 2010, had the primary objective of generating a global Digital Elevation Model (DEM) with the unprecedented accuracy below 2 m at 90% confidence level [25], much higher than the accuracy around 10 m achieved by the preceding NASA/JPL Shuttle Radar Topography Mission (SRTM) [26]. As the first bistatic SAR satellite mission, TanDEM-X remains the state-of-the-art in many aspects to this day [27, 28].

TanDEM-X implements a helix formation to enable a complete mapping of Earth's land and ice surfaces with a stable performance by using a small number of formation settings while guaranteeing a safe spacecraft operation without the necessity for autonomous control. Figure 1.2 shows the helix formation employed in the TanDEM-X mission. The two non-crossing orbits are shown on the left, while the effective baseline, which drives the interferometric sensitivity, is shown on the right.

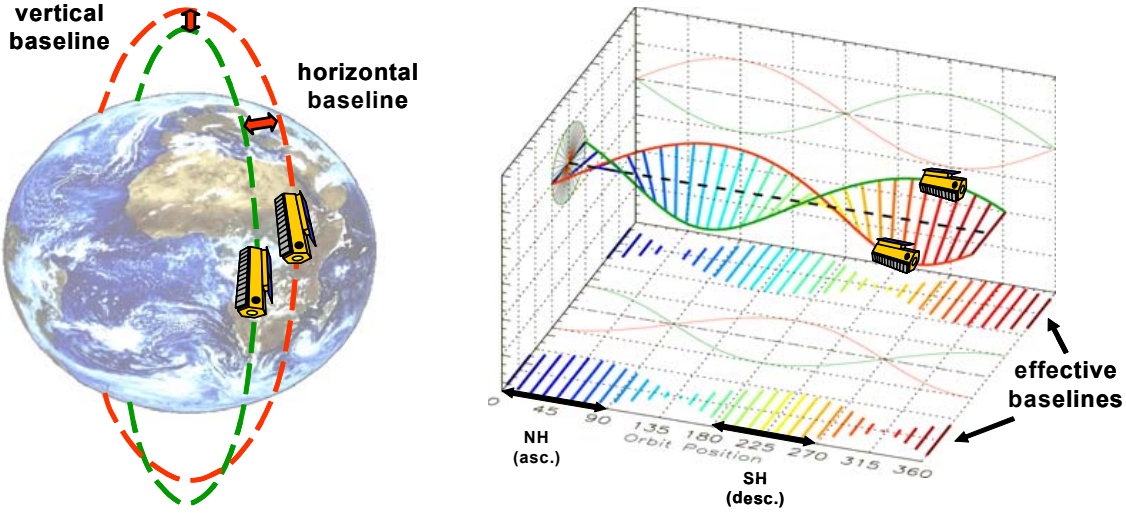

Figure 1.2: (left) Illustration of TanDEM-X mission flying in a helix formation, (right) effective baselines along the orbit [27].

For synchronization, TanDEM-X employs mutual exchange of radar pulses between the two satellites [29]. For this purposes, nominal radar acquisition is interrupted and the pulse is redirected to one of six dedicated synchronization horn antennas, as illustrated in Figure 1.3.

Currently, the German Aerospace Center (DLR) is proposing an X-band mission based on the MirrorSAR concept to enhance and continue the data legacy of TanDEM-X. This proposed mission features a multistatic system with four satellites, aiming to improve the DEM resolution by one order of magnitude compared to currently available DEM products [31].

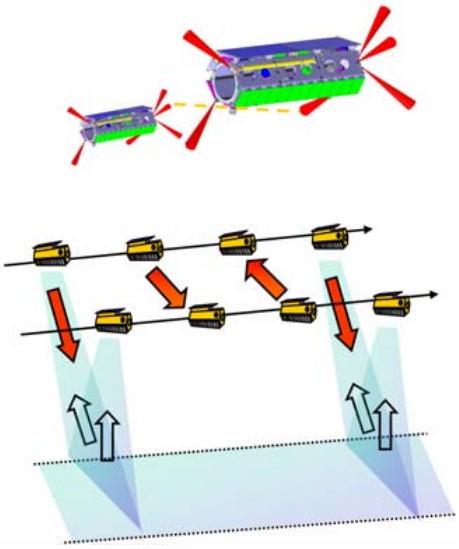

Figure 1.3: Illustration of synchronization links used in the TanDEM-X mission [30].

More recently, the L-band Chinese mission LuTan-1/2 was launched in 2022 with the primary objective of monitoring China's natural resources, generating DEMs, and monitoring land deformation [32]. It is the first spaceborne bistatic mission in L-band. In 2023, the multistatic mission Hongtu-1 was launched, implementing the configuration called interferometric cartwheel [33]. The mission, illustrated in Figure 1.4, consists of one active satellite and three passive receive satellites with the goal of generating DEMs and monitoring terrain changes. The cartwheel formation provides baseline diversity through the many possible satellite pairings, enabling frequently available set of appropriate baselines for high-performance results. Both LuTan-1/2 and Hongtu-1 also employ microwave links as synchronization solution, similar to TanDEM-X.

Figure 1.4: Illustration of HongTu-1 mission flying in a cartwheel formation [34].

ESA's tenth Earth Explorer mission, Harmony [35], is a testament to how powerful the concept of multistatic SAR can be, whilst not escalating the complexity of the individual satellites belonging to the system. It will consist of two passive companion satellites that will fly alongside the already operational Copernicus Sentinel-1C satellite [36]. By using a combination of SAR and thermal infrared measurements, the mission will provide high-resolution simultaneous measurements of surface stress, surface currents, sea surface temperature, and wave spectra over oceans, 3-D deformation vectors over solid Earth, and time series of surface elevation changes over volcanic areas and land ice masses [37].

The data will be used to measure subtle changes in Earth's surface that occur during events like earthquakes and volcanic eruptions to minimize the risks of such events. Additionally, the system will enable a better understanding of the relationship between ice mass loss and rising sea levels. Finally, the mission will monitor ocean surface conditions such as wind and currents to improve the ocean models and weather forecasting capabilities. Before Harmony, a similar mission concept, SESAME, was proposed, featuring two companion satellites for Sentinel-1 [38].

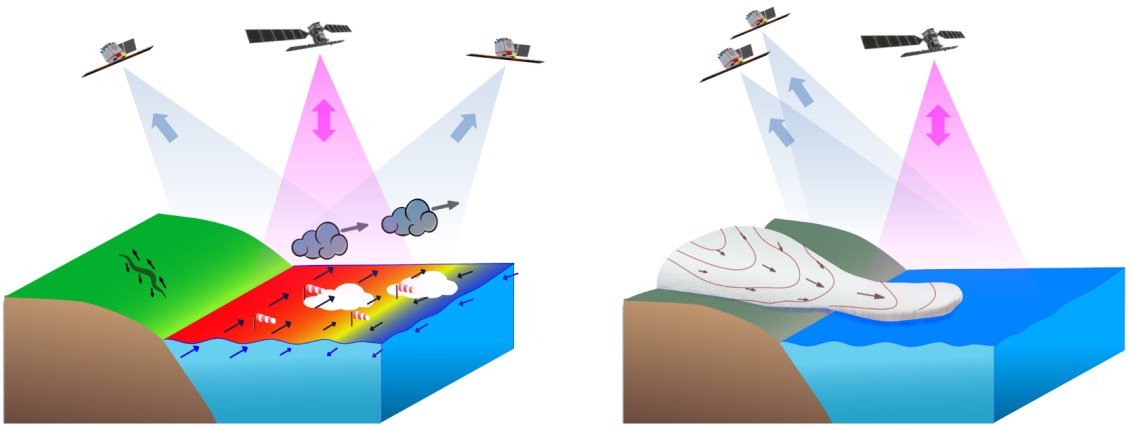

Figure 1.5: Illustration of Harmony's stereo (left) and cross-track (right) formations (Image credit: Harmony Mission Advisory Group) [37].

In addition to the missions mentioned above, several other concepts have been proposed. For example, in [39], the authors introduce the RODiO mission, consisting of four passive CubeSats with X-band radar receivers flying in formation and using the PLATiNO-1 SAR mission [40] as an illuminator of opportunity.

Table 1.1: Overview of major proposed, planned, and launched multistatic SAR missions. Missions without a defined launch date are labeled as Proposed Concepts (PC).

Mission	#Sat	Prime	Launch	Band	Main applications
TanDEM-X	2	DLR	2007	X	Digital Elevation Model (DEM) generation
SAOCOM-CS	2	CONAE / ESA	PC	L	Soil Moisture and vegetation analysis
LuTan-1/2	2	CNSA	2022	L	Deformation mapping and Digital Elevation Model (DEM) generation
Siwei Gaojing 2 (SuperView Neo 2)	2	Siwei	2022-2024	X	Digital Elevation Model (DEM)
HongTu-1/2	4	PIESAT	2023-2024	X	Deformation mapping and Digital Elevation Model (DEM) generation
PLATiNO-1	2	ASI	2026	X	Long-baseline bistatic SAR techniques
Harmony	3	ESA	2029	C	High-resolution measurements of surface stress, surface currents and wave spectra over oceans, 3-D deformation vectors over solid Earth, and time-series of surface elevation changes over volcanic areas and land ice masses
MirrorSAR	4	DLR	PC	X	Deformation mapping and Digital Elevation Model (DEM) generation
RODiO	4	ASI	PC	X	High-resolution imaging

1.3.1 SAR Synchronization

The need for precise time and phase synchronization solutions to enable bistatic and multistatic missions has been emphasized since the earliest proposals for such missions [42, 43]. Single-pass interferometry, arguably the most important application of bistatic and multistatic SAR, also has some of the most demanding synchronization requirements. For example, the generation of DEMs with TanDEM-X requires the knowledge of relative phases within a few degrees, corresponding to timing accuracy better than one picosecond, to avoid systematic modulations in the measurements [27]. As mentioned, synchronization with the required accuracy was achieved by exchanging pulses at the radar carrier frequency between the satellites through a direct microwave link [29].

Phase synchronization using dedicated synchronization links for spaceborne systems is currently the most established and widely applied solution in the few operational multistatic missions launched to date. The use of radar pulse exchange via synchronization links was extensively analyzed during the development of the TanDEM-X mission [44, 45]. In the LuTan-1/2 mission, synchronization pulses are transmitted between radar-pulses without interrupting radar operations [46]. This alternative approach to synchronization links was thoroughly analyzed as part of the mission's development [47, 48].

Although effective and flight proven, this solution requires additional hardware, including dedicated antennas, which could strain the mass and power budgets. Integrating direct links can be challenging due to mismatched development timelines among constellation elements, a common issue in companion SAR missions [49]. Synchronization links also add complexity to the RF design and antenna accommodation because of the requirement

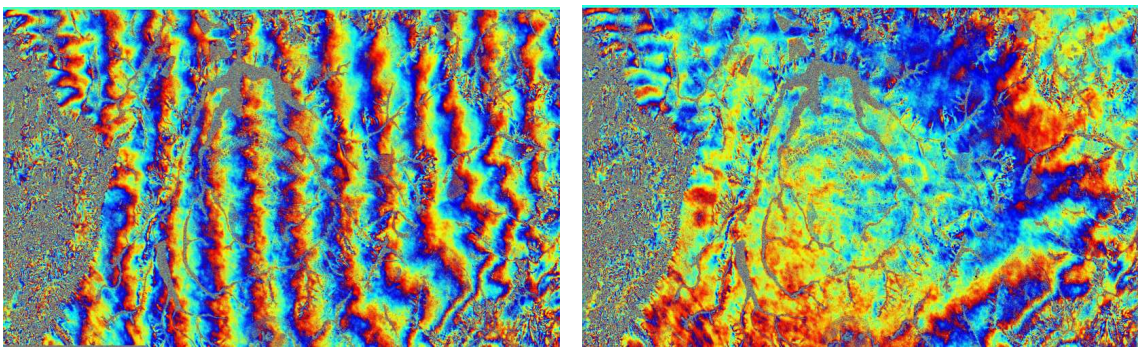

Figure 1.6: Synchronization results of bistatic 11-day repeat-pass interferometry with TanDEM-X. The interferogram before synchronization is shown on the left and after automatic synchronization on the right [41].

of full-sphere (4π steradian) coverage for operational applications. In constellations with multiple satellites, the need to multiplex synchronization signals to prevent interference further increases system complexity. Additionally, synchronization links are inherently cooperative, limiting their use across independently developed systems. The transmitter satellite must be equipped with all necessary hardware to support potential future companions, which in turn significantly constrains the design of those companion satellites.

As an alternative to synchronization links, data-based approaches can be used to compensate for the residual phase errors introduced by the differential phase drift of the oscillators. The earliest data-based phase correction techniques were developed to correct effects of turbulence in the troposphere and/or ionosphere [50], or residual motion effects and phase center variation effects on the SAR data [51], with a method named autofocus.

In [52], the authors proposed a processing chain including automatic synchronization for spaceborne bistatic SAR. The method was applied in the TanDEM-X mission, demonstrating for the first time the automatic synchronization in a spaceborne SAR system [41, 53]. The concept was later proposed as a synchronization solution for the SAOCOM-CS mission concept [54]. More recent advancements have focused on refining the technique [55, 56]. However, data-driven approaches produce estimates whose quality varies depending on the backscatter characteristics of the observed scene, limiting their suitability as a primary synchronization solution for interferometric SAR missions.

Most phase synchronization solutions can be categorized as either data-based approaches or synchronization links, though a few alternative methods have also been proposed. In [57], the authors propose a synchronization scheme for bistatic and multistatic radar based on the Global Positioning System (GPS), where the transmitter and the receiver in different platforms use an Ultra Stable Oscillator (USO) disciplined by the output pulse-per-second (PPS) signal generated by the embedded GPS receiver. It combines the advantages of the good short-term stability of high-quality USO with the long-term stability of the PPS signal generated by the GPS receiver. The technique, however, relies largely on the evaluation of the received data to compensate for time fluctuations of the PPS signal and the short-term phase variations of the USO and is, therefore, not self sufficient.

In [58], a complete system architecture, referred to as MirrorSAR, is envisaged to avoid the demodulation of the radar signals using a different oscillator, and in [59] a detailed analysis of the concept is presented. The approach consists of having the receivers act like transponders, re-routing

the radar echoes to another element of the constellation (i.e., the transmitter) having access to the oscillator used in the modulation. Although a MirrorSAR architecture requires a direct link between the satellites, not necessarily in the microwave range, it still keeps the potential for relevant spacecraft simplification by the possible removal of complete hardware blocks for demodulation, data storage, downlink, or digital control in the receivers. The technique, however, shares some drawbacks of synchronization links, namely the fact that it is fully cooperative. Additionally, it increases the complexity of the transmitting satellite, which needs to demodulate the signals of all the receiving satellites.

1.3.2 Multistatic SAR Formation Flying

One of the earliest proposed formations for multistatic SAR interferometry is the interferometric cartwheel, described in [42]. This formation is designed to ensure stability in both vertical and horizontal baselines with alternating pairs of satellites. Subsequently, the helix formation was proposed in [27] to provide passive safety for the bistatic systems in addition to baseline diversity. The non-intersecting orbits of the helix formation enable safe close formations that can rely on ground control, rather than requiring autonomous formation control. These two formations remain the only ones currently implemented in bistatic and multistatic missions.

Given the increasing interest in employing formation flying missions for SAR applications, considerable literature on orbit and formation design specific to these applications was published over the last decades.

In [60], the authors detail the formation acquisition and station-keeping strategy for the aforementioned TerraSAR-X/TanDEM-X bistatic formation, which was successfully demonstrated in 2012 [61]. In [62], the specific application of tomography is explored, where the author proposes formation geometries to fulfill the associated geometric requirements. In [63], the authors presented low-thrust maneuvers designed for multi-satellite formations applied to a concept study for distributed radiometry missions with satellites flying only a few meters apart. An autonomous relative orbit control algorithm using relative orbital elements for imaging with very high resolution is presented in [64]. In [65], formation flying under perturbation due to the Earth's oblateness is characterized, with a focus on high-precision DEM and Ground Moving Target Indicator (GMTI) applications.

In spaceborne distributed SAR imaging applications, specially those involving any kind of beamforming, control accuracy on the order of decimeters or even centimeters could be required during the imaging intervals [24]. For those applications, the guidance system must be optimized to counter only the necessary orbital disturbances. Otherwise, the accumulated compensation of short-term relative accelerations can quickly result in high fuel consumption. The relative motion when defining the formation control strategy highly impacts the feasibility of multistatic SAR systems.

The long-standing interest in the fields of distributed space missions and satellite rendezvous, spanning several decades and intensifying over the last thirty years, has driven the development of numerous relative motion models. Comprehensive compilations of these models can be found in [66] and [67]. The basic linear description of satellites flying in formation, where the primary satellite (or chief) follows a circular, unperturbed orbit, is provided by the well-known Hill-Clohessy-Wiltshire (HCW) equations. These equations were developed independently by Hill in 1878 [68] and Clohessy and Wiltshire in 1960 [69]. The former was developed to describe the motion of the Moon with respect to the Earth given that both are orbiting the Sun, and the latter in the context of satellite rendezvous. These equations were later expanded to incorporate additional factors in various formulations of satellite state dynamics.

Relative motion models are commonly derived either through a direct Cartesian parametrization in the Local Horizontal Local Vertical (LHLV) frame, as described in [70], or by modeling the motion using Relative Orbital Elements (ROEs) and, if necessary, transforming them into Cartesian coordinates via a linear transformation. The latter approach is examined in [71], which utilizes differences in orbital elements, and [72], which employs an alternative set of ROEs. Additionally, [73] presents an alternative method for modeling relative motion under disturbances, leveraging an equivalence between Keplerian and Cartesian representations identified in [74].

The inherent linearity of relative satellite dynamics for satellites at close distances allows the trajectory design and control problem to be formulated as convex optimization problems. This approach has been extensively explored in the literature, as demonstrated by recent works [75, 76, 77, 78, 79]. This thesis investigates the potential of formulating formation flying as a convex optimization problem to address one of the most challenging orbit design issues in spaceborne multistatic SAR applications: precision formation flying for distributed SAR imaging applications.

1.4 Motivation, Scope and Structure of the Thesis

This work addresses two of the most important challenges of multistatic SAR missions: synchronization and formation flying. Regarding the challenge of synchronization, this thesis aims to provide an alternative to existing solutions that is scalable, easy to implement, and capable of achieving phase accuracy around 1 degree, required for stringent interferometric applications. For that purpose, a solution is proposed using GNSS signals as a common reference, without requiring a dedicated subsystem or sophisticated data-based techniques.

Regarding the challenge of formation flying, this work aims to develop an optimization framework that accounts for SAR-specific formation geometry to derive the most suitable and practical formations for any set of input positioning requirements and constraints. Special focus is given to beamforming applications for distributed imaging that require almost constant baselines—either in along-track or cross-track direction—which is particularly challenging to obtain over sustained periods with natural formations.

This thesis is structured as follows. Chapter 2 presents the principles necessary to understand the work, and is divided into three themes: principles of conventional and distributed SAR systems and associated synchronization requirements; principles of Global Navigation Satellite Systems (GNSS) technology, of which the most known example is the GPS, including the segments of the GNSS systems, an overview of the working principles of GNSS receivers, and the GNSS observables; and fundamentals of satellite formation flying and satellite formation control. The following four chapters present the contributions of this thesis, with Chapters 3 and 4 addressing the synchronization problem and Chapters 5 and 6, addressing the problem of formation flying for multistatic SAR missions.

Chapter 3 introduces the proposed GNSS-based phase synchronization. It presents an error analysis and evaluates the performance in an orbital scenario through simulation. Chapter 4 presents an experimental proof-of-concept of the GNSS-based phase synchronization and a covariance matrix estimation algorithm to optimize the weighting of the GNSS carrier phase observables used in the relative phase estimation.

Chapter 5 presents a general method to find optimal natural formations (i.e., without the use of thrusters to counter Earth's gravity) considering the SAR appropriate Earth-fixed formation geometries and active imaging during limited sections of the orbit. The method is applied to find

viable multistatic SAR formation solutions for along-track reconstruction and cross-track beamforming. Chapter 6 presents an algorithm to derive an optimal guidance law to minimize fuel consumption, taking into account the full disturbances due to Earth's oblateness (without excluding the short-term periodic terms) while maintaining the excellent geometric fit obtained by the optimization algorithm based on a Keplerian model. The guidance law is tested in a realistic simulation environment for the along-track reconstruction and cross-track beamforming cases analyzed in the Chapter 5.

Chapter 7 closes the work with the conclusions, a summary of the results, and recommendations for the future research on synchronization and formation flying strategies for multistatic SAR missions.

1.5 Main Contributions

The main contributions of this work are listed below:

1. The proposition of a novel non-cooperative GNSS-based method to estimate the oscillator phase difference in bistatic and multistatic SAR systems complemented by an error analysis. The proposed technique uses GNSS carrier phase measurements, assuming that both radar and navigation receivers share the same master oscillator, and uses Precise Baseline Determination (PBD) to compensate for the effect of the differential motion between the platforms in the GNSS data. It operates non-cooperatively, requiring no direct communication between satellites, and is independent of the characteristics of the imaged area. These characteristics make it an ideal general synchronization solution in terms of scalability and compatibility across independently designed systems.
2. The proof-of-concept and the calibration procedure for the proposed GNSS-based phase synchronization. For the first time, a GNSS-based synchronization experiment incorporating a dedicated calibration and filtering approach demonstrates sufficient accuracy for bistatic and multistatic SAR missions in a lab environment.
3. A novel general optimization method for natural satellite formations (i.e., formations maintained without continuously counteracting gravitational acceleration) considering the SAR-relevant geometry in an Earth-fixed reference frame accounting for the limited

duty cycle typically imposed by power constraints in satellite operations. The method was applied to the distributed imaging concepts of azimuth reconstruction and beamforming in elevation. The approach successfully identifies natural formation configurations for distributed systems in along-track and cross-track for broad latitude ranges, achieving formations conforming with strict positioning requirements for a high portion of the orbit.

4. A novel general optimization method for quasi-natural formations, i.e., including minor systematic thrusting, considering SAR-relevant geometry in an Earth-fixed reference frame, in addition to a method for deriving a guidance law that optimizes fuel consumption for SAR formations. This method accounts for major systematic deviations from circular Keplerian relative motion, such as the slight orbital eccentricity in frozen orbits and Earths oblateness. Realistic simulations demonstrate for the first time low fuel budgets, of the order of a few meters per second per year, while meeting strict control requirements compatible with positioning-critical SAR applications, particularly beamforming. The method represents a significant step towards enabling high-performance distributed SAR systems with low-thrust, fuel-limited small platforms.

In general, the contributions comprise solutions for synchronization and formation flying compatible with low-complexity small platforms, which pave the way to enabling future inter-system compatibility, new bistatic and multistatic missions, and high-performance SAR products with lower-complexity, and lower-cost systems.

A part of the results presented in this doctoral thesis were published in the peer-reviewed journal papers [80, 81, 82], and in the conference papers [83, 84, 85, 86].

2 Fundamentals of Multistatic SAR, GNSS, and Formation Flying

This chapter presents the basic concepts required to understand the content of this thesis. It covers three main topics: (i) the fundamentals of SAR remote sensing, to provide context for the applications of the work developed, highlight its relevance for those applications, and clarify the driving requirements; (ii) the basics of GNSS, to support understanding of the general synchronization solution proposed in the thesis; (iii) the fundamentals of formation flying, to provide a basis for the more specific case of formation flying applied to multistatic SAR, discussed in later chapters.

Section 2.1 introduces the basics of conventional spaceborne SAR remote sensing. It provides a detailed explanation of the fundamental limitations of conventional SAR systems, specifically the trade-off between swath width and azimuth resolution, and the minimum required antenna area. Section 2.2 then introduces bistatic and multistatic SAR, followed by an explanation of the two main applications that are the focus of this work: SAR interferometry and distributed imaging. Finally, it introduces the critical technical challenge of phase synchronization in bistatic and multistatic SAR systems. For more in-depth information on conventional SAR, refer to [11].

Section 2.3 provides an overview of GNSS technology. It introduces the key components of the GNSS system and explains the fundamental working principles of GNSS receivers. Additionally, it presents a detailed mathematical description of the raw GNSS measurements, specifically the code delay and carrier phase observables. Extensive and detailed information on GNSS technology can be found in [87] and [88].

Section 2.4 introduces the fundamentals of satellite formation flying, which are essential for distributed SAR missions. It begins by describing the relative motion parametrization and dynamics, introducing the chief satellite-centered frame used in formation flying. The section then discusses the basic linear model developed by Hill and Clohessy-Wiltshire (HCW equations), which form the foundation for formation flying and satellite rendezvous, along with their analytical solutions. Finally, it introduces the Linear Quadratic Regulator (LQR), an optimal feedback control technique

which can be used for satellite formations with stringent positioning requirements. The basics of formation flying are necessary for understanding Chapters 5 and 6. More details on formation flying can be found in [89].

2.1 Synthetic Aperture Radar

2.1.1 SAR Principles

Figure 2.1 illustrates the SAR observation geometry of a typical SAR system.

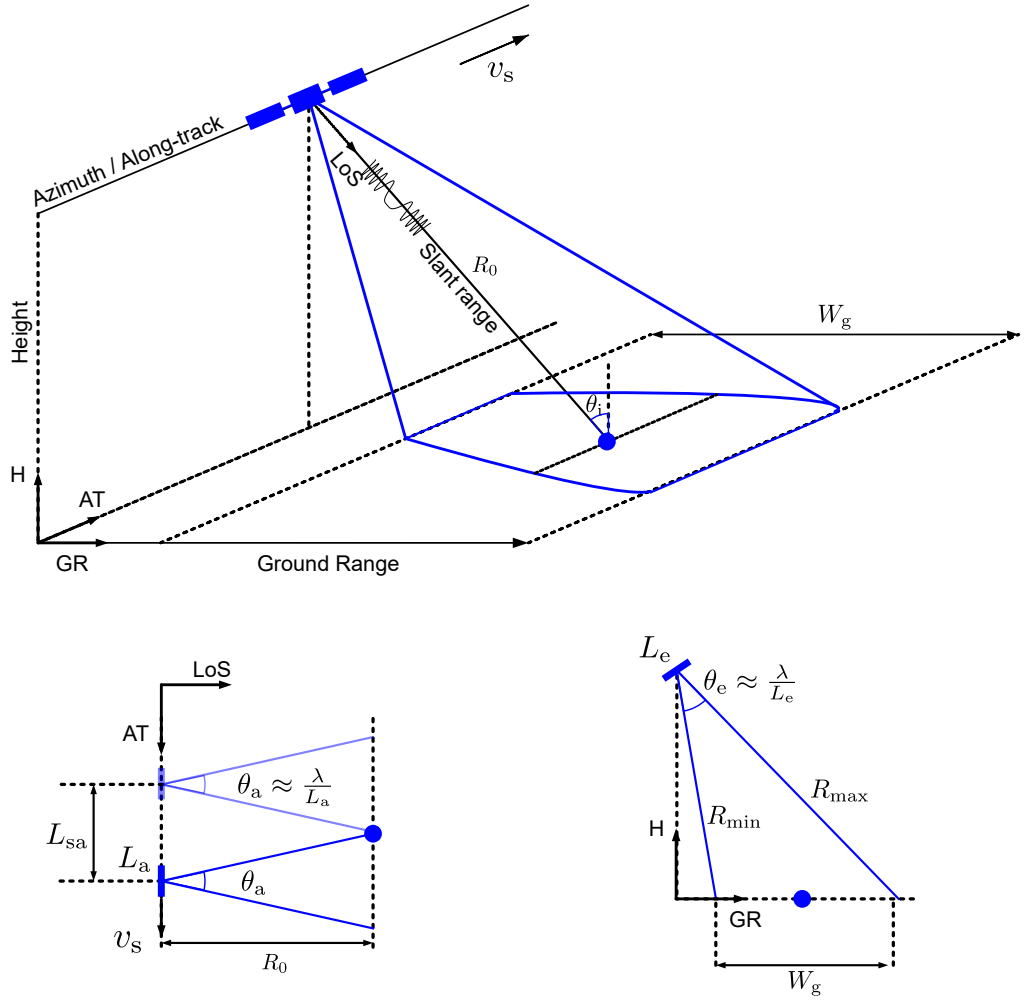

Figure 2.1: Illustration of the geometry of a typical SAR system. The radar platform moves in the along-track direction with a velocity v_s with respect to the scene, transmitting frequency-modulated pulses in the Line-of-Sight (LoS) direction. The length of the trajectory over which a point on the ground is illuminated (i.e., the synthetic aperture) is denoted L_{sa}. The ground swath width is denoted W_g.

The system consists of a side-looking radar mounted on an airborne or spaceborne platform, moving with velocity v_s, which transmits frequency-modulated pulses and receives echoes backscattered from the scene. The pulses, transmitted in the Line-of-Sight (LoS) direction at a set Pulse Repetition Frequency (PRF), illuminate the ground at an incident angle θ_i. The azimuth and elevation beamwidths, θ_a and θ_e respectively, are determined by the signal carrier wavelength λ and antenna dimensions L_a (azimuth) and L_e (elevation). The azimuth beamwidth determines the length of the trajectory over which a point on the ground is illuminated. The elevation beamwidth, together with the slant-range, determines the swath width (W_g).

The raw SAR data have the form of a 2D matrix with the rows representing different echoes from subsequent pulses, and the columns corresponding to time samples of the backscattered pulse. The raw data are typically downloaded from the platform and processed on ground into a focused radar image, a two-dimensional complex image of the scene in azimuth and range. Each pixel contains a complex reflectivity, with the amplitude containing information on the target reflectivity, and the phase carrying information on the range distance. The azimuth dimension corresponds to the position along the platform trajectory. The range corresponds to the distance to the target, derived from the time delay between transmission and reception. The side-looking geometry ensures that each ground-range position, as illustrated in Figure 2.1, has a distinct slant-range. Consequently, under flat terrain or low topographic variation, delay between transmission and reception is unique for each point on ground.

The commonly used pulses are linearly frequency-modulated waveforms (chirps), which enable longer pulse duration with higher transmitted energy while preserving high range resolution. The high resolution is recovered through pulse compression during the image generation, where the received signal is correlated with a replica of the transmitted chirp. The range resolution after compression δ_r is given by

$$\delta_r = \frac{c}{2B_r}, \tag{2.1}$$

where c is the wave propagation speed, and B_r is the transmitted signal bandwidth.

For a real aperture radar (i.e., without synthetic aperture processing), the azimuth resolution (δ_a) corresponds to the antenna footprint on ground along azimuth, as expressed in

$$\delta_\mathrm{a} \approx R_0 \cdot \theta_a \approx R_0 \cdot \frac{\lambda}{L_\mathrm{a}}, \tag{2.2}$$

where R_0 is the slant range. To improve the azimuth resolution, SAR systems coherently combine echoes received over time, synthesizing a larger aperture (i.e., a synthetic aperture) corresponding to the platform's traveled distance while illuminating the target (L_sa). Given the relation

$$L_\mathrm{sa} \approx R_0 \cdot \theta_\mathrm{a} \approx R_0 \cdot \frac{\lambda}{L_\mathrm{a}}, \tag{2.3}$$

the azimuth resolution, using the synthetic aperture length (L_sa) instead of the physical antenna length (L_a), becomes

$$\delta_\mathrm{a} \approx R_0 \cdot \frac{\lambda}{2L_\mathrm{sa}} \approx \frac{L_\mathrm{a}}{2}. \tag{2.4}$$

where the factor 2 appears because of the two-way path from transmission to reception. This resolution is far higher than the real aperture radar, and often enables resolutions comparable to the achieved range resolution.

2.1.2 SAR Signal Model

The transmitted radar signal (u_tx) is typically a linear frequency-modulated (FM) signal, known as a chirp, modulated onto a carrier. The baseband signal $u_\mathrm{tx,b}$ as a function of time t is described by the equation

$$u_\mathrm{tx,b}(t) = w_\mathrm{tx}(t) \cdot \exp\left(\mathrm{j} \cdot \pi \cdot K \cdot t^2\right), \tag{2.5}$$

where K is the chirp rate, and $w_\mathrm{tx}(t)$ is the window function given by

$$w_\mathrm{tx}(t) = \mathrm{rect}\left(\frac{t}{\tau_\mathrm{pulse}}\right), \tag{2.6}$$

where τ is the chirp duration, and rect is the rectangular function, defined as

$$\mathrm{rect}(x) = \begin{cases} 1, & \text{if } |x| \leq \frac{1}{2} \\ 0, & \text{otherwise} \end{cases}. \tag{2.7}$$

The modulated transmit signal is then given by

$$u_{\mathrm{tx}}(t) = u_{\mathrm{tx,b}}(t) \cdot \exp\left(\mathrm{j} \cdot 2\pi \cdot \frac{\mathrm{c}}{\lambda} \cdot t\right). \tag{2.8}$$

After undergoing propagation, backscattering, return propagation, and downconversion, the received baseband signal after IQ demodulation $u_{\mathrm{rx,b}}(t)$ is given by

$$u_{\mathrm{rx,b}}(t) = \Gamma \cdot w_{\mathrm{a}}(t) \cdot \underbrace{u_{\mathrm{tx,b}}\left(t - \frac{2R(t)}{\mathrm{c}}\right)}_{s_{\mathrm{rng}}(t)} \cdot \underbrace{\exp\left(-\mathrm{j} \cdot 2\pi \cdot \frac{2R(t)}{\lambda}\right)}_{s_{\mathrm{az}}(t) = e^{-\mathrm{j}\cdot\varphi_{\mathrm{az}}(t)}}, \tag{2.9}$$

where Γ is a complex constant accounting for the scene reflectivity, propagation attenuation, chain gains, and other losses; w_{a} represents the weighting by the joint transmit and receive antenna pattern; and $R(t)$ is the range history, i.e., the time-varying distance from the platform to the target.

Equation (2.9) shows that the received signal comprises a product of the weighted reflectivity signal with two modulation components: one range modulation corresponding to the time-delayed backscattered chirp (s_{rng}), and another corresponding to the azimuth modulation (s_{az}), whose phase depends on the time-varying range history $R(t)$ due to platform motion, with the factor 2 accounting for the two-way signal path (to the target and back).

Figure 2.2 illustrates the raw SAR data acquisition for a point target as the satellite moves along its trajectory while transmitting pulses at regular Pulse Repetition Intervals (PRI = 1/PRF), shown as white circles. The frequency modulated chirps are backscattered by the target and the signal is recorded within a time window between the reception time of the signal at near-range and at far-range (R_{min} and R_{max}, respectively, as illustrated in Figure 2.1). The received signal in range corresponds to the transmitted chirp, and it is received within echo windows. This window moves describing approximately a parabola over the synthetic aperture, given the reception delay varies with the range to the point target. In the receiver, the signal is sampled at a rate that is larger than the signal bandwidth, ensuring the proper range information recovery after processing.

The phase variation (φ_{az}), indicated in (2.9) can be approximated by a second-order Taylor series expansion, resulting in

$$\varphi_{\mathrm{az}}(t) = -\frac{4\pi}{\lambda} \cdot R(t) \approx -\frac{4\pi}{\lambda} \cdot \left(R_0 + \frac{v_{\mathrm{g}} \cdot v_{\mathrm{s}}}{2R_0} \cdot t^2\right), \tag{2.10}$$

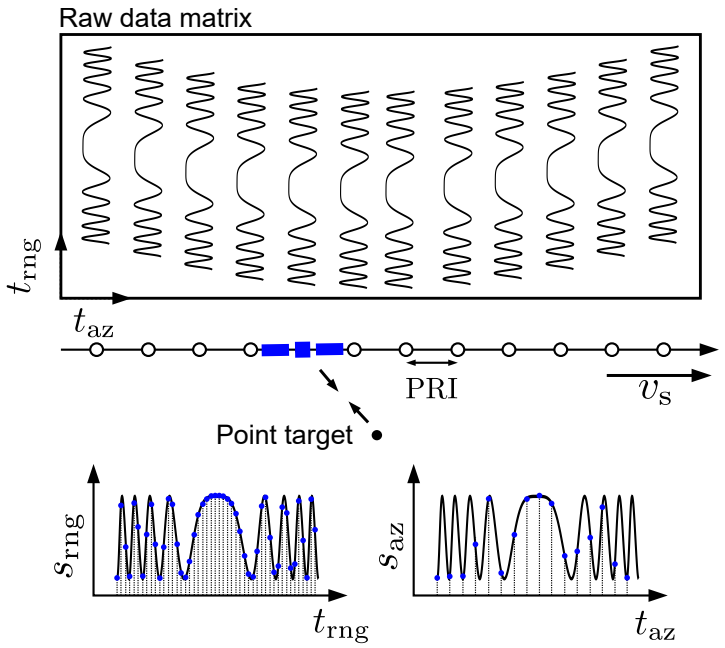

Figure 2.2: Illustration of the SAR raw data acquisition and the respective azimuth (s_{az}) and range (s_{rng}) modulation components of the signal. The platform moves with a velocity v_{s} and records backscattered signal from a point target.

where v_{s} is the satellite velocity, and v_{g} is the velocity of the antenna footprint. Equation 2.10 shows that the azimuth modulation signal (s_{az}) describes approximately a chirp as the satellite travels along the synthetic aperture length (i.e., the so-called slow-time), similarly to the s_{rng}.

The associated expected azimuth modulation frequency f_{az}, corresponding to the Doppler frequency with respect to the target, is then given by

$$f_{\mathrm{az}}(t) = \frac{1}{2\pi} \cdot \frac{\partial}{\partial t} \varphi_{\mathrm{az}}(t) \approx -\frac{2v_{\mathrm{g}} \cdot v_{\mathrm{s}}}{\lambda \cdot R_0} \cdot t\,. \tag{2.11}$$

The goal of SAR processing is to extract reflectivity and phase information in both the range and azimuth directions to produce the high-resolution complex (i.e., phase preserving) reflectivity map of the observed scene. This process can be conceptually described as the application of two matched filters, one in range and one in azimuth direction.

The first step is to compress the transmitted chirp signals into short pulses. To reduce computational complexity, this is done in the frequency domain by multiplying each range line by the complex conjugate of the transmitted chirp's spectrum. This yields a so-called range-compressed image. Azimuth compression follows the same principle: the signal is correlated with a reference function, which is the complex conjugate of the expected azimuth response from a point target on the ground. Between these two

stages, range cell migration must be corrected. This effect is the apparent shift of a targets range bin caused by changes in slant range as the platform approaches and then recedes from the target.

2.1.3 Ambiguities and Minimum Antenna Area

In order to successfully perform the azimuth compression, the azimuth modulation must be sampled at an appropriate rate, following Nyquist's criterion. An insufficient sampling rate results in aliases, showing as shifted repetitions of the scene superimposed to the true image. These aliases constitute the so-called azimuth ambiguities. As illustrated in Figure 2.2, the azimuth modulation is sampled through pulse transmission and reception in slow-time, with the corresponding sampling frequency determined by the PRF.

The Doppler bandwidth determines the necessary system PRF to avoid azimuth ambiguities. It is determined by the synthetic aperture length L_{sa}, or equivalently, the illumination time $T_{\text{sa}} = L_{\text{sa}}/v_{\text{s}}$, and can be calculated as

$$B_{\text{az}} = f_{\text{az}}\left(\frac{T_{\text{sa}}}{2}\right) - f_{\text{az}}\left(\frac{-T_{\text{sa}}}{2}\right) \approx 2v_{\text{g}} \cdot \frac{L_{\text{sa}}}{\lambda \cdot R_0}. \tag{2.12}$$

Replacing from (2.3) into (2.12) leads to the equation that determines the necessary PRF as a function of the nominal azimuth resolution

$$\text{PRF} \geq B_{\text{az}} \approx \frac{v_{\text{g}}}{\delta_{\text{a}}}. \tag{2.13}$$

This equation shows that a fine azimuth resolution requires a long synthetic aperture, which in turn demands a high PRF to sample the fast signal variations at the beam edges due to high Doppler at those locations [7].

In principle, the PRF could be defined exclusively based on this criterion. However, if the PRF is too high, the reception windows of different pulses could overlap, causing the so-called range ambiguities. This problem is illustrated in Figure 2.3, which shows the pulse transmission and reception timing for one example with range ambiguity and another without it.

In Figure 2.3, the rectangles indicate transmitted pulses, while the irregular shapes represent received echoes. To facilitate visualization, pulses are drawn alternating red and blue. Both graphs illustrate the same system with a given swath width and the same maximum range (R_{max}) and minimum range (R_{min}). The top plot shows the pulse transmission and reception timing for a high PRF (and thus low PRI), while the bottom plot

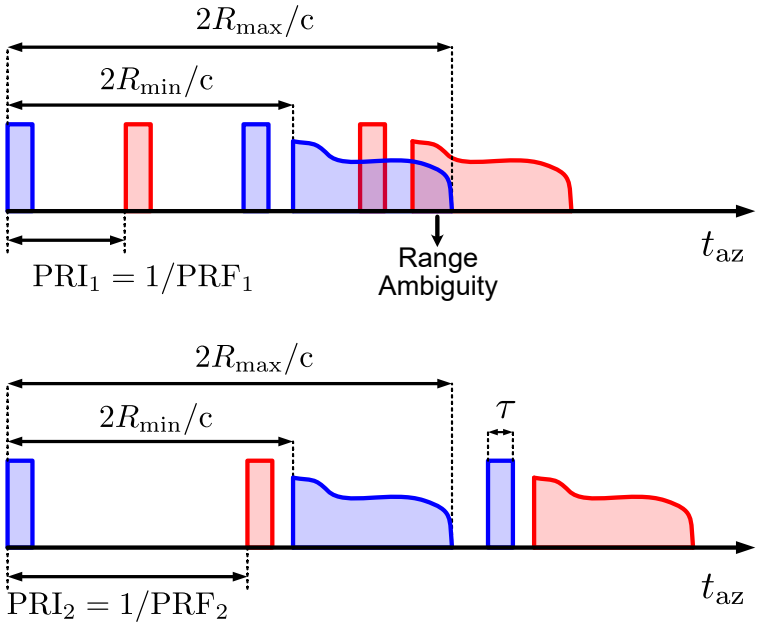

Figure 2.3: Illustration of the range ambiguities in SAR. For the same system with a given minimum and maximum range ($R_{\min}$ and $R_{\max}$), a higher PRF on the top and a lower PRF on the bottom. The high PRF results in the overlapping of consecutive received pulses, resulting in the so-called range ambiguities.

illustrates the reception timing for a low PRF, and thus a high PRI. In the high PRF case, the echo window of two consecutive pulses overlap, unlike in the lower PRF case, where there is enough time between transmissions to allow for the reception of the backscattered pulse.

Considering the flat-Earth approximation—i.e., assuming the swath is narrow enough so the Earth curvature can be ignored—the constraint on the PRF to guarantee that there is enough time between two transmissions for the full reception of the signal is given by

$$\mathrm{PRF} \leq \frac{c}{2 \sin \theta_i \cdot W_g}, \tag{2.14}$$

where W_g is the ground swath width, as illustrated in Figure 2.1. This equation shows that a wider swath results in a larger difference between near and far range, requiring longer pulse receive windows. This, in turn, limits the available time between transmissions (PRI) and therefore the allowable azimuth bandwidth for unambiguous imaging. The conflicting constraints (2.13) and (2.14) express the fundamental trade-off in SAR between azimuth resolution and swath width, which limits the system performance.

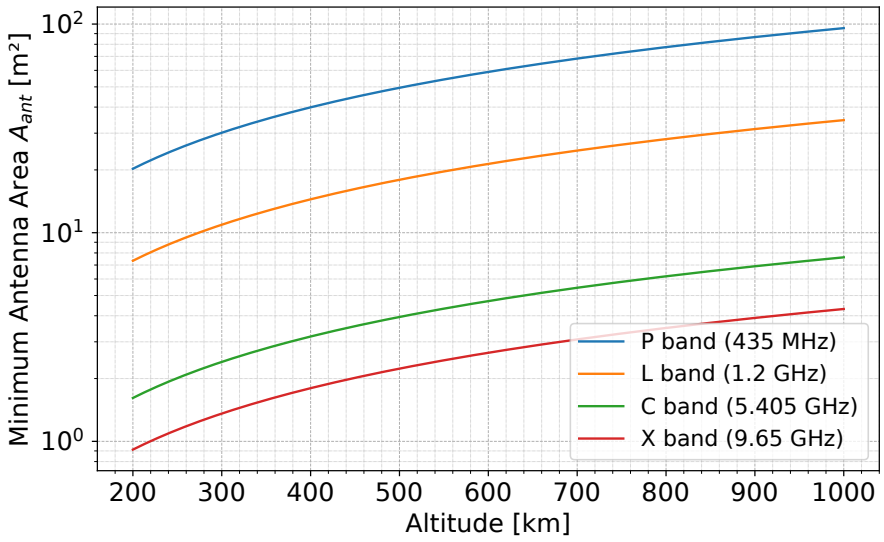

Figure 2.4: Minimum antenna requirement for different altitudes and frequencies. The incident angle is 45°.

Equations (2.13) and (2.14) also lead to a fundamental constraint on the minimum radar antenna area (A_{ant}). Assuming a rectangular antenna, the following limitation can be derived

$$A_{\text{ant}} = L_{\text{e}} \cdot L_{\text{a}} > \frac{4\lambda \cdot R_0 \cdot v_{\text{s}} \cdot \tan\theta_i}{\text{c}}. \tag{2.15}$$

This equation is known as the minimum antenna area constraint for SAR [90]. Figure 2.4 shows this constraint for different altitudes and frequencies, assuming an incident angle of 45°.

As shown in the plot, the required minimum antenna area, on the order of tens of squared meters at lower frequencies, necessitate either very large satellites or deployable antennas. This, in turn, increases weight, cost, risk, and system complexity.

Note that there exists concepts which allow for operating outside the minimum antenna area constraint [18, 91], but these approaches generally involve other trade-offs, like increased system complexity, heavier calibration demands, or resolution degradation.

2.2 Bistatic and Multistatic SAR

Bistatic systems are configurations with two radar satellites, in which one transmits the pulses and the other, or both, receive the backscattered echoes.

Multistatic systems involve three or more satellites, with one or more transmitting the pulses and the others, or all, receiving the same backscattered echoes. These architectures are inherently power-efficient, since transmit power is shared, and they enable applications distinct from those of monostatic SAR systems. The following subsection explains two key applications that will drive the targeted requirements for the solutions presented in the subsequent chapters: SAR interferometry and distributed SAR imaging.

2.2.1 SAR Interferometry

SAR interferometry (InSAR) is a remote sensing technique in which the phase information between two complex SAR images acquired from different positions is used to derive additional geophysical parameters. In cross-track interferometry, a baseline orthogonal to the line-of-sight between two observations of the same scene adds sensitivity to the terrain elevation, enabling the generation of 3-D information about the scene. In along-track interferometry, a baseline in the flight direction adds sensitivity to motion along the ground by detecting the Doppler shift between the two images.

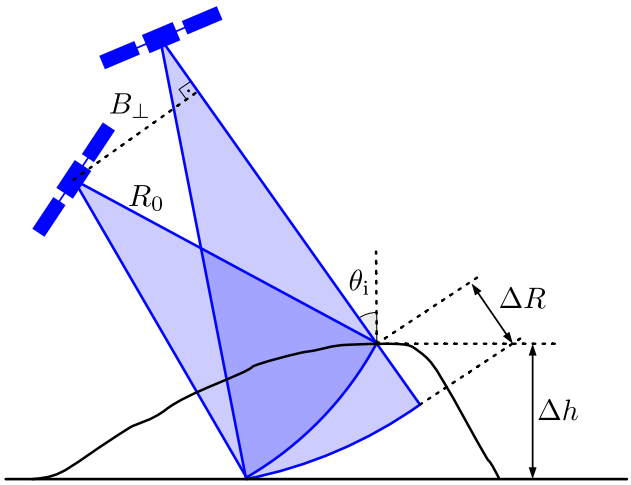

Figure 2.5: Geometric principles of Interferometric Synthetic Aperture Radar (InSAR). Two slightly offset satellite positions, characterized by the perpendicular baseline $B_\perp$, acquire SAR images of the same area. The difference in the path length (ΔR) to a point on the terrain, observed at an incident angle (θ_i), allows for the estimation of the terrain height difference (Δh).

Interferometric processing begins by co-registering the two SAR images, aligning corresponding pixels between them. The phase difference between matched pixels is then computed to generate a two-dimensional

phase difference map denominated interferogram. Figure 2.5 illustrates this principle for cross-track interferometry—central to this thesis due to its stringent synchronization requirements—applied to determine the relative height of a point located at the top of an elevated surface.

For large slant-range distances (R_0) and short perpendicular baselines ($B_\perp$), a valid approximation for spaceborne geometries, a difference in topographic height Δh with respect to a reference surface introduces a range difference ΔR between the two satellite observations, which can be approximated as

$$\Delta R \approx \frac{B_\perp}{R_0 \cdot \sin(\theta_i)} \cdot \Delta h\,, \tag{2.16}$$

In bistatic mode, this range difference leads to a phase difference $\Delta\phi$ between the two SAR images given by

$$\Delta\phi = \frac{2\pi}{\lambda} \cdot \Delta R\,. \tag{2.17}$$

Therefore, the interferogram carries information on the topography of the imaged area. Cross-track interferometry can be performed either by repeating passes at slightly different positions relative to the scene (known as repeat-pass interferometry) or by having two platforms simultaneously imaging the same scene (single-pass interferometry) [9]. The latter avoids the temporal decorrelation between images which arises when the backscatter distribution of the scene changes between the two acquisitions.

2.2.2 Distributed SAR Imaging

Numerous techniques have been developed to enable SAR imaging with antenna areas smaller than those dictated by the minimum antenna area constraint, particularly through the use of multistatic systems [92, 93]. In this approach, the receive antenna is effectively divided into multiple subapertures, each mounted on a different satellite with an independent receive chain, while all illuminate the same ground area. Figure 2.6 illustrates these concepts, highlighting also the equivalent multichannel monostatic system.

Distributed imaging with multistatic systems still remains a conceptual approach, with a few mission concepts proposed in the recent years [39, 94, 95]. This approach has the potential to enable SAR imaging using small, simple individual satellites, which could be produced in series, resulting in a system with high redundancy and reduced risk. These concepts can

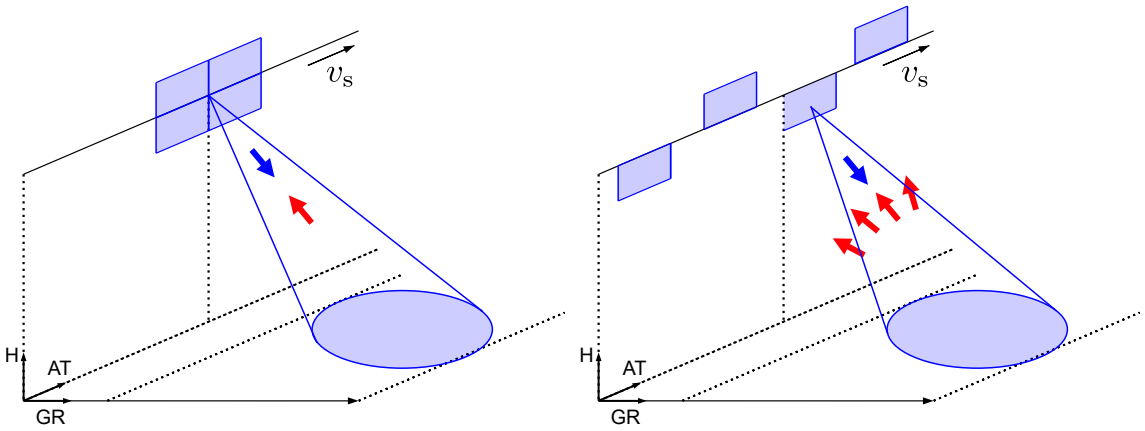

Figure 2.6: Multichannel SAR systems employing digital beamforming to mitigate azimuth and/or elevation ambiguities. The left panel illustrates a monostatic multichannel configuration, while the right panel depicts a distributed multistatic system.

distribute the mass, power and antenna area of a hypothetical large, costly, and complex monostatic system across multiple satellites. Additionally, these systems would allow for physical reconfiguration and therefore increased flexibility. However, their main drawbacks include the increased complexity due to synchronization, detailed in Section 2.2.3, and stringent relative positioning requirements [15].

Figure 2.7 illustrates a simplified processing chain for distributed imaging with multistatic systems. Received signals are downconverted, digitized, and downlinked to a ground station. The data then undergoes signal reconstruction, generally consisting of Digital Beamforming (DBF), which allows for synthesizing narrow beams that suppress ambiguities by combining complementary information from the different channels. The result is a single image with highly improved quality compared to the one obtained by the individual satellites. An additional synchronization step is required prior to reconstruction to eliminate the effect of the different clock drift between the platforms.

The apertures are distributed across multiple platforms flying in formation and are displaced in the antenna plane, either in the azimuth (along-track) direction or in elevation (i.e., perpendicular to the along-track direction in the antenna plane). The theoretical system illustrated in Figure 2.6 combines both configurations.

The concept where apertures are distributed in the elevation direction is called beamforming in elevation. In this concept, the PRF is selected to prevent azimuth ambiguities, and the individual apertures are intentionally smaller than the minimum required to prevent range ambiguities. This

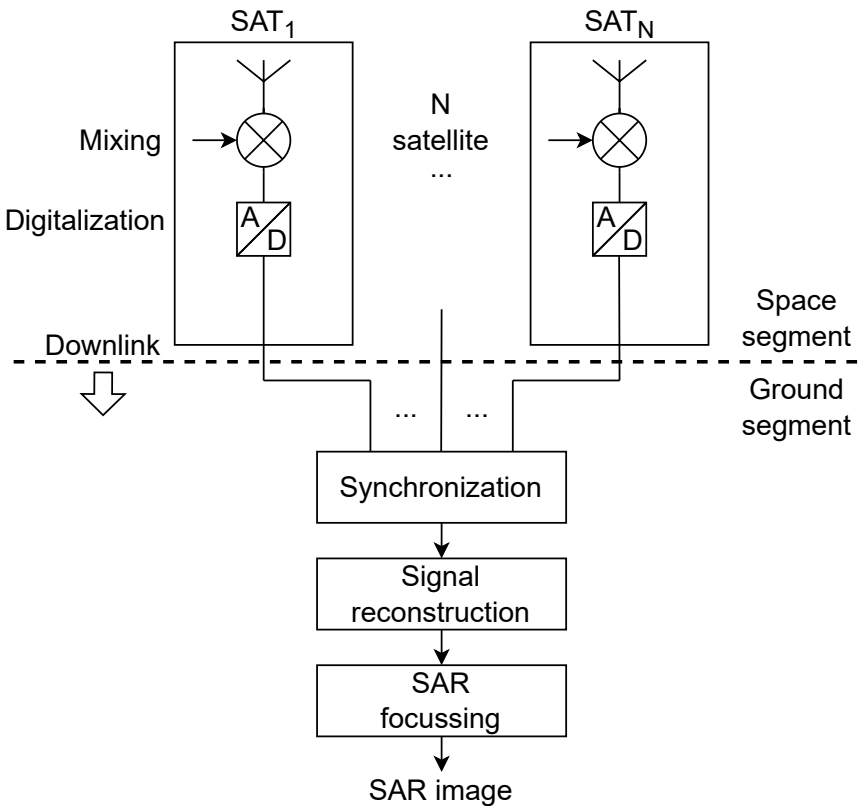

Figure 2.7: Block diagram of a multistatic system for distributed imaging. The signals are mixed, digitized, and transmitted to the ground segment by each satellite, where they undergo a pre-processing stage involving synchronization of individual satellite clocks. The signals are then processed in the subsequent digital beamforming stage, similar to a monostatic multi-channel system.

design results in a wide beam, and thus a wide swath, but high range ambiguities. By applying varying weights to the SAR data from each aperture, an adaptive effective antenna pattern is generated which suppresses the ambiguities [96].

The concept where antennas are distributed in the along-track direction requires azimuth reconstruction, which can also be interpreted as beamforming in azimuth. In this concept, the apertures are positioned to sample complementary parts of the range history. This ensures that combined samples meet the Nyquist criterion with a reduced PRF, sufficient to avoid range ambiguities.

Note that a generic case, as illustrated in Figure 2.6, would require a more complicated 2D reconstruction. Details on the processing, however, is out of the scope of this thesis.

2.2.3 The Phase Synchronization Problem

The multistatic SAR applications discussed in this section require precise phase synchronization between the radar payloads, as the radar carrier is modulated and demodulated using independent oscillators. This problem is illustrated in Figure 2.8.

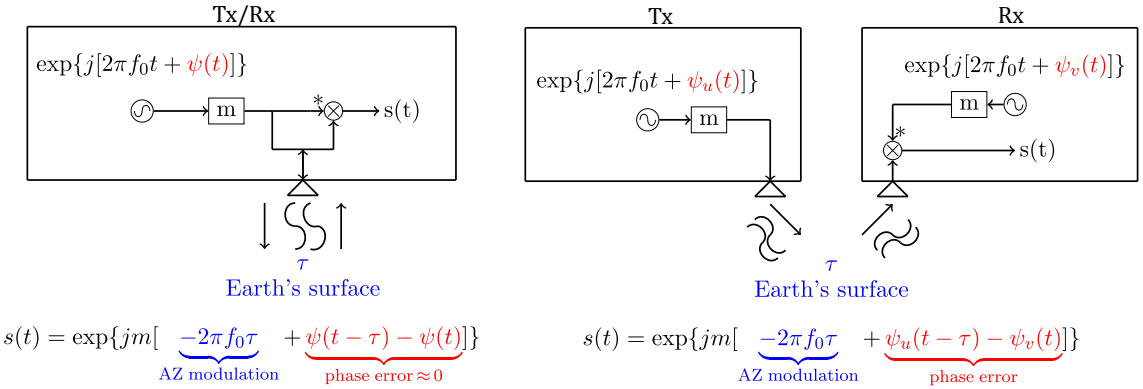

Figure 2.8: Comparison between monostatic (left) and bistatic (right) SAR regarding the impact of the oscillators' phase noise. In the monostatic SAR depicted on the left, the shared oscillator ensures that its phase noise ψ is eliminated during signal demodulation, and only the phase due to the round-trip delay τ to the target remains. Conversely, the multistatic SAR on the right, employing independent oscillators, results in residual phase noise in the received signal, affecting image quality.

In the monostatic case, shown on the left, the carrier signal phase is compared with the delayed version caused by the pulse delay τ, which is negligible compared to the time scales of the differential oscillator phase variations for typical SAR oscillators. As a result, the oscillators phase deviation ψ, comprising both phase noise and phase offset, mostly cancels out. In the bistatic case, shown on the right, the phase deviations from the transmitter ψ_u and receiver ψ_v do not cancel out, and the resulting residual phase introduces additional and unwanted variations on top of the azimuth phase modulation.

The implications become clearer when considering (2.9). This equation assumes a monostatic system, where the phase evolution over azimuth of a point target follows a known function of the range history. This a priori knowledge of the azimuth phase modulation of a target at a given range is used to obtain high azimuth resolution, as explained earlier. In the multistatic case, the time-varying phase difference between the oscillators is added to the range history component. Consequently, matched filtering

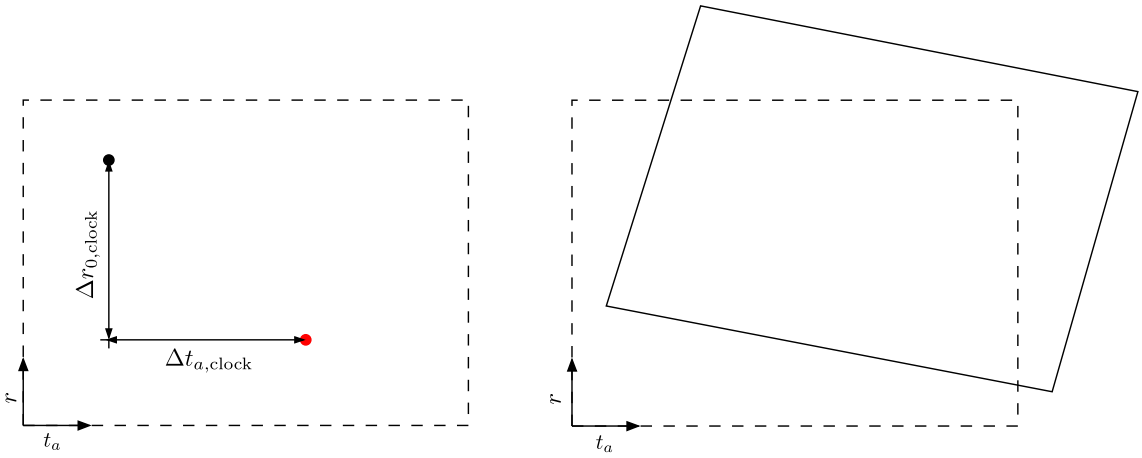

Figure 2.9: Example of differential clock errors impact on (left) the focused targets and on (right) the focused image assuming positive $\delta f_{0,\text{clock}}$. The red dot represents the introduced phase errors to the point target.

with the phase signal corresponding to the expected azimuth phase history will not properly compress the impulse response, leading to various issues in the SAR image, such as time-variant shifts, spurious sidelobes, and broadening of the impulse response [23].

The phase error introduced by the operation with different oscillators in bistatic SAR data is proportional to the difference in oscillator phase output between the transmitter and the receiver [21, 22] as follows

$$\psi_{\text{clock}}(t) = \psi_{0,\text{clock}} + 2\pi \cdot \int_{t_0}^{t} \delta f_{\text{clock}}(\tau) \cdot \mathrm{d}\tau \,, \tag{2.18}$$

where $\psi_{0,\text{clock}}$ is a constant not relevant for the analysis, and $\delta f_{0,\text{clock}}$ is a random process representing the instantaneous difference in the radar carrier of the transmitter and the receiver. The term δf_{clock} can be further expressed as a constant carrier offset $\delta f_{0,\text{clock}}$ and a zero-mean random process $\delta f_{\text{st,clock}}$ as follows

$$\delta f_{\text{clock}}(t) = \delta f_{0,\text{clock}} + \delta f_{\text{st,clock}}(t) \,. \tag{2.19}$$

Figure 2.9 illustrates the approximate effect of the clock error on a focused point target (left) and on the focused image (right). The focused point target suffers 2-D positioning errors, slight defocusing, and interferometric phase errors, represented by the color change in the left image. The focused image suffers a distortion in range and azimuth roughly proportional to the carrier offset between the transmitter and receiver, as well as a bulk range offset due to the uncertainty in the bistatic time reference, as shown in the right drawing.

Single-pass interferometry using bistatic or multistatic systems relies on detecting small phase changes between platforms, corresponding to a fraction of the wavelength, making synchronization especially critical for these applications. The introduced phase error contaminates the topographic signatures as per (2.17), compromising its utility if not addressed [97]. Since height variations are proportional to the measured phase, achieving improved height accuracy requires higher phase sensitivity, which in turn imposes more stringent requirements on phase synchronization.

To solve this issue, a synchronization step must be added to compensate for clock phase differences in the raw SAR data before conventional SAR processing. This requires estimating phase differences, either by inferring them from the SAR data itself or by employing external synchronization methods [98].

2.3 Fundamentals of Global Navigation Satellite Systems

2.3.1 GNSS System Overview

Global Navigation Satellite Systems (GNSS) is the general term for constellations of satellites that provide global positioning and navigation through trilateration. The most widely known GNSS is the Navigation by Satellite Ranging and Timing Global Positioning System (NAVSTAR GPS), owned by the United States Space Force. The American GPS and the Soviet/Russian *Globalnaya Navigazionnaya Sputnikovaya Sistema* (GLONASS) were the first GNSS to be developed, becoming operational in 1993. Europe and China developed their own systems, named Galileo and Beidou, which went into operation in 2016 and 2012, respectively. In addition to the global ones, there are regional satellite navigation systems, including the Japanese Quasi-Zenith Satellite System (QZSS) and the Indian Navigation with Indian Constellation (NavIC).

Figure 2.10 shows an overview of the GNSS architecture components. The system consists of a space segment, a control segment and the user equipment. The space segment comprises the constellation of satellites, also named space vehicles (SV), which broadcast to users globally, and exchange telecommands and telemetry with the control segment. For global systems, i.e., GPS, GLONASS, Galileo, and Beidou, the satellites are uniformly distributed in 3 to 6 orbital planes, with inclinations of 64.8 degrees for GLONASS and around 55 degrees for the other systems. The satellites operate in Medium Earth Orbits (MEO), at altitudes between 19,000 km

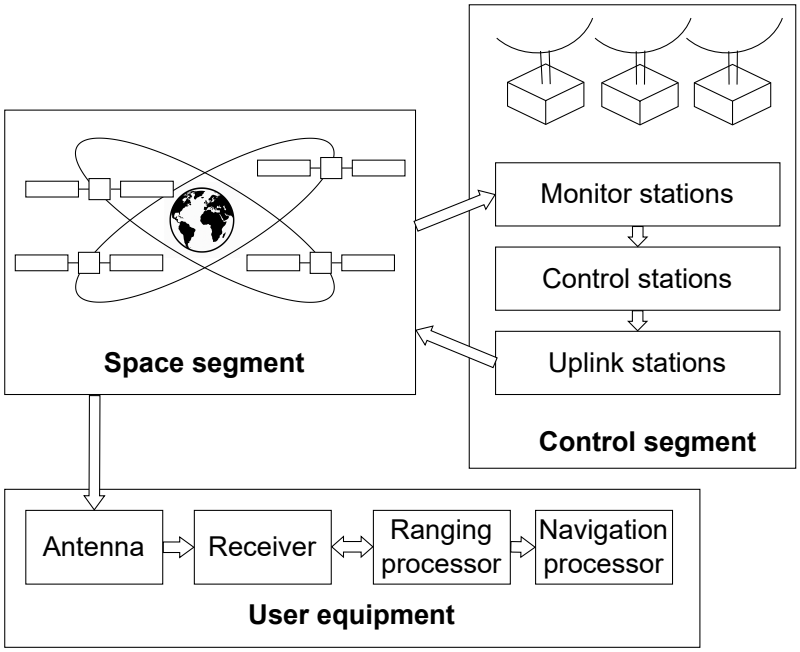

Figure 2.10: Overview of the GNSS architecture. The system is divided into the space segment, consisting of the GNSS constellation, at the control segment for orbit determination, clock calibration, monitoring and control of the constellation, and finally the user equipment, consisting of the GNSS receivers.

and 24,000 km. The constellation geometry is designed to ensure that at least four satellites are visible from any position on Earth at any time. Each full GNSS constellation consists of at least 24 satellites, each weighting around 1,000 kg.

The control segment comprises a network of monitor stations, one or a few control stations, and uplink stations. Monitor stations acquire highly accurate ranging information, enabled by their precisely surveyed locations, synchronized clocks, and sometimes laser ranging. These data are sent to control stations, where it is used to precisely determine the satellite orbits and clock information. This information is then sent to the satellites through the uplink stations for broadcast.

The user equipment receives the signal transmitted by the GNSS system and is able to determine its position from the information provided in the signal, which include timing and GNSS orbit data.

2.3.2 GNSS Receiver Working Principles

GNSS satellites broadcast multiple signals at different frequencies, containing a ranging code and a navigation message. The transmitted GNSS signal (s_{gnss}) can be described by

$$s_{\text{gnss}}(t) = \sqrt{2P} \cdot C(t) \cdot D(t) \cdot \cos(2\pi \cdot f_{\text{ca}} \cdot t + \varphi_{\text{gnss0}}) \tag{2.20}$$

where P is the transmitted power, $C(t)$ is a Pseudorandom Noise (PRN) code used for spreading the signal's spectrum, $D(t)$ is the navigation data, f_{ca} is the GNSS carrier frequency, and φ_{gnss0} is a constant phase term. The navigation data $D(t)$ consist of a low-rate binary signal carrying information such as satellite ephemeris, clock correction, satellite health status, etc. These data are present in most GNSS signals, but in some cases they are omitted to improve tracking performance.

The code and navigation data are applied to the carrier using different types of modulation depending on the constellation and signal. Common modulation types include Binary Phase Shift Keying (BPSK), Binary Offset Carrier (BOC), and Quadrature Phase Shift Keying (QPSK) [88]. Modulating the GNSS signal with a PRN code allows multiplexing between GNSS signals transmitted in the same band and enables retrieval of the difference between transmission and reception times, from which ranging information is derived.

The working principle of the GNSS receiver is illustrated in Figure 2.11. The figure shows all steps from reception to range processing for a single channel to obtain GNSS observables. A real receiver commonly has more than one RF front-end and dozens of digital signal processor channels, each tracking a single GNSS signal. Additionally, sampling and multiplication with the internally generated signals are always performed for both in-phase and quadrature; for simplicity, the two signals are represented by a single line in the diagram.

The signal is received by an antenna with peak sensitivity around the GNSS carrier. Then it is filtered, amplified, downconverted and sampled at an intermediate frequency. The Automatic Gain Control (AGC) is used to adjust the signal strength to maintain a consistent output level before sampling, and minimize quantization losses.

The receiver generates digital replicas of the GNSS signal at an intermediate frequency and correlates them with the received signal by performing a two-dimensional grid search over various code delays and Doppler frequencies. A correlation peak indicates the presence of the signal and a

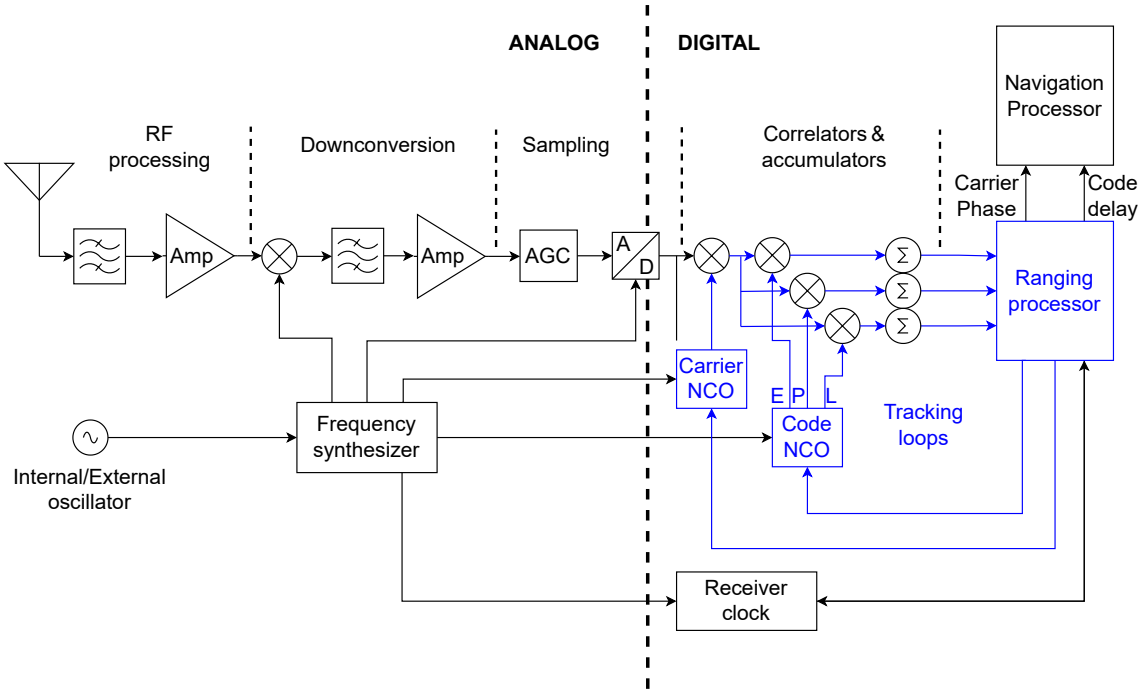

Figure 2.11: GNSS receiver overview for one tracking channel. All stages from analog to digital processing are illustrated in the diagram. To facilitate visualization, the in-phase and quadrature signals are represented with a single line. The elements comprising the phase and code delay tracking loops are highlighted in blue. Note that there are variants of the front-end design, often with several downconversion steps and, in rare cases, with direct sampling of the GNSS signal at the carrier.

coarse alignment between the replica and the incoming signal. This process, known as acquisition, is aimed at detecting the presence of the GNSS signal.

After acquisition, the receiver enters the tracking phase, which aims at keeping an internal replica closely aligned to the incoming signal through tracking loops (see elements highlighted in blue in Figure 2.11). In this phase, the digitalized incoming GNSS signal is multiplied by three replicas and summed for a given integration time. The replicas correspond to an estimate of the current state of the signal, denominated Prompt (P), a version with the code slightly advanced in time, denominated Early (E), and a version slightly delayed denominated Late (L).

A small misalignment between the prompt code and the incoming GNSS signal causes an asymmetry in the late and early code correlations, which can be used to estimate the tracking error. This error is processed in a feedback controller—i.e., a Delay-Locked Loop (DLL)—which constantly adjusts the internal reference to track the incoming signal. A similar process is used to track the carrier phase—i.e., a Phase-Locked Loop (PLL)—but,

in this case, the prompt phase is sufficient for estimating the misalignment in carrier phase between the replica and the incoming signal [99]. GNSS signal tracking enables precise estimation of the delay between the internally generated replica and the transmitted signal. This delay contains information about the distance between the GNSS satellite and the receiver antenna's phase center. The data, available for all tracked satellites, is processed by the navigation processor to produce the positioning and timing information.

In addition to allowing for ranging, the PRN code has the role of spreading interference over the code bandwidth. After the correlation process, this bandwidth is reduced to the one necessary to decode the navigation message, which eliminates most of the spread interference. This allows GNSS to operate with very low power per unit bandwidth, well below thermal noise.

All processes in the receiver are coherent with the same master oscillator, including the signal used for downconversion of the GNSS signal, the Analog-to-Digital Converter (ADC), and the Numerically Controlled Oscillators (NCOs) used to generate the carrier and code replicas. This preserves the master oscillator's phase information up to the pseudoranges observable, meaning this phase is reflected in the estimated clock error. This coherence enables GNSS to support high-precision timing, in addition to the conventional positioning application [99].

2.3.3 GNSS Observables

The transmission time $t^{(i)}$ from GNSS satellite i and the reception time t_u at receiver u, as maintained by their respective internal clocks, are given by

$$t^{(i)}(t) = t + \delta t^{(i)}(t)\,, \tag{2.21}$$

$$t_u(t) = t + \delta t_u(t)\,, \tag{2.22}$$

where t is the time instant, $\delta t^{(i)}$ and δt_u are the internal clock errors of GNSS satellite i and user equipment u, respectively. In this thesis, the superscript $^{(i)}$ denotes GNSS satellite i, and the subscript $_u$ denotes receiver u. Denoting $\tau_u^{(i)}$ as the signal travel time, the detected time delay by the GNSS receiver ($t_u^{(i)}$) is

$$t_u^{(i)}(t) = t_u(t) - t^{(i)}(t - \tau_u^{(i)}) = \tau_u^{(i)}(t) + \delta t_u(t) - \delta t^{(i)}(t - \tau_u^{(i)}(t))\,. \tag{2.23}$$

This delay represents the cumulative offset applied to the internal PRN code to maintain alignment with the incoming GNSS signal. Since the PRN code repeats, with periods ranging from 1 ms to 100 ms (for the signals intended for civilian applications), the resulting code delay is ambiguous. For example, a repetition period of 1 ms corresponds to a range ambiguity of approximately 300 km. This ambiguity can be easily resolved by combining data from multiple tracked signals, and using satellite orbit and transmission time information provided in the navigation message [87].

Multiplying (2.23) by the speed of light c yields, in an ideal scenario, the most basic GNSS measurement, the code-delay pseudorange

$$P_u^{(i)}(t) = \rho_u^{(i)}(t) + \mathrm{c} \cdot \left(\delta t_u(t) - \delta t^{(i)}(t - \tau_u^{(i)}(t)) \right), \tag{2.24}$$

where $\rho_u^{(i)}$ is the geometric distance between the satellite and receiver antenna phase centers. Since clock biases and positions of the GNSS satellites are available in the navigation message, (2.24) is a function of four unknowns: the three receiver coordinates and a clock bias. Thus, four pseudorange measurements from four different satellites are sufficient to solve for these unknowns and determine the receiver position and clock bias.

GNSS satellites transmit on multiple frequencies, and pseudorange measurements are subject to various external error sources. A more complete model is therefore given by [100]

$$\begin{aligned} P_{u,k}^{(i)}(t) =& \rho_u^{(i)}(t) + \mathrm{c} \cdot \left(\delta t_u(t) - \delta t^{(i)}(t - \tau_u^{(i)}(t)) \right) + I_{u,k}^{(i)}(t) + \\ & M_{uP,k}^{(i)}(t) + \eta_{uP,k}^{(i)}(t), \end{aligned} \tag{2.25}$$

where the index k denotes the GNSS carrier frequency with wavelength λ_k, the term $I_{u,k}^{(i)}(t)$ accounts for the ionospheric delay and $M_{uP,k}^{(i)}(t)$ represents systematic errors including time-varying internal delays, multipath and cross-talk, while $\eta_{uP,k}^{(i)}(t)$ accounts for the effect of thermal noise. The ionospheric delay can be modeled as [87]

$$I_{u,k}^{(i)}(t) = 40.3 \cdot \frac{\lambda_k^2}{\mathrm{c}^2} \cdot \mathrm{TEC}_u^{(i)}(t), \tag{2.26}$$

where $\mathrm{TEC}_u^{(i)}$ is the total electron content in Total Electron Content Units (TECUs) between the receiver and the GNSS satellite.

While pseudoranges enable solving the positioning and timing problems with sufficient accuracy for conventional applications, they fall short in high-precision applications such as precise baseline determination [100],

which aims at estimating the baseline vector between two satellites with millimeter-level accuracy. For such applications, more precise ranging information can be obtained from the tracked GNSS carrier phases.

Similar to interferometric SAR, the carrier phase difference between the received and internally generated signals provides information about the distance between the GNSS transmitter and receiver with sub-wavelength precision, although ambiguous modulo the wavelength λ. The carrier phase observable $\phi_u^{(i)}$, as tracked by the receiver, is given by

$$\phi_u^{(i)}(t) = \phi_u(t) - \phi^{(i)}(t - \tau_u^{(i)}(t)) + N_u^{(i)}, \tag{2.27}$$

where ϕ_u is the phase of the internal replica generated in the GNSS receiver, $\phi^{(i)}$ is the phase of the transmitted GNSS carrier at the phase center of the GNSS satellite antenna, and $N_u^{(i)}$ is the integer ambiguity term, corresponding to the number of full cycles between the transmitter and receiver phase centers. Expanding these two phases as a function of time yields

$$\phi_u(t) = \phi_u(t_0) + 2\pi f \cdot (t - t_0) + 2\pi f \cdot (\delta t_u(t) - \delta t_u(t_0)), \tag{2.28}$$

and

$$\begin{aligned}\phi^{(i)}(t - \tau_u^{(i)}(t)) =& \phi^{(i)}(t_0) + 2\pi f \cdot \left(t - \tau_u^{(i)}(t) - t_0\right) + \\ & 2\pi f \cdot \left(\delta t^{(i)}(t - \tau_u^{(i)}(t)) - \delta t^{(i)}(t_0)\right),\end{aligned} \tag{2.29}$$

where f is the transmitting frequency. Replacing (2.28) and (2.29) into (2.27) results in

$$\phi_u^{(i)}(t) = 2\pi f \cdot \tau_u^{(i)}(t) + 2\pi f \cdot \left(\delta t_u(t) - \delta t^{(i)}(t - \tau_u^{(i)}(t))\right) + A_u^{(i)}, \tag{2.30}$$

where $A_u^{(i)}$ is an ambiguity encompassing all constant terms, given by

$$A_u^{(i)} = N_u^{(i)} + \phi_u(t_0) - 2\pi f \cdot \delta t_u(t_0) - \phi^{(i)}(t_0) + 2\pi f \cdot \delta t^{(i)}(t_0). \tag{2.31}$$

Like the code-delay pseudorange, carrier phase observables are also affected by several additional error factors. Multiplying (2.30) by $\lambda_k/2\pi$ and including a zero-mean random noise contribution ($\eta_{u,k}^{(i)}$), systematic errors

($M_{u,k}^{(i)}$), and the ionospheric delay, the carrier phase observable ($L_{u,k}^{(i)}$) for a signal k, in meters, is given by [100]

$$\begin{aligned} L_{u,k}^{(i)}(t) =& \rho_u^{(i)}(t) + \mathrm{c} \cdot (\delta t_u(t) - \delta t^{(i)}(t - \tau_u^{(i)}(t))) - \\ & I_{u,k}^{(i)}(t) + \lambda_k \cdot A_{u,k}^{(i)} + M_{u,k}^{(i)}(t) + \eta_{u,k}^{(i)}(t)\,. \end{aligned} \tag{2.32}$$

The carrier phase observable is essential for high-precision positioning and timing applications. However, it comes with the drawback of requiring resolution of the ambiguity term, which is absent in the code-delay.

2.4 Fundamentals of Satellite Formation Flying

Satellite formation flying characterizes the motion of a spacecraft, known as the deputy, relative to a reference spacecraft, referred to as chief. Its theoretical foundation was initially developed in the context of the rendezvous problem. This relative motion is conveniently described in the Local-Horizontal, Local-Vertical (LHLV) frame, also known as the Hill-Clohessy-Wiltshire (HCW) frame, named after the pioneers of lunar motion, George William Hill, and satellite rendezvous, William H. Clohessy and Richard S. Wiltshire. Figure 2.12 illustrates this frame.

In the figure, $\vec{\rho}$ denotes the position of the deputy satellite relative to the chief $\hat{i}_{\mathrm{hcw}}$, $\hat{j}_{\mathrm{hcw}}$, and $\hat{k}_{\mathrm{hcw}}$ denote the unit vectors of the HCW frame, $\vec{r}$ is the position vector of the chief satellite with respect to the Earth's center, $\vec{v}_{\mathrm{eci}}$ is the velocity of the chief satellite in an Earth-Centered Inertial (ECI) frame, and $\vec{h}$ denotes the orbit angular momentum vector of the chief satellite.

The HCW frame is defined by

$$\hat{i}_{\mathrm{hcw}} = \frac{\vec{r}}{||\vec{r}||}\,, \tag{2.33a}$$

$$\hat{k}_{\mathrm{hcw}} = \frac{\vec{r} \times \vec{v}_{\mathrm{eci}}}{||\vec{r} \times \vec{v}_{\mathrm{eci}}||}\,, \tag{2.33b}$$

$$\hat{j}_{\mathrm{hcw}} = \hat{k}_{\mathrm{hcw}} \times \hat{i}_{\mathrm{hcw}}\,. \tag{2.33c}$$

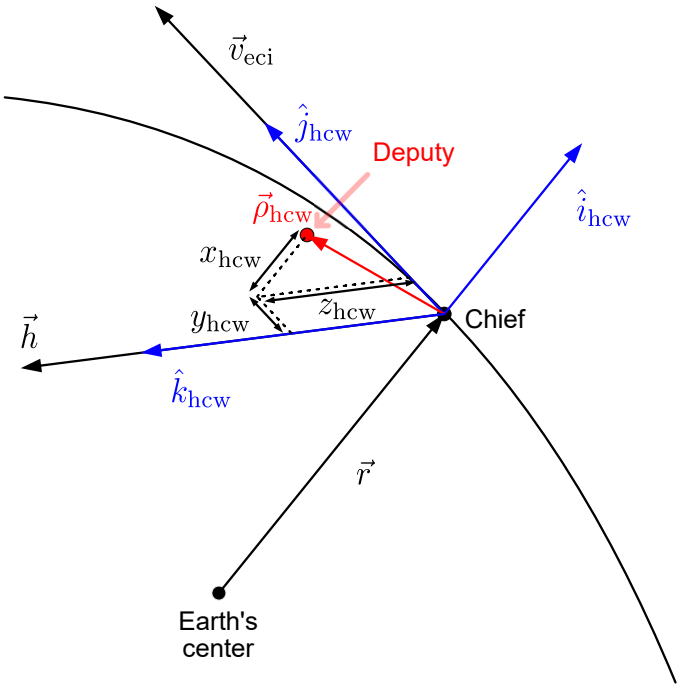

Figure 2.12: Definition of the Hill-Clohessy-Wiltshire (HCW) frame. The frame, with components $\hat{i}_{\text{hcw}}$, $\hat{j}_{\text{hcw}}$ and $\hat{k}_{\text{hcw}}$, are defined from the position $\vec{r}$ and velocity vectors $\vec{v}_{\text{eci}}$ of the chief satellite in an ECI frame. The position of the deputy relative to the chief is denoted $\vec{\rho}$.

The deputy satellite's relative state $\delta\vec{X}$ is then defined as:

$$\delta\vec{X} \triangleq \begin{pmatrix} x_{\text{hcw}} \\ y_{\text{hcw}} \\ z_{\text{hcw}} \\ \dot{x}_{\text{hcw}} \\ \dot{y}_{\text{hcw}} \\ \dot{z}_{\text{hcw}} \end{pmatrix} = \begin{pmatrix} \vec{\rho} \cdot \hat{i}_{\text{hcw}} \\ \vec{\rho} \cdot \hat{j}_{\text{hcw}} \\ \vec{\rho} \cdot \hat{k}_{\text{hcw}} \\ \dot{\vec{\rho}} \cdot \hat{i}_{\text{hcw}} + \vec{\rho} \cdot \dot{\hat{i}}_{\text{hcw}} \\ \dot{\vec{\rho}} \cdot \hat{j}_{\text{hcw}} + \vec{\rho} \cdot \dot{\hat{j}}_{\text{hcw}} \\ \dot{\vec{\rho}} \cdot \hat{k}_{\text{hcw}} + \vec{\rho} \cdot \dot{\hat{k}}_{\text{hcw}} \end{pmatrix}. \tag{2.34}$$

where the upper dot ($\dot{\square}$) denotes time derivative. To simplify the notation, in the remainder of this chapter the x, y, and z components in the HCW frame will be written without subscripts.

The general nonlinear relative motion equations for an arbitrary Keplerian chief orbit are derived in [89] as

$$\begin{aligned} \ddot{x} - 2\dot{\nu}\cdot\dot{y} - \ddot{\nu}\cdot y - \dot{\nu}^2\cdot x &= -\frac{\mu\cdot(r+x)}{[(r+x)^2+y^2+z^2]^{3/2}} + \frac{\mu}{r^2} + d_x \\ \ddot{y} + 2\dot{\nu}\cdot\dot{x} + \ddot{\nu}\cdot x - \dot{\nu}^2\cdot y &= -\frac{\mu\cdot y}{[(r+x)^2+y^2+z^2]^{3/2}} + d_y \qquad , \\ \ddot{z} &= -\frac{\mu\cdot z}{[(r+x)^2+y^2+z^2]^{3/2}} + d_z \end{aligned} \tag{2.35}$$

where μ is the standard gravitational parameter of Earth, and d_x, d_y, and d_z are components of the differential disturbances (i.e., any arbitrary deviation from central gravitational force), r is the magnitude of the chief position vector, and ν is the true anomaly of the chief satellite.

In a general scenario, including disturbances on the chief satellite's orbit, the deputy's relative motion dynamics in the HCW frame are determined by two components: the rotation of the HCW frame itself, which depends exclusively on the chief satellite's absolute dynamics; and the relative acceleration between the two satellites. For satellites of similar mass and shape, gravitational disturbances will dominate the relative accelerations.

Given that the separation distances in typical formation-flying missions are small compared to the absolute orbital radius, these differential gravitational accelerations can be accurately approximated as linear functions of the deputy's relative position. The rotation of the HCW frame introduces three fictitious forces: the Euler force, the Coriolis force, and the centrifugal force; all of which are linear with respect to the deputy's relative state vector. Consequently, despite the inherently non-linear nature of absolute orbital motion, the relative motion in formation flying scenarios, including major perturbations, can be effectively approximated using linear dynamics [89].

In case the relative position components are much smaller than r, the first components on the right in (2.35), corresponding to the differential central gravitational force, can be approximated by a first-order Taylor expansion around the HCW frame's origin as follows

$$-\frac{\mu\cdot(r+x)}{[(r+x)^2+y^2+z^2]^{\frac{3}{2}}} \approx \frac{\mu}{r^3}\cdot(2x-r)\,, \tag{2.36}$$

$$-\frac{\mu\cdot y}{[(r+x)^2+y^2+z^2]^{\frac{3}{2}}} \approx -\frac{\mu}{r^3}\cdot y\,, \tag{2.37}$$

$$-\frac{\mu \cdot z}{[(r+x)^2+y^2+z^2]^{\frac{3}{2}}} \approx -\frac{\mu}{r^3} \cdot z\,. \tag{2.38}$$

Substituting equations (2.36), (2.37), and (2.38) into (2.35) yields

$$\begin{aligned} \ddot{x} - 2\dot{v} \cdot \dot{y} - \ddot{v} \cdot y + \left(-\dot{v}^2 - \frac{2\mu}{r^3}\right) \cdot x &\approx d_x \\ \ddot{y} + 2\dot{v} \cdot \dot{x} + \ddot{v} \cdot x + \left(-\dot{v}^2 + \frac{\mu}{r^3}\right) \cdot y &\approx d_y \cdot \\ \ddot{z} + \frac{\mu}{r^3} \cdot z &\approx d_z \end{aligned} \tag{2.39}$$

The homogeneous form of (2.39), i.e., assuming no disturbances, correspond to a system of linear time-varying first-order differential equations in the state space with respect to $\delta\vec{X}$, taking the form

$$\delta\dot{\vec{X}}(t) = \mathrm{F}(t) \cdot \delta\vec{X}(t)\,, \tag{2.40}$$

where $\mathrm{F}(t)$ is the system matrix, which depends solely on the chief satellite's state, and thus on time. The solution to this system can be written using the state transition matrix $\Phi(t_0, t)$, which propagates the state from an initial time t_0 to a time t, hence

$$\delta\vec{X}(t) = \Phi(t_0, t) \cdot \delta\vec{X}_0\,, \tag{2.41}$$

where $\delta\vec{X}_0$ is the state at the initial time t_0. This formulation forms the foundation for powerful linear control and navigation techniques in formation flying, and will be used extensively in this thesis, especially in Chapter 6, where the problem of optimal guidance is addressed.

2.4.1 Hill-Clohessy-Wiltshire Equations

Assuming a circular Keplerian chief orbit with a radius equal to the semi-major axis a and no external disturbances or control inputs, and defining the satellite's mean motion (i.e., the orbital angular speed) as $n = \sqrt{\mu/a^3}$, (2.39) is reduced to the following linear time-invariant system of equations

$$\begin{aligned} \ddot{x} - 2n \cdot \dot{y} - 3n^2 \cdot x &= 0 \\ \ddot{y} + 2n \cdot \dot{x} &= 0\,. \\ \ddot{z} + n^2 \cdot z &= 0 \end{aligned} \tag{2.42}$$

These are the well-known Hill-Clohessy-Wiltshire (HCW) equations. Denoting the components of the initial state as $\delta\vec{X}(t_0) = [x_0, y_0, z_0, \dot{x}_0, \dot{y}_0, \dot{z}_0]^T$, the solution to (2.42) is given by

$$\begin{aligned}
x(t) &= 4x_0 + \frac{2\dot{y}_0}{n} + \frac{\dot{x}_0}{n} \cdot \sin(nt) - \left(3x_0 + \frac{2\dot{y}_0}{n}\right) \cdot \cos(nt) \\
y(t) &= -(6n \cdot x_0 + 3\dot{y}_0) \cdot t + y_0 - \frac{2\dot{x}_0}{n} + \\
&\quad \left(6x_0 + \frac{4\dot{y}_0}{n}\right) \cdot \sin(nt) + \frac{2\dot{x}_0}{n} \cdot \cos(nt) \\
z(t) &= \frac{\dot{z}_0}{n} \cdot \sin(nt) + z_0 \cdot \cos(nt) \\
\dot{x}(t) &= \dot{x}_0 \cdot \cos(nt) + (3n \cdot x_0 + 2\dot{y}_0) \cdot \sin(nt) \\
\dot{y}(t) &= -(6n \cdot x_0 + 3\dot{y}_0) + (6x_0 \cdot n + 4\dot{y}_0) \cdot \cos(nt) - 2\dot{x}_0 \cdot \sin(nt) \\
\dot{z}(t) &= \dot{z}_0 \cdot \cos(nt) - z_0 \cdot n \cdot \sin(nt)
\end{aligned} \quad . \tag{2.43}$$

The corresponding state transition matrix is given by

$$\Phi(0,t) = \begin{pmatrix}
4 - 3\mathrm{c}(nt) & 0 & 0 & \frac{\mathrm{s}(nt)}{n} & \frac{2}{n} - \frac{2}{n}\mathrm{c}(nt) & 0 \\
-6nt + 6\mathrm{s}(nt) & 1 & 0 & 2 - \frac{2}{n}\mathrm{c}(nt) & \frac{4}{n}s(nt) - 3t & 0 \\
0 & 0 & \mathrm{c}(nt) & 0 & 0 & \frac{\mathrm{s}(nt)}{n} \\
3n\mathrm{s}(nt) & 0 & 0 & \mathrm{c}(nt) & 2\mathrm{s}(nt) & 0 \\
-6n + 6n\mathrm{c}(nt) & 0 & 0 & -2\mathrm{s}(nt) & -3 + 4\mathrm{c}(nt) & 0 \\
0 & 0 & -n\mathrm{s}(nt) & 0 & 0 & \mathrm{c}(nt)
\end{pmatrix}, \tag{2.44}$$

where, for compactness, $\mathrm{s}(\cdot)$ and $\mathrm{c}(\cdot)$ denote the sine and cosine functions, respectively. This analytical model is sufficiently accurate for many practical applications and offers valuable insights into the design and characterization of natural relative trajectories.

Equation (2.43) shows that the relative motion in all three directions is harmonic, with the y direction including a linear term that grows over time. This term corresponds to a drift between the two satellites when their orbits have different periods. The condition for bounded (i.e., non-drifting) motion is given by:

$$\dot{y}_0 = -2n \cdot x_0 \,. \tag{2.45}$$

Slight deviations from this initial condition (e.g., due to navigation and control uncertainties) result in drift along the y direction. This makes the motion along this axis unstable. As a result, for many formation flying applications, the formation is designed to maintain a minimum separation throughout the orbit in the plane formed by the cross-track and radial directions. This is the case, for example, for the helix formation used in the TanDEM-X mission.

2.4.2 Relative Orbital Elements Parameterization

The Relative Orbital Elements (ROEs) parametrization of the relative state, proposed in [72], is particularly useful for intuitively characterizing the design space of bounded relative motion. Additionally, it enables a simple formulation of passive collision safety conditions [101], and improves the accuracy of the general HCW solution [72]. This parametrization is defined as:

$$\delta\vec{\alpha} \triangleq \begin{pmatrix} \delta a \\ \delta l \\ \delta e_x \\ \delta e_y \\ \delta i_x \\ \delta i_y \end{pmatrix} \triangleq \begin{pmatrix} (a_\mathrm{d} - a)/a \\ u_\mathrm{d} - u + (\Omega_\mathrm{d} - \Omega) \cdot \cos i \\ e_\mathrm{d} \cdot \cos\omega_\mathrm{d} - e \cdot \cos\omega \\ e_\mathrm{d} \cdot \sin\omega_\mathrm{d} - e \cdot \sin\omega \\ i_\mathrm{d} - i \\ (\Omega_\mathrm{d} - \Omega) \cdot \sin i \end{pmatrix}, \tag{2.46}$$

where the conventional notation for the orbital elements is used, i.e., a is the semi-major axis, e is the eccentricity, i denotes the inclination, ω is the argument of perigee, Ω is the right ascension of the ascending node, and $u = \omega + M$ is the mean argument of latitude, with M being the mean anomaly. The orbital elements of the chief satellite are written without subscripts, and the elements of the deputy satellite are denoted by d. The individual ROEs are named as follows: δa is the relative semi-major axis, δl is the relative mean longitude, $\delta\vec{e} = (\delta e_x, \delta e_y)$ are the components of the relative eccentricity vector, and $\delta\vec{i} = (\delta i_x, \delta i_y)$ are the components of the relative inclination vector.

The integration constants of the HCW equations can be written as a function of the ROEs [72], which leads to the following reformulation of (2.43)

$$\begin{aligned}
x(t) &= a\delta a - a\delta e_x \cdot \cos(nt) - a\delta e_y \cdot \sin(nt) \\
y(t) &= a\delta l + 2a\delta e_x \cdot \sin(nt) - 2a\delta e_y \cdot \cos(nt) \\
z(t) &= a\delta i_x \cdot \sin(nt) - a\delta i_y \cdot \cos(nt) \\
\dot{x}(t) &= n \cdot a\delta e_x \cdot \sin(nt) - n \cdot a\delta e_y \cdot \cos(nt) \\
\dot{y}(t) &= -3na/2 \cdot \delta a + 2n \cdot a\delta e_x \cdot \cos(nt) + 2n \cdot a\delta e_y \cdot \sin(nt) \\
\dot{z}(t) &= n \cdot a\delta i_x \cdot \cos(nt) + n \cdot a\delta i_y \cdot \sin(nt)
\end{aligned} \quad . \tag{2.47}$$

Figure 2.13b shows the relation between the trajectory in the HCW frame and the ROEs in the case of bounded motion, i.e., for $\delta a = 0$. it presents two scenarios: in (a), the eccentricity vector is kept constant while the inclination vector is rotated; in (b), the magnitudes of both vectors and the angle between them remain fixed, but the vectors are jointly rotated to different absolute orientations.

As shown in Figure 2.13a, the shape of the trajectory in the plane formed by the cross-track and radial directions (ZX) is an ellipse centered at the origin and inscribed in a rectangle with length $2a \cdot ||\delta\vec{i}||$ and height $2a \cdot ||\delta\vec{e}||$. The angle between the relative eccentricity and inclination vectors determines the ellipse's orientation within this rectangle. When $\delta\vec{e}$ and $\delta\vec{i}$ are parallel, the minimum distance between the chief and deputy in the ZX plane is maximized. When the vectors are orthogonal, the trajectory degenerates into a line segment passing through the origin twice per orbit.

In the plane formed by the along-track and radial directions (YX), the trajectory is an ellipse determined solely by the eccentricity vector. The semi-major axis of this ellipse is aligned with the Y direction and has the length $2a \cdot ||\delta\vec{e}||$, while the semi-minor axis has the length $a \cdot ||\delta\vec{e}||$. The center of ellipse is offset in the along-track direction by $a\delta l$, and is always in the Y axis for non-drifting formations.

The relation between the deputy's position in the formation, and the chief satellite's position in its orbit is determined by the absolute orientation of the eccentricity and inclination vectors. This relation illustrated in Figure 2.13b, where the vectors maintain fixed magnitudes and relative orientation but are rotated together. While the shape of the trajectory remains unchanged across the examples, the timing of specific positions—exemplified in the figure by the ascending equatorial crossing, indicated by the rectangles—varies depending on the vectors' absolute orientation.

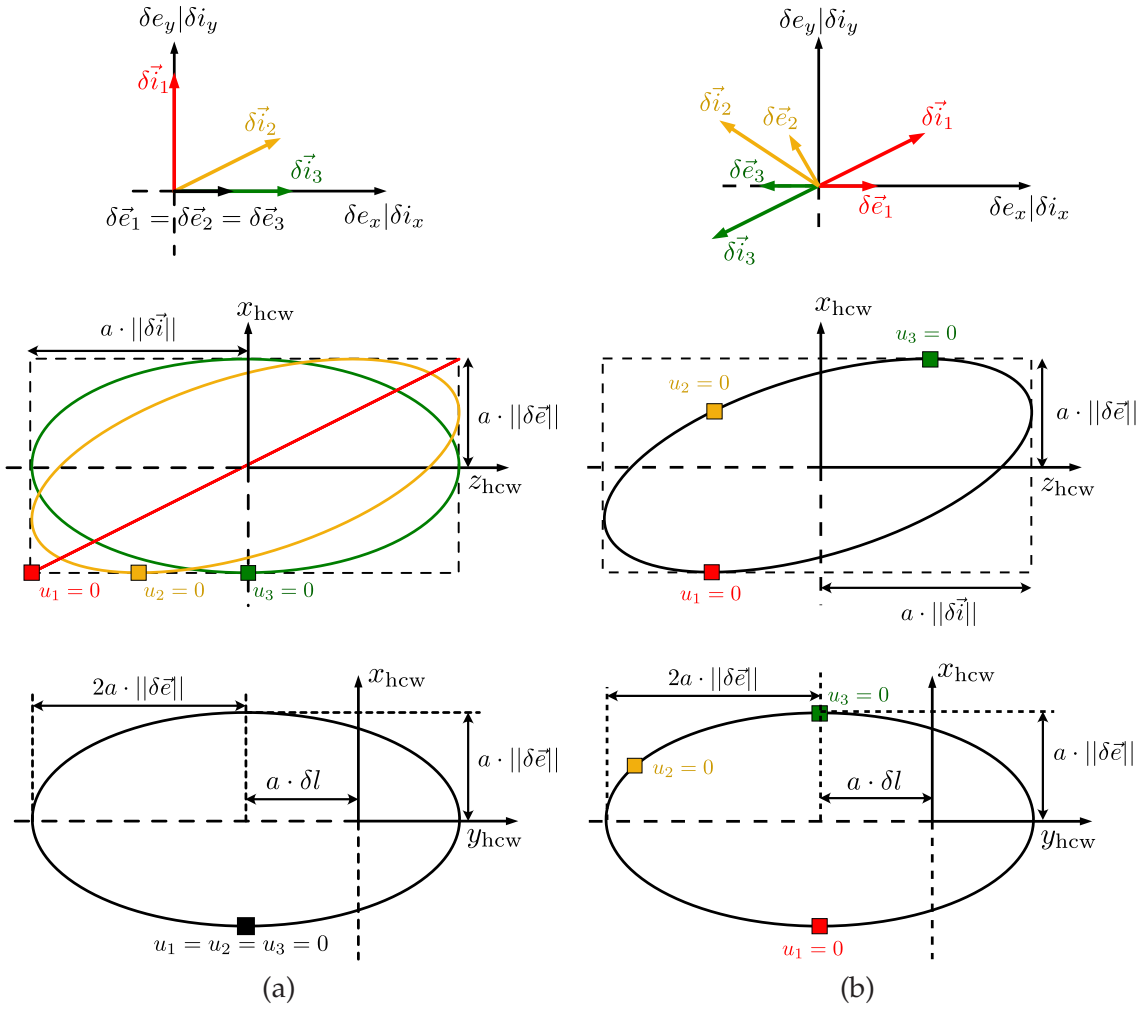

Figure 2.13: Illustration of the design space of bounded natural relative orbits according to the HCW equations, and its relation to the relative orbital elements. The red, yellow and green colors illustrate three distinct examples, and the black color illustrates positions and trajectories common to all examples. The squares indicate the relative position at the equator at the ascending pass. (a) Effect of the relative eccentricity and inclination vectors' relative orientation. (b) Effect of absolute orientation of relative eccentricity and inclination vectors.

Figure 2.13 reveals an incompatibility between the allowable relative trajectory shapes and the cross-track baseline requirements for SAR interferometric and tomographic applications, as well as for those involving beamforming in elevation. As the deputy satellite oscillates around the origin of the XZ plane over the orbit, an optimal cross-track baseline, as illustrated in Figure 2.5, can be achieved only two or four times per orbit, and only for brief instants. This indicates that achieving ideal configurations for important SAR applications over the entire orbit is not possible with natural orbits.

The HCW frame provides the foundational geometry for formation flying theory. However, for SAR-specific applications, the effect of Earth's rotation is relevant and it introduces additional complexity. This is addressed in detail in Chapter 5, as part of the original contribution of this thesis. Nonetheless, the HCW geometry described here serves as a starting point for the following developments.

2.4.3 Formation Maintenance

In a realistic scenario, the relative satellite dynamics are continuously affected by disturbances. Additionally, there are uncertainties in both the absolute and relative states, as well as in the controller actuation. To ensure the satellite follows a predetermined relative orbit, feedback control must be employed.

Figure 2.14 shows a general feedback control scheme for autonomous formation maintenance. Its main components include a reference trajectory, a feedback controller implementing the control algorithm, actuators, the relative dynamics, and sensors for relative navigation. The objective of the control system is to achieve precise positioning relative to the mission requirements while minimizing fuel consumption. The total deviation from the required positioning consists of two components: (i) the deviation of the controlled position from the reference trajectory (i.e., control accuracy) and (ii) the deviation of the reference trajectory from the actual requirement.

The accuracy of state estimation—provided by relative navigation using sensor data—directly influences control accuracy. Control accuracy is also affected by the feedback controller design and by the precision of thrust execution. Fuel consumption depends largely on the difference between the dynamics assumed in the reference trajectory and the actual orbital dynamics, including disturbances, since this mismatch must be corrected through thruster-generated accelerations. Tight positioning requirements, such as

those for distributed imaging missions, often conflict with the natural orbital dynamics. Designing the reference trajectory therefore requires balancing two competing objectives: conforming closely to mission requirements versus aligning with the natural relative dynamics to save fuel. This trade-off is discussed in detail in Chapter 6, where a complete example of feedback control is implemented in a realistic simulation.

This subsection briefly discusses the disturbances affecting formation control and presents a control strategy suitable for precise formation control.

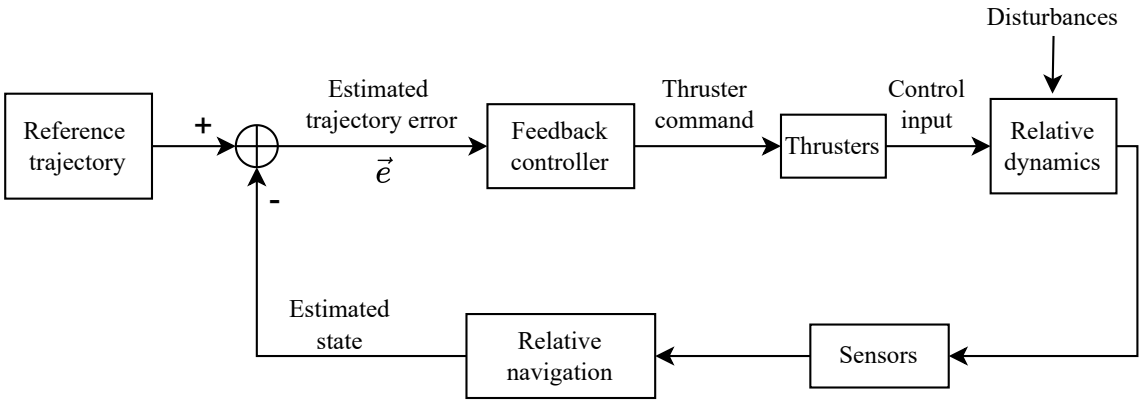

Figure 2.14: General overview of autonomous formation maintenance.

Orbital Disturbances in Formation Flying

Orbital disturbances refer to deviations from ideal Keplerian dynamics. These include irregularities in Earth's gravitational field—since Keplerian motion applies only to a perfectly spherically symmetric mass distribution of the central planet—as well as atmospheric drag and solar radiation pressure. These are typically the most predominant disturbances affecting formation flying [89].

The acceleration due to drag $\vec{a}_{\text{drag}}$ is given by [102]:

$$\vec{a}_{\text{drag}} = -\frac{1}{2}\frac{c_{\text{d}} \cdot A_{\text{cs}}}{m} \cdot \rho_{\text{atm}} \cdot ||\vec{v}_{\text{atm}}|| \cdot \vec{v}_{\text{atm}}, \tag{2.48}$$

where c_{d} is the adimensional drag coefficient, A_{cs} is the cross-sectional area, $\vec{v}_{\text{atm}}$ is the platform's velocity relative to the atmosphere, and m is the platform's mass. The differential atmospheric drag in a formation flying scenario is negligible in case the formation consists of satellites with the same

shape and mass, which will be the focus of the examples discussed further in the thesis.

The acceleration due to solar radiation pressure is given by [102]:

$$\vec{a}_{\text{srp}} = \text{P}_{\text{srp}} \cdot \frac{c_{\text{r}} \cdot A_{\odot}}{m} \cdot \hat{i}_{\odot}, \tag{2.49}$$

where P_{srp} is the solar radiation pressure, c_{r} is the spacecraft's reflectivity, $A_{\odot}$ is the exposed area to the sun, and $\hat{i}_{\odot}$ is a unit vector in the direction from the spacecraft to the sun. For satellites with similar mass and shape, this component can also be considered negligible.

Hence, the dominant disturbance in formation flying tends to be that caused by Earth's oblateness, referred to as the J2 perturbation, corresponding to the second term in the spherical harmonic expansion of the gravitational field [89]. This perturbation is caused by the mass bulge around the equator resulting from Earth's rotation around its axis. Since it is a disturbance of gravitational origin, it results in an acceleration independent of the shape and mass of the satellite. It depends only on the spacecraft position relative to Earth, and is therefore expected to generate differential accelerations that will also affect the relative motion. The acceleration due to the J2 perturbation is given by [103]:

$$\vec{a}_{\text{J2}} = -\frac{3\text{J}_2 \cdot \mu \cdot \text{R}_{\text{e}}{}^2}{2r^4} \cdot \begin{pmatrix} 1 - 3\sin^2(i) \cdot \sin^2(\omega + \nu) \\ \sin^2(i) \cdot \cos^2(\omega + \nu) \\ \sin(2i) \cdot \sin(\omega + \nu) \end{pmatrix}, \tag{2.50}$$

where J_2 is the second zonal harmonic coefficient in the expansion of Earth's gravitational potential, R_{e} is Earth's radius, and ν is the true anomaly of the satellite's orbit. Since this is a gravitational disturbance, the linearizing assumptions applied to the main gravitational field in the derivation of the HCW equations also hold. Therefore, although the HCW equations do not apply in the presence of this perturbation, equations (2.40) and (2.41) remain valid.

Linear Quadratic Regulator

The Linear Quadratic Regulator (LQR) is a popular technique used for autonomous formation control, particularly effective for trajectory tracking. This controller will be used in the formation control examples later in

the thesis and is described below. Its application to formation flying was demonstrated in the Canadian mission CanX-4&5 [104].

The LQR is an optimal control technique applied to linear systems described by the following general equation

$$\dot{\vec{e}} = \mathrm{A} \cdot \vec{e} + \mathrm{B} \cdot \vec{u}\,. \tag{2.51}$$

where $\vec{e}$ denotes the tracking error, A is the system matrix, and B is the control matrix. The LQR finds the optimal control input $\vec{u}$ which minimizes the cost function

$$\mathcal{J} = \frac{1}{2}\int_0^{t_f} (\vec{e}^{\,T} \cdot \mathrm{Q} \cdot \vec{e} + \vec{u}^{\,T} \cdot \mathrm{R} \cdot \vec{u}) \cdot \mathrm{d}t\,, \tag{2.52}$$

where t_f is the final time, i.e., the time horizon to which the optimization applies, and Q and R are positive semi-definite weighting matrices. In the limit as $t_f \to \infty$, the following control law minimizes the cost $\mathcal{J}$ in (2.52)

$$\vec{u} = -\mathrm{K} \cdot \vec{e}, \tag{2.53}$$

where $\mathrm{K} = \mathrm{R}^{-1} \cdot \mathrm{B}^T \cdot \mathrm{S}$, with S satisfying the Algebraic Riccati Equation (ARE) given below

$$\mathrm{S} \cdot \mathrm{A} + \mathrm{A}^T \cdot \mathrm{S} - \mathrm{S} \cdot \mathrm{B} \cdot \mathrm{R}^{-1} \cdot \mathrm{B}^T \cdot \mathrm{S} + \mathrm{Q} = 0\,. \tag{2.54}$$

The solution to (2.54) is positive definite if the pair (A, B) is controllable—meaning that the system can be driven from any initial state to any final state using suitable inputs—and the pair $(\mathrm{A}, \mathrm{Q}^{1/2})$ is observable—meaning that the internal states of the system can be inferred from its outputs over time. The positive definiteness of S guarantees closed-loop stability [89].

The Discrete-time Linear Quadratic Regulator (DLQR) formulation is a discretized version of the continuous LQR, defined as minimizing

$$\mathcal{J} = \sum_{k=0}^{N-1} \left[\vec{e}^{\,T}(t_k) \cdot \mathrm{Q} \cdot \vec{e}(t_k) + \vec{u}^{\,T}(t_k) \cdot \mathrm{R} \cdot \vec{u}(t_k) \right], \tag{2.55}$$

subject to the state equation

$$\vec{e}(t_{k+1}) = \mathrm{A}_d \cdot \vec{e}(t_k) + \mathrm{B}_d \cdot \vec{u}(t_k)\,, \tag{2.56}$$

where t_k denotes the time step of index k. Like in the continuous-time derivation, a discrete-time algebraic Riccati equation results when N is large. The discrete-time Riccati equation is

$$\mathrm{A}_d^T \cdot \mathrm{S} \cdot \mathrm{A}_d - \mathrm{S} - \mathrm{A}_d^T \cdot \mathrm{S} \cdot \mathrm{B}_d \cdot (\mathrm{R} + \mathrm{B}_d^T \cdot \mathrm{S} \cdot \mathrm{B}_d)^{-1} \cdot \mathrm{B}_d^T \cdot \mathrm{S} \cdot \mathrm{A}_d + \mathrm{Q} = 0\,, \quad (2.57)$$

resulting in the feedback control law

$$\vec{u}(t_k) = -\mathrm{K} \cdot \vec{e}(t_k) = -(\mathrm{R} + \mathrm{B}_d^T \cdot \mathrm{S} \cdot \mathrm{B}_d)^{-1} \cdot \mathrm{B}_d^T \cdot \mathrm{S} \cdot \mathrm{A}_d \cdot \vec{e}(t_k)\,. \quad (2.58)$$

In formation flying, the controller must minimize the relative state error with respect to a given reference $\delta\vec{X}_\mathrm{r}(t)$

$$\dot{\vec{e}}(t_k) = \delta\vec{X}(t_k) - \delta\vec{X}_\mathrm{r}(t_k)\,. \quad (2.59)$$

The control law can then be used to track this reference, with the A matrix replaced by the state transition matrix Φ given in (2.44).

3 GNSS-Based Phase Synchronization for Bistatic and Multistatic SAR

3.1 Introduction

This chapter proposes an approach to estimate the differential oscillator phase in bistatic and multistatic SAR which does not require a dedicated subsystem nor any major modification in the ground segment processing chain. The technique is based on the evaluation of carrier phase observables from the GNSS receivers located on two or several receiving satellites, in conjunction with a baseline solution obtained via Precise Baseline Determination (PBD), provided both the radar and the navigation receivers share the same master oscillator. In principle, this method only requires GNSS carrier phase data for the entire SAR acquisition period. Since the carrier phase data from both spacecraft's GNSS receivers must be available to determine the synchronization solution, this technique is best applied on the ground during the calibration and processing of the SAR data.

The necessary high-accuracy relative positioning (i.e., baseline determination) using GNSS has been extensively demonstrated in space. In the GRACE mission, an accuracy of 1 mm compared to a K-band ranging system [105] was reported. TanDEM-X achieved accuracy in the order of 1 to 2 mm through calibration based on the evaluation of the raw topographic maps acquired under different geometries [106]. Both missions used geodetic GPS receivers, capable of receiving two frequencies for correcting the effects of the ionosphere. The PRISMA mission, on the other hand, demonstrated the capability of achieving sub-centimeter relative positioning precision using a low-cost single-frequency GPS receiver [107]. An associated capability for high-accuracy relative timing can be inferred from the dependency between time and position accuracy in GNSS-based Precise Orbit Determination (POD).

This chapter is organized as follows. Section 3.2 details the proposed GNSS-based synchronization method. Section 3.3 analyzes the associated error sources. Section 3.4 presents a representative system example demonstrating achievable synchronization accuracy. Finally, Section 3.5 summarizes the findings and conclusions.

3.2 GNSS-Based Synchronization Approach

Figure 3.1 provides a conceptual illustration of the proposed technique, using the Harmony mission as an example of its application to companion satellite missions. The GNSS signal transmitted by a single GNSS satellite is coherently received by the radar transmitter and both passive platforms, serving as a common reference.

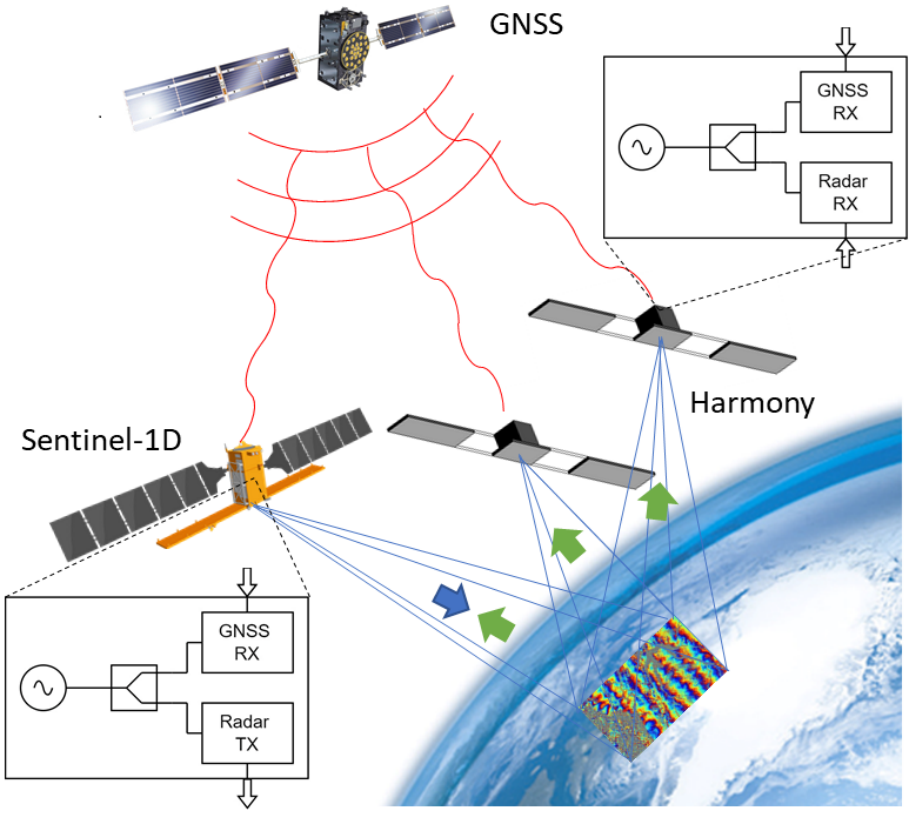

Figure 3.1: GNSS-based phase synchronization scheme (Satellite models credits: ESA). Sentinel-1D is the main TX/Rx SAR satellite, whereas the Harmony mission consists of two receive-only satellites building a multistatic SAR system [35]. The GNSS signal is indicated in red, the transmitted radar pulses in blue, and backscattered echoes in green. The technique can be used to synchronize transmitter and receiver, or two passive receivers.

Figure 3.2 shows the block diagram with more details of a possible system implementation. In the figure, and throughout this chapter, t denotes the

GPS time, and all variables are expressed in the Geocentric Celestial Reference Frame (GCRF). Without loss of generality, the measurement models do not take into account relativistic effects.[1]

In the proposed architecture, the same Ultra Stable Oscillator (USO) is used for generating the radar carrier and the reference signal in the GNSS receiver. Therefore, a pre-requisite for this technique is that the GNSS receiver is able to switch its reference to an external oscillator, a feature characteristic of GNSS receivers for time-transfer present in some space-qualified receivers (e.g., Beyond Gravity PODRIX used in Sentinel-1 [110]). The carrier phase single-differences between the two spacecraft then will contain information on the phase noise difference between the oscillators at the different platforms measured at the navigation carriers. The suggested approach is based on the assumption that this measurement will provide, after appropriate calibration and scaling, a good estimation of the phase difference between the two radar carriers.

3.2.1 Phase and Timing Model

For clarity, the notation, partially introduced in Subsection 2.3.3, is summarized as follows. The upper index $()^{(i)}$ denotes relating to the GNSS satellite i, the lower indexes $()_u$ and $()_v$ relating to the receivers in the satellites u and v, and the lower index followed by a comma, as in $()_{u,k}$, denotes the reference frequency, with navigation carrier frequency denoted by k, the oscillator nominal frequency by os, and the radar carrier by 0. Furthermore, the difference between quantities are denoted by $()_{uv} = ()_v - ()_u$.

Under the assumption of ideal upconversion stages, the phases of the radar reference signal $\psi_{u,0}$ and the phase of the master oscillator input of the GNSS receiver clock $\psi_{u,\mathrm{os}}$ are related as follows

$$\psi_{u,0}(t) = \psi_{\mathrm{b}u,0} + \frac{f_0}{f_{\mathrm{os}}} \cdot \psi_{u,\mathrm{os}}(t)\,, \tag{3.1}$$

where $\psi_{\mathrm{b}u,0}$ is a phase bias, f_0 is the nominal carrier frequency of the radar, and f_{os} is the nominal frequency of the master oscillator. The equation (3.1) suggests that any phase drift in the output of the master oscillator

[1] The SAR processing equations and geometry are described in an Earth-Centered-Earth-Fixed Frame (ECEF), resulting in a non-simultaneity effect between the two frames which may cause considerable time, phase, and frequency deviations, which are larger the longer the baseline is [108]. These effects are deterministic and can be calculated and compensated in the data processing. For more details on the relativistic effects on GNSS measurements, refer to [109]. Details on the relativistic effects on SAR processing are given in [108].

will be replicated in all reference signals derived from it, only scaled by the appropriate up-scaling or down-scaling factors. This assumption requires the spectral purity of the up-converting stages in the radar electronics, to be further elaborated in Section 3.3. Furthermore, the clock biases of the receivers ideally exhibit a linear relationship with the frequency and phase variations of the master oscillator, since the local time is generally derived by counting cycles of the oscillator's periodic signal. Denoting the clock biases by $\delta t_\star$, the initialization times difference by $\delta t_{0\star}$, and the oscillator phases at initialization as $\psi_{\star,\mathrm{os}}(t_{0\star})$, the linear relation between timing and phase is given by the equations

$$\delta t_u(t) = \delta t_{0u} + \frac{1}{2\pi \cdot f_{\mathrm{os}}} \cdot \left[\psi_{u,\mathrm{os}}(t) - \psi_{u,\mathrm{os}}(t_{0u})\right], \tag{3.2}$$

$$\delta t_v(t) = \delta t_{0v} + \frac{1}{2\pi \cdot f_{\mathrm{os}}} \cdot \left[\psi_{v,\mathrm{os}}(t) - \psi_{v,\mathrm{os}}(t_{0v})\right], \tag{3.3}$$

and, the differential time offset between clocks is given by

$$\delta t_{uv}(t) = \delta t_{0uv} + \frac{\psi_{uv,\mathrm{os}}(t)}{2\pi \cdot f_{\mathrm{os}}}, \tag{3.4}$$

where

$$\delta t_{0uv} = \delta t_{0v} - \delta t_{0u} - \frac{1}{2\pi \cdot f_{\mathrm{os}}} \cdot \left[\psi_{v,\mathrm{os}}(t_{0v}) - \psi_{u,\mathrm{os}}(t_{0u})\right]. \tag{3.5}$$

Equation (3.4) suggests that the differential phase drift of the master oscillator can be recovered from the difference between receiver clock biases.

The phase of the master oscillator at each receiver $\psi_{u,\mathrm{os}}(t)$ and $\psi_{v,os}(t)$ can be decomposed into a linear component due to a constant frequency deviation from the nominal $\Delta f_\star$, a random process $\varphi_\star(t)$, and a constant offset $\varphi_{0\star}$ as follows

$$\psi_{u,\mathrm{os}}(t) = 2\pi \cdot \Delta f_u \cdot t + \varphi_u(t) + \varphi_{0u}, \tag{3.6}$$

$$\psi_{v,\mathrm{os}}(t) = 2\pi \cdot \Delta f_v \cdot t + \varphi_v(t) + \varphi_{0v}. \tag{3.7}$$

Note that the phase noise affecting the bistatic radar measurements is the scaled version of the differences between the transmitter and receiver oscillators evaluated at times delayed by τ_{az}, the two-way travel time of the radar signals, as acknowledged in [23]. This lag, typically in the order of milliseconds, is beyond the inverse of the bandwidth relevant to the calibration of the bistatic SAR data, which allows for the approximation

$$\varphi_v(t - \tau_{\mathrm{az}}) - \varphi_u(t) \approx \varphi_v(t) - \varphi_u(t). \tag{3.8}$$

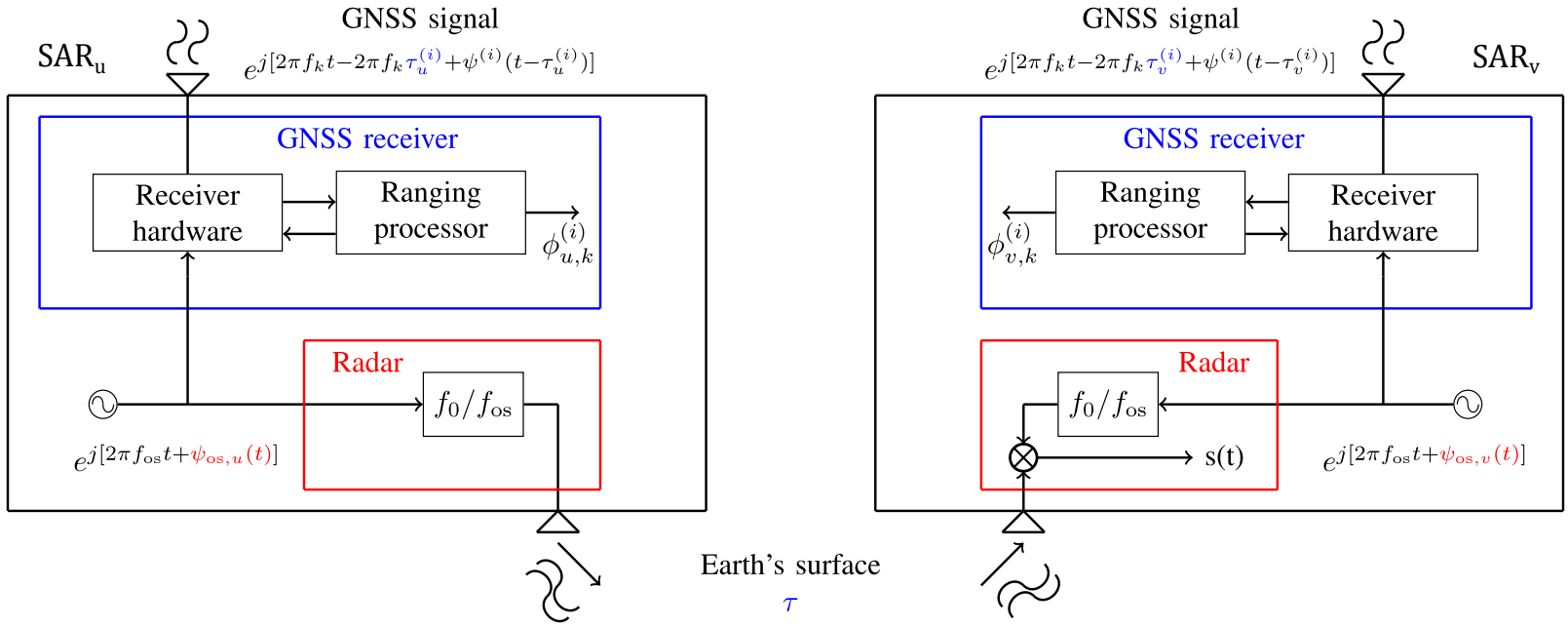

Figure 3.2: Block diagram of the system architecture for radar phase synchronization based on GNSS, also used as the basis for the analysis. In this figure, $\tau_{()}^{(i)}$ are the delays from GNSS satellite i to the SAR satellites.

3.2.2 Estimation of the Synchronization Phase

The proposed estimator is illustrated in Figure 3.3. It isolates the clock term from the systematic components present in the single differences of the carrier phases using information derived from precise orbit and baseline determination, such as the baseline solution, ambiguities and bulk ionospheric delays.

The differential phase of the oscillators on the two satellites can be extracted from the single differences in case the other factors can be determined with sufficient accuracy by other means. In that case, the estimates of the differential phase noise would be obtained at the sampling rate of the carrier phase measurements. The differential signal path length and ionospheric delay can be determined with high accuracy from the POD process.

The baseline and phase difference estimations could, in principle, also be done in a single step. This single-step approach, however, is not expected to improve noticeably the accuracy of the estimation due to the different temporal scales of the clock phase noise (with much faster variations) and the changes in spacecraft acceleration (much slower).[2] This work sticks to the two-step solution because it allows the PBD and the phase synchronization to be implemented in two independent modules in the ground segment. This avoids the need to use a common time step for both estimations, which would complicate the PBD due to the additional computational load for the segments requiring phase synchronization. Additionally, the two-step approach allows for more flexibility to implement different filtering techniques to the relative phase solution.

From (2.32), the relationship between the differential carrier phase measurements $L_{uv,k}^{(i)}$—directly scaled by a factor $\lambda_k/2\pi$ and therefore expressed in units of meters—and the clock bias δt_{uv} is given by

$$\begin{aligned} L_{uv,k}^{(i)}(t) =& \rho_{uv}^{(i)}(t) + \mathrm{c}\cdot\delta t_{uv}(t) - \left(\frac{\lambda_k}{\lambda_1}\right)^2 \cdot I_{uv}^{(i)}(t) - \\ & \lambda_k \cdot A_{uv,k}^{(i)} + M_{uv,k}^{(i)}(t) + \eta_{uv,k}^{(i)}(t)\,, \end{aligned} \tag{3.9}$$

where $\rho_{uv}^{(i)}$ is the difference between the distances from receivers v and u to the i-th navigation satellite, respectively, c is the speed of light in vacuum, $I_{uv}^{(i)}$ denotes the difference between the biases caused by the ionospheric delays for a signal at wavelength λ_1, $A_{uv,k}^{(i)}$ is the ambiguity difference, $M_{uv}^{(i)}(t)$

[2] For reference, [111] provides an example where increasing the sampling rate does not lead to improved navigation solution precision.

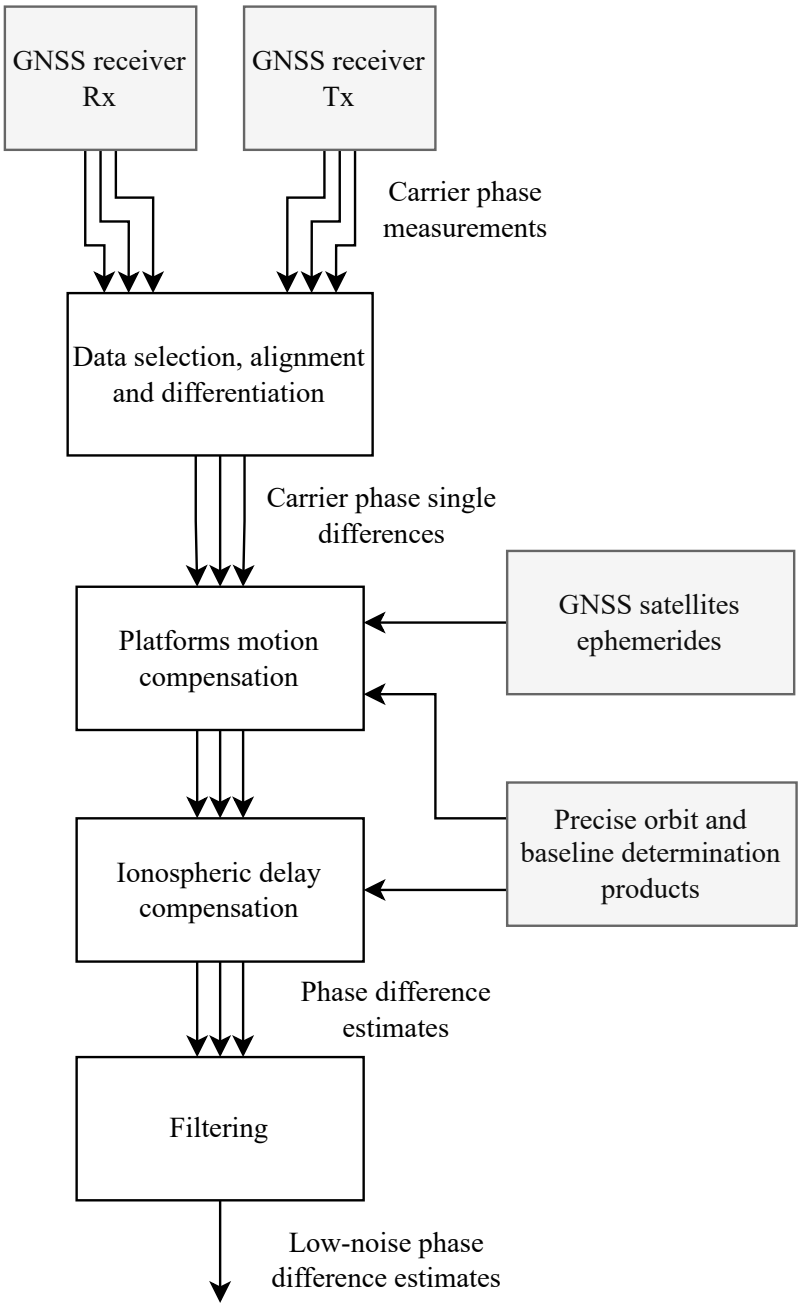

Figure 3.3: Block diagram of the proposed GNSS-based estimation process of the radar carriers phase difference.

describes other systematic error components including multipath, cross-talk, tracking channel bias and phase wind-up, and $\eta_{uv}^{(i)}(t)$ is a zero-mean random noise process. Substituting from (3.1) and (3.4), results in the relationship between navigation data and the clock synchronization solution as follows

$$\begin{aligned}\frac{\lambda_0}{2\pi}\cdot\psi_{uv,0}(t) =& L_{uv,k}^{(i)}(t)+\lambda_k\cdot A_{uv,k}^{(i)}-\rho_{uv}^{(i)}(t)+\\ &\left(\frac{\lambda_k}{\lambda_1}\right)^2\cdot I_{uv}^{(i)}(t)+\frac{\lambda_0}{2\pi}\cdot\psi_{\mathrm{b}uv,0}-\mathrm{c}\cdot\delta t_{0uv}-\\ &M_{uv,k}^{(i)}(t)-\eta_{uv,k}^{(i)}(t)\,.\end{aligned}\tag{3.10}$$

where $\psi_{\mathrm{b}uv,0}$ is a constant bias. A clock synchronization solution can then be derived as a weighted average over all navigation satellites in sight (i.e., N) and all the $n_\lambda^{(i)}$ received GNSS frequencies, mitigating the effect of measurement noise comprised of both $M_{uv,k}^{(i)}$ and $\eta_{uv,k}$, as follows

$$\begin{aligned}\tilde{\psi}_{uv,0} =& \frac{2\pi}{\lambda_0}\cdot\sum_{i=1}^{N}\sum_{k=1}^{n_\lambda^{(i)}}\alpha_k^{(i)}\cdot\Bigg[L_{uv,k}^{(i)}+\lambda_k\cdot\tilde{A}_{uv,k}^{(i)}-\tilde{\rho}_{uv}^{(i)}+\\ &\left(\frac{\lambda_k}{\lambda_1}\right)^2\cdot\tilde{I}_{uv}^{(i)}\Bigg]+\tilde{\psi}_{\mathrm{b}uv,0}-\frac{2\pi\cdot\mathrm{c}}{\lambda_0}\cdot\delta\tilde{t}_{0uv}\,,\end{aligned}\tag{3.11}$$

where $\tilde{()}$ indicates the PBD estimate for all the terms and $\alpha_k^{(i)}$ are the weights for the signal from each navigation satellite according to its quality (e.g., signal-to-noise ratio), with the sum of $\alpha_k^{(i)}$ being equal to one. Note that the terms in the second sum have been assumed to be sampled according to the condition in (3.8). (3.11) provides an estimation under the assumption that $M_{uv,k}^{(i)}$ is negligible, $\eta_{uv,k}^{(i)}$ is a zero-mean process, and no relevant biases are introduced in the baseline determination process. As hinted earlier, the term under the summation contains systematic error components which may, if not properly removed, bias the resulting estimates.

Assuming the measurements are statistically independent Gaussian processes, the value of $\alpha_k^{(i)}$ which minimizes the variance of the estimator is given by

$$\alpha_k^{(i)}=\frac{(\sigma_k^{(i)})^{-2}}{\sum_{i=1}^{N}\sum_{j=1}^{n_\lambda^{(i)}}(\sigma_j^{(i)})^{-2}}\,,\tag{3.12}$$

where the $\sigma_k^{(i)}$ correspond to the standard deviation of the measurements (e.g., of the residuals of the POD). Two reasonable assumptions for the derivation of the estimator performance are i) a successful calibration of relevant systematic components and ii) the measurement is dominated by thermal noise in the receiver. Under these circumstances, for a Phase-Locked Loop discriminator, $\sigma_k^{(i)}$ can be expressed as a function of the carrier-to-noise ratio $(\mathrm{c}/n_0)_k^{(i)}$ as follows

$$\sigma_k^{(i)} \approx \sqrt{\frac{B_{\mathrm{L-CA}}}{(\mathrm{c}/n_0)_k^{(i)}}}, \tag{3.13}$$

where $B_{\mathrm{L-CA}}$ is the carrier tracking bandwidth of the GNSS receiver [99], i.e., the effective closed-loop bandwidth of the PLL used to track the carrier phase. Substituting (3.13) into (3.14) results in

$$\alpha_k^{(i)} = \frac{(\mathrm{c}/n_0)_k^{(i)}}{\sum_{i=1}^{N}\sum_{j=1}^{n_\lambda^{(i)}}(\mathrm{c}/n_0)_j^{(i)}}, \tag{3.14}$$

The c/n_0 values estimated by the GNSS receiver itself can be used for obtaining the weights. Note that these values may change during the data acquisition period, which would result in time-varying weights $\alpha_k^{(i)}$. In case the individual phase error estimates are biased, this variation would cause undesirable dynamic error components. Therefore, it is recommended to fix the values of $\alpha_k^{(i)}$ for the whole data acquisition period by using, for example, an average of the (c/n_0) measurements.

The assumption in (3.12) that the noise-like random error component, assumed driven by thermal noise, being uncorrelated across carrier phase observables is common in POD literature. However, this assumption is not always strictly valid. A more general model for the random error will be presented in Chapter 4, supported by experimental evidence. While the weighting scheme proposed in (3.14) may not be strictly optimal in all cases, it provides satisfactory performance and is recommended when detailed information on the carrier phase error characteristics of the employed receiver is unavailable, or when thermal noise is the dominant error source.

A similar estimator can be derived using the code delay measurements instead of the carrier phases. However, the code delay, despite unambiguous,

is much less precise, typically by about two orders of magnitude. Therefore, the resulting synchronization precision would not be nearly sufficient for typical distributed SAR applications.

3.2.3 Remarks on Time Synchronization

Time synchronization in multistatic and bistatic radars involves the precise timing of individual pulse reception to ensure correct range bin alignment and full recording of echo signals. Although this thesis focuses on phase synchronization, which is in general the most challenging synchronization problem, the hardware configuration required for the proposed technique also enables time synchronization. In this setup, the receiver hardware is coherent with the GNSS timing system, allowing individual received signal samples to be time-tagged with GNSS timing precision, typically below 50 ns for real-time PVT solutions and potentially below 1 ns with POD solutions [112].

Furthermore, the time difference between transmission and reception can be tracked with much greater accuracy using the phase synchronization solution itself. Due to the coherence between the generated carrier and timing signals, time and phase differences are directly proportional to each other. As a result, the transmission-reception time difference could, in principle, be determined a-posteriori according to the results that will be presented further in Section 4.4, which in terms of time corresponds to a few picoseconds or less, provided that hardware delays are calibrated. This approach resembles the solution employed in TanDEM-X, where a PPS generated by the radar oscillator is compared with PPS signals from the GNSS receiver, and the resulting difference is used to compensate for the echo window drift of the receiving radar system [27].

3.3 Error Analysis

A further elaboration of the system model suggests the incorporation of other systematic phase signatures occurring in the radar and navigation receiver electronics, specially in the interface with the external oscillator. Under these circumstances, the phase differences at radar and navigation carriers between the two satellites with the relative clock bias can be related as follows

$$\delta t_{uv}(t) = \delta t_{0\,uv} + \frac{1}{2\pi \cdot f_0} \cdot \left[\psi_{uv,0}(t) + \delta\psi_{\mathrm{HW}uv,0}(t)\right], \tag{3.15}$$

where $\delta\psi_{\mathrm{HW}uv,0}$ denotes the residual signature caused by radar and navigation receiver hardware.

The error in the estimation of the differential phase at the radar carrier $\epsilon_{uv,0}$ can be derived after combining (3.11), (3.9) and (3.15) as follows

$$\begin{aligned}\epsilon_{uv,0}(t) = \sum_{i=1}^{N}\sum_{k=1}^{n_\lambda^{(i)}} \frac{2\pi}{\lambda_0}\cdot\alpha_k^{(i)}\cdot\Bigg\{\tilde{\rho}_{uv}^{(i)}(t) - \rho_{uv}^{(i)}(t) - \eta_{uv,k}^{(i)}(t) - \\ M_{uv,k}^{(i)}(t) + \left(\frac{\lambda_k}{\lambda_1}\right)^2\cdot\left[I_{uv}^{(i)}(t) - \tilde{I}_{uv}^{(i)}(t)\right] + \\ \lambda_k\cdot\left(A_{uv,k}^{(i)} - \tilde{A}_{uv,k}^{(i)}\right)\Bigg\} + \psi_{\mathrm{b}uv,0} - \tilde{\psi}_{\mathrm{b}uv,0} - \\ \frac{2\pi\cdot\mathrm{c}}{\lambda_0}\cdot(\delta t_{0uv} - \delta\tilde{t}_{0uv}) - \delta\psi_{\mathrm{HW}uv,0}(t)\,. \end{aligned} \tag{3.16}$$

The equation (3.16) describes the error in the estimation of the phase difference between the two master oscillators at the radar carrier frequency. Since the error components are proportional to the inverse of the radar wavelength, the estimation error is expected to increase for higher radar frequencies. The following subsections discuss in more detail the impact of the error terms in (3.16).

3.3.1 Thermal Noise

The thermal noise contribution describes the boundary of the performance of the algorithm in the absence of the other systematic components. Under the assumption of statistical independence and identical noise power for all frequencies corresponding to the measurement of a given navigation satellite, the standard deviation of the phase estimator, combining all observables, due to thermal noise can be expressed as

$$\sigma_\epsilon = \frac{2\pi}{\lambda_0}\cdot\sqrt{\sum_{i=1}^{N}\frac{(\alpha^{(i)}\cdot\sigma_{uv}^{(i)})^2}{n_\lambda^{(i)}}}, \tag{3.17}$$

where $\sigma_{uv}^{(i)}$ is the standard deviation of the differential noise process corresponding to the signal received from the navigation satellite i. Under the assumption that both parts receive the signals of satellite i with signal-to-noise ratio, and therefore same standard deviation $\sigma^{(i)}$—reasonable for

standard baselines and identical GNSS receivers—and substituting from (3.13), the previous expression may be approximated as

$$\sigma_\epsilon \approx \frac{2\pi}{\lambda_0} \cdot \sqrt{\frac{2}{n_\lambda} \cdot \frac{1}{\sum_{i=1}^{N} (\sigma^{(i)})^{-2}}}, \tag{3.18}$$

where the same number of available navigation frequencies n_λ for all satellites has been assumed. The accuracy of the estimation improves with an increasing number of satellites and frequencies tracked. The noise boundary for the performance of the GNSS-based estimation of the synchronization phase can be expressed as

$$\sigma_\psi \approx \sigma_\epsilon \cdot \sqrt{\frac{B_\psi}{f_{\text{gnss}}}} \approx \frac{2\pi}{\lambda_0} \cdot \sqrt{\frac{2 \cdot B_\psi}{n_\lambda \cdot f_{\text{gnss}}} \cdot \frac{1}{\sum_{i=1}^{N} (\sigma^{(i)})^{-2}}}, \tag{3.19}$$

where B_ψ represents the bandwidth of the oscillator phase noise relevant for the correction of the bistatic SAR data and f_{gnss} corresponds to the rate at which the pseudoranges are made available by the GNSS receivers. The value of B_ψ depends on the characteristics of the master oscillator and the carrier frequency of the radar; for interferometric applications typical values for B_ψ are in the order of a few Hertz. In the case of TanDEM-X, the direct link is operated at a rate of 5 Hz, a value consistent with the performance estimation reported in [27].

Figure 3.4 shows an example of the expected contribution of the thermal noise performance in terms of noise for the proposed GNSS-based synchronization scheme in the case of a 5.405 GHz SAR payload.[3] The receiver noise performance is based on the single-frequency GPS receiver Phoenix developed by the German Space Operations Center (GSOC) of DLR [113]. The specific values used in the simulation are listed in Table 3.1. The results indicate a performance around one degree for a moderate number of tracked GNSS signals, which is comparable to that achieved by TanDEM-X. The low signal levels of the received GNSS signals therefore are not an impediment for the technique to achieve the required synchronization accuracy.

[3] The simulated case corresponds to that of a bistatic companion of ESA's Sentinel-1 satellite and has been used by the authors as a reference for the phase 0 study of ESA Earth Explorer 10 mission Harmony.

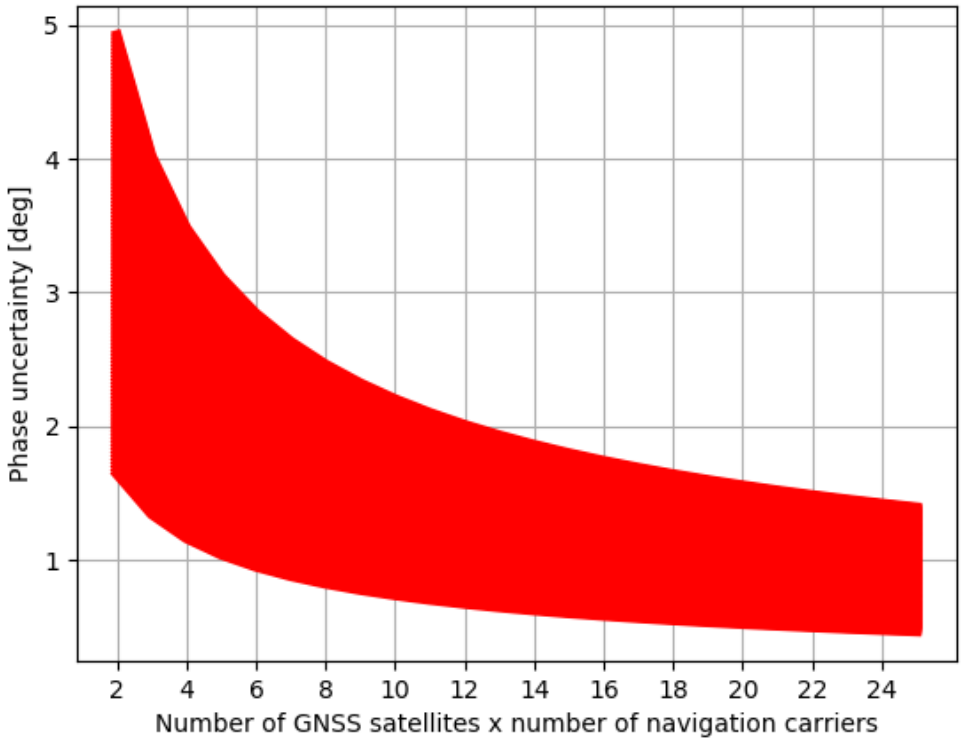

Figure 3.4: Standard deviation of the phase error due to thermal noise according to the model in (3.19) for a 5.405 GHz SAR payload, with the number of satellites in view N varying from two to twelve and the number of frequencies n_λ up to two. The standard deviation in ranging caused by thermal noise has been assumed to vary between 1.2 and 0.4 mm, values consistent with the technical specification of the Phoenix receiver of DLR [113]. The final phase uncertainty depends on the standard deviation of the individual satellites, but in this example would be necessarily within the shaded region.

Table 3.1: Simulation parameters for phase uncertainty calculation

Parameter	Value
Radar carrier frequency [GHz]	5.405
Thermal ranging accuracy [mm]	[0.4, 1.2]
Number of GNSS satellites	[2, 12]
n_λ	[1, 2]
B_ψ [Hz]	2
f_{gnss} [Hz]	5

3.3.2 Baseline Errors

As suggested by (3.16), baseline estimation errors directly appear as residual phase signatures in the estimated solutions. The baseline error term in (3.16) includes the error in the PBD and the error in the estimated position of the phase centers of the navigation and the radar antennas. The latter can be assumed to be negligible for a well calibrated system and accurate attitude determination.

The PRISMA mission provides some useful figures for assessing the shape and magnitude of the baseline error. The mission conducted various experiments on formation flying with two spacecraft. In the initial phase of the mission, the two spacecraft were physically attached, which allowed for an independent, highly accurate, baseline reference using the attitude information [107]. The baseline was estimated in this initial phase with GNSS data, and compared with the baseline reference. The comparison result showed the baseline error magnitude and its variation over time. The radial, along-track, and cross-track components of the baseline error describe, most of the time, a sinus-like shape over an orbital period (i.e., around 90 minutes) with amplitudes of a few millimeters. This suggests that, for acquisitions of only a few minutes, the baseline will vary little, and can be approximated by a linear term.

The PRISMA data show, however, some discontinuities in the baseline error which would translate into abrupt phase jumps in the estimator here proposed. These jumps should be avoided or eliminated from the estimates used for the derivation of the synchronization solution.

Linear baseline errors will be equivalent in the synchronization solution as carrier frequency offset. In the case of interferometric applications on static surfaces, the resulting carrier offset can be easily estimated in the data processing if it is constant over scales of a few minutes [41]. For other applications, the carrier offset would result in artifacts on the synthesized image. This issue is particularly severe for moving-surface applications, where the effect of a small frequency offset cannot be isolated from the SAR product.

An approximate explicit relation between the baseline and phase synchronization errors is derived in the following paragraphs to provide further insight into its impact. The baseline determination error for each GNSS satellite can be approximated as follows by linearizing the error term around zero as a function of the baseline solution [100]

$$\rho_{uv}^{(i)} - \tilde{\rho}_{uv}^{(i)} \approx -\tilde{\vec{e}}_{v}^{(i)} \cdot \Delta\vec{r}_{uv} - \tilde{\vec{e}}_{uv}^{(i)} \cdot \Delta\vec{r}_{u} + \tilde{\vec{e}}_{uv}^{(i)} \cdot \Delta\vec{r}^{(i)}\,, \tag{3.20}$$

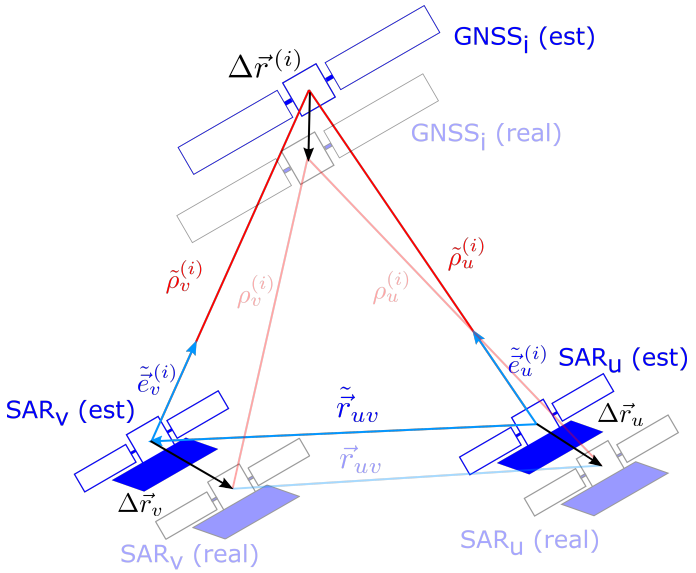

Figure 3.5: Basic geometry for the derivation of the baseline determination error.

in which the $\tilde{\vec{e}}_u^{(i)}$ are unit vectors in the direction from the estimated position of SAR satellite u to GNSS satellite i, $\Delta\vec{r}^{(i)}$ is the error in the position of GNSS satellite i, $\Delta\vec{r}_{uv}$ is the baseline error, and $\Delta\vec{r}_u$ is the error in the position of SAR satellite u, as shown in Figure 3.5.

For baselines of up to a few kilometers, the vectors $\tilde{\vec{e}}_u^{(i)}$ and $\tilde{\vec{e}}_v^{(i)}$ are nearly parallel, rendering the term $\tilde{\vec{e}}_{uv}^{(i)}$ effectively negligible. Consequently, the contributions of $\tilde{\vec{e}}_{uv}^{(i)} \cdot \Delta\vec{r}_u$ and $\tilde{\vec{e}}_{uv}^{(i)} \cdot \Delta\vec{r}^{(i)}$ are much smaller than the remaining term in the equation. Under this condition, the individual orbit determination errors can be approximated as

$$\sum_{i=1}^{N}\sum_{j=1}^{n_\lambda^{(i)}} \alpha_k^{(i)} \cdot \left[\rho_{uv}^{(i)}(t) - \tilde{\rho}_{uv}^{(i)}(t)\right] \approx -\Delta\vec{r}_{uv}(t) \cdot \sum_{i=1}^{N} \alpha^{(i)} \cdot \tilde{\vec{e}}_v^{(i)}(t)\,, \tag{3.21}$$

with

$$\alpha^{(i)} = \sum_{k=1}^{n_\lambda^{(i)}} \alpha_k^{(i)}\,. \tag{3.22}$$

The summation on the right in (3.21) corresponds to a weighted average of unit vectors distributed more or less uniformly in a semi-sphere. Since the weights $\alpha^{(i)}$ depend on the signal-to-noise ratio, higher elevations will receive a higher weight. Assuming an antenna pattern symmetrical with respect to the direction of the main lobe, the terms in the along-track and

Figure 3.6: Components of the GNSS-SAR average direction vector for a 500 km altitude circular orbit and expected phase estimation error per millimeter baseline error for a 5.405 GHz SAR payload.

across-track in the individual vectors $\tilde{\vec{e}}_v^{(i)}$ will tend to cancel out when taking the average. These two factors contribute to making this summation term a vector predominantly in the radial direction. Since the final result is the scalar product of the baseline error with this roughly radial vector, the radial component of the baseline error will tend to dominate the final error in the baseline estimation.

Figure 3.6 shows an example to illustrate the influence of each component of the baseline error in the phase synchronization solution.

It corresponds to the application of (3.21) to simulated orbital data considering a 5.405 GHz SAR payload. The GNSS orbits are obtained from propagated publicly available GPS Two-line Elements (TLE) data. It gives an idea of the order of magnitude and structure resulting from the baseline error and corroborates the higher influence of the radial component. Note the plot shows the behavior of the error over a period of hours. Within the temporal scales of the synthetic aperture or SAR acquisitions, from about a second to a few minutes, the observed variations remain negligible (e.g., below one second of arc per millimeter for one minute).

Based on (3.21), the carrier offset due to baseline velocity errors is expected to be negligible. Considering, for example, a 5.405 GHz SAR payload, a baseline velocity error of 0.008 mm/s in the radial direction—loosely based

on results from the PRISMA mission [107]—and a radial component of the GNSS-SAR average direction vector of -0.6 would result in a carrier offset of about 0.086 mHz, which might be visible as a residual ramp in interferometric acquisitions over several minutes.

3.3.3 Residual Signatures of the Receiver and Up-Converting Electronics

The model in (3.1) assumes the ideal behavior and spectral purity of all up-converting and frequency synthesizer electronics in the radar transmitter and receiver. The residual signature considered in (3.15) will directly contaminate the solution if any of those conditions are not satisfied. This error source is common to all received signals and, unlike thermal noise, cannot be reduced by averaging measurements across different frequencies and GNSS satellites. Thus, it corresponds to a fundamental performance limit for the synchronization technique discussed here.

As discussed in Section 2.3.2, GNSS receivers usually uses many local oscillators locked to the master oscillator through PLLs, and a Digitally Controlled Oscillator (DCO) to generate the internal reference signal [99]. A PLL can also be used to lock an internal oscillator to an external frequency source in some designs. The jitter added by these frequency generation devices within the receiver is expected to cause a deviation from the ideal proportionality between the clock term of the carrier phase measurement and the phase noise of the master oscillator.

Among the many architectural implications of the conditions above (e.g., low-phase noise of mixers, PLLs, and other active elements especially in the navigation receivers), it is pertinent to focus on the selection of the master frequency of the system. Above all, the use of other oscillators only impacting either the navigation receiver or the radar electronics should be avoided, unless they are made coherent to the master oscillator through a PLL.

The performance floor contribution from receiver electronics, added to the carrier phase tracking error due to thermal noise, can be determined by calculating the single differences of the carrier phase measurements between two receivers taking as input the same GNSS signal (e.g., using the same antenna) and the same master oscillator. Results from such experiments are reported in [114], which shows that a performance floor of 1 mm RMS in the L1 band, corresponding to 1.9 degrees, is achievable with currently available dual-frequency geodetic-grade receivers. Chapter 4 will present

results from similar experiments, demonstrating that this error can be majorly reduced through the use of appropriate receivers.

The simulation presented in Section 3.4 assumes that the performance floor established by the receiver and radar electronics is well below the thermal noise component at the tracking loop of each signal. This chapter is focused on the error sources which cannot be mitigated in the receiver and radar payload design, i.e., the thermal noise and the positioning uncertainties. The other factors major contributors will be evaluated and characterized in the Chapter 4 through experiments.

3.3.4 Ionospheric Delay

As mentioned before, the ionospheric delays can be estimated in the POD along with the clock bias, position, and other parameters. For short baselines, of less than one kilometer, ionospheric path delays for the two satellites are expected to be highly correlated. For example, in the GRACE mission, the differential path delays were dominated by carrier phase measurement noise, which resulted in a scatter of roughly 1 cm [115]. The differential ionospheric delay thus is expected to be very low and the error from the differential ionospheric delay estimation is expected to be even lower.

In case the differential ionospheric delay component is not negligible, it can be directly eliminated by employing a dual-frequency receiver (or with more bands). From (3.10), the observables from a dual-frequency receiver can be modeled as

$$\frac{\lambda_0}{2\pi}\cdot\psi_{uv,0} - I_{uv}^{(i)} = L_{uv,1}^{(i)} + \lambda_1\cdot A_{uv,1}^{(i)} - \rho_{uv}^{(i)} - \mathrm{c}\cdot\delta t_{0\,uv} - \eta_{uv,1}^{(i)}, \tag{3.23}$$

$$\frac{\lambda_0}{2\pi}\cdot\psi_{uv,0} - \left(\frac{\lambda_2}{\lambda_1}\right)^2\cdot I_{uv}^{(i)} = L_{uv,2}^{(i)} + \lambda_2\cdot A_{uv,2}^{(i)} - \rho_{uv}^{(i)} - \mathrm{c}\cdot\delta t_{0\,uv} - \eta_{uv,2}^{(i)}. \tag{3.24}$$

Isolating the phase error from the system of equations above, and considering the errors as independent zero-mean Gaussian processes, results in

$$\psi_{uv,0} = \frac{2\pi}{\lambda_0}\cdot\left(\frac{\lambda_2^2}{\lambda_2^2-\lambda_1^2}\right)\cdot\left[L_{uv,1}^{(i)} + \lambda_1\cdot A_{uv,1}^{(i)} - \left(\frac{\lambda_1}{\lambda_2}\right)^2\cdot\left(L_{uv,2}^{(i)} + \lambda_2\cdot A_{uv,2}^{(i)}\right) - \left(1-\frac{\lambda_1^2}{\lambda_2^2}\right)\cdot\rho_{uv}^{(i)}\right] - \frac{2\pi\cdot\mathrm{c}}{\lambda_0}\cdot\delta t_{0\,uv} + \eta_{uv,12}^{(i)}, \tag{3.25}$$

where

$$\eta_{uv,12}^{(i)} = \frac{2\pi}{\lambda_0} \cdot \left(\frac{\lambda_2^2}{\lambda_2^2 - \lambda_1^2} \right) \cdot \left(\eta_{uv,1}^{(i)} + \frac{\lambda_1^2}{\lambda_2^2} \cdot \eta_{uv,2}^{(i)} \right). \tag{3.26}$$

Each pair of differential measurements will result in a single estimate of the phase noise which is free from the effect of the ionospheric delay. The phase error can be estimated as a weighted average of all the differential measurements for each GNSS satellite in view, which results in

$$\begin{aligned} \tilde{\psi}_{uv,0} = & \frac{2\pi}{\lambda_0} \cdot \left(\frac{\lambda_2^2}{\lambda_2^2 - \lambda_1^2} \right) \cdot \sum_{i=1}^{N} \alpha_i \Bigg[L_{uv,1}^{(i)} + \lambda_1 \cdot A_{uv,1}^{(i)} - \\ & \left(\frac{\lambda_1}{\lambda_2} \right)^2 \cdot \left(L_{uv,2}^{(i)} + \lambda_2 \cdot A_{uv,2}^{(i)} \right) - \left(1 - \frac{\lambda_1^2}{\lambda_2^2} \right) \cdot \tilde{\rho}_{uv}^{(i)} \Bigg] - \frac{2\pi \cdot \mathrm{c}}{\lambda_0} \cdot \delta \tilde{t}_{b\,uv}. \end{aligned} \tag{3.27}$$

Compared to the estimator given by (3.11), the one given by (3.27) is derived from half the number of observables, since a single ionosphere-free observable requires two carrier phase measurements. Additionally, each ionosphere-free carrier phase measurement has a higher standard deviation. For the L1 and L2 frequencies from GPS (1575.42 MHz and 1227.6 MHz, respectively), the final standard deviation of the estimation error will be multiplied by the factor

$$\frac{\sigma_{\text{ion-free}}}{\sigma_{\text{dual}}} = \sqrt{2} \cdot \frac{\sqrt{\lambda_2^4 + \lambda_1^4}}{\lambda_1^2 - \lambda_2^2} = 4.20. \tag{3.28}$$

The performance degradation resulting from the use of ionosphere-free combinations instead of individual measurements will be demonstrated in Section 3.4, with results consistent with the theoretical estimates presented above. This combination, or a high-frequency point-by-point estimation of the differential ionospheric delay in case more frequencies are available, should be used when the time variation of the differential ionospheric delay is considerably higher than the noise level of the carrier phase measurements.

3.3.5 Unmodeled Components

Another error source in the GNSS measurement are the phase center variations of the receiver antenna depending on direction of the received GNSS

signal. If this variation is not accounted for, it will introduce a bias and a slowly varying additional error to the carrier phase measurement. This error can be calibrated on ground for posterior compensation. This is a common procedure in PBD and was implemented, for example, in the CHAMP and GRACE missions [116]. However, as remarked in [117], even after applying the calibration, other azimuth and elevation-dependent unmodeled variations can persist. These errors can be reduced by applying frequency-dependent patterns from in-orbit calibration, as demonstrated in [116], where after calibration the carrier phase precision is improved to a level close to the pure receiver noise.

One of the potentially most critical error sources is the multipath, which results from the superposition of the signal received directly from the GNSS satellite and the signal reflected by other surfaces of the spacecraft. This error depends on the signal difference, the strength, and polarization of the reflected radiation, as well as the internal characteristics of the receiver [100]. Multipath is confined to a quarter of the navigation signal wavelength [118]. This error, which depends on the spacecraft shape, can be a significant, and the system must be designed to suppress or avoid it. For example, the two spacecraft used in the GRACE mission did not employ deployable solar panels and antennas. The PRISMA mission, which also performed experiments on POD, had the GPS antennas on the tips of the solar panels, which may have contributed to mitigating multipath. The strategy used in PRISMA is of particular relevance for low-cost SAR missions since their high power demand may require the use of deployable solar panels. On the other hand, this approach may introduce errors from residual solar panel vibrations and attitude uncertainties, which must be carefully evaluated and taken into consideration in early design trade-off studies.

The effect of multipath in the final phase estimation can be directly quantified from the corresponding component in (3.16), and it will consist of the weighted average of the contribution of each signal used in the estimation. The total multipath contribution to the synchronization error budget can be predicted by simulating the individual multipath errors, for example, through the procedure explained in [119], and applying the weighted averaging. One possible approach to mitigating multipath could be to identify the signals strongly affected by it and eliminate them from the estimation. This work puts forward in Chapter 4 a method for evaluating the variance of the errors affecting individual carrier phase observables which can be used for this purpose. Experiments using real GNSS signals demonstrate the robustness of the proposed synchronization technique to multipath.

This robustness can be attributed to the high geometric diversity of visible GNSS signals, which increases the likelihood that at least some signals will have favorable multipath conditions.

In addition to the aforementioned errors, the phase measurements are affected by the wind-up effect, which corresponds to the phase accumulation due to the rotation of the antennas about the line-of-sight between the GNSS transmitter and receiver [100]. This effect arises due to the electromagnetic nature of circularly polarized waves such as the GNSS signals. This error is not expected to be as significant as, for example, multipath [120], and it can be compensated in an operational scenario by applying the analytical correction derived in [121] if necessary.

3.3.6 Ambiguities

As shown in (3.16), errors in the ambiguity estimation for each signal will affect the final phase estimate. The constant receiver delays also will bias the carrier phase ambiguities [100]. This could be a relevant error source for a SAR application in which absolute phase reference is necessary. Having absolute phase calibration independent from external data in the synchronization solution is relevant only for specific applications. For interferometry, for example, having an absolute phase reference could make it possible to resolve the unknown ambiguity interval in the interferometric DEM without the need for height referencing on ground [106].

Since the ambiguities are constant for any given tracking arc, the corresponding error component will not change as long as the receiver remains locked to the same GNSS satellites during the SAR data acquisition time. This will most likely be the case for an acquisition time of a few minutes. If a GNSS satellite comes into view or goes out of view, using its carrier phase data may introduce a discontinuity into the relative phase estimate, which might appear masked in the estimated solution if inspected after averaging over navigation satellites.

The trivial but effective way to mitigate this problem would be to use only data from the GNSS satellites to which the receiver remains locked during the entire data acquisition period. This can result in discarding useful data for long acquisitions, but it is not expected to considerably degrade the performance of the technique because the satellites with visibility time of less than the short acquisition period will be few, and they will necessarily be seen at a low elevation, offering measurements with lower SNR.

3.3.7 Long Versus Short Baseline Scenarios

Among the error sources discussed in this section, two are expected to increase significantly with distance: the baseline error and the ionospheric delay. The GRACE mission demonstrated sub-millimeter baseline determination accuracy using GNSS alone over a separation of approximately 220 km [122]. Therefore, Precise Baseline Determination (PBD) accuracy is not expected to be a limiting factor at least up to this distance—and likely beyond—provided that a GNSS receiver with capabilities comparable to those used on GRACE is employed.

In contrast, synchronization performance over long baselines is expected to degrade substantially due to decorrelation of ionospheric effects on the carrier phases received by the two satellites. In [115], the authors analyzed differential ionospheric delays on dual-frequency carrier-phase measurements from the GRACE mission during a longitude swap maneuver, in which the satellites crossed at separations below 2 km. Their results indicated that ionospheric delays remained below the carrier-phase noise level for distances up to approximately 5 km, but became increasingly significant at greater separations. As discussed in Section 3.3.4, this effect can, in principle, be mitigated by applying a linear combination of inter-frequency carrier-phase data, albeit at the cost of increased measurement noise. Therefore, while the proposed technique remains applicable for baselines of up to 220 km—such as those encountered in very long baseline bistatic systems like the Harmony mission—its performance is expected to be degraded due to ionospheric decorrelation effects.

In the case of companion missions, taking Harmony as an example, the transmitter could be at a distance of a couple of hundred kilometers from the receiver satellites. The receiver satellites, in turn, could either be separated by a few hundred meters or by several hundreds of kilometers, depending on the mission phase [35]. The two Harmonies could be seamlessly synchronized using the GNSS-based synchronization technique presented here during the cross-track interferometric phase, in which the satellites will fly at a baseline of a few hundred meters in a helix configuration. The technique could also be applied for baselines of a couple of hundred kilometers in case degraded performance can be tolerated.

3.4 System Example

This section presents an example of the GNSS-based phase estimation technique estimation for a C-band bistatic SAR system equipped with simple

GNSS receivers. The example is based on a simulation including thermal noise, ionospheric delay, and baseline determination errors. Radar parameters are based on the ESA Earth Explorer 10 mission Harmony, while positioning error parameters are derived from results of the PRISMA mission [107] and the performance characteristics of the GSOC Phoenix GPS receiver [113]. The simulation evaluates the combined impact of orbit determination errors and receiver thermal noise on system performance. Figure 3.7 illustrates the data flow and main components of the simulation.

The simulation represents the two C-band bistatic SAR satellites flying in close formation, with a 320 m initial baseline, and with the suggested hardware configuration implemented. The navigation antennas on the radar spacecraft have direct visibility with nine GPS satellites during the simulation period. The orbits of all satellites are propagated using NASA's open-source software GMAT [123]. The software allows for the numerical integration of all orbits using an accurate gravitational model that includes drag and third-body attractions. The errors in the position and velocity of the radar satellites resulting from the precise orbit determination have been simulated by introducing an absolute bias in the initial state of the satellites prior to orbit propagation. For convenience, historic GPS ephemerides are imported and propagated directly using the Systems Tool Kit (STK) software.

After propagating the orbits, the ranges between the radar satellites and the GNSS satellites in view at a minimum elevation of 10 degrees are calculated. The navigation raw data is simulated by adding the following error components to the expected code and phase signal: ionospheric delay, initial clock bias, thermal noise, and clock drift.

The phase drift realization is derived from real measurement done with the synchronization link of TanDEM-X. The ionospheric delay is calculated assuming a background component only of a constant vertical total electron content (VTEC) and applying the elevation-only dependent mapping function by Lear [124]. In this case, even if simulated in the navigation raw data, the difference in the ionospheric delays affecting the signals in the satellites is negligible, and was not considered in the phase estimator.

The simulations assume a single-frequency GNSS receiver, consistent with the Phoenix receiver, with noise characteristics modeled according to its specifications. The resulting error levels are on the order of a few millimeters, comparable to those achieved in the PRISMA mission, which also employed a single-frequency GNSS receiver. The clock phase difference is estimated using (3.11), with weighting factors defined in (3.14).

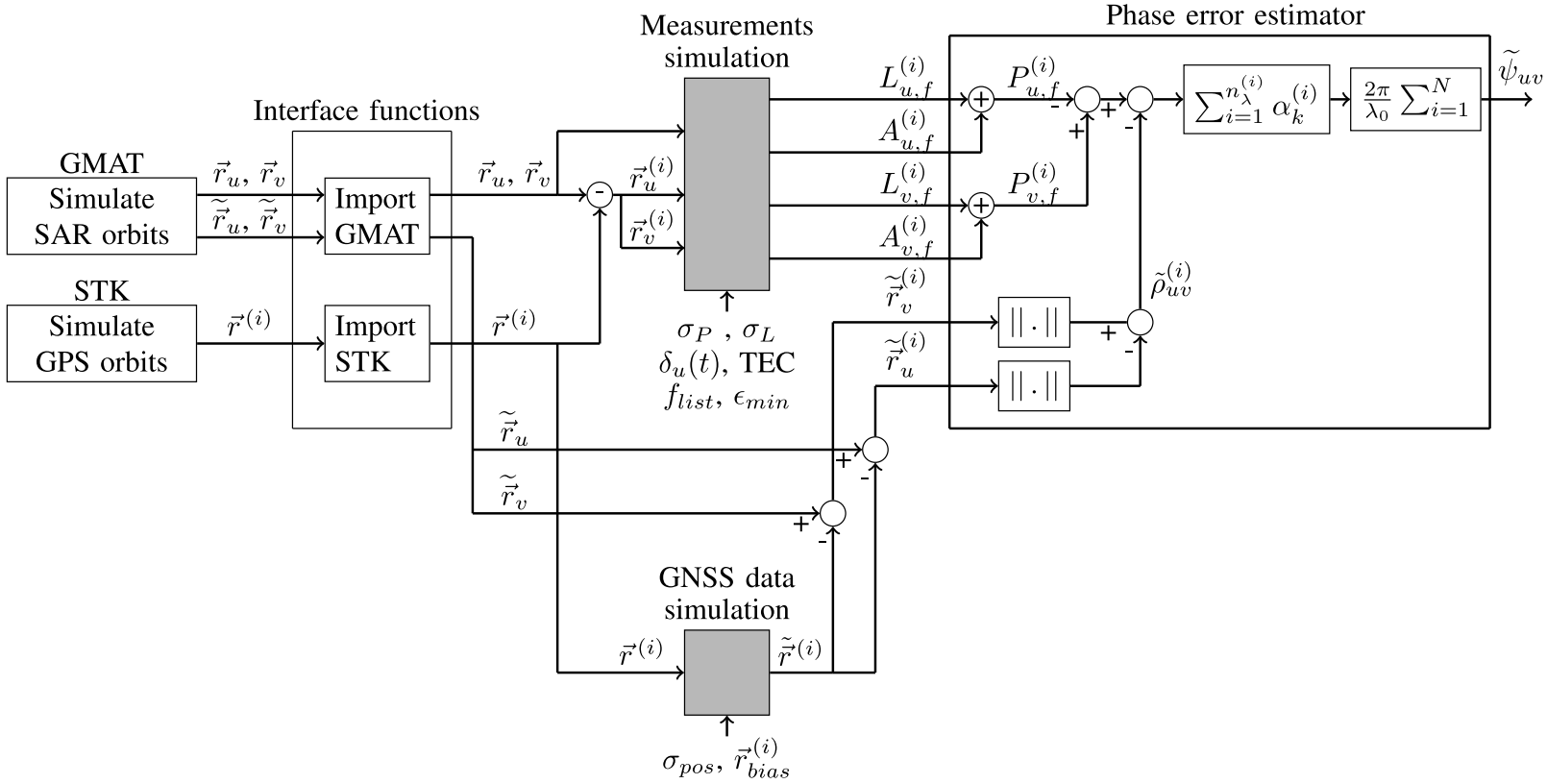

Figure 3.7: Block diagram of the simulation framework used to test the proposed GNSS-based estimation of the radar carrier synchronization phase.

Table 3.2 shows the simulation parameters and baseline errors concerning the specific cases shown in this section. Figures 3.8 and 3.9 show the results of the simulation.

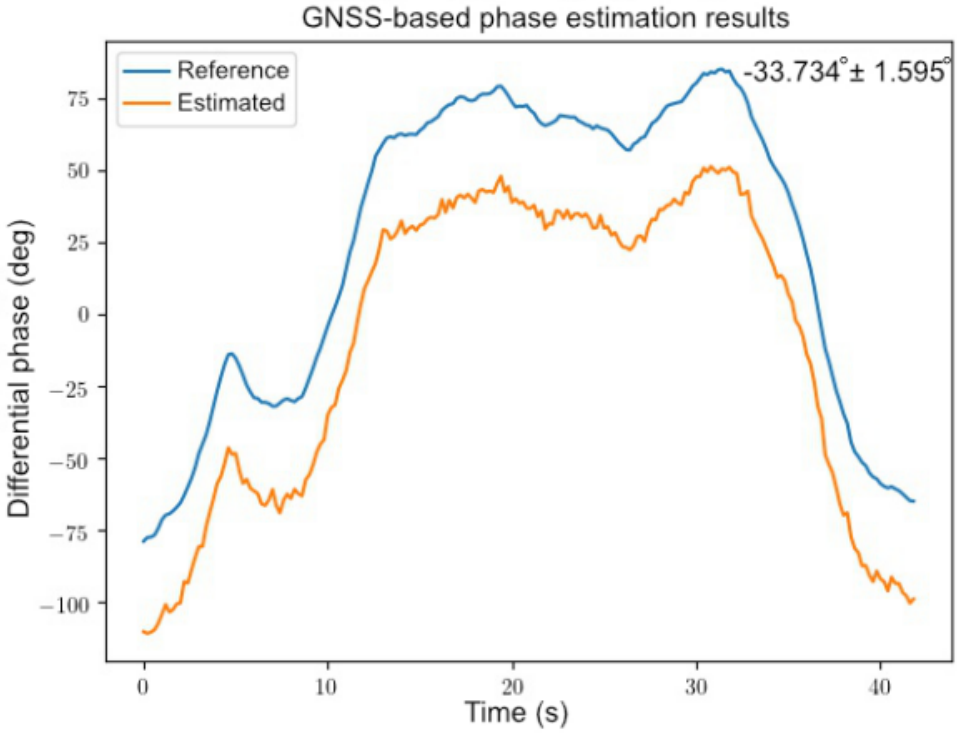

Figure 3.8: Simulated phase drift data and results from GNSS-based phase error estimation.

As expected, the estimation of the oscillator phase error scaled to the radar carrier is biased but replicates the shape of the original error with a standard deviation below two degrees for the simulation case. In Figure 3.9, the estimation error presents a drift component caused by an error in the baseline velocity, resulting in a difference of about one degree in the average error over the simulation period. The negligible phase ramp corroborates the conclusion that technique could be used in applications where phase ramps due to oscillator signatures cannot be separated from the useful data.

Under the assumptions of the simulation, this estimate can be regarded as conservative, as it assumes a single-frequency receiver compatible with only one constellation. With hardware capable of receiving multiple constellations and frequencies, the standard deviation could be reduced to below one degree.

Table 3.2: Simulation parameters of the GNSS-synchronization performance analysis. The position and baseline errors are randomly generated with variance in agreement with reported values in the literature.

Parameter	Value
GNSS signal frequency	1575.42 MHz
Radar payload frequency	5405 MHz
Carrier phase standard deviation	0.95 °
GNSS position bias standard deviation	1.5 m
Minimum elevation for visibility	10°
Number of GNSS satellites	9
Vertical Total Electron Content (VTEC)	50 TECU
Radial baseline	0 m
Along-track baseline	315 m
Cross-track baseline	56 m
Radial position error	1.478 m
Along-track position error	0.54 m
Across-track position error	-0.34 m
Radial velocity error	0.082 m/s
Along-track velocity error	0.010 m/s
Across-track velocity error	-0.007 m/s
Radial baseline error	8.248 mm
Along-track baseline error	1.177 mm
Across-track baseline error	0.767 mm
Radial baseline velocity error	0.0057 mm/s
Along-track baseline velocity error	-0.0077 mm/s
Across-track baseline velocity error	-0.0027 mm/s

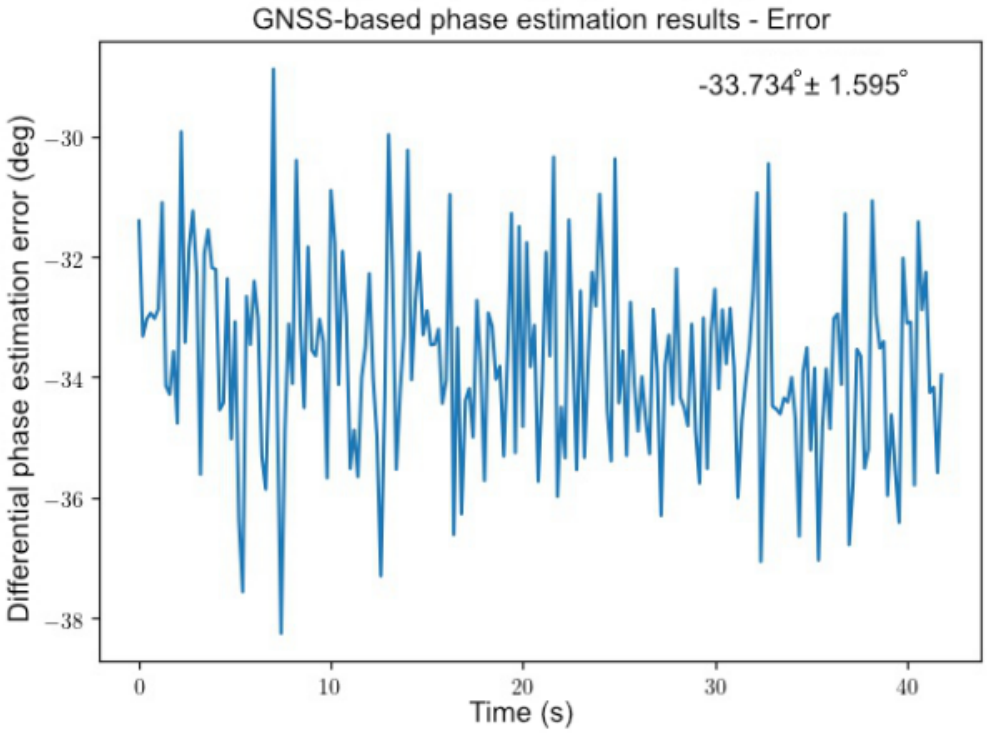

Figure 3.9: Error in the GNSS-based phase estimation.

Note that not all systematic errors discussed in Section 3.3 have been included in the simulation because the remaining error contributions, especially contamination within the GNSS receiver, are better evaluated using representative experimental data. As mentioned, the focus of this chapter is on the effect of thermal noise and geometric aspects. The latter is a critical error factor which can only be evaluated at this stage through simulation. A comprehensive experimental validation of the remaining error factors is shown in Chapter 4, which complements the validation of the technique introduced in this chapter.

As discussed in Section 3.3, the effects due to multipath or up-converting electronics may be unavoidable and degrade the precision and accuracy of the solution. In case interferometric data is available, the integration of the suggested technique with a data-based synchronization algorithm (e.g., AutoSync) [41, 125, 126] may be considered for the calibration of unmodeled error sources which do not remain constant during the radar integration time, especially in the band of the clock phase errors. The simulation, however, indicates that the technique here presented wouldn't have to rely on data-based synchronization and, therefore, would be suitable also for scenes with overall low coherence. Note the estimation model considered

in this chapter does not relies on any assumption on the stochastic behavior of the radar clock. A better-suited estimator might further reduce the estimation error, as will be more detailed in Chapter 4.

Finally, Figure 3.10 shows the estimation results applying the ionosphere-free phase error estimator. In the simulation, a difference of 5 TECU was introduced in the Vertical Total Electron Content (VTEC) between the two satellites. Carrier phase data from dual-frequency GPS receivers was simulated to enable estimation of the ionospheric delay. The remaining simulation parameters are shown in Table 3.2.

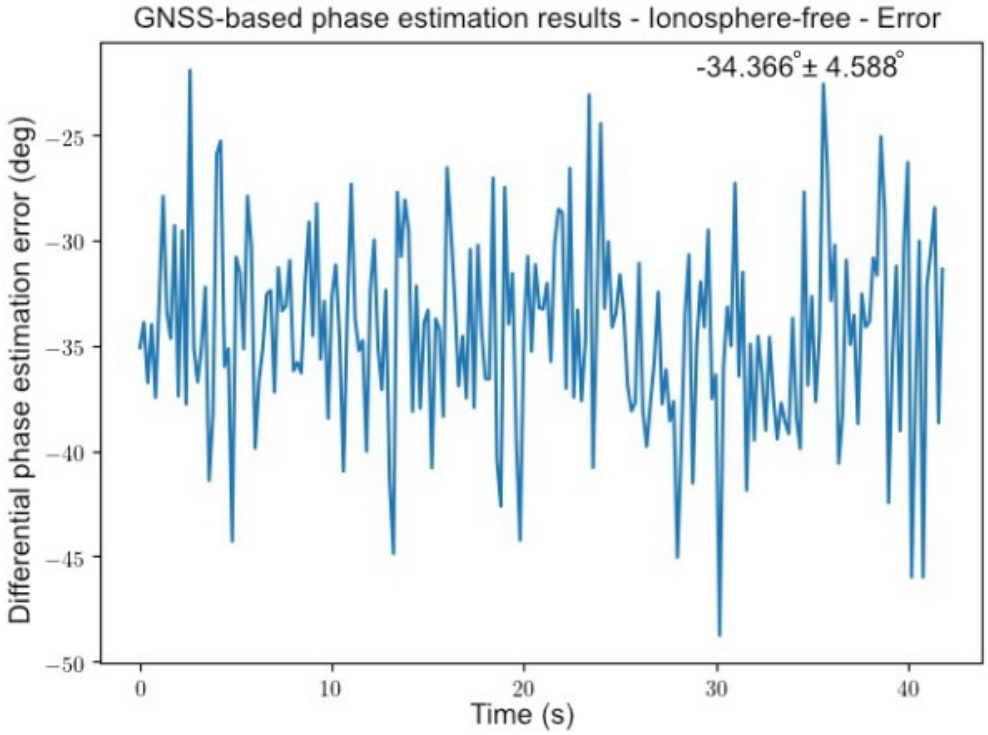

Figure 3.10: Simulated phase drift data and results from GNSS-based phase error estimation using a dual-frequency receiver and ionosphere-free linear combinations.

By using the ionosphere-free algorithm, the standard deviation was increased by a factor of 2.9 compared to the results using a single-frequency receiver. This ratio is still close to what predicts (3.28), since single-frequency receivers are expected to yield a phase error estimation with a standard deviation $\sqrt{2}$ higher than dual frequency receivers, in the absence of high ionospheric delay differences ($\sqrt{2} \cdot 2.9 \approx 4.1$). This multiplicative factor on the noise-like component of the estimation error is the penalty for estimating the ionospheric delay at each time step and corresponds to a worst-case

scenario considering dual-frequency receivers. In case the ionospheric delay error remains approximately constant for the SAR integration time, or if it can be accurately interpolated from the PBD solution, the previous estimator given by (3.11) is recommended, since it yields more precise results.

3.5 Conclusions

This chapter proposes a system architecture and an algorithm for phase synchronization considering a bistatic mission where, in each satellite, the radar payload and the GNSS receiver share the same oscillator. It also presents an error model, a performance assessment and a simulation framework for evaluating the technique. The phase error between the radar payloads can be derived from the differential carrier phase measurements provided by the GNSS receiver. Assuming that other error sources are either suppressed or compensated, the carrier phase measurement is affected by short-term phase noise variations of the oscillator and by the continuously changing geometry between the receivers and the GNSS satellite. The analysis indicates that the short variations in the carrier phase measurement due to phase noise from the oscillator can be isolated from the component due to geometric variations by using PBD results, since they vary at different time scales.

The technique presented here offers a solution for phase synchronization in bistatic or multistatic radar constellations which requires minimal effort in the hardware implementation. It has the potential for scalability since each additional satellite designed to employ the technique can be easily integrated into the multistatic system without adding to the complexity of the other elements of the space segment.

The simulations indicate that precision of 1.6° (standard deviation) or better at C band could be obtained from low-cost single-frequency GNSS receivers compatible only with the GPS constellation, in case preservation of the phase signature of the oscillator within the radar payload and GNSS receiver can be achieved, so that thermal noise constitutes the main error source. The solution relies on very precise relative positioning data, in the sub-centimeter level. The performance can be improved considering the widespread availability of navigation receivers compatible also with Galileo and BeiDou. The use of receivers operating with several frequencies is advised for the improvement of the phase accuracy and the calibration of ionospheric signatures, especially in scenarios with large baselines.

The error analysis indicates some critical issues that must be addressed for the technique to work. Of particular concern are multipath effects, which must be reduced to a minimum by carefully addressing the spacecraft design. The radar up-converters must be carefully designed to avoid contamination of the oscillator phase signature. Finally, contamination within the GNSS receiver must be as low as possible, as it represents a critical component inherent to the receiver design and cannot be modified by the satellite or radar system developers. Unlike using a synchronization link operated at the radar carrier, the errors of the GNSS-based estimation are expected to degrade at least linearly for increasing frequencies and could be at the edge of usability for X-band radar systems. The most critical error contributors identified in the error analysis are characterized in the following chapter through experiments with real hardware.

4 Proof-of-Concept and Calibration of GNSS-Based Phase Synchronization

This chapter presents the experimental validation of the GNSS-based synchronization technique described in Chapter 3. The proposed experimental procedure serves as a general proof-of-concept of the technique, a method for assessing the achievable synchronization accuracy for a given GNSS receiver, and a method to estimate the covariance matrix in order to optimize the weighting between the various carrier phase observables. The chapter presents both point-to-point estimation and smoothing approaches.

Following the conclusions of the analysis presented in the previous chapter, the GNSS-based technique introduced in this research was adopted by the Harmony mission as its baseline phase synchronization solution, complemented by data-driven methods [127]. The experimental validation presented in this chapter was carried out partly within the scope of that mission. A test with a simulated orbital scenario is presented, where both the GNSS receivers and the orbital configurations reflect those used in Harmony, serving as a preliminary assessment of the synchronization performance.

The chapter is organized as follows. Section 4.1 introduces the error model assumed throughout the chapter and the associated optimal weighting. Section 4.2 describes the experimental methods and hardware setup. Section 4.3 presents a method to calibrate the estimation algorithm. Section 4.4 presents the experimental results and assesses the achievable accuracy of the technique with different GNSS receivers. Finally, Section 4.5 summarizes the conclusions of the experiments.

4.1 General Optimal Weighting

Each carrier-phase measurement provides an independent estimate of the differential phase, along with an associated error that must be properly characterized to enable optimal weighting. A primary objective of the experiments presented in the next sections is to characterize these errors.

From (3.9), the individual biased estimates $\tilde{\psi}_{0,k}^{(i)}$ of the reference phase difference at the radar carrier frequency are given by[1]

$$\tilde{\psi}_{0,k}^{(i)} = \frac{2\pi}{\lambda_0} \cdot \left[L_{uv,k}^{(i)} - \tilde{\rho}_{uv}^{(i)} + \left(\frac{\lambda_k}{\lambda_1} \right)^2 \cdot \tilde{I}_{uv}^{(i)} \right] . \tag{4.1}$$

Assuming millimeter-level precision PBD, the variation of the baseline error over the duration of a single acquisition can be neglected, as discussed in Subsection 3.3.2. Similarly, for short baselines, the variation in differential ionospheric delay can also be disregarded, as noted in Subsection 3.3.4.

For clarity, the systematic errors $M_{uv,k}^{(i)}$ in the differential carrier phase measurements, first introduced in (3.9), can be decomposed as follows

$$M_{uv,k}^{(i)} = M_{\text{ext},k}^{(i)} + M_{\text{int},k} , \tag{4.2}$$

where $M_{\text{ext},k}^{(i)}$ accounts for external terms such as multipath, which depend on both the GNSS signal frequency and direction of reception, and therefore the specific GNSS satellite from where the signal originates, and $M_{\text{int},k}^{(i)}$ is an empirically observed internal error source. This internally generated error is dependent on the signal type but is independent of the GNSS satellite. It can include, for example, phase noise added in the front-ends for each GNSS frequency band.

The terms which will be common across the differential phase derived from different carrier phase observables can be aggregated in a common mode term $\psi_{\text{hw},k}$, as expressed in

$$\delta\psi_{\text{hw},k} = \frac{2\pi}{\lambda_0} \cdot M_{\text{int},k} + \delta\psi_{\text{HW}uv,0} , \tag{4.3}$$

where $\psi_{\text{HW}uv,0}$ corresponds to the error added in the radar payload and oscillator interfaces, introduced in (3.15).

[1] To simplify the notation, for the remainder of this chapter the u and v indexes identifying the satellites to be synchronized are assumed constant, since only two receivers are considered in the experiments. Therefore, these indexes are omitted from the newly defined terms. To maintain consistency which Chapter 3, where the notation is defined to accommodate for multistatic systems, the previously defined terms are kept unaltered.

Considering these definitions, the time-varying tracking error $\epsilon_{uv,k}^{(i)}$ of the individual estimate, i.e., after removing its mean, is given by

$$\epsilon_{uv,k}^{(i)} = \frac{2\pi}{\lambda_0} \cdot M_{\text{ext},k}^{(i)} + \frac{\lambda_k}{\lambda_0} \cdot \delta\psi_{\text{hw},k} + \frac{2\pi}{\lambda_0} \cdot \eta_{n,k}^{(i)}, \tag{4.4}$$

Note that the error model in (4.4) can be seen as an update to the one in (3.9) common in the literature.

The biased version of the phase difference estimator at the carrier frequency can be derived as

$$\tilde{\psi}_{uv,0} = \sum_{i=1}^{N} \sum_{k=1}^{n_\lambda^{(i)}} \alpha_k^{(i)} \cdot \tilde{\psi}_{0,k}^{(i)}, \tag{4.5}$$

Defining the model matrix A as a matrix of one column and the number of rows equal to the number of carrier phase observables $n_{\text{cp}} = \sum_{i=1}^{N} n_\lambda^{(i)}$ as follows

$$\mathrm{A} = \begin{bmatrix} 1 \\ 1 \\ \vdots \\ 1 \end{bmatrix}_{n_{\text{cp}} \times 1}, \tag{4.6}$$

the optimal set of weights in a least-squares sense is given by

$$\mathrm{W} = \left[\alpha_k^{(i)}\right]_{1 \times n_{\text{cp}}} = \left(\mathrm{A}^T \cdot \mathrm{S}^{-1} \cdot \mathrm{A}\right)^{-1} \cdot \mathrm{A}^T \cdot \mathrm{S}^{-1}, \tag{4.7}$$

in which S is the covariance matrix of the set of carrier phase observables defined by

$$\mathrm{S}_{kl}^{(ij)} = \mathrm{Cov}\left(\epsilon_{uv,k}^{(i)}, \epsilon_{uv,l}^{(j)}\right), \tag{4.8}$$

where k and l are indexes denoting the GNSS signal (e.g., GPS L1 C/A, Galileo E5, etc).

Although the estimation algorithm is developed under ideal assumptions, it is crucial to evaluate the impact of deviations from these ideal models. The geometric terms, ionosphere, and ambiguities were thoroughly analyzed in Chapter 3, which also explains how the technique can employ

ionosphere-free linear combinations when the ionosphere's time-varying effects are significant. However, this scenario is unlikely for short distances below one kilometer and is certainly not applicable to the experiments with physical antennas and real GNSS signals presented in this chapter.

The geometric terms, as stated previously, should be derived from PBD utilizing algorithms such as those detailed in [109]. Accurate GNSS satellite positions can be obtained from various International GNSS Service (IGS) and Multi-GNSS Experiment (MGEX) analysis centers, which provide precise position data through public archives with a-posteriori accuracy below the decimeter level [128]. For short baselines spanning only a few meters, such as those used in the short baseline experiments presented further in this chapter, the GNSS position errors effectively cancel out. As a result, the inaccuracies introduced can be safely disregarded, even when using the less precise broadcast ephemerides.

4.2 Experimental Method

4.2.1 Hardware Setup

Figures 4.1, 4.2 and 4.3 illustrate the experimental setups used. The sequence of experiments is designed so that the expected error factors are introduced gradually, and more terms are taken into account at each iteration. The objective of each experiment is to access the capability of the technique to recover differential phase information between two oscillators using given GNSS receiver.

In the Single-Oscillator Zero-Baseline (SOZB) experiment, illustrated in Figure 4.1, the same oscillator signal is fed to the two GNSS receivers, so the GNSS-based synchronization will compare the oscillator to itself, and the same GNSS signal is used for GNSS-based estimation. This setup isolates the thermal noise and the common-mode error, defined in (4.3). In the Two-Oscillators Zero-Baseline (TOZB) experiment, illustrated in Figure 4.2, the receivers operate with independent master oscillators, which are compared through an independent mean, while still using the signal from the same antenna. This experiment isolates the impact of incoherent sampling of the carrier phase measurements between the receivers. Finally, the Two-Oscillators Short-Baseline (TOSB) experiment, illustrated in Figure 4.3, employs two independent oscillators and separate GNSS antennas, thus accounting for most error sources.

Three different receivers were used: the development kit of the OEM729 manufactured by Novatel, which is a product aimed at mass production for

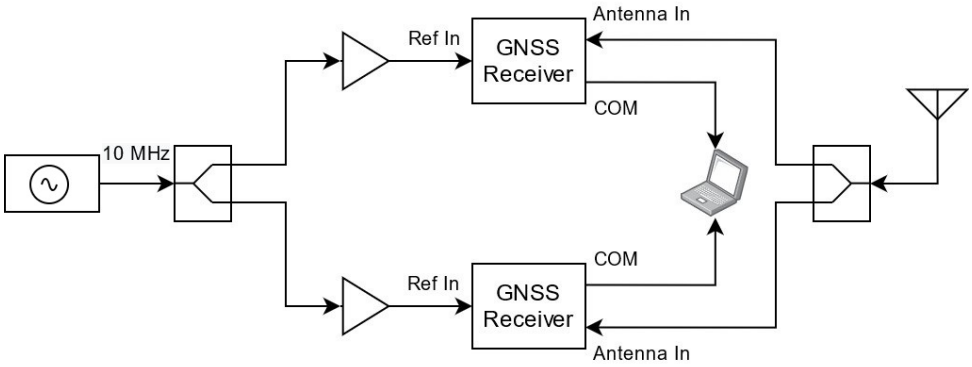

Figure 4.1: Single-Oscillator Zero-Baseline (SOZB) experimental setup.

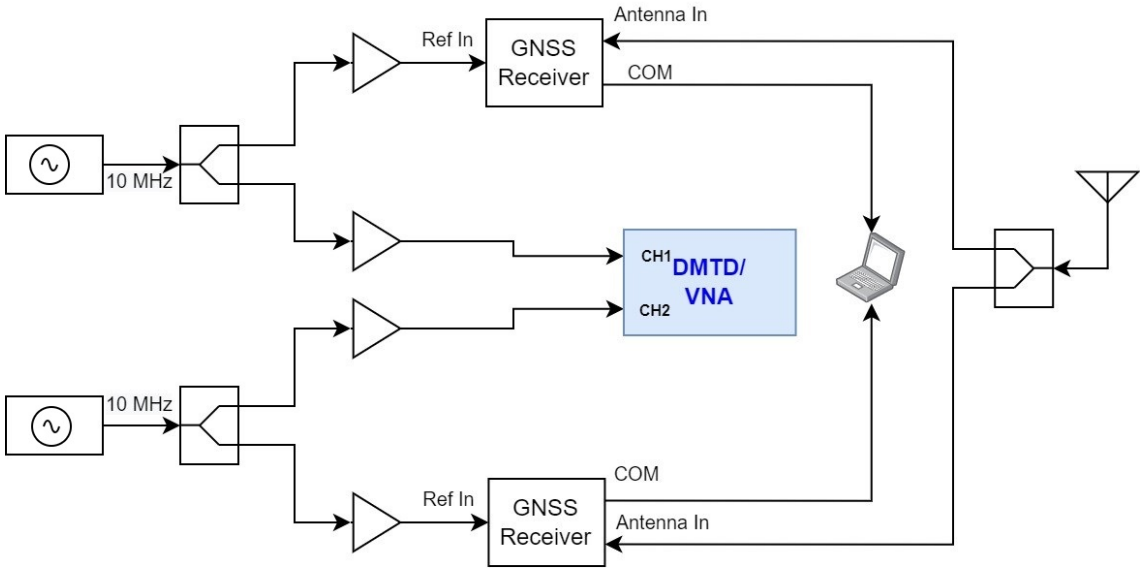

Figure 4.2: Two-Oscillators Zero-Baseline (TOZB) experiment setup.

a broad range of applications [129]; the PolaRx5TR receiver manufactured by Septentrio, a more specialized equipment targeted at high-performance time-transfer and geodetic applications [130]; and the space-grade PODRIX receivers, a high-end radiation hardened receiver manufactured by Beyond Gravity and which has been used in several missions for precise orbit determination [131] and time synchronization [132]. The receivers are powered on for at least two hours before each experiment, a time empirically verified to be sufficient for the receivers to reach thermal equilibrium. The frequency of the external oscillators under analysis were adjusted to have a frequency difference well below 0.2 Hz through their respective command interfaces. Experiments revealed that, above this threshold, the frequency offset introduces errors on the clock term of the carrier phase that could not be distinguished from the phase noise signature of the oscillators.

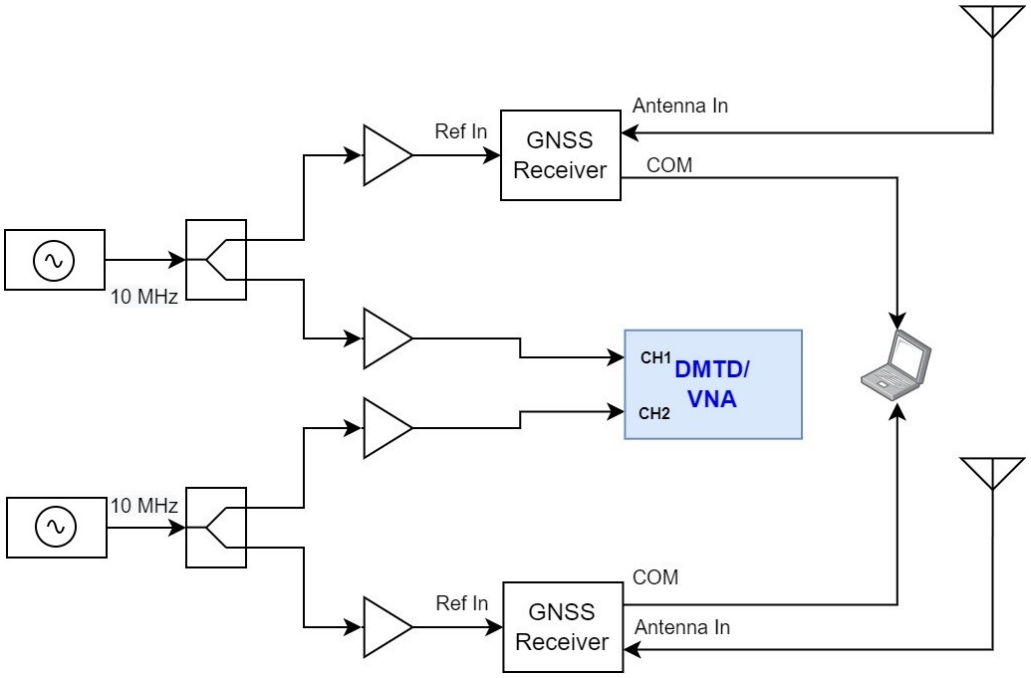

Figure 4.3: Two-Oscillators Short-Baseline (TOSB) experiment setup.

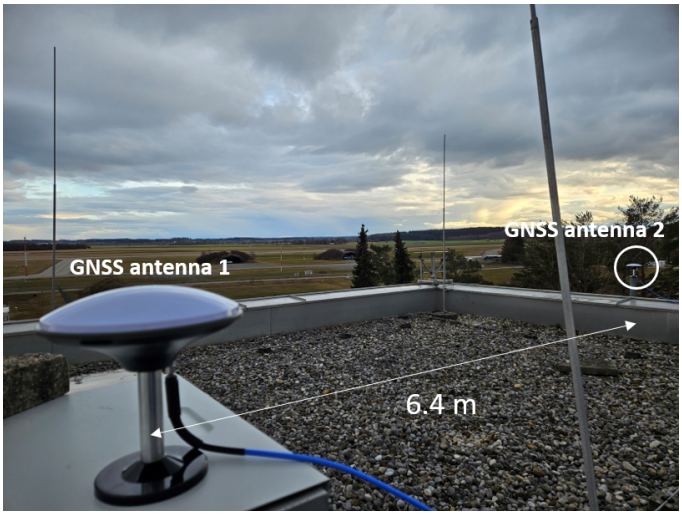

Figure 4.4: Antenna placement in the experiments with the PolaRx5TR receivers on the roof of a building at DLR site in Oberpfaffenhofen.

For the short baseline experiments illustrated in Figure 4.3, the differential range histories from GNSS satellites to the fixed antennas are used to calibrate the carrier phase measurements, as expressed in (4.1). Figure 4.4 shows the antenna placement for those experiments. The employed antenna has no multipath suppression, and despite it being suitable for geodetic applications, considerable contamination from ground reflections is expected.

Figure 4.5 shows the test setup assembled as a proof-of-concept for orbital scenarios and a preliminary assessment of the phase tracking performance of the PODRIX receivers under simulated orbital conditions. The test consists of a variation of the TOSB experiment. The high-end GSS9000 GNSS signal simulator from Spirent was used to generate the signals received in a formation flying scenario for a sun-synchronous orbit around 700 km altitude and baselines of the order of 400 m in a helix-like orbit formation. This simulator has been previously used for testing POD applications for LEO orbits [133]. The PODRIX receivers are planned to be used in Harmony for precise orbit determination and synchronization, and this experiment was part of the phase-A activities for that mission.

This experiment with the PODRIX receivers also serves as a proof-of-concept for an orbital scenario for the GNSS-based phase synchronization technique, as it employs space-grade hardware and simulated GNSS signals with Doppler and baselines representative of satellite formation flying conditions. The clock contamination mentioned in Subsection 3.3.3 could be coming from GNSS processing residual correlations, or be a hardware effect sensitive to the central frequency of the incoming signal. Therefore, it is necessary to verify if the conditions leading to this contamination of the clock term are not aggravated by a much higher Doppler variations observed in orbital scenarios.

Finally, it is important to emphasize that none of the GNSS receivers used in the tests were modified or customized in any way for this purpose. Commercial off-the-shelf OEM729 and PolaRx5TR receivers were used. The space qualified PODRIX receivers are manufactured on-demand and therefore two flight models were not available. Instead, an Engineering Model (EM) and Engineering Qualification Model (EQM) of the PODRIX receiver were used, both of which were designed and manufactured to be representative of the flight models for test purposes.

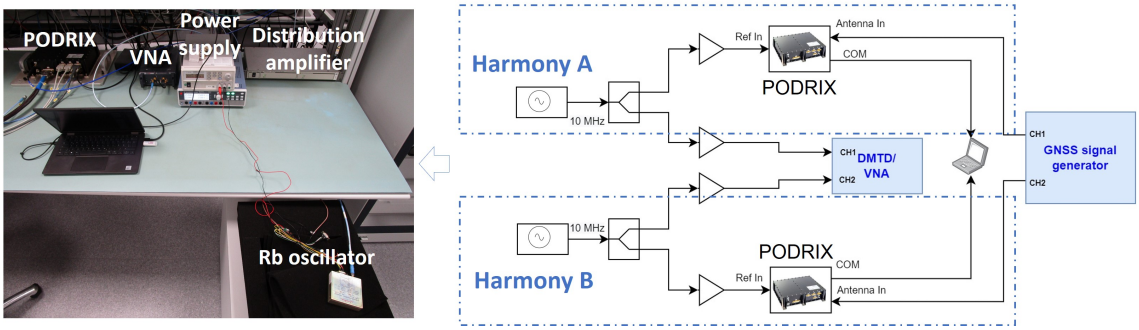

Figure 4.5: Two-oscillators validation setup with simulated formation flying.

4.2.2 Reference Synchronization Rate and Reference Bandwidth Determination

A boundary for the necessary estimation rate of the clock phase differences can be derived based on data collected with a TanDEM-X calibration datatake. The data consist of synchronization pulses only, exchanged at a rate of around 3 kHz, which allows a proper sampling of the phase noise spectrum of the two oscillators. The data have been scaled from the carrier frequency of TerraSAR-X to the carrier frequency of Sentinel-1, and the spectral shape has been maintained. The underlying assumption for the validity of the presented results is that the TanDEM-X master oscillators have similar phase noise characteristics to both the Sentinel-1 and Harmony oscillators. Because measurements with more representative oscillators are unavailable, the TanDEM-X case represents a reasonable approximation for an operational scenario.

Figure 4.6 shows the reconstruction error after down-sampling the data to different rates. The plot shows that an estimation rate of 2 Hz seems to capture most of the energy of the phase noise spectrum. This suggests that an estimation rate between 1 and 2 Hz might be sufficient for a C-band Harmony case with oscillators of similar quality to those of TanDEM-X. An estimation rate of 2 Hz will be used as a reference in the evaluations presented in this chapter.

4.2.3 Differential Phase Ground Truth Comparison

The so-called Dual Mixer Time Difference (DMTD) method [134], implemented in the phase noise analyzers, is conventionally used to compare references very close to each other (e.g., a difference of much less than 1 Hz for a 10 MHz reference) and is reported to achieve accuracy of a few hundred, or even a few tens, of femtoseconds. Some Vector Network Analyzers (VNAs) can also measure the phase of an incoming signal with respect to an internal or external reference, and high-accuracy phase measurements can be obtained using those devices analogously to the DMTD method.

For all the experiments in which two independent frequency references are used, the phase between the oscillators is measured simultaneously by using the VNA P5024A. Figure 4.7 describes the overall measurement setup for those cases. The device is configured for a bandwidth of 100 Hz, which can capture the variations of the phase difference between the 10 MHz oscillators, filtered with a 50-sample moving average filter. In each data take, the direct relative phase data acquisition begins before the acquisition with GNSS and ends after the acquisition with GNSS. The reference is decimated

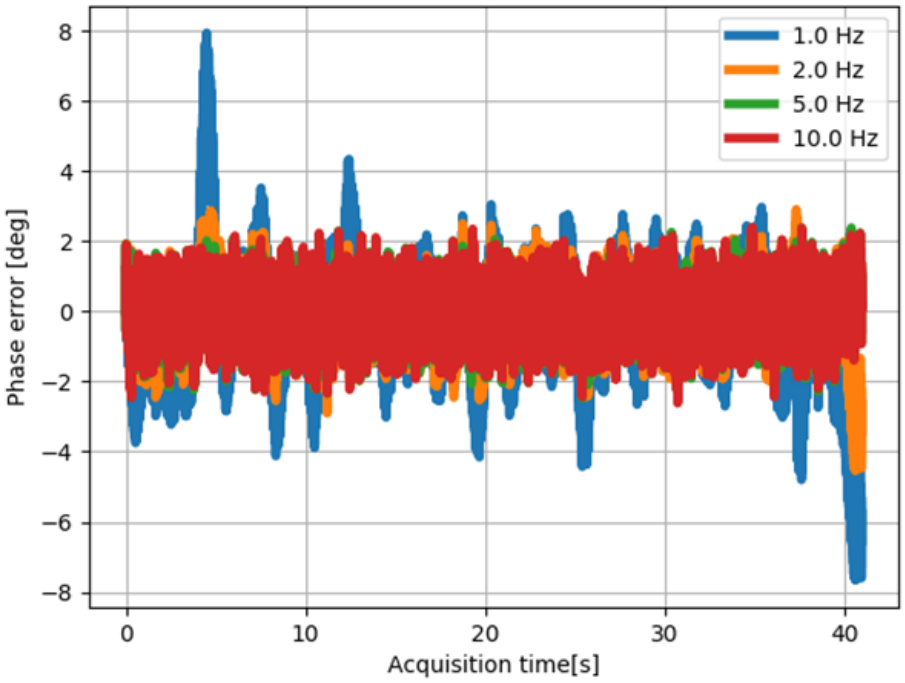

Figure 4.6: Reconstruction error after downsampling-then-interpolating TanDEM-X synchronization data with different rates.

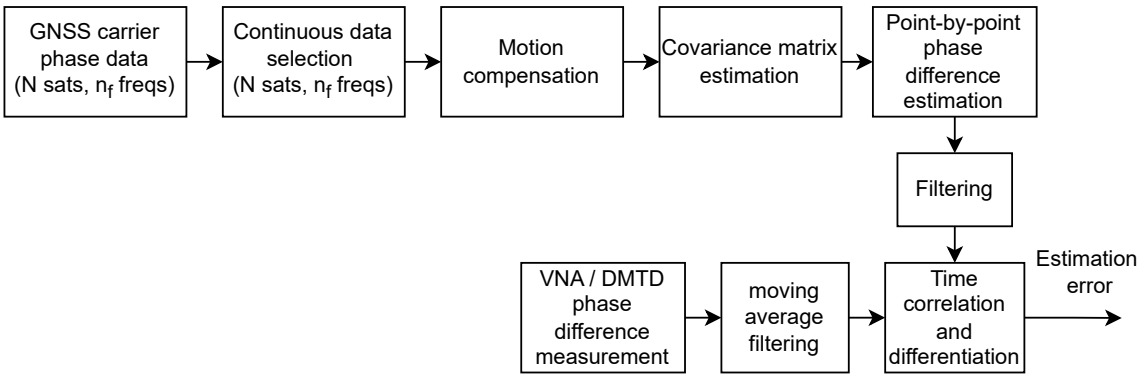

Figure 4.7: Data processing chain and comparison to reference.

to the sampling rate of the GNSS data and correlated until the peak is found to allow for the alignment of the two independent measurements. The decimation is done for all the possible data combinations, and the maximum correlation data set is selected. Finally, the data obtained through GNSS and the independent instrument are compared, and the estimation errors are calculated. The moving average filter applied to the reference emulates the effect of the SAR processing on the phase noise contained in the raw SAR data [23].

4.2.4 Remarks on the Synchronization Time Scales

From the standpoint of bistatic and multistatic SAR applications, phase synchronization needs to be ensured in the time scales slightly below the synthetic aperture and within the acquisition time, which usually is in the order of minutes. The results presented in this chapter consist of short-duration data-takes of a couple of minutes, separated by hours or days, with duration exceeding that of conventional synthetic apertures and being representative of typical interferometric acquisitions. For longer data-takes lasting tens of minutes, for example, performance may degrade, potentially becoming dominated by factors such as slow temperature variations and the accuracy of precise orbit determination.

Due to the short duration, the experiments presented in this chapter capture only a limited number of GNSS geometry instances. However, this does not compromise the validity of the results. The technique relies on PBD to compensate for the relative motion, which involves fitting a highly accurate dynamic model to GNSS data over multiple orbits with varied visibility geometry. Consequently, unlike in conventional position, velocity and time (PVT) applications, the instantaneous geometry does not directly influence the instantaneous estimation. Instead, the differential phase estimation is driven by the number of tracked signals of sufficient quality, i.e., with sufficiently high elevation. The number of satellites in view is expected to consistently exceed seven for each major constellation [135]. In the case of multi-frequency, multi-constellation receivers—which are recommended for this application—the number of tracked signals is likely constrained by the number of available GNSS channels rather than the local geometry. In conclusion, GNSS variability is not expected to cause a performance discrepancy that would hinder the overall usability. This is supported by analysis, experiments, and the consistency of results presented in this chapter across various hardware configurations.

The applicability of the technique for long-term accurate phase tracking could be useful in an operational scenario to obtain, for example, consistent absolute phase referencing. For that case, a piece-wise estimation could be employed, which would only require the estimation of a constant offset between the pieces, something which can be easily done using data-based approaches [136]. Events suddenly degrading the estimations (e.g., bubbles in the ionosphere, rebooting of the receivers, signal fading, etc.) are unlikely to happen, but even if they do happen, they are expected to represent just rare or sporadic loss of a data take.

4.3 Calibration and Filtering

4.3.1 Covariance Matrix Measurement

This subsection presents a method for computing the covariance matrix of synchronization error of the set of differential clock estimates derived from the differential carrier phases. The goal is to determine the optimal weighting between these estimates, as expressed in (4.7).

The receiver-induced error calibration procedure proposed in this section is based on the SOZB setup illustrated in Figure 4.1. Most of the terms in the differential carrier phase expressed in (4.1) cancel out in this setup. In an ideal case, the differential carrier phase obtained in this experiment would consist of a constant signal plus a noise component in line with the thermal noise specification of the receiver. However, the observed noise level exceeded these specifications and exhibited correlation across measurements. This correlation depends mainly on the type of signal being tracked but is independent of the GNSS satellites from which it originates, and is expressed in the error model (4.4) by the term $\delta\psi_{\mathrm{hw},k}$.

Assuming the thermal noise and multipath components in the error model (4.4) uncorrelated, the covariance matrix's off-diagonal terms (i.e., S_{kl}^{ij} in which $i \neq j$ or $k \neq l$) are given by:

$$\mathrm{S}_{kl}^{ij} = \mathrm{Cov}\left(\frac{\lambda_k}{\lambda_0} \cdot \delta\psi_{\mathrm{hw},k}, \frac{\lambda_l}{\lambda_0} \cdot \delta\psi_{\mathrm{hw},l}\right). \tag{4.9}$$

Under these conditions, averaging the correlations of carrier phase measurements in the SOZB experiment yields an estimate of the off-diagonal terms of S as shown in the following equations.

For $k \neq l$

$$\mathrm{S}_{kl}^{ij} = \frac{1}{N_k \cdot N_l} \cdot \sum_{i=1}^{N_k} \sum_{j=1}^{N_l} \mathrm{Cov}\left(\tilde{\psi}_{0,k}^{(i)}, \tilde{\psi}_{0,l}^{(j)}\right), \tag{4.10}$$

and for $k = l$

$$\mathrm{S}_{kl}^{ij} = \frac{1}{N_k \cdot N_l - 1} \cdot \sum_{i=1}^{N_k} \sum_{j=1}^{N_l} (1 - \delta_{ij}) \cdot \mathrm{Cov}\left(\tilde{\psi}_{0,k}^{(i)}, \tilde{\psi}_{0,l}^{(j)}\right), \tag{4.11}$$

where N_k and N_l are the number of GNSS satellites in view transmitting the frequency k and l, respectively, and δ_{ij} is the Kronecker delta, equal to one when $i = j$ and zero otherwise.

Next, the diagonal elements of the matrix, corresponding to the error variance of the individual synchronization solutions, need to be determined. Unlike the off-diagonal elements, they are strongly influenced by situational factors such as satellite elevation and multipath effects. Consequently, they cannot be accurately predicted in advance and must be estimated directly from the individual data set.

Defining the motion compensated and scaled double differences $\mathrm{DD}_{kl}^{(ij)}$ as

$$\mathrm{DD}_{kl}^{(ij)} = \tilde{\psi}_{0,k}^{(i)} - \tilde{\psi}_{0,l}^{(j)}\,, \tag{4.12}$$

the following equation can be derived from (4.4)

$$\mathrm{Var}\left(\epsilon_{uv,k}^{(i)}\right) + \mathrm{Var}\left(\epsilon_{uv,l}^{(j)}\right) = \mathrm{Var}\left(\mathrm{DD}_{kl}^{(ij)}\right) + 2 \cdot \mathrm{S}_{kl}^{ij}\,. \tag{4.13}$$

The terms on the left correspond to two distinct diagonal elements of the covariance matrix S to be estimated. The term $\mathrm{Var}(\mathrm{DD}_{kl}^{(ij)})$ can be computed from the carrier phase data set that will be used to estimate the differential phase noise. The term S_{kl}^{ij} can be replaced by the previously calibrated off-diagonal terms obtained from a SOZB experiment. Applying (4.13) to all possible combinations of signals, i.e., for all i, j, k, and l, with $i \neq j$ or $k \neq l$, results in an overdetermined linear system of equations, which can be solved using simple least squares estimation. Note that the least squared estimator already yields good results when assigning uniform weights to each equation, but there is still potential to improve it by including a non-identity weight matrix.

The effectiveness of the estimation can be assessed in a TOSB experiment, where the covariance matrix can be directly measured. Figure 4.8 shows the estimated covariance matrix and the estimation error. Different data sets were used to calibrate the covariance matrix and to test the technique. The good conformance between estimated and measured covariance matrices demonstrates that the approach here presented is able to characterize the variances and covariances of a given set of differential carrier phase observables.

One implicit assumption in the proposed estimation procedure is that the variance of the common-mode (or covariance of the carrier phases)

remains constant. This implies that any environmental factors influencing the common-mode, particularly thermal conditions, must be kept stable. In an orbital scenario, the covariance may need to be reassessed as part of in-orbit testing routines, potentially requiring an external reference. This could be achieved, for instance, through auto-sync on specific, well-characterized scenes [136].

Finally, it is worth noting that the possibility of completely avoiding the common-mode cannot be ruled out if greater control over receiver hardware is available. This work presents a procedure that significantly improves results from the user's perspective, while receiver design considerations remain out of scope. Since the common-mode is a key performance factor for the proposed technique, a more detailed future analysis of the GNSS receiver characteristics or the signal properties contributing to it is necessary.

4.3.2 Filtering

This subsection presents a filtering approach used to improve the differential phase estimates throughout the experiments, based on the phase noise error model of the oscillators. The differential phase between the oscillators ($\psi_{uv,\mathrm{os}}$) in a multistatic system can be modeled as follows:

$$\psi_{uv,\mathrm{os}}(t) = 2\pi \cdot f_{uv} \cdot t + \phi_{uv}(t) + \phi_0\,, \tag{4.14}$$

where f_{uv} is a frequency offset, ϕ_0 is a constant phase, and $\phi_{uv}(t)$ is a random phase error. The component $\phi_{uv}(t)$ can be further described as a stationary random process with the two-sided Power Spectral Density (PSD) given by the composite power law below [137]:

$$S_\phi(f) = \frac{a_4}{f^4} + \frac{a_3}{f^3} + \frac{a_2}{f^2} + \frac{a_1}{f} + a_0\,, \tag{4.15}$$

where a_4 describes the random walk frequency noise, a_3 is the frequency flicker noise, a_2 is the white frequency noise, a_1 describes the flicker phase noise, and a_0 describes the white phase noise.

Modelling the baseband phase noise as a random walk, corresponding to integrating a Gaussian noise process (i.e., assuming dominance of the $1/f^2$

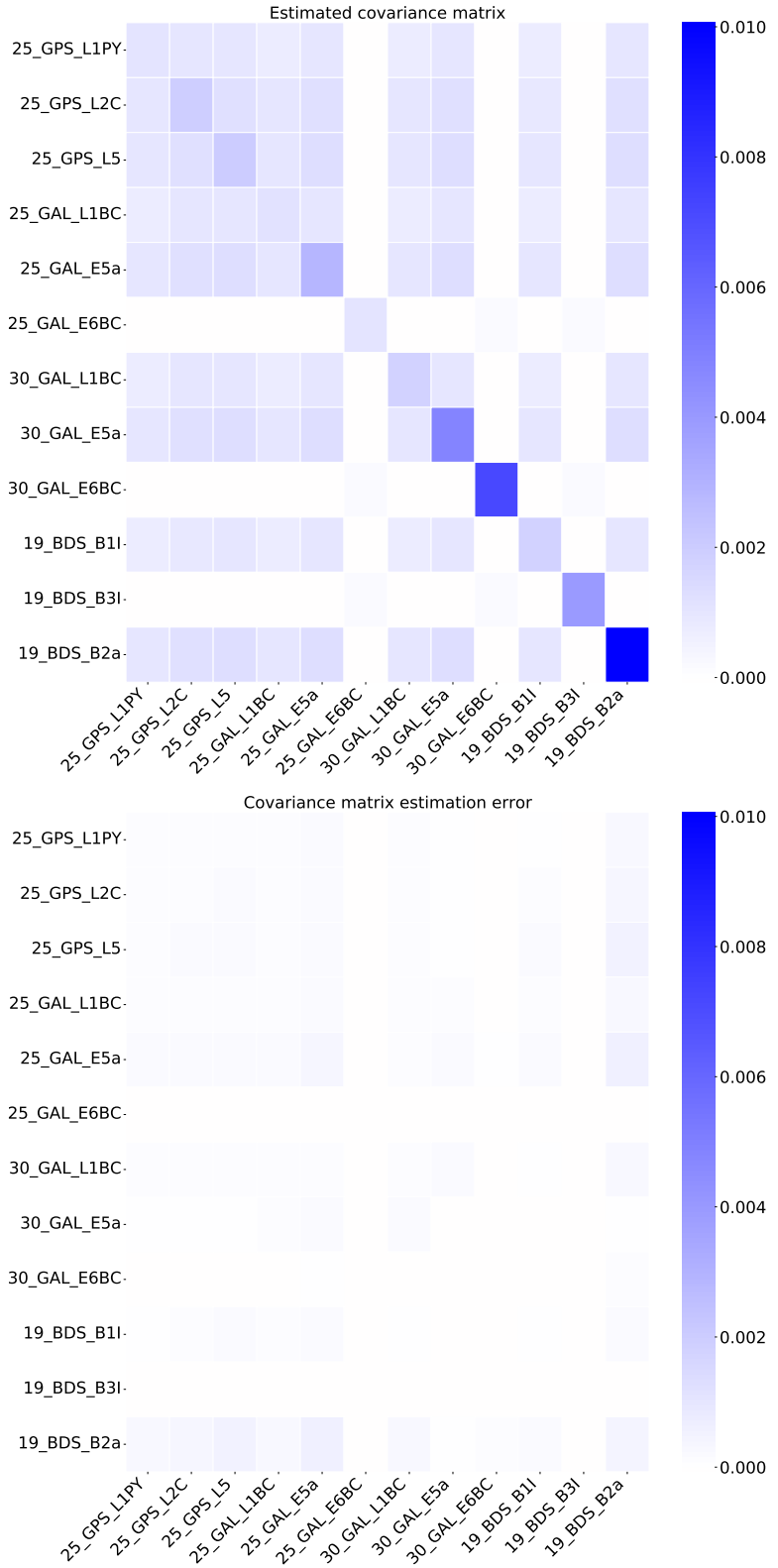

Figure 4.8: Samples of covariance estimation results for the SOZB experiment with the PolaRx5TR receiver.

component), a Kalman filter can be formulated using the following simplified model

$$x_{\mathrm{KF}}[k] = \psi_{uv,0}[k] - 2\pi \cdot k \cdot \Delta t \cdot f_{uv} = x_{\mathrm{KF}}[k-1] + w_{\mathrm{KF}}[k]\,, \tag{4.16}$$

$$z_{\mathrm{KF}}[k] = \tilde{\psi}_{uv,0}[k] - 2\pi \cdot k \cdot \Delta t \cdot \tilde{f}_{uv} = x_{\mathrm{KF}}[k] + v_{\mathrm{KF}}[k]\,. \tag{4.17}$$

where k here denotes the time step index, $\tilde{f}_{uv}$ is the frequency offset estimated through least-squares linear regression, Δt is the sampling period, x_{KF} is the Kalman filter state variable, z_{KF} is the measurement, $w_{\mathrm{KF}} \sim \mathcal{N}(0, q_{\mathrm{KF}})$, and $v_{\mathrm{KF}} \sim \mathcal{N}(0, r_{\mathrm{KF}})$ are the process and measurement noise, respectively. The variance q can be derived from the stability specifications of the oscillator in the time domain or calculated from direct phase difference measurements between oscillators of the same model in a controlled environment. The variance r can be determined from the SOZB experiment described previously.

The filter described above was applied to the experiments shown throughout this chapter and demonstrated good performance. However, the underlying model is not universally applicable to every oscillator. In some cases, other terms like the frequency flicker ($1/f^3$ term) may dominate [138]. Nevertheless, this approach could still be effective as an empirical filtering method for other scenarios.

Alternatively, or additionally to Kalman filters, empirically tuned least square smoothing or a Wiener filter could be used. Irrespective of the filter used, the power of error components—mainly the residual signatures of the receiver, thermal noise and multipath—limits the effectiveness of a filtering approach in the same bandwidth as the legitimate phase noise signatures originating from the oscillators. Therefore, the more concentrated the oscillator power is around the main frequency, the greater the error reduction through filtering. In this sense, the high short-term stability required for radar payloads will favor the error budget of the GNSS-based technique presented here. In the end, the error budget for a specific system will depend mainly on the phase noise signatures of the oscillators, how successful the multipath isolation and suppression is, and the phase-noise characteristics of the master oscillator.

4.4 Experimental Results

4.4.1 Single-Oscillator Zero-Baseline (SOZB)

Figures 4.9 and 4.10 present the scaled and unbiased individual carrier phase measurement observables, as defined in equation (4.1), for a SOZB experiment conducted using the OEM729 and PolaRxTR receivers, respectively. In this setup, the baseline components are effectively canceled, and the differential clock is nominally zero. As a result, the signals depicted in these figures provide a direct representation of phase estimation errors in the individual observables.

Both signals exhibit characteristics of a colored signal, with the PolaRxTR showing a significantly lower level compared to the OEM729. Analyzing the 10-second time scale in Figure 4.9 clearly reveals a common contamination in the OEM729, which far exceeds its noise level. This contamination likely arises from disturbances in the clock path, environmental sensitivity, or phase noise introduced at the interface within the development kit.

The short time span in the results from PolaRx5TR shown in Figure 4.10 reveals a slowly varying common-mode, although the overall error is dominated by a noise-like signal. The correlation between signals in the PolaRx5TR receiver is more clearly illustrated in Figure 4.8, which depicts the covariance matrix between differential phase estimation errors obtained from a SOZB experiment. The figure reveals that for this receiver, the correlation depends primarily on the signal type and is largely independent of the originating GNSS satellite. Notably, Galileo E6 and Beidou B3 exhibit minimal correlation with all other signals, even those from satellites within the same frequency band. The presence of uncorrelated signals indicates the absence of common hardware contamination in the receiver clock interfaces, which would induce an error common to all signals, as occurs in the OEM729.

In operational scenarios where antennas are separated and oscillators operate independently, a common mode affecting all GNSS signal bands, like the one observed in the OEM729, cannot be identified directly from the carrier phase. It can only be mitigated through filtering and remains unaffected by averaging different carrier phase observables. In contrast, for the PolaRx5TR, where the common mode affects only one or two bands rather than all, it still degrades performance, but sensibly less than in cases where all signals are contaminated.

This result emphasizes that the phase tracking accuracy of the receiver is generally not driven by thermal noise in the signal reception, rather by

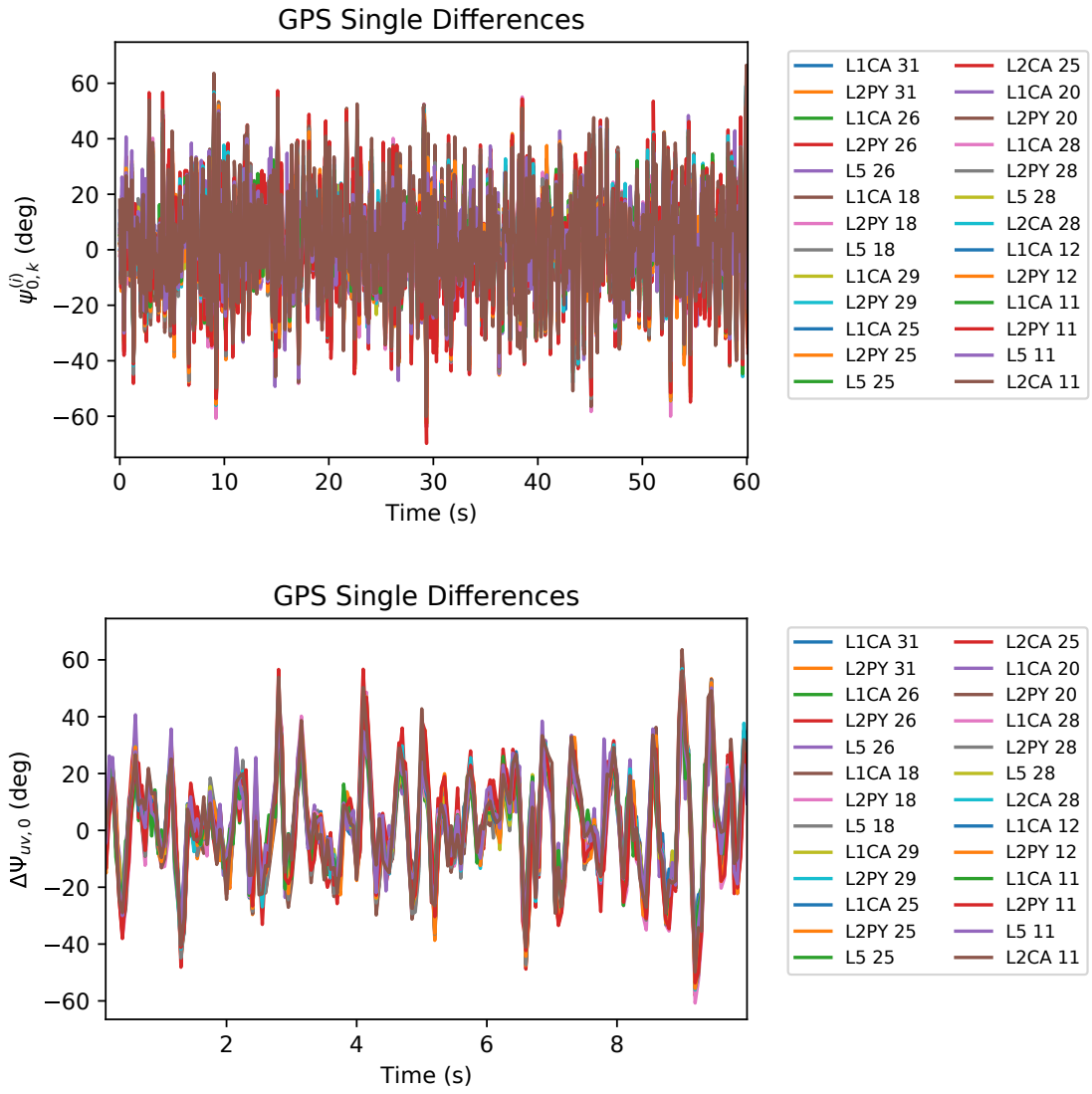

Figure 4.9: Carrier phase single-differences scaled to reference 5.4 GHz radar frequency for SOZB experiment with the OEM729 receiver in two time scales.

internal contamination, which must be determined experimentally. The simplest approach is to evaluate the covariance using the calibration procedure described in the Subsection 4.3.1, based on the SOZB experiment. The experiment is straightforward to conduct, requiring only a pair of GNSS receivers under evaluation and no separate device for independent differential phase measurement.

It is important to note that in these experiments both receivers exhibited a clear temperature sensitivity in data collected immediately after being powered on. Temperature variations introduce time-dependent delays in hardware components, leading to a common drift carrier phase observables. As mentioned above, environmental factors can also contribute to

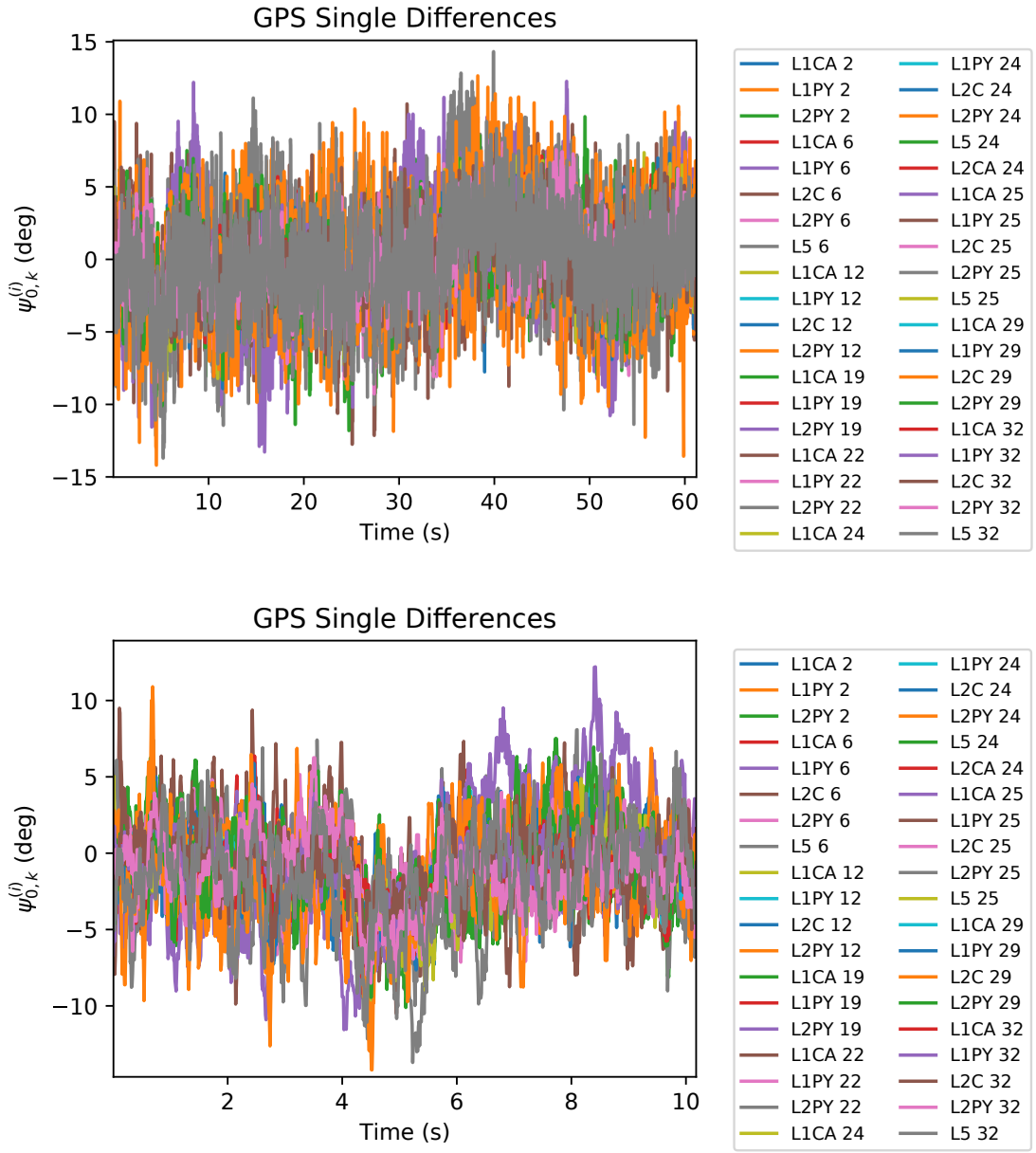

Figure 4.10: Carrier phase single-differences scaled to reference 5.4 GHz radar frequency for the SOZB experiment with the PolaRx5TR receiver in two time scales.

common mode effects. Therefore, for repeatable phase-tracking performance, it is essential that both receivers operate under thermally stable conditions, are properly isolated from environmental influences (in the case of a ground-based experiment), and are identically configured to minimize differences in thermal behavior.

4.4.2 Two-Oscillators Zero-Baseline (TOZB)

The primary results from the two-oscillator zero-baseline experiments are presented in Figure 4.11. In this experiment, external effects such as multipath, atmospheric effects, and antenna phase center variations are the same for the two receivers sharing the same antenna, and therefore are canceled in the carrier phase single differences. This leaves only noise and receiver contributions to affect the result, representing an ideal scenario. The measurements are scaled to C band (5.4 GHz), L band (1.2 GHz), and X band (9.8 GHz). For both receivers, like in the SOZB experiments, the error signal resembles filtered noise, with no evidence of long-term drift or other systematic effects.

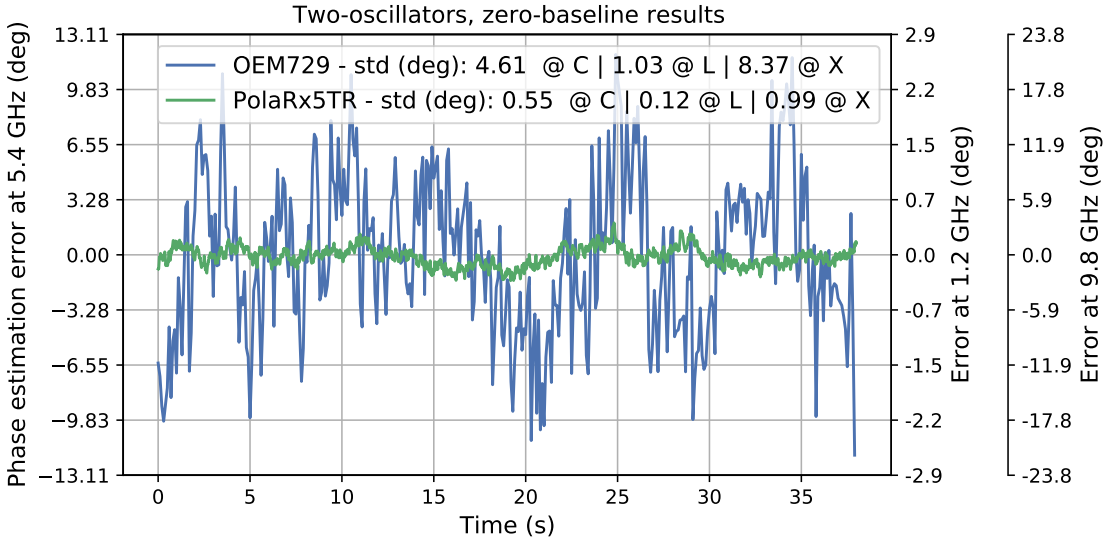

Figure 4.11: Synchronization errors for TOZB experiment with the PolaRx5TR and OEM729 receivers, compared to direct differential phase measurements obtained with a VNA. The standard deviation of the synchronization phase error at C band equals 0.58 and 4.61 degrees, respectively.

Figure 4.12 shows the histograms of the synchronization errors for the different processing stages, from an estimate based on a single differential carrier phase, to the estimate based on a filtered weighted average using all observables. The figure also highlights the effect of applying the optimal weights in contrast to weighting based on the Carrier-to-Noise Ratio (CNR) estimated by the receiver as in (3.14). The results demonstrate that proper filtering and weighting based on characterizing the carrier phase

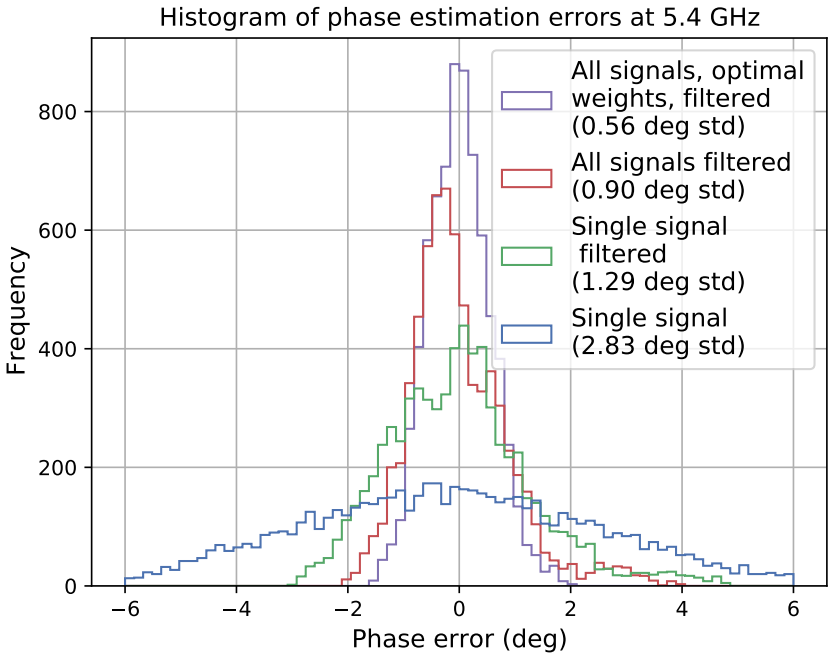

Figure 4.12: Phase synchronization error histograms for different processing steps for a TOZB experiment with PolaRx5TR receivers. The standard deviation of the synchronization phase error equals 1.29 degrees.

measurements and oscillator phase noise largely improves the synchronization results. The standard deviation dropped from 0.9 to 0.58 degrees when applying optimal weights, reflecting a reduction of outliers. The error distribution obtained was more symmetric and concentrated around zero.

As a final remark, the performance results at different radar carrier frequencies presented in this and the following sections are derived from simple scaling. This approach implicitly assumes that the carrier generation at the radar payload does not introduce significant contamination from the oscillator to the output, or that any such contamination is eliminated a-posteriori, for instance, using a calibration loop. To satisfy this payload coherence maintenance requirement, high-quality and carefully tuned Phase-Locked Loops (PLLs) and filters is recommended for carrier generation.

4.4.3 Two-Oscillators Short-Baseline (TOSB)

Figure 4.13 shows the results from the TOSB experiment with the PolaRx5TR receiver. The figure shows three datasets taken at three different times and different sets of GNSS satellites in view. The two sub-plots correspond to the results using the weighting based on the CNR, and the

results using the estimated optimal weights with the covariance estimation method suggested in Subsection 4.3.1.

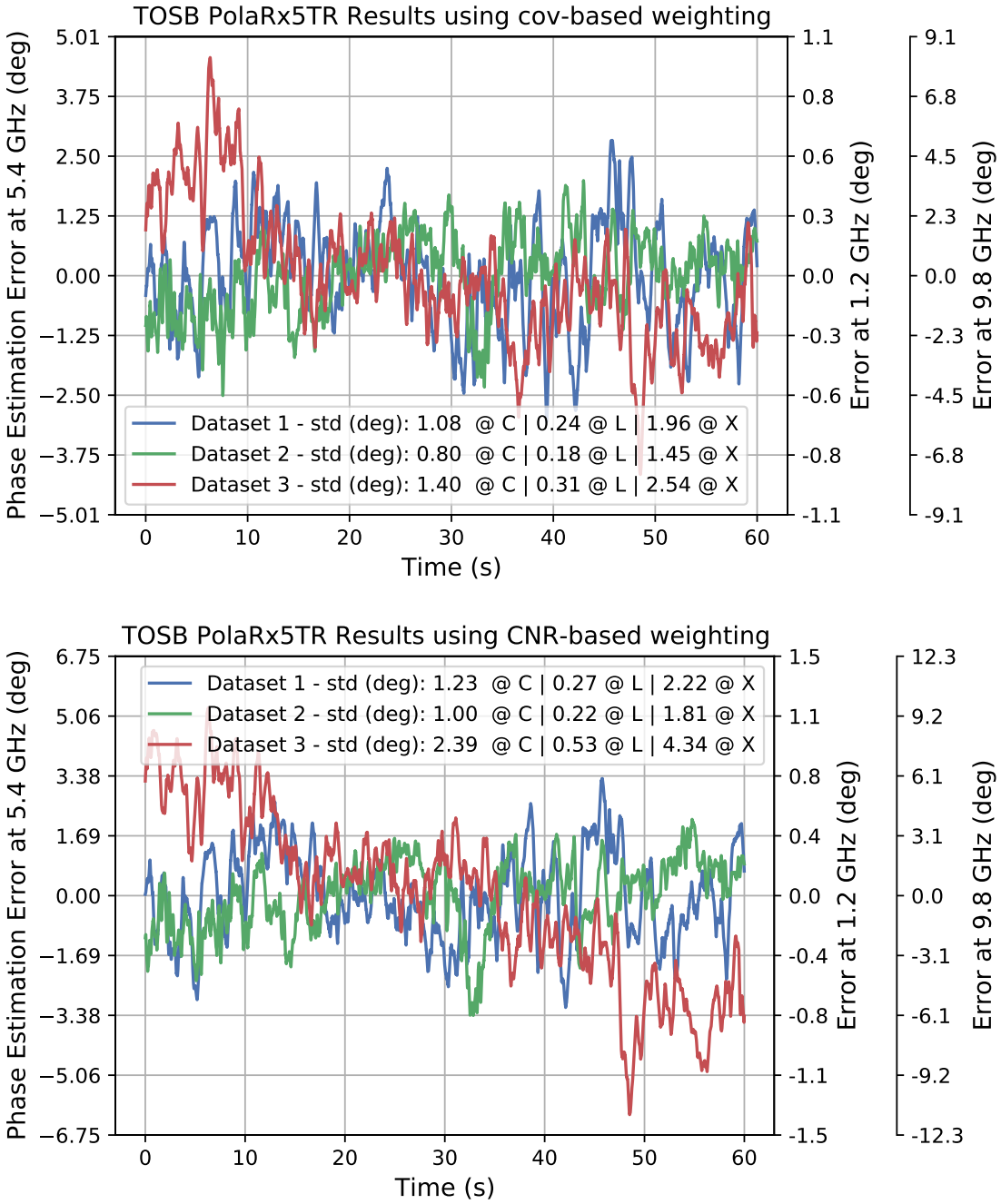

Figure 4.13: Synchronization results for TOSB experiments using the PolaRx5TR receiver. The top plot shows weighting based on estimated covariances, while the bottom plot shows weighting based on measured CNR. Three datasets taken at different times and using different sets of GNSS satellites are shown.

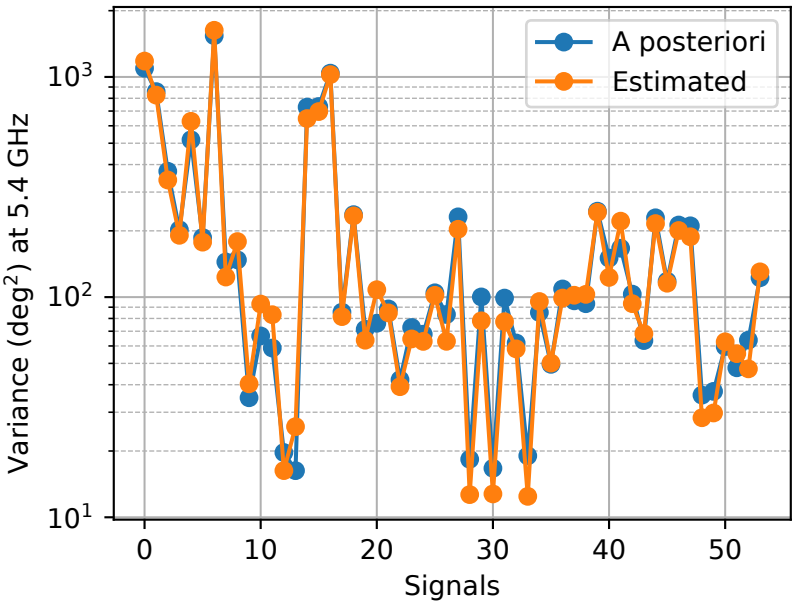

Figure 4.14: Comparison between scaled carrier signals error variances measured a-posteriori and the variances estimated, taken from a TOSB experiment with the PolaRx5TR.

Compared to the zero-baseline experiments, the results reveal a pronounced increase in phase error, with the introduction of a slowly varying systematic error. The error, however remains acceptable, particularly for system operating in lower frequency bands. This increase is most likely caused by multipath, given the proximity of the antennas to the ground and the lack of multipath suppression in them. It is worth noting, however, that in a spaceborne application, multipath interference is expected to be significantly lower, making the result in an operational scenario most likely between the one depicted in Figure 4.11 and the one depicted in Figure 4.13. This outcome depends on whether other error contributions such as multipath, cross-talk, and the thermal environment are effectively mitigated and assumes that no other previously unidentified factors are driving the results besides multipath.

When comparing the results of the weighting methods, it becomes clear that using estimated covariances yields better outcomes. However, the improvement is less pronounced compared to the optimal weighting observed in the zero-baseline experiment shown in Figure 4.12. This is because in this case multipath effects dominate the error budget, exerting a far greater influence than receiver contamination. The latter is the main factor mitigated by giving higher weights to signals unaffected by the common-mode.

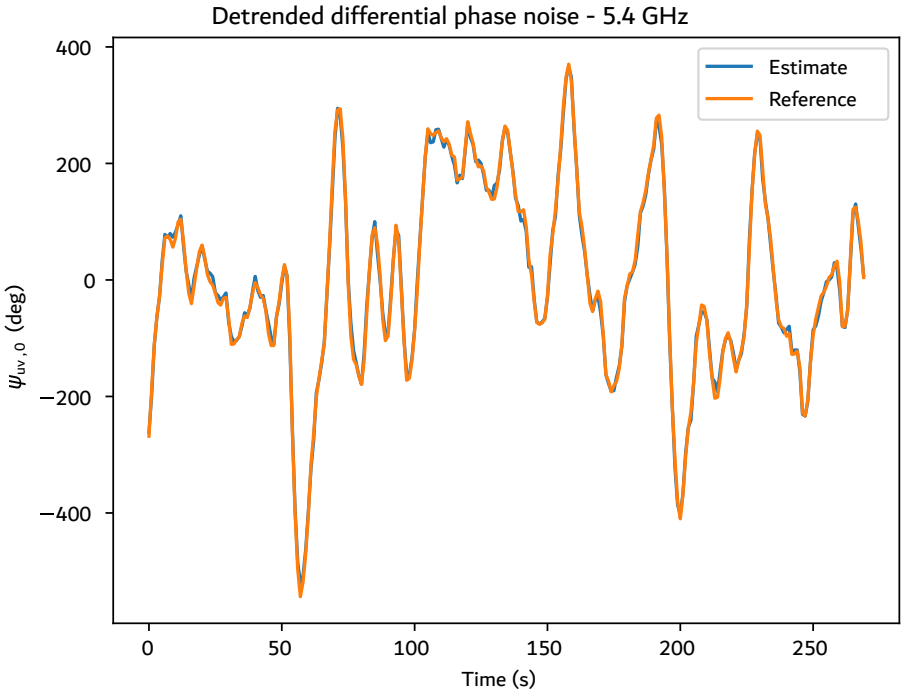

Figure 4.15: Detrended synchronization results for two-oscillators experiment with simulated formation flying using the PODRIX receivers in comparison with direct measurement. Due to setup limitations, only L1 and E1 signals were used, and the sampling rate was limited to 1 Hz. The standard deviation of the synchronization phase error equals 8.46 degrees. .

Figure 4.14 compares the variances from the short-baseline experiment using the PolaRx5TR, calculated a posteriori and estimated. The figure demonstrates a good agreement between the a posteriori error variances and the estimated ones. It also reveals that some signals in the physical setup are affected by errors several orders of magnitude higher than expected from simple thermal noise, corroborating the hypothesis of the results being driven by multipath interference. Despite the severe multipath effect in most of the carrier phase observables, the algorithm successfully identified and assigned lower weights to the more affected measurements, achieving performance degraded but still comparable to the zero-baseline experiments. These results demonstrate the robustness of the technique its effectiveness in assessing errors in individual carrier-phase observables under such conditions.

Figures 4.15 and 4.16 present the results of the short-baseline, two-oscillator experiments conducted with the PODRIX receiver in a simulated formation-flying scenario using a GNSS signal simulator. Figure 4.15 shows the detrended phase noise estimates at the 5.4 GHz reference frequency and the detrended reference obtained through the direct phase measurement device. The linear component was eliminated to facilitate visualization, but

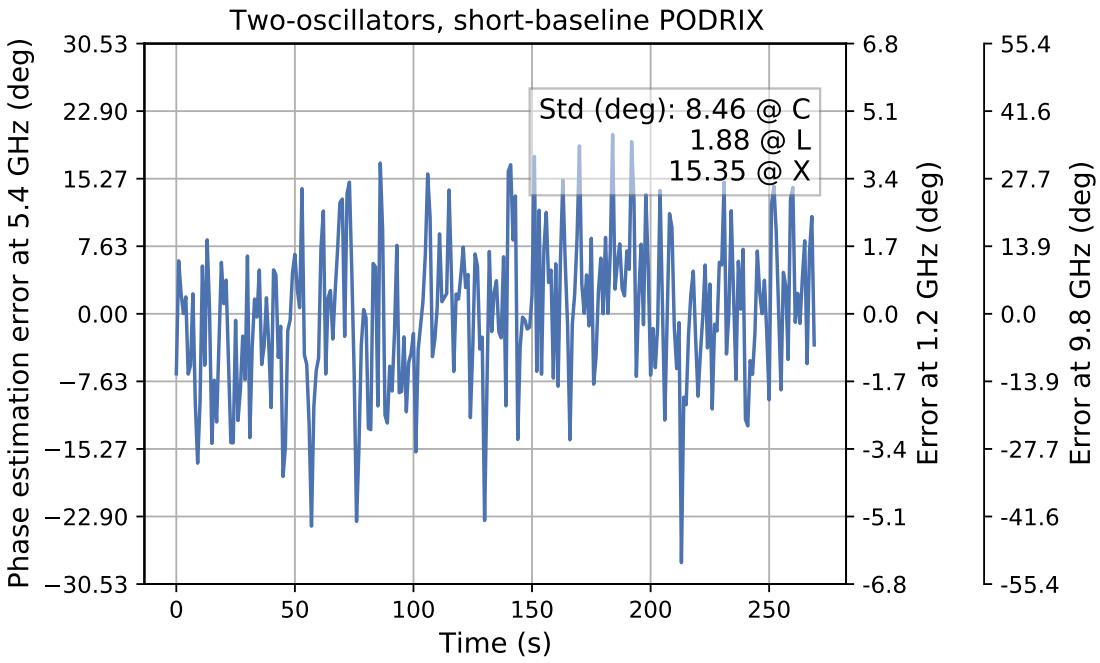

Figure 4.16: Synchronization results for two-oscillators, simulated formation flying experiment using the PODRIX. Due to setup limitations, only L1 and E1 signals were used, and the sampling rate was limited to 1 Hz. The standard deviation of the synchronization phase error equals 8.46 degrees. The upper plot was detrended to facilitate visualization.

note that the residual frequency is estimated seamlessly along with the phase noise by the algorithm. Figure 4.16 illustrates the corresponding total differential phase error, including the estimated frequency offset, at different reference frequencies. Similarly to the zero-baseline scenario, no distinctive systematic effects are observed.

The results in Figure 4.16 demonstrate effective motion compensation, as the relative motion contribution a dominant factor in formation-flying scenarios was practically eliminated, yielding an estimated differential phase noise that closely matches the reference.

However, the synchronization phase error obtained (8.46 degrees) was much higher than that of the PolaRx5TR. This discrepancy is at least partially attributable to differences in test conditions. In all experiments involving the PODRIX receiver, the carrier phase measurement update rate was fixed at 1 Hz due to limitations in the experimental setup. This low sampling rate may not only be insufficient to capture the differential phase noise spectrum, leading to interpolation errors, but also limits the potential for improvement through filtering. Additionally, only the L1 band could be simulated in the formation-flying scenario, reducing the number of signals available for averaging.

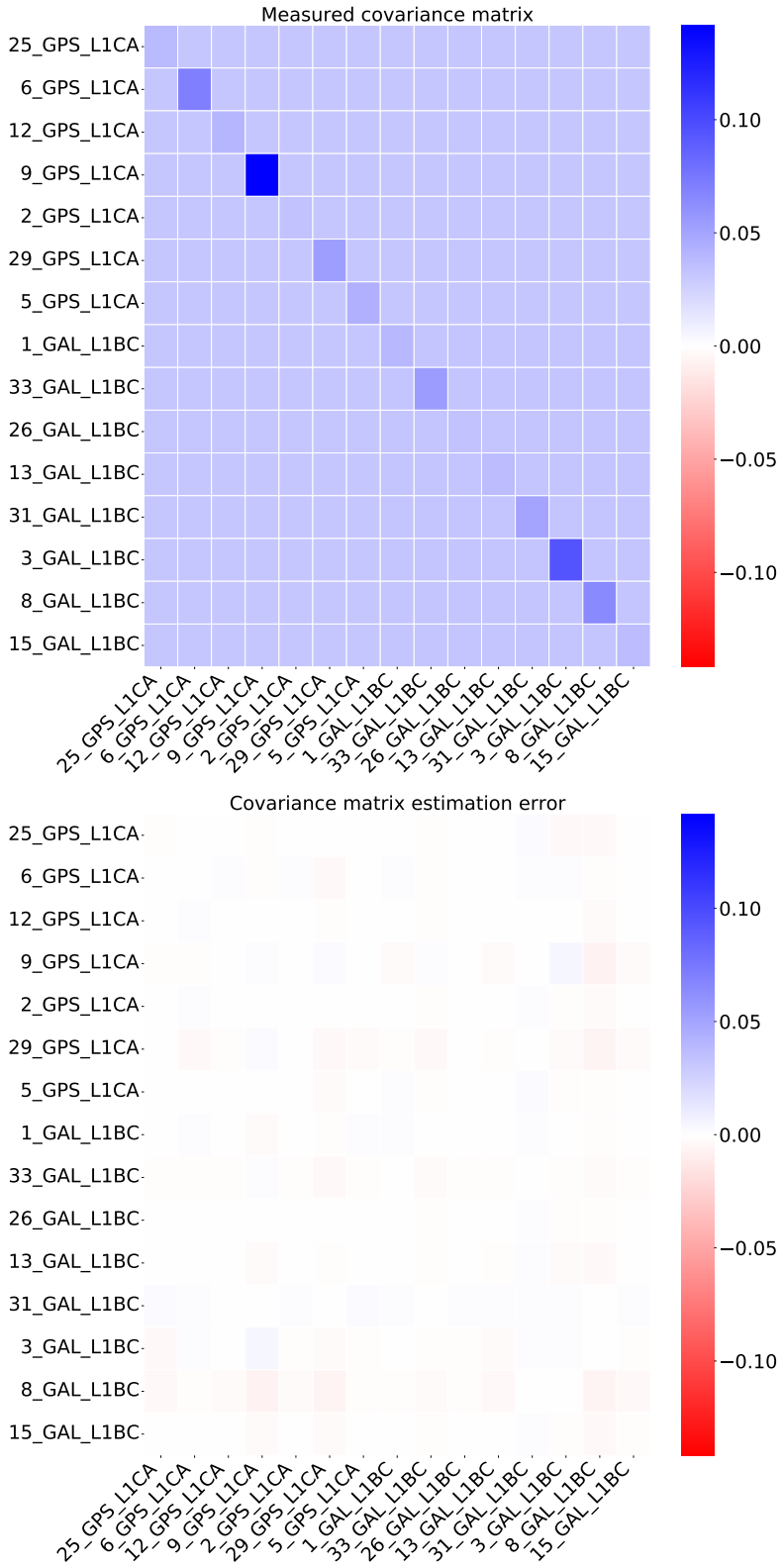

Figure 4.17: Samples of covariance estimation results for the TOSB experiment with the PODRIX receiver.

Figure 4.17 shows the measured covariance matrix between signals in the formation-flying scenario with the PODRIX receiver, along with the error compared to the estimated matrix obtained by calibrating the off-diagonal terms in a SOZB experiment, as described in Section 4.3. The individual errors were measured by scaling the carrier phase single-difference observables and compensating for the relative motion, followed by subtracting the measured differential phase drift. The covariance matrix was directly estimated from these errors. The strong agreement between the estimated and calculated covariance matrices shown in Figure 4.17 demonstrates that the substantial Doppler differences between receivers in a formation-flying scenario do not significantly amplify the critical common-mode component, an effect that could otherwise undermine the concept. This experiment thus provides key validation of the technique's applicability to orbital scenarios. However, determining the final performance of the PODRIX receivers for this application would require an improved test setup. A higher sampling rate and a multi-band GNSS antenna in a zero-baseline setup would be needed to characterize the covariance between all the different signals. This would allow the determination of the achievable noise reduction through point-by-point averaging and filtering.

4.5 Conclusions

The proof-of-concept of the GNSS-based phase synchronization conducted in this study was successful. To the author's knowledge, this has been the first time that a GNSS-based synchronization experiment with a especially designed calibration and filtering approach has been shown to be accurate enough for a bistatic or multistatic SAR mission, with a synchronization phase error as low as 0.8 degrees at C band and 1.45 degrees in X band in a short-baseline experiment. This synchronization performance is comparable to the one degree required for TanDEM-X, which operates in X band. The precision achieved by the technique depends, however, on several factors. The main performance drivers identified in the experiment were the reference tracking precision of the receiver and multipath suppression. The experiments revealed that the accuracy of the technique can be increased considerably by appropriate inspection of the signals, calibration of the covariance matrix of the measurement, and appropriate filtering.

The results show that the GNSS-based synchronization has the potential to be a simple and scalable solution for bistatic and multistatic SAR systems, which could guarantee compatibility of different systems designed and launched completely independently, opening many possibilities for data combinations across missions operating in the same band. They show

that current technology could potentially achieve sufficient accuracy up to C band and hint at the potential of applicability to systems up to X band with incremental changes or the use of better-performing devices, as long as the previously identified main error contributions, such as multipath and cross-talk, are either suppressed or mitigated.

Finally, an important general conclusion drawn from the experiments is that the performance can be improved through precautions in the receiver design to prevent clock path contamination and potentially through adjustments in the configuration of the tracked signals.

5 Zero-Doppler Formation Geometry and Optimization

5.1 Introduction

The effectiveness of swath and Doppler spectrum reconstruction algorithms in multistatic SAR formations heavily rely on the precise positioning of individual spacecraft. Ideally, a static array configuration is desired, where the satellites are evenly distributed in an Earth-referenced frame, i.e., with respect to the imaged scene. However, maintaining this ideal configuration is not feasible without implementing constant active flight control to counter the relative dynamics of the satellites. An alternative approach is to design natural trajectories that result in the desired formation geometry within an acceptable margin for a limited fraction of the orbital period. This chapter addresses the issue of formation design for multistatic SAR systems, with focus on stringent relative positioning requirements (i.e., low deviations from the nominal relative positions) for beamforming using apertures distributed across multiple platforms. The aim is to propose an algorithm to design natural solutions that conform to the distributed SAR requirements at a given range of latitudes.

This chapter is organized as follows. Section 5.2 presents the definition of a spacecraft-centered frame, namely the zero-Doppler (ZD) frame, in which the positioning requirements for distributed SAR are defined, and derives the transformation matrix to the Hill-Clohessy-Wiltshire (HCW) frame, in which the design space of bounded relative trajectories is well known and easily characterized. Section 5.3 presents the distributed SAR imaging concepts for azimuth reconstruction and beamforming in elevation and formulates the positioning requirements for each concept. Section 5.4 presents the proposed formation optimization algorithm. Section 5.5 presents examples of design of along-track and cross-track systems using the proposed algorithms, and the associated positioning performance and coverage. Finally, the results and conclusions of the chapter are summarized in Section 5.6.

5.2 Earth-Fixed Relative Motion Description

This section describes SAR geometry from a formation-flying perspective. First, it introduces the conventional reference frame used in formation flying, followed by the frame best suited for describing the relative positioning of apertures in SAR applications. These frames are then defined mathematically and the corresponding transformation matrices are derived. This foundation facilitates relating the relative motion models from formation flying literature to the multistatic SAR positioning requirements.

As explained in Section 2.4, the relative dynamics in the HCW frame are governed by a system of linear second-order differential equations, which, for circular chief orbits, admit an analytical solution that depends linearly on the initial conditions. This solution reveals that bounded relative motion, where satellites remain close without drifting apart, is confined to elliptical trajectories or, in special cases, degenerate elliptical forms such as lines and points.

In SAR remote sensing, this frame—along with its simplified dynamic and kinematic description of relative motion—cannot be directly applied because SAR geometry is referenced to the Earth's surface rather than an inertial frame. This distinction is illustrated in Figure 5.1, where ω_e represents Earth's angular velocity, $\vec{v}_{eci}$ denotes the satellite velocity in the Earth-Centered Inertial (ECI) frame, and $\vec{v}_{ecef}$ corresponds to the satellite velocity relative to Earth, i.e., in the Earth-Centered, Earth-Fixed (ECEF) frame. Additionally, $\vec{r}$ is the position vector of the reference satellite relative to Earth's center, while $\vec{h} = \vec{r} \times \vec{v}_{eci}$ represents the orbit's specific angular momentum, which remains constant throughout the orbit considering Keplerian motion.

The figure shows two satellites in the same orbit, arranged in a train-like formation, and therefore following an identical trajectory in an inertial frame. Because of the Earth's rotation, the satellites do not follow the same trajectory with respect to Earth, which can be seen in the ground swaths illustrated in green. To ensure the same trajectory with respect to Earth, the deputy satellite would have to be continuously aligned with $\vec{v}_{ecef}$. Therefore, the SAR geometry requirements are best described using the so-called zero-Doppler frame, defined in this thesis by the set of equations (5.1). The

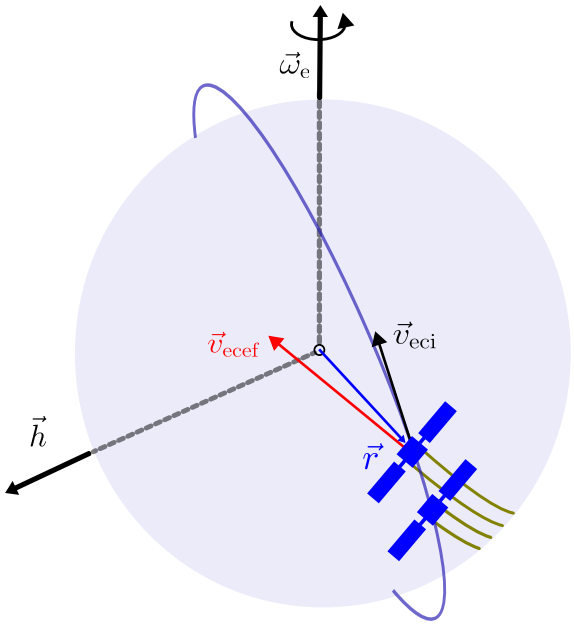

Figure 5.1: Illustration of the effect of Earth rotation on the formation geometry. The swath of a nadir-looking sounder instrument is indicated in green. Alignment with $\vec{v}_{ecef}$ and not $\vec{v}_{eci}$ guarantees matching ground tracks and swaths of the chief and deputy satellites.

definition of the HCW frame was introduced in the set of equations (2.33).

$$\hat{j}_{zd} = \frac{\vec{v}_{ecef}}{||\vec{v}_{ecef}||}, \tag{5.1a}$$

$$\hat{k}_{zd} = \frac{\vec{r} \times \vec{v}_{ecef}}{||\vec{r} \times \vec{v}_{ecef}||}, \tag{5.1b}$$

$$\hat{i}_{zd} = \hat{j}_{zd} \times \hat{k}_{zd}. \tag{5.1c}$$

Both ZD and HCW frames are centered on a reference satellite, denoted the chief. It is important to note that the classification of the satellite as "chief" or "deputy" does not imply any specific functional role in the SAR operation. Any element of the formation may be configured to transmit, receive, or perform both functions as part of an energy-optimized utilization of spacecraft resources.

In the ZD frame defined above, the J-axis is aligned with the instantaneous velocity of the satellite with respect to Earth. The plane IK (i.e., defined by the vectors $\hat{i}_{zd}$ and $\hat{k}_{zd}$) in this frame corresponds to the zero-Doppler (ZD) plane, hence the name [139]. The frame is defined so that the I-axis is nearly parallel to the radial direction. This makes it close to the I-axis of the HCW frame while ensuring that the J-axis remains perfectly aligned with the velocity vector relative to the Earth's surface.

Figure 5.2 shows the relation between the two frames and the sequence of rotations to transform from the HCW to the ZD frame. It isolates the vectors shown in Figure 5.1 and shows only their relative orientation. In the top plot, the satellite's inertial velocity $\vec{v}_{\text{eci}}$ is decomposed into a radial component $\vec{v}_{\text{r}}$ parallel to $\vec{r}$, and a component $\vec{v}_{\text{t}}$ tangential to the trajectory in the ECI frame. The figure assumes the general case in which the orbit of the chief satellite is eccentric. The figure also expresses the relation

$$\vec{v}_{\text{ecef}} = \vec{v}_{\text{eci}} - \vec{\omega}_{\text{e}} \times \vec{r}. \tag{5.2}$$

The transformation from HCW to ZD frame corresponds to a rotation

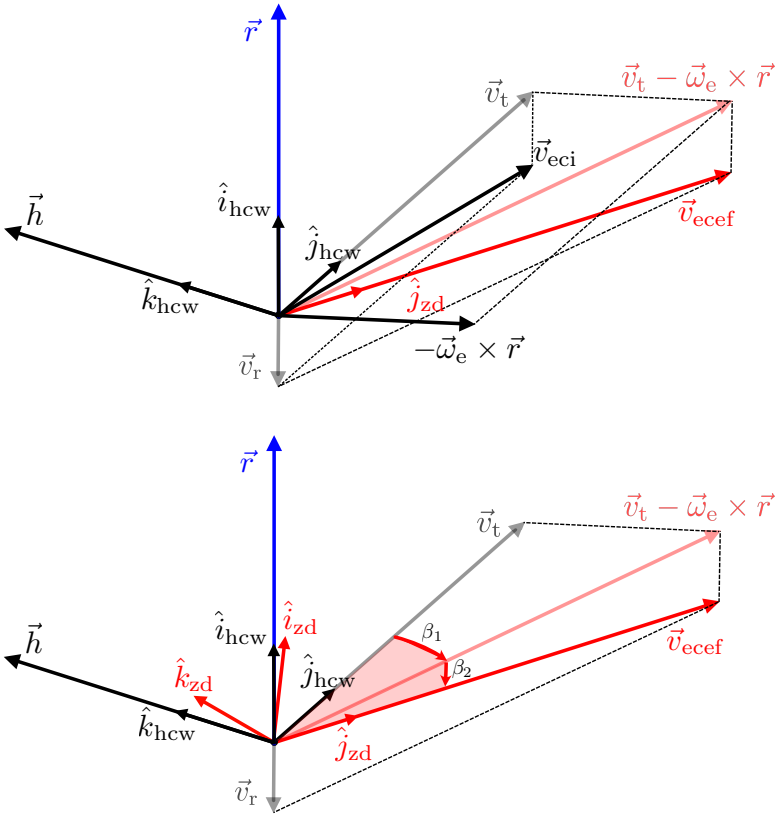

Figure 5.2: Rotation sequence from HCW frame to ZD frame. The ZD plane can be visualized in the lower illustration as the one defined by vectors $\hat{i}_{\text{zd}}$ and $\hat{k}_{\text{zd}}$.

around the I-axis followed by a rotation around the K-axis. From Figure

5.2, one can derive the rotation angles and the transformation matrix from ZD to HCW, denoted by $\mathrm{T}_{\mathrm{zd}\rightarrow\mathrm{hcw}}$. The transformation is given by

$$\beta_1 = \arctan\left(\frac{(-\vec{\omega}_\mathrm{e}\times\vec{r})\cdot(-\vec{h}/||\vec{h}||)}{(\vec{v}_\mathrm{t}-\vec{\omega}_\mathrm{e}\times\vec{r})\cdot\vec{v}_\mathrm{t}/||\vec{v}_\mathrm{t}||}\right), \tag{5.3}$$

$$\beta_2 = \arctan\left(\frac{\vec{v}_\mathrm{r}\cdot(-\vec{r}/||\vec{r}||)}{||\vec{v}_\mathrm{t}-\vec{\omega}_\mathrm{e}\times\vec{r}||}\right), \tag{5.4}$$

$$\mathrm{T}_{\mathrm{zd}\rightarrow\mathrm{hcw}} = \mathrm{R}_\mathrm{K}(\beta_2)\cdot\mathrm{R}_\mathrm{I}(-\beta_1), \tag{5.5}$$

where $R_\mathrm{I}(\beta)$ denotes a frame rotation matrix around the I-axis by an angle β, and $R_\mathrm{K}(\beta)$ denotes a frame rotation matrix around the K-axis by β. The transformation from HCW to ZD frame can be easily obtained by transposing $\mathrm{T}_{\mathrm{zd}\rightarrow\mathrm{hcw}}$.

The zero-Doppler geometry described above and the resulting transformation matrix to the HCW frame is similar to the one described in [139], with the difference that here the Earth rotation axis is not approximated as orthogonal to the equator. The difference could be considerable for decimeter-level relative positioning requirements and along-track separations of a few hundred meters or more.

For near-circular orbits, the radial component of the velocity ($\vec{v}_\mathrm{r}$) is much lower than the tangential component ($\vec{v}_\mathrm{t}$). In that case the transformation matrix can be approximated by a single rotation around the I-axis [140], conveniently expressed as a function of the chief's orbital elements [139] by

$$\mathrm{T}_{\mathrm{zd}\rightarrow\mathrm{hcw}} \approx \mathrm{R}_\mathrm{I}\left(\arctan\left(\frac{\omega_\mathrm{e}\cdot\sin i\cdot\cos(\omega+\nu)}{n-\omega_\mathrm{e}\cdot\cos i}\right)\right), \tag{5.6}$$

where, as previously introduced in Section 2.4.2, ω denotes the chief orbit argument of perigee, ν is the true anomaly, i is the orbit inclination, n is the orbit mean motion. The equation shows an oscillation around the I-axis with the highest values at the equator and lowest at the highest latitudes. This rotation will introduce an asymmetry in the relative trajectories when transforming from the HCW-frame to the ZD-frame. In addition, it adds a new degree of freedom to the formation design as it introduces a coupling between the along-track and the cross-track separations. As shown in the following sections, those factors open up new possibilities of relative trajectories. Note that the transformation matrix influences the shape of the relative trajectories in the ZD frame. This effect occurs regardless of relative distances, so it is incorrect to assume that multistatic SAR systems flying in close formation are approximately unaffected by the Earth's rotation, as the examples shown in Section 5.5 will demonstrate.

5.3 Canonical Formations for Distributed SAR

This section characterizes the baseline requirements for distributed multistatic SAR configurations for reconstruction in azimuth and beamforming in elevation. The relative positioning requirements for SAR will be expressed in coordinates in the ZD frame introduced in the previous section.

Note that the following subsections describe the relative positioning with respect to the monostatic equivalent of each receiver. Also note that the geometrical arguments and analytical derivations assume a small-baseline approximation (on the order of a few hundred meters to a few kilometers), consistent with the system examples provided at the end of this chapter and the conclusions drawn from them. The optimization procedures presented in this chapter remains applicable for longer baselines, requiring only the adjustment to the positioning requirements accordingly.

5.3.1 Along-track Formations for Azimuth Ambiguity Suppression

The along-track formation specified in this section is based on the distributed imaging concept presented in [141] and [142], and analyzed in detail in [16], [18], and [24]. In this concept, the individual satellites employ small antennas that do not satisfy the minimum antenna area constraint 2.15. A low Pulse Repetition Frequency (PRF) is selected to ensure good range ambiguity suppression. However, this PRF falls below the Nyquist rate for Doppler sampling, leading to significant azimuth ambiguities. To obtain high-quality SAR imagery, data from multiple platforms are jointly processed to reconstruct a wider Doppler spectrum, thereby enabling effective suppression of azimuth ambiguities. These algorithms are based on Doppler domain processing, which is effective and highly efficient in terms of processing time but imposes strict positioning requirements, and ideally very low cross-track baselines.

Azimuth reconstruction with considerable cross-track baselines is an active research field, and different approaches were proposed in the last years to address the problem [143, 144, 145, 146]. These techniques, however, have the inherent problem of requiring a-priori knowledge of the topography. This can cause performance degradation due to topography uncertainty, which is particularly problematic for dynamic scenes such as glaciers and urban areas, and for areas where the available DEM models have considerably different penetration capabilities than the intended frequency band

for the system. Finally, tightly controlled formations provide a significant advantage by preventing overlap between azimuth samples from different satellites. This ensures better and more consistent azimuth ambiguity suppression.

The Doppler frequency history for any given point in the imaged surface is determined by the range history of the satellite to that point. Therefore, for all the satellites in the along-track formation to sample different parts of the same Doppler history, they would need to describe the same trajectory in an Earth-fixed geometry, only delayed in time. The concept is illustrated in Figure 5.3, where the Doppler spectrum is reconstructed using three aligned platforms.

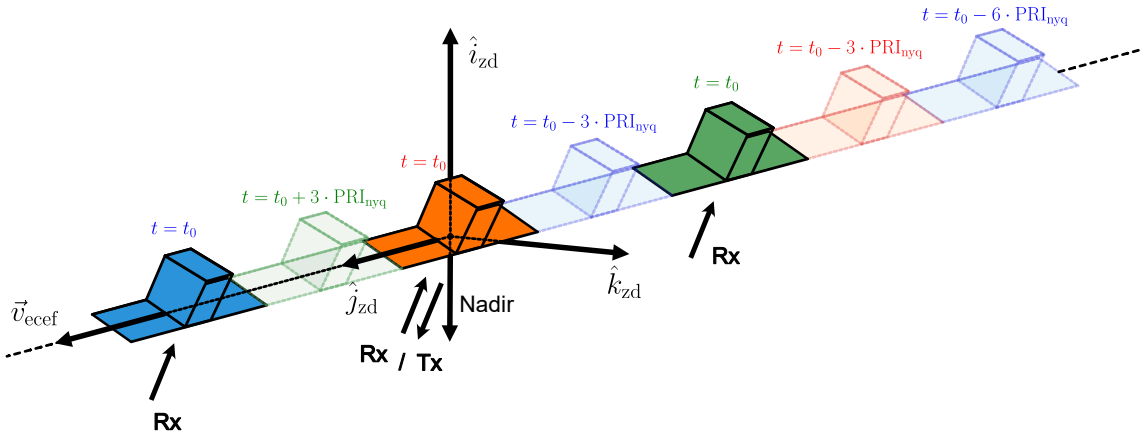

Figure 5.3: Along-track spacecraft distribution of multistatic SAR constellations for efficient Doppler spectrum reconstruction, as suggested in [16]. The satellites are positioned to acquire complementary Doppler samples at the signal reception times, allowing the use of a reduced PRF. Each color denotes a different platform, and the opaque satellites represent the configuration a given instant. In the illustrated example, the chief satellite acts as both transmitter and receiver.

In the figure, the solid satellites represent the physical positions at a given sampling instant, while the transparent satellites show the positions at past or future sampling instants. The effective Pulse Repetition Interval (PRI) after reconstruction is denoted $\mathrm{PRI}_{\mathrm{nyq}}$, where $\mathrm{PRI}_{\mathrm{nyq}} = 1/\mathrm{PRF}_{\mathrm{nyq}}$. The joint system can therefore sample the nominal Doppler history at an appropriate rate, allowing the elements to be separated by relatively large distances, provided that they occupy complementary positions at the sampling instants and are able to receive the echoes from the transmitting element.

For a formation of N satellites, each identified by a unique aperture index k, the required positions in the ZD frame ($\vec{\rho}_{\mathrm{zd}_k}$) are given by

$$\vec{\rho}_{\mathrm{zd}_k} = \begin{pmatrix} 0 \\ \frac{2 \cdot v_{\mathrm{ecef}}}{\mathrm{PRF}} \cdot \left(\frac{k}{N} + n_k \right) \\ 0 \end{pmatrix}, n_k \in \mathbb{Z}, k = 0, 1, ..., N-1, \tag{5.7}$$

where v_{ecef} is the magnitude of the satellite velocity with respect to Earth, n_k is an arbitrary integer number, and the vector notation represents the I, J, K components from top to bottom, respectively. Note that for large baselines (in the order of kilometers), the appropriate curved geometry of the orbit would need to be considered. In that case, the same expression would be more accurate when expressed in curvilinear coordinates [147].

To prevent coinciding azimuth samples, each satellite's relative position must remain within one resolution cell of the reconstructed signal—that is, within the distance traveled during the pulse repetition interval (PRI) after azimuth reconstruction—relative to its nominal sampling position. This condition can be expressed as

$$\delta\rho_{\mathrm{at}} = \zeta \cdot \frac{L_{\mathrm{a}}}{2N}, \tag{5.8}$$

where $\delta\rho_{\mathrm{at}}$ is the maximum deviation in along-track, L_a is the azimuth antenna length and ζ is a design factor smaller than one [24].

Displacements in cross-track may result in time-and-range variant reconstruction errors, which can be interpreted as a topography-dependent model mismatch and, therefore, must be limited. The maximum allowed cross-track displacement $\delta\rho_{\mathrm{xt}}$ to avoid significant effects of the topography can be expressed as a function of the maximum allowed phase excursion ϵ_ϕ as follows [24]

$$\delta\rho_{\mathrm{xt}} = \frac{\epsilon_\phi}{\pi} \cdot \frac{\lambda_{\mathrm{radar}} \cdot R_{0\mathrm{n}} \cdot \sin\theta_{\mathrm{ni}}}{\delta h}, \tag{5.9}$$

where δh is the maximum topographic variation within the scene, $R_{0\mathrm{n}}$ is the near slant range, θ_{ni} is the near incident angle, and λ_{radar} is the radar carrier wavelength. This implies control requirements lower than $20\lambda_{\mathrm{radar}}$ for good azimuth ambiguity performance [24].

5.3.2 Cross-Track Formations for Range Ambiguity Suppression

The relative positioning of a cross-track formation for range ambiguity suppression is illustrated in Figure 5.4. In this concept, the total system antenna is distributed in the cross-track direction, and the individual satellites have a PRF high enough to provide good azimuth ambiguity rejection. The short height of the antennas, combined with the high PRF, would result in the superimposition of signals from different transmitted pulses and, therefore, high-range ambiguities. Beamforming on ground combining data acquired at different platforms is performed to achieve sufficient range ambiguity suppression. The concept is discussed in several references, including monolithic satellites with multi-array antennas [148] and distributed platforms [20].

Neglecting the signal power difference, a displacement orthogonal to the aperture plane shown in Fig. 5.4 is approximately equivalent to a time delay, which could be compensated in the signal processing. Moderate displacement in the along-track is also allowed, considering that the PRF is high enough so that azimuth samples can be interpolated without introducing considerable errors.

Beamforming in cross-track could also be used in radar-sounding applications for narrowing the beam of an otherwise omnidirectional antenna, synthesizing very large apertures in HF/VHF bands [149]. In this case, the aperture plane illustrated in Figure 5.4 would coincide with the horizontal plane.

Independent of the application, the key requirement in this concept is that the array elements are displaced between each other by a fixed optimal distance Δr_e in the projected nominal array direction. This distance varies depending on the application and could correspond, for example, to the antenna length in elevation (L_e), emulating a monolithic multichannel system (as illustrated in Figure 5.4), or it could be much larger—on the order of tens of meters—for applications like distributed radar sounders [149]. Denoting $\hat{i}_{arr}$ the nominal array direction in the ZD plane, this requirement is expressed in (5.10) to (5.12):

$$r_{zd_k} = -\frac{(N-1)\cdot\Delta r_e}{2} + k\cdot\Delta r_e\,,\; k = 0,1,...,N-1\,, \tag{5.10}$$

$$\hat{i}_{arr} = \begin{pmatrix} \sin\theta_{arr} \\ 0 \\ \cos\theta_{arr} \end{pmatrix}, \tag{5.11}$$

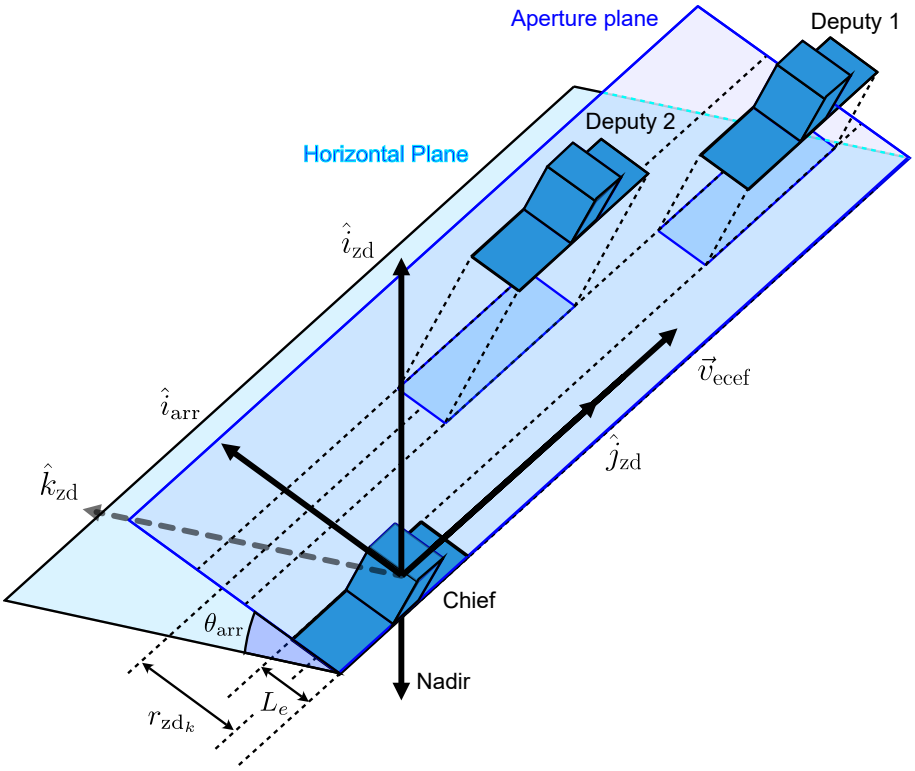

Figure 5.4: Cross-track multistatic imaging concept. In this example, the antennas are vertically displaced and complement each other, emulating a monolithic system with multiple elevation channels.

$$\vec{\rho}_{\mathrm{zd}_k} \cdot \hat{i}_{\mathrm{arr}} = r_{\mathrm{zd}_k}, \tag{5.12}$$

where N is the total number of satellites, k is the aperture index, and θ_{arr} is the angle between the aperture plane and the horizontal plane, which is approximately equal to the central look angle.

Deviations from the optimal Δr_{e} spacing degrade the beamforming performance and hence the ambiguity suppression capability. Notably, this degradation can be mitigated by increasing the number of phase centers (or satellites, in this case), but at the expense of a higher system cost.

5.4 Natural Formations Optimization

This section introduces algorithms to optimize natural formation geometries for distributed multistatic SAR configurations. First, relative motion is described as a function of a set of fixed parameters and the orbit of the chief satellite, which is assumed to be predefined. Then, the algorithms are introduced and explained conceptually and their principle is illustrated. Finally, this section provides the mathematical details of the optimization

approach applied to the two multistatic imaging concepts discussed in the previous section.

The relative motion of a deputy satellite with respect to a chief satellite can be parameterized employing the relative orbit elements (ROEs) as defined in (2.46). Just as the six Keplerian orbital elements define a satellite's state (i.e., its position and velocity), the six ROEs characterize the relative state of a deputy satellite with respect to the chief satellite's orbit. The position of the deputy satellite in the HCW frame ($\vec{\rho}_{\text{hcw}}$) at an arbitrary point of the chief orbit ,i.e., for an arbitrary argument of latitude (u) can be calculated as [72]

$$\vec{\rho}_{\text{hcw}}(u) = a \cdot \begin{bmatrix} 1 & 0 & -\cos u & -\sin u & 0 & 0 \\ -\frac{3u}{2} & 1 & 2\sin u & -2\cos u & 0 & 0 \\ 0 & 0 & 0 & 0 & \sin u & -\cos u \end{bmatrix} \cdot \delta\vec{\alpha}\,. \tag{5.13}$$

As expressed in (5.5), the position in the ZD frame is also given by a linear function of the position in the HCW, dependent only on the chief orbit. Therefore, the relative position at any instant in time is also a linear function of the ROEs.

This linear parametrization of the relative motion majorly simplifies the positioning optimization problem. The algorithm is reduced to determining the set of constant relative orbital elements that minimize the least squares deviation of natural relative motion with respect to the positioning requirements for the specific multistatic SAR concept. Although the requirements for the two canonical formations defined in this chapter are distinct, the algorithms share the same underlying logic, expressed in Algorithm 1.

Figures 5.5 and 5.6 illustrate the geometric concept behind the algorithm for fixed cross-track and along-track formations, respectively. In the figures $\mathrm{T}(u)$ denotes a transformation matrix that maps the ROEs to the position in the ZD frame.

Figure 5.5 shows the top-down view of the trajectory projected on the aperture plane (also illustrated in Figure 5.4). The relative trajectory is discretized, resulting in a set of points with a linear dependency on $\delta\vec{\alpha}$. These parameters are adjusted to fit the curve to the constant cross-track criteria by minimizing the squared sum of the errors (red horizontal lines) for each point within the region of interest. Since each u of the chief orbit corresponds to a specific latitude and flight direction (either ascending or descending), the selected range of u defines the latitude range and flight direction for which the formation is optimized.

Figure 5.6 illustrate the geometric concept behind the optimization algorithm for along-track formations. It presents a top-down view of the trajectory projected onto the horizontal plane. This plane is also depicted in

Algorithm 1 Compute Optimal ROEs for Required Positions

Require: orbital elements of the chief spacecraft
Require: ideal deputy positions in the ZD frame
Require: ranges of the argument of latitude (u) corresponding to latitudes of interest (ascending or descending flight direction)
Ensure: optimal ROEs for least squared positioning error in the ZD frame

1: discretize the selected range of arguments of latitude into $\{u_1, u_2, \ldots, u_n\}$,
2: **for** each discretized argument of latitude u_i **do**
3: compute the desired deputy position in the ZD frame at u_i,
4: formulate the positioning error as a linear function of the ROEs.
5: **end for**
6: perform least squares curve fitting to calculate the optimal ROEs that minimize the positioning error over all u_i.

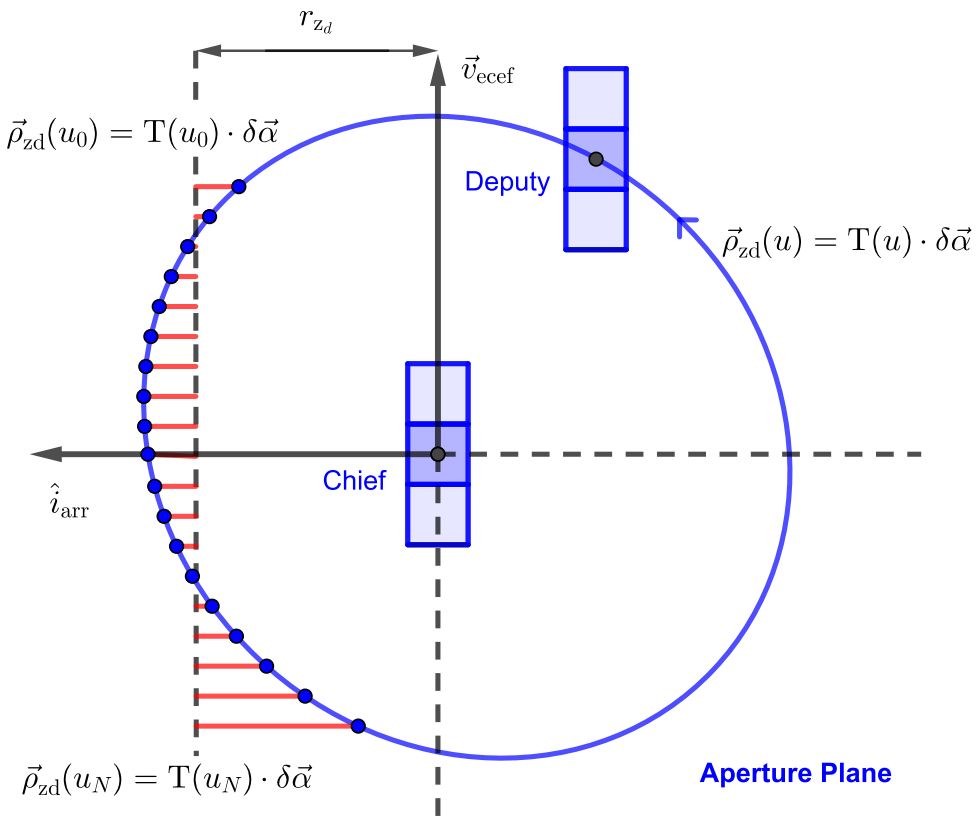

Figure 5.5: Optimization geometry illustration for cross-track formations. The blue track corresponds to the relative trajectory over one period of a single deputy satellite in the formation (i.e. a fixed aperture index k). The dashed vertical line corresponds to the required cross-track displacement r_{zd} calculated from (5.10).

Figure 5.4. Although the underlying principle remains the same, in this case, the optimization minimizes the sum of squared differences from the

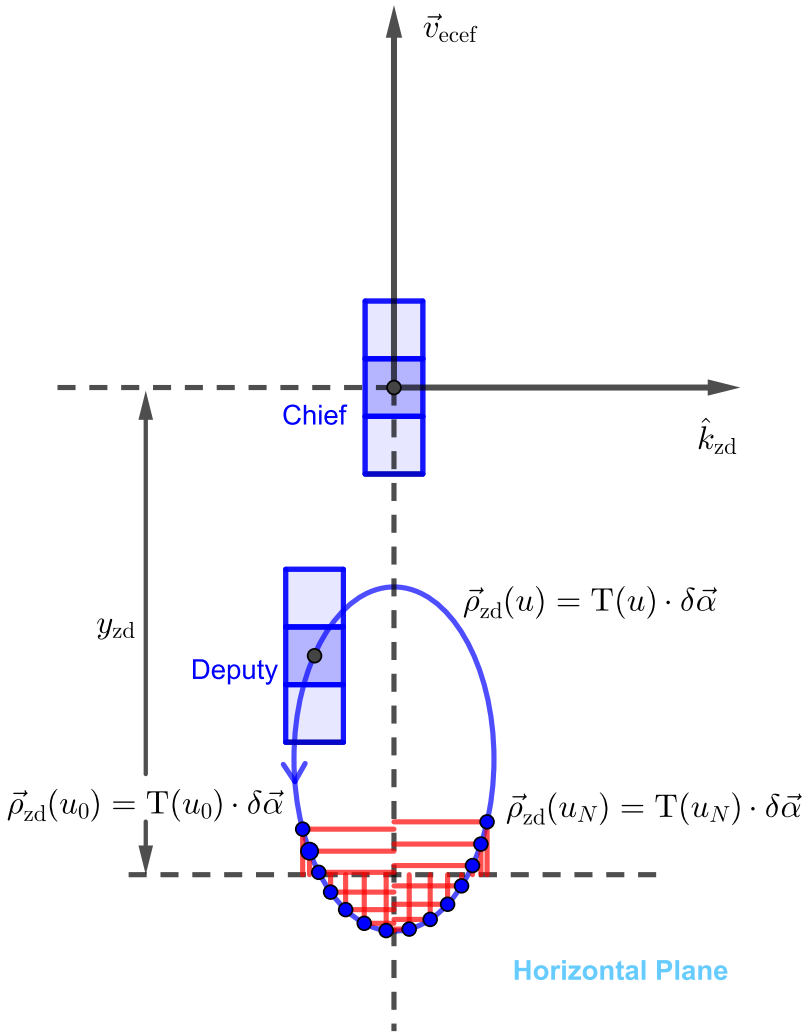

Figure 5.6: Optimization geometry illustration for along-track formations. The blue track corresponds to the relative trajectory over one period of a single deputy satellite in the formation (i.e. a fixed aperture index k). The dashed horizontal line corresponds to the required nominal along-track displacement, here denoted by y_{zd}, which can be calculated from (5.7).

positioning requirements across all three coordinates. For clarity, the Figure 5.6 displays two of these coordinates.

In this chapter, the analysis is limited to near-circular orbits of low altitude, which are an approximation for orbits with very low eccentricity, frequently used in remote sensing. The relative motion can be more accurately modeled by incorporating the effects of the chief orbit eccentricity and the J2 perturbation, with the latter being the dominant factor. However, including these effects would greatly complicate the analytical description of the relative motion.

The general solution for the complete problem, including a detailed dynamic model, is presented in Chapter 6. The algorithm presented in this

chapter is useful especially for multistatic SAR system designers for its ease of implementation, while resulting in solutions very close to the ones considering all disturbances. The model used in this chapter could also be used for the further development of approximated analytical models for the solutions in the future.

The following subsections provide a detailed mathematical description of the algorithms and briefly qualitatively describe the formation solutions that can be obtained by applying them.

5.4.1 Optimal Along-Track Formations

The condition for bounded relative motion in the absence of perturbations is that the chief and deputy satellites have the same semi-major axis (a), i.e., $\delta a = 0$. Defining

$$\mathrm{T}_{\delta\mathrm{lei}\to\mathrm{hcw}} = \begin{bmatrix} 0 & -a\cdot\cos u & -a\cdot\sin u & 0 & 0 \\ a & 2a\cdot\sin u & -2a\cdot\cos u & 0 & 0 \\ 0 & 0 & 0 & a\cdot\sin u & -a\cdot\cos u \end{bmatrix}, \tag{5.14}$$

in that case, the position in the HCW frame as a function of the ROEs can be written from (5.13) as follows

$$\vec{\rho}_{\mathrm{hcw}}(u) = \mathrm{T}_{\delta\mathrm{lei}\to\mathrm{hcw}}(u)\cdot \begin{bmatrix} \delta l \\ \delta e_x \\ \delta e_y \\ \delta i_x \\ \delta i_y \end{bmatrix}. \tag{5.15}$$

where δl is the relative mean longitude, $(\delta e_x, \delta e_y)$ are the components of the relative eccentricity vector, and $(\delta i_x, \delta i_y)$ are the components of the relative inclination vector, as defined in Subsection 2.4.2. The positioning error in the HCW frame for an element k of the distributed aperture is given by

$$\delta\vec{\rho}_{\mathrm{zd}_k}(u) = \mathrm{T}_{\mathrm{hcw}\to\mathrm{zd}}(u)\cdot\vec{\rho}_{\mathrm{hcw}_k}(u) - \vec{\rho}_{\mathrm{zd}_k}, \tag{5.16}$$

where the ideal position in the ZD frame $\vec{\rho}_{\mathrm{zd}_k}$ is given by (5.7), and the transformation matrix $\mathrm{T}_{\mathrm{hcw}\to\mathrm{zd}}$ is given by (5.3) to (5.5).

The optimizer must minimize the cost function $\mathcal{J}_k$, consisting of the sum of the squared differences between the desired positions and the trajectory for a given set of ROEs, given by the equation

$$\mathcal{J}_k = \sum_{j=0}^{N} \delta\rho_{\mathrm{zd}_k}(u_j)^T \cdot \mathrm{W} \cdot \delta\rho_{\mathrm{zd}_k}(u_j)\,, \tag{5.17}$$

where the u_j are the elements of the discretized range of arguments of latitude of interest, and W is a diagonal weight matrix that allows for assigning different weights to the three components of the error and different arguments of latitude. Defining

$$\mathrm{A}_k = \begin{bmatrix} \mathrm{T}_{\mathrm{hcw}\to\mathrm{zd}}(u_0) \cdot \mathrm{T}_{\delta l\mathrm{ei}\to\mathrm{hcw}}(u_0) \\ \mathrm{T}_{\mathrm{hcw}\to\mathrm{zd}}(u_1) \cdot \mathrm{T}_{\delta l\mathrm{ei}\to\mathrm{hcw}}(u_1) \\ \vdots \\ \mathrm{T}_{\mathrm{hcw}\to\mathrm{zd}}(u_N) \cdot \mathrm{T}_{\delta l\mathrm{ei}\to\mathrm{hcw}}(u_N) \end{bmatrix}, \tag{5.18}$$

and

$$\mathrm{Y}_k = \begin{bmatrix} \vec{\rho}_{\mathrm{zd}_k} \\ \vec{\rho}_{\mathrm{zd}_k} \\ \vdots \\ \vec{\rho}_{\mathrm{zd}_k} \end{bmatrix}, \tag{5.19}$$

the optimal solution can be calculated through the least-squares solution below

$$\begin{bmatrix} \delta l \\ \delta e_x \\ \delta e_y \\ \delta i_x \\ \delta i_y \end{bmatrix}_k = \left(\mathrm{A}_k^T \cdot \mathrm{W} \cdot \mathrm{A}_k\right)^{-1} \cdot \mathrm{A}_k^T \cdot \mathrm{W} \cdot \mathrm{Y}_k\,. \tag{5.20}$$

An example of the solution for an along-track formation is shown in Subsection 5.5.1, but the overall concept is illustrated in Figure 5.7. The coupling between along-track and cross-track in the transformation from HCW to ZD frame shows that a separation in the argument of latitude also causes cross-track oscillation. This effect, however, can be largely compensated by offsetting the right ascension of the ascending node (RAAN) between the satellites by $\Delta\Omega$ to cause an oscillation in the opposite direction. This RAAN offset is automatically accounted for by the optimizer. The resulting formation can be seen as a corrected string-of-pearl or train formation.

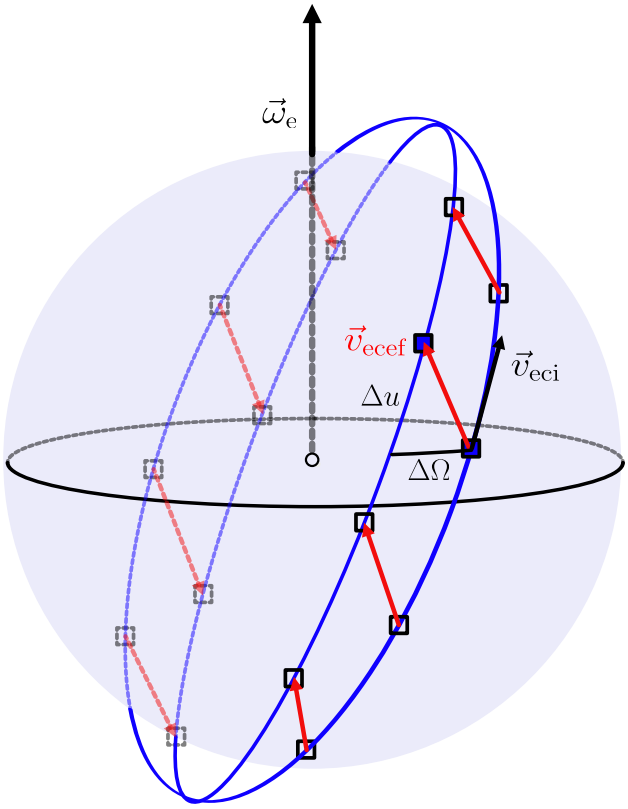

Figure 5.7: Illustration of the compensation for the coupling effect between along-track and cross-track motion on the ZD plane caused by Earth's rotation, achieved through an offset in the longitude of the ascending node (RAAN). The figure shows the positions of a two-satellite formation at different instants. The deputy satellite, advanced in argument of latitude by Δu, remains approximately aligned with the chief's velocity vector relative to Earth ($\vec{v}_{ecef}$) due to the RAAN offset ($\Delta\Omega$).

5.4.2 Optimal Cross-Track Formations

For cross-track multistatic concepts, the basic positioning constraint does not impose specific along-track displacements, and, in principle, the system designer has the freedom to choose or optimize for the mean along-track offset between the elements of the formation. This displacement is essential because the highly constrained solutions for beamforming do not allow for considerable separation in the radial/cross-track plane in small baseline cases. Therefore, maintaining separation in along-track is necessary to avoid collision. A reasonable separation in along-track also facilitates visibility by relative navigation sensors and allows for the mitigation of eventual problems with plume impingement. This separation can be imposed by fixing each satellite's relative longitude δl. In this case, one degree of freedom of the bounded relative motion is eliminated, and the

optimization would only solve for the inclination and eccentricity vectors. Defining

$$\mathrm{T}_{\delta\mathrm{ei}\to\mathrm{hcw}} = \begin{bmatrix} -a\cdot\cos u & -a\cdot\sin u & 0 & 0 \\ 2a\cdot\sin u & -2a\cdot\cos u & 0 & 0 \\ 0 & 0 & a\cdot\sin u & -a\cdot\cos u \end{bmatrix}, \tag{5.21}$$

and

$$\delta\vec{\rho}_l = \begin{bmatrix} 0 \\ a\cdot\delta l \\ 0 \end{bmatrix}, \tag{5.22}$$

the position in the HCW frame as a function of the optimization algorithm is given by

$$\vec{\rho}_{\mathrm{hcw}}(u) = \mathrm{T}_{\delta\mathrm{ei}\to\mathrm{hcw}}(u)\cdot\begin{bmatrix}\delta e_x \\ \delta e_y \\ \delta i_x \\ \delta i_y\end{bmatrix} + \delta\vec{\rho}_l\,. \tag{5.23}$$

For cross-track formations, the difference between the projection of the relative position in array direction and the nominal cross-track baseline must be minimized. This difference is given by the equation

$$\delta\rho_{\mathrm{zd}_k}(u) = \left[\mathrm{T}_{\mathrm{hcw}\to\mathrm{zd}}(u)\cdot\vec{\rho}_{\mathrm{hcw}_k}(u)\right]\cdot\hat{i}_{\mathrm{arr}} - r_{\mathrm{zd}_k}, \tag{5.24}$$

which leads to the least-squares solution with the following matrices:

$$\mathrm{A}_k = \begin{bmatrix} \hat{i}_{\mathrm{arr}}^T\cdot\mathrm{T}_{\mathrm{hcw}\to\mathrm{zd}}(u_0)\cdot\mathrm{T}_{\delta\mathrm{ei}\to\mathrm{hcw}}(u_0) \\ \hat{i}_{\mathrm{arr}}^T\cdot\mathrm{T}_{\mathrm{hcw}\to\mathrm{zd}}(u_1)\cdot\mathrm{T}_{\delta\mathrm{ei}\to\mathrm{hcw}}(u_1) \\ \vdots \\ \hat{i}_{\mathrm{arr}}^T\cdot\mathrm{T}_{\mathrm{hcw}\to\mathrm{zd}}(u_N)\cdot\mathrm{T}_{\delta\mathrm{ei}\to\mathrm{hcw}}(u_N) \end{bmatrix}, \tag{5.25}$$

and

$$\mathrm{Y}_k = \begin{bmatrix} r_{\mathrm{zd}_k} - [\mathrm{T}_{\mathrm{hcw}\to\mathrm{zd}}(u_0)\cdot\delta\vec{\rho}_l]\cdot\hat{i}_{\mathrm{arr}} \\ r_{\mathrm{zd}_k} - [\mathrm{T}_{\mathrm{hcw}\to\mathrm{zd}}(u_1)\cdot\delta\vec{\rho}_l]\cdot\hat{i}_{\mathrm{arr}} \\ \vdots \\ r_{\mathrm{zd}_k} - [\mathrm{T}_{\mathrm{hcw}\to\mathrm{zd}}(u_N)\cdot\delta\vec{\rho}_l]\cdot\hat{i}_{\mathrm{arr}} \end{bmatrix}. \tag{5.26}$$

An example of a solution for one single range of arguments of latitude is shown in Subsection 5.5.2. The concept can be illustrated by Figure 5.4.

In this solution, tight conformance to the constant cross-track baseline for a considerable contiguous segment of the orbit is achieved by allowing the satellites to move arbitrarily in the along-track and line-of-sight directions.

Alternatively, a pendulum-like solution, such as the one presented in [150], can be obtained by imposing two ranges of arguments of latitude of interest separated by 180°. This results in one coverage region in each hemisphere, one in the ascending direction, and one in the descending direction. A similar solution can also be obtained by reformulating the algorithm to optimize for fixed positions in the ZD plane. This configuration is illustrated in Figure 5.8.

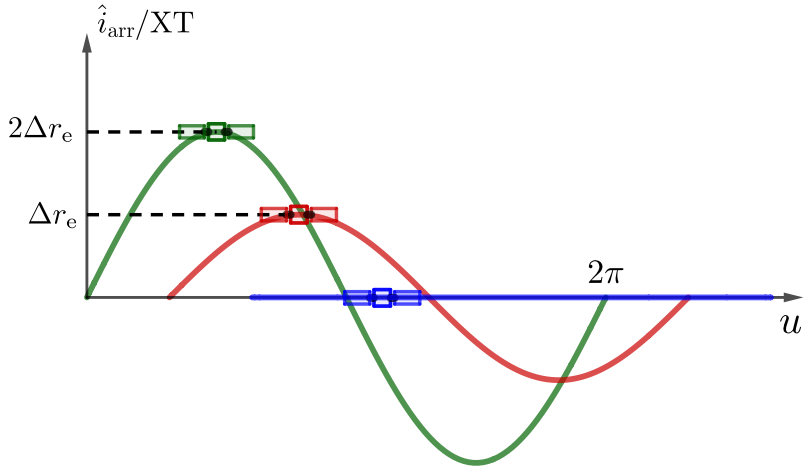

Figure 5.8: Illustration of solution for cross-track configurations. The cross-track position oscillates as the satellites progress in the orbit, always keeping an along-track separation.

The satellite position oscillates around the chief orbit's position. At around two points in the orbit—one during the ascending pass and one during the descending pass—the satellite achieves close to ideal cross-track positioning. The satellites are maintained at a safe separation in the along-track direction to prevent collisions as the orbits intersect.

The pendulum solution results in much larger deviations from the nominal positioning requirement in the ZD plane if the line-of-sight angle is constant. The positioning error of the satellites in the direction orthogonal to the aperture plane can be greatly improved by steering the attitude of all the elements of the constellation, including the transmitter. This is possible because, in these pendulum-like formations, the elements of the formation

uniformly expand and contract, keeping the distance between consecutive satellites equal during the whole orbit, as illustrated in Figure 5.9.

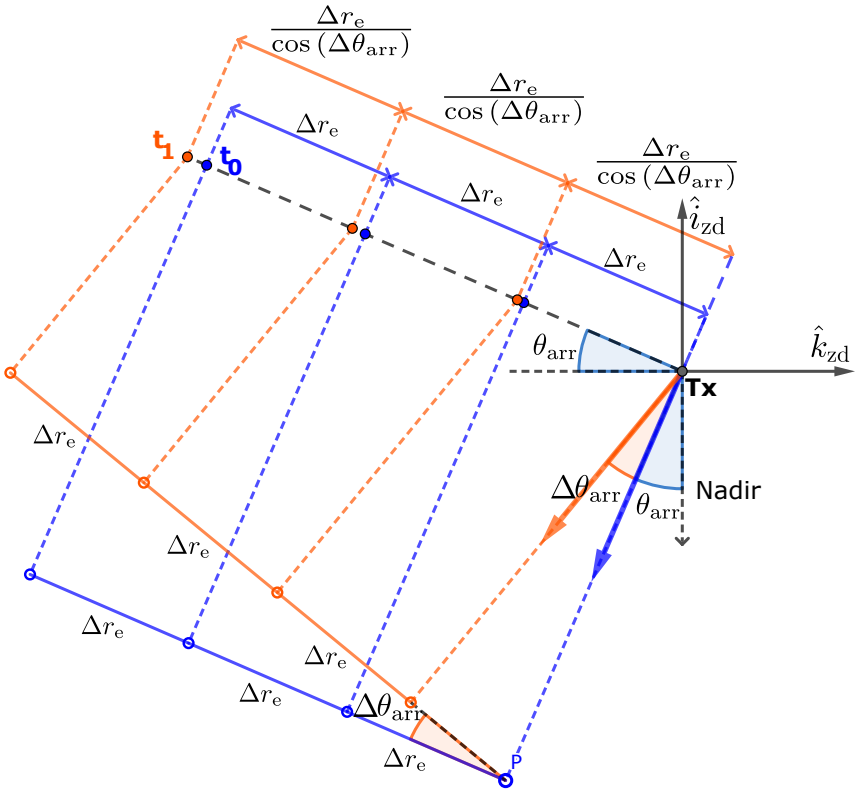

Figure 5.9: Illustration of attitude compensation for non-ideal satellite spacing for cross-track formations. The formation is designed so that the satellites are evenly spaced in the ZD plane. The transmitter satellite (Tx) look angle is adjusted by $\Delta\theta_{arr}$ to keep the cross-track spacing equal to the ideal (Δr_e).

In the figure, the blue and orange circles represent a snapshot of the formation at two different time instants (t_0 and t_1), and $\Delta\theta_{arr}$ is the change in the aperture plane direction through steering that would make the two arrays have the same optimal spacing orthogonal to the line-of-sight.

Although the optimal steering is a function of the argument of latitude and continuously changes, the optimal attitude profile remains consistent for the same scene. This consistency enables applications such as repeat-pass interferometry and time-series trend analysis despite the constant attitude steering.

5.5 System Example

This section presents examples of SAR performance and coverage enabled by the distributed formations optimized using the algorithm introduced in the previous section. In the examples, small SAR satellite systems operating in X band are considered, with small planar antennas, which would individually be incapable of providing unambiguous imaging. A near-polar circular orbit is used as the reference chief satellite orbit. The parameters are shown in Table 5.1, along with the simulated baseline error with respect to the ideal aperture positions. For simplicity, in the SAR performance as-

Chief's orbital parameters	
Altitude at equator	580 km
Eccentricity	0
Inclination	97.7°
Right Ascension of the Ascending Node (RAAN)	0°
Baseline deviations from nominal	
Along-track relative accuracy (3σ)	9 cm
Cross-track relative accuracy (3σ)	9 cm

Table 5.1: Orbital parameters of the chief satellite used throughout the chapter.

sessment, deviations from the nominal aperture positions are simulated as Gaussian positioning errors with a standard deviation that reflects a realistic budget, accounting for state-of-the-art relative navigation and control [151, 152]. These deviations include the differences between the reference natural solution and the ideal positions, as outlined in the following subsection for each imaging concept, as well as the control error.

The imaging performance of the distributed SAR systems presented in the following subsections was designed using a dedicated simulator developed by DLR. This performance is assessed using five main metrics: The 2-D resolution; The Noise Equivalent Sigma Nought (NESN), defined as the backscatter coefficient which causes the signal power to be equal to the noise power, representing the instrument sensitivity to noise independent of the imaged target; The Azimuth-Ambiguity-to-Signal Ratio (AASR), defined as the ratio of the power of the azimuth ambiguities to the power of the signal; The Range Ambiguity-to-Signal Ratio (RASR), corresponding to

System parameters	
Number of satellites	5
Wavelength	3.11 cm
Antenna look angle	27.8°
Acquisition mode	Stripmap
Antenna length	1.3 m
Antenna height	0.4 m
Pulse repetition frequency (PRF)	2.33 kHz
Processed azimuth bandwidth (all satellites)	10.3 kHz
Average power	1.17 kW
Noise figure	3 dB
Total losses	1.5 dB
Range bandwidth	53.0 MHz
Input coverage latitude range	0° to 82°

Table 5.2: System parameters of the multistatic system example employing azimuth reconstruction imaging in distributed SAR configurations.

the ratio of the range ambiguities power to that of the desired signal; and, finally, the swath width.

These imaging performance concepts are not discussed in detail in this work, as the focus is on synchronization and formation flying. For a more comprehensive understanding and the mathematical definitions of these metrics, [11] can be consulted.

5.5.1 Along-Track Formation Design

The nominal system parameters for the along-track formation example are shown in Table 5.2. The optimal trajectories in the ZD and HCW frames, calculated using the algorithm described in Section 5.4, are shown in Figure 5.10. In this example, a uniform weight was assigned to the errors at different latitudes. A weight ten times higher was assigned to the positioning error in along-track than in the other directions, reflecting the overall more stringent requirement along that axis.

The cross-track and radial deviations of the optimal relative trajectory are below three wavelengths for the radial displacements and below one wavelength for the cross-track displacement. These deviations are very low and are not expected to result in significant phase errors due to topography. The resulting natural relative trajectories, therefore, effectively overcomes

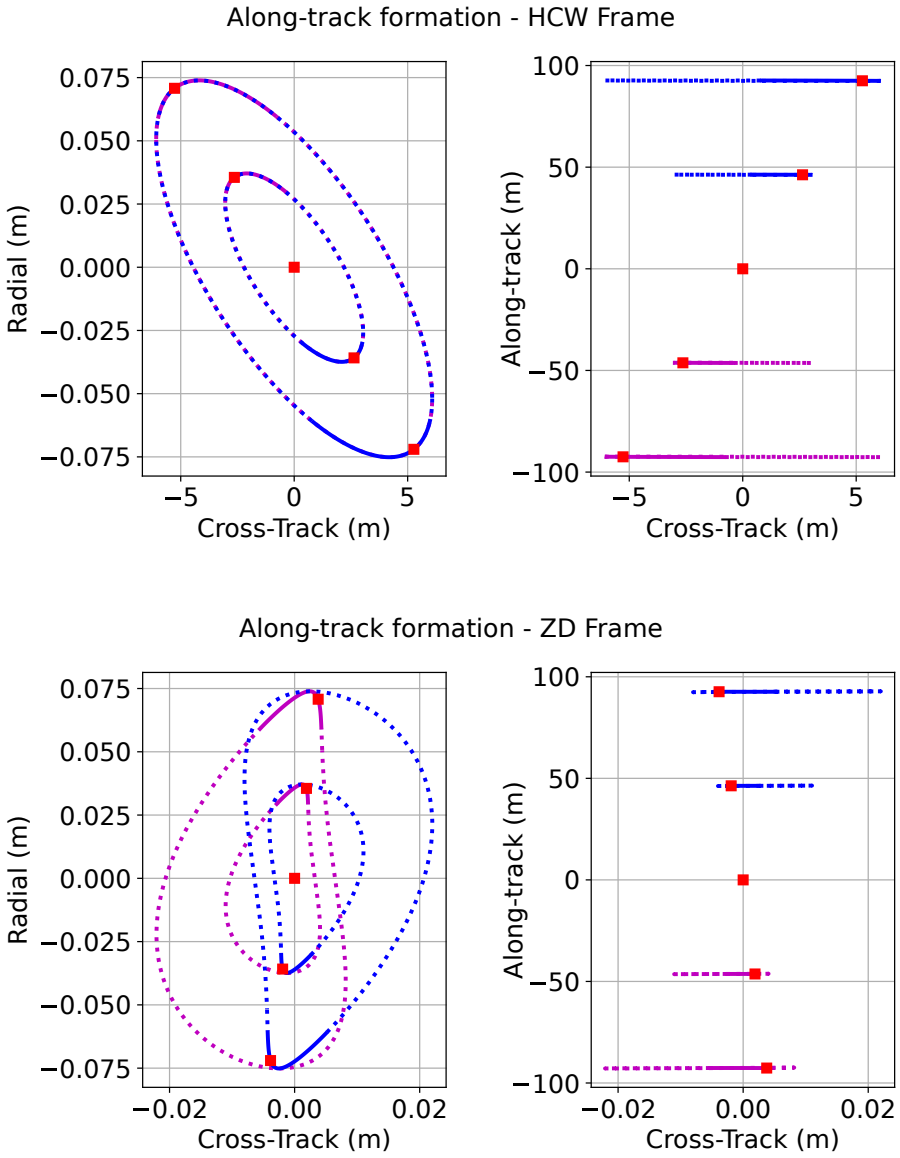

Figure 5.10: Designed trajectories in ZD and HCW frames for along-track reconstruction. The active imaging region is highlighted with solid lines. The red boxes exemplify the position of the satellites at one common instant. Trajectories behind and ahead of the chief in along-track are represented in magenta and blue, respectively.

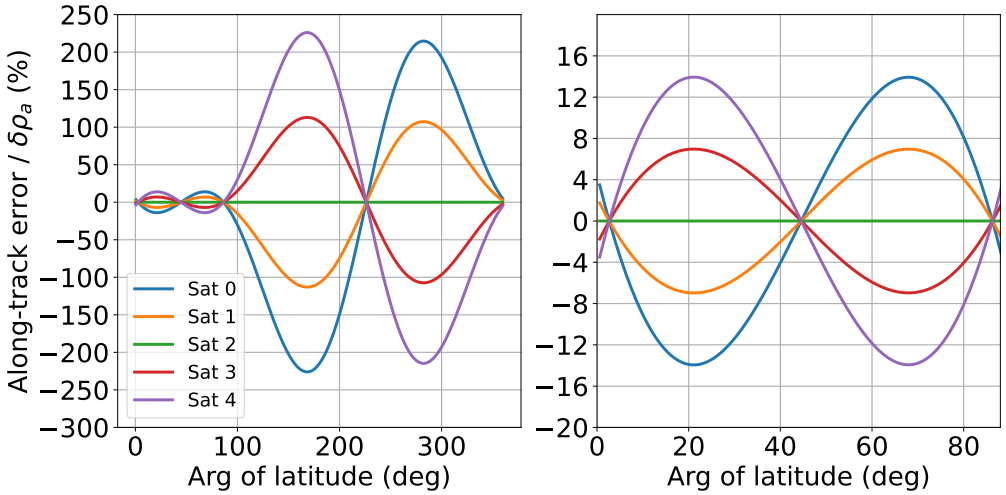

Figure 5.11: Along-track positioning error for the along-track reconstruction example, shown relative to the nominal distribution, with satellites spaced approximately 50 m apart along-track. The y-axis indicates the percentage relative to the maximum allowed deviation of 9.8 cm, computed using (5.8) with a design factor $\zeta = 0.7$. The right-hand plot provides a zoomed-in view of the range of argument of latitude corresponding to the input latitude range during the ascending pass.

the key challenge of performance degradation caused by cross-track topography sensitivity in train formations, making them much more attractive for high-performance SAR imaging with small satellites.

Figure 5.11 shows the spacing errors relative to the nominal along-track positions. As depicted in the plot on the left, the designed trajectories deviate by less than 2 cm across the optimized range of argument of latitude from 0° to 82°, corresponding to approximately 25% of the orbit. The spacing error is shown as a percentage of the maximum allowable value of 9.8 cm, derived using (5.8) and assuming a design factor $\zeta = 0.7$. This result accommodates most conventional mission requirements.[1]

Table 5.3 presents the SAR performance for the individual spacecraft and the complete system after reconstruction. The azimuth ambiguity improvement from 2.8 dB to less than -20.0 dB indicates successful azimuth reconstruction. Note that the distributed system enabled SAR imaging with small apertures, which would be unattainable with the individual platforms in this specific system due to the high azimuth ambiguities.

[1] For reference, the Canadian RADARSAT constellation mission was designed with an average 15 minutes of imaging time per orbit per satellite, with peak imaging of 25 minutes per orbit per satellite outside the eclipse season, resulting in orbit duty cycles between 10% and 25% [153].

Imaging performance in monostatic mode	
Azimuth Ambiguity-to-Signal Ratio (AASR)	<2.8 dB
Range Ambiguity-to-Signal Ratio (RASR)	<-20.0 dB
Swath width	53 km
Imaging performance in multistatic mode	
2-D Single Look Image Resolution	4 m^2
Noise Equivalent Sigma Nought (NESN)	<-20.0 dB
Azimuth Ambiguity-to-Signal Ratio (AASR)	<-20.0 dB
Range Ambiguity-to-Signal Ratio (RASR)	<-20.0 dB
Swath width	53 km

Table 5.3: Along-track reconstruction performance for a 9-cm along-track positioning error (3σ) based on 1000 Monte Carlo realizations. The high AASR value in monostatic mode is a consequence of the short azimuth antenna length and PRF optimized for achieving a RASR better than -20 dB. In this case, 5 satellites are assumed to be operated in the multistatic mode.

The system achieves a 2-D single-look resolution of 4 m^2, while maintaining a NESN better than -20 dB across a 53-km swath. This performance is enabled by an average transmit power of 1.17 kW. The high required power is consistent with the high resolution. Further improvements in resolution are contingent upon the capabilities of the SAR electronics and platform subsystems—such as power amplifiers, solar panels, and energy storage systems—to support higher peak and average transmit power levels.

5.5.2 Cross-Track Formation Design

Table 5.4 shows the nominal system parameters for the cross-track formation example. In this case, the distributed arrays are designed to form a continuous array in the ZD plane when projected on the aperture plane, as illustrated in Figure 5.4. The cross-track formation is evaluated based on performance models for an optimal beamformer, as outlined in [154].

Table 5.5 shows the achievable performance using cross-track beamforming for range ambiguity suppression. The system was designed to maintain the same 2-D resolution and swath width as the along-track example shown in the previous section. The distributed system with five satellites achieves a RASR better than -20.0 dB, a substantial improvement compared to the 7.8 dB ratio of the individual satellites. The system achieves a 2-D single-look resolution of 4 m^2 with a NESN better than 20 dB, enabled by

an average transmit power of 1.9 kW. This performance indicates the ability of the cross-track multistatic concept to enable image reconstruction with systems whose antenna dimensions are too small to allow for sufficient ambiguity suppression over the desired swath.

System parameters	
Number of satellites	5
Wavelength	3.11 cm
Antenna look angle	27.8°
Acquisition mode	Stripmap
Antenna length	1.3 m
Antenna height	0.4 m
Pulse Repetition Frequency (PRF)	12.8 kHz
Processed azimuth bandwidth	10.3 kHz
Average power	1.9 kW
Noise figure	3 dB
Total losses	1.5 dB
Range bandwidth	53.0 MHz
First input coverage latitude range	10° to 82°
Second input coverage latitude range	-10° to -82°

Table 5.4: System parameters of the multistatic system example employing beamforming in elevation for range-ambiguity suppression.

The subsections below present the coverage figures for two test cases: one optimized for a single coverage region and the other optimized for two coverage regions separated by 180° in argument of latitude.

Case I - One Latitude Coverage Region

Figures 5.12 and 5.13 show the resulting optimal trajectories for one coverage regions, and the corresponding coverage range, respectively. The results show that the optimizer finds a solution in which the Earth rotation has an asymmetric effect on the trajectory, flattening one of the sides of the formation so that it describes an approximately straight line orthogonal to the array direction for the range of arguments of perigee of interest.

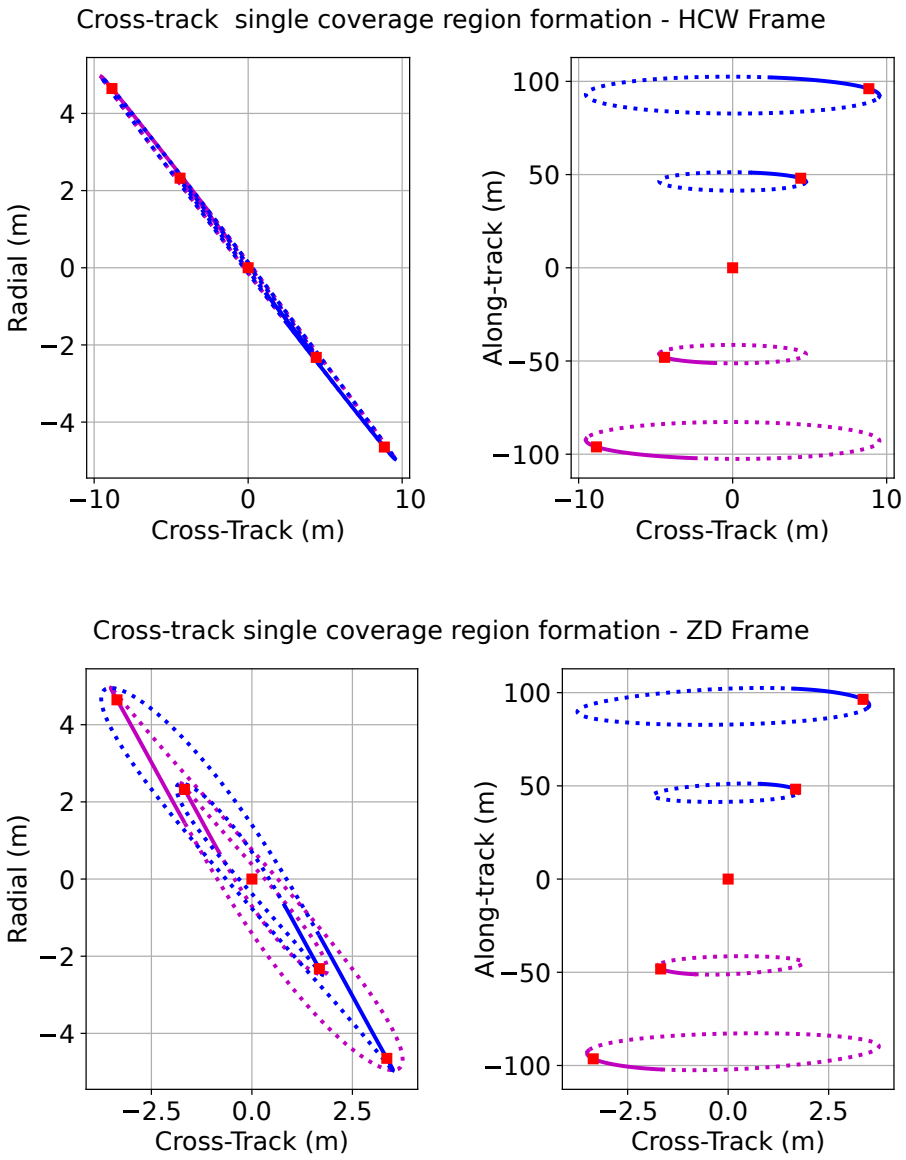

Figure 5.12: Designed trajectories in ZD frame and HCW frame for cross-track beamforming with single coverage region. The active imaging region is highlighted with solid lines. The red boxes exemplify the position of the satellites at one common instant. Trajectories behind and ahead of the chief in along-track are represented in magenta and blue, respectively.

Imaging performance in monostatic mode	
Azimuth Ambiguity-to-Signal Ratio (AASR)	<-20.0 dB
Range Ambiguity-to-Signal Ratio (RASR)	<7.8 dB
Swath width	53 km
Imaging performance in multistatic mode	
2-D Single Look Image Resolution	4 m^2
Noise Equivalent Sigma Nought (NESN)	<-20.0 dB
Azimuth Ambiguity-to-Signal Ratio (AASR)	<-20.0 dB
Range Ambiguity-to-Signal Ratio (RASR)	<-20.0 dB
Swath width	53 km

Table 5.5: Cross-track beamforming performance for a 9-cm (3σ) positioning error with respect to the nominal projected array, based on 1000 Monte Carlo realizations. The high RASR value in monostatic mode is due to the short antenna length in elevation and the PRF optimized for achieving AASR better than -20 dB. In this case, 5 satellites are assumed to be operated in a multistatic mode.

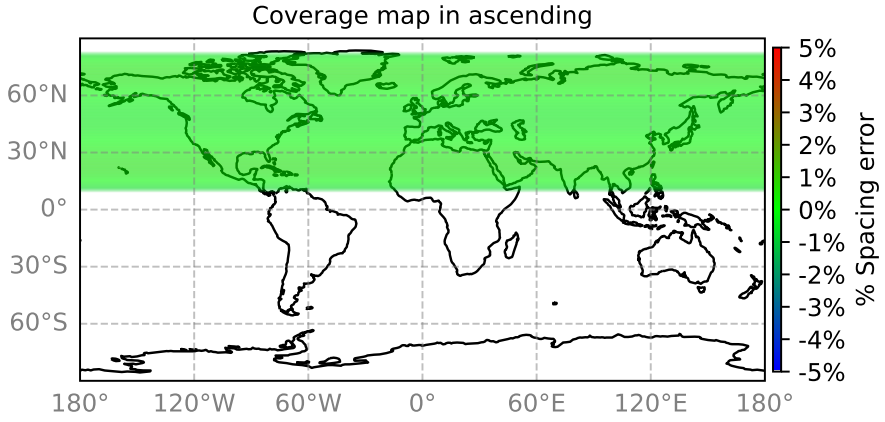

Figure 5.13: Coverage of beamforming in cross-track with a single coverage region in ascending pass. The color code expresses the percentage error of the baselines projected on the direction orthogonal to the aperture plane.

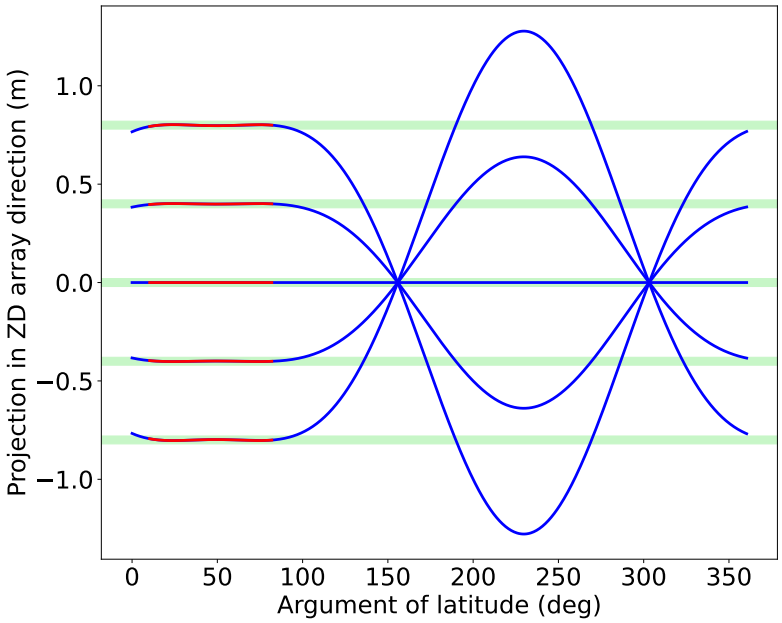

Figure 5.14: Array projection orthogonal to the aperture plane in the cross-track multistatic concept with a single coverage region. The regions within ±5% around the nominal positions are highlighted in green. The positions within the input range of arguments of latitude are plotted in red.

Figure 5.14 shows the projected position of the satellites. The figure highlights the position ranges within tolerances of ±5% of the nominal antenna length in green. It shows that almost perfectly uniform arrays can be obtained, with deviations from the nominal array position of less than 1.5%, for a broad range of latitudes covering nearly the entirety of the northern hemisphere. This uniform distribution is strictly maintained, even though the satellites move with respect to each other in the along-track as well as in the direction orthogonal to the aperture plane.

Since a continuous range of argument of latitude must be selected, restricting this range to ascending or descending passes ensures that the formation, when in a suitable configuration (i.e., during the SAR operation), accesses the maximum area on the globe. Alternatively, the formation could cover higher or lower latitudes in both ascending and descending passes, which would reduce the total coverage area by half but improve the revisit time for those specific regions by the same factor.

This configuration results in parallel ground tracks with constant cross-track displacements for long stretches of the orbit, which is thought of as impossible with natural orbits if one assumes the classic formation flying theory described in the HCW frame to be directly applicable to formation flying applications for SAR.

Compared to a hypothetical forced formation that maintains cross-track alignment by continuously counteracting differential gravity over the orbit, the main drawback of the solution presented here is that repeat passes over the same region take approximately twice as long. This occurs because the descending portion of the orbit leads to an unfavorable formation geometry. However, the approach offers the significant advantage of avoiding the prohibitive fuel consumption required for continuous thrust, making it not only feasible in practice but also a strong solution in terms of positioning conformance and coverage. Relative to using a single satellite with a large antenna or a monostatic multichannel system, it provides greater flexibility and enables comparable performance with smaller spacecraft. Furthermore, the coverage region can be extended into the descending node by widening the input range of arguments of latitude, though this increases the array spacing error.

Finally, note that for both the along-track and cross-track formations presented in this chapter, reconfiguring the formation to switch coverage regions is expected to require sufficiently low delta-V to be performed regularly (e.g., on a monthly basis). This strategy could therefore enable global coverage while maintaining the high positioning conformance provided by these formations.

Case II - Two Latitude Coverage Regions

Figures 5.15, 5.16, and 5.17 show the resulting optimal trajectories for two coverage regions, the cross-track baselines along with the adjusted tilt angle, and the corresponding coverage ranges, respectively. In this case, attitude steering is used to compensate for the low conformance to the nominal array, as illustrated in Figure 5.9. The transmitter steering variation is limited to $\pm 5°$. The coverage region and duty cycle greatly expand, but the array conformity to the nominal significantly degrades. This is, nevertheless an attractive configuration in case the transmitter can be steered. However, this would likely not be the case if this is intended as a cluster of passive companion satellites.

Figure 5.18 shows the effect of the attitude maneuvering tolerance on the orbit duty cycle. The red line represents the coverage over the full latitude range of interest used as input for the optimization. The coverage improves significantly when allowing for attitude maneuverability up to around $\pm 3°$. Beyond this threshold, the improvement becomes more gradual, approaching the maximum slowly.

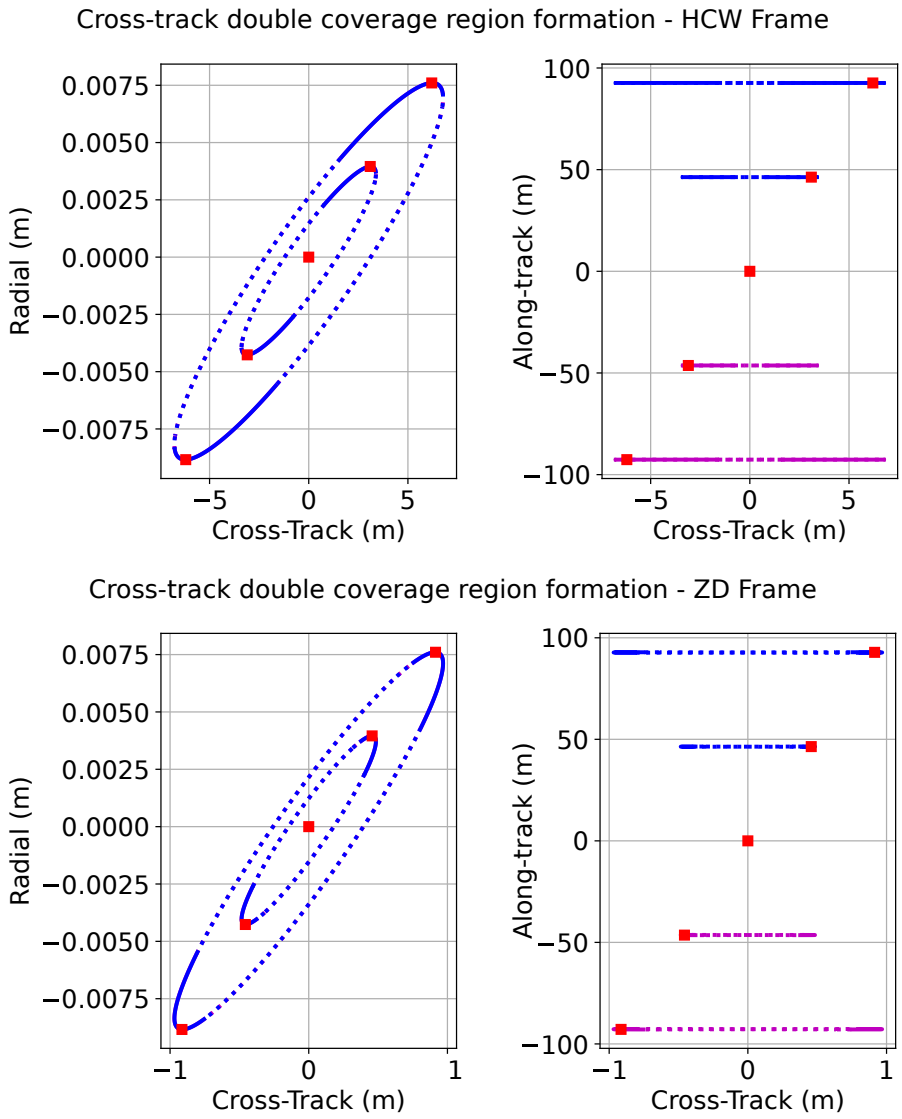

Figure 5.15: Designed trajectories in ZD and HCW frames for cross-track beamforming with two coverage regions. The active imaging region is highlighted with solid lines. The red boxes exemplify the position of the satellites at one common instant. Trajectories behind and ahead of the chief in along-track are represented in magenta and blue, respectively.

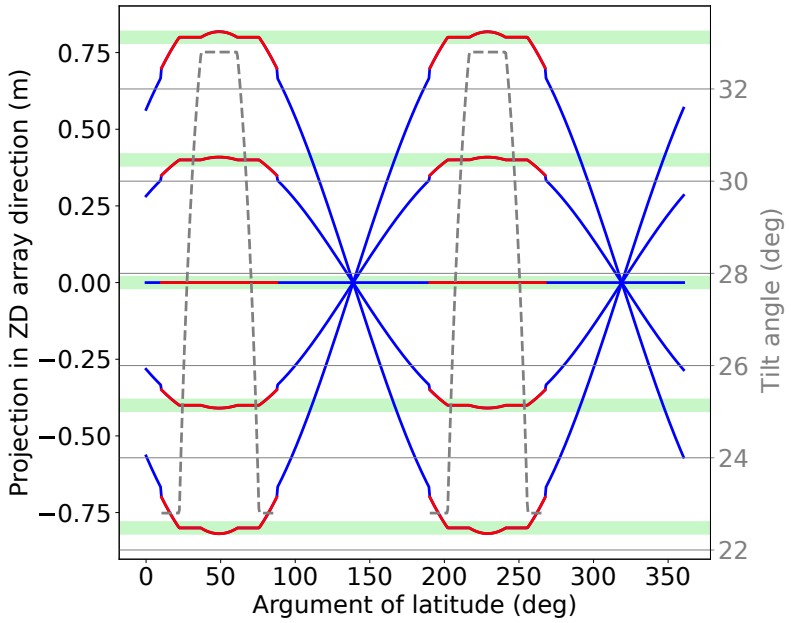

Figure 5.16: Array projection orthogonal to the aperture plane in the cross-track concept with two coverage regions. The regions within ±5% around the nominal positions are highlighted in green. The positions within the input range of arguments of latitude are plotted in red.

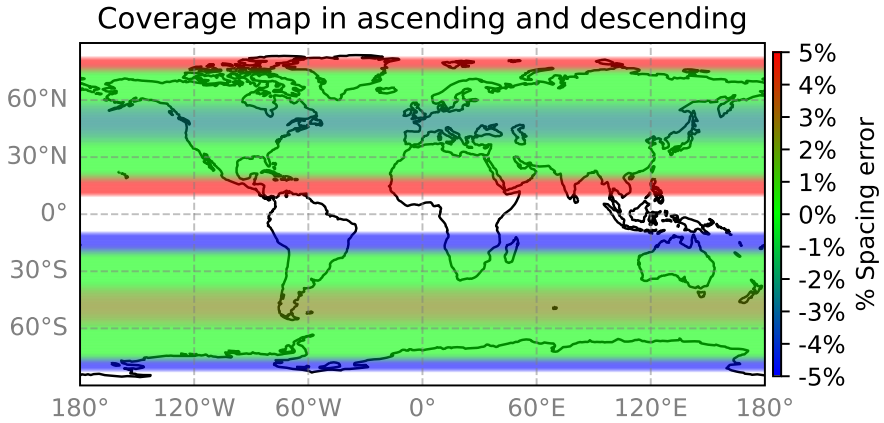

Figure 5.17: Coverage of beamforming in cross-track with two coverage regions in ascending pass in the northern hemisphere and descending in the southern hemisphere. The color code expresses the percentage error of the baselines projected on the direction orthogonal to the aperture plane.

5.5.3 Distributed Sounder

This section presents briefly an example of applying the solution to uniformly distributed arrays in cross-track for radar sounding. In this case, the analysis is limited to the geometric aspects only. The example is based on the work developed for radar sounders in [149] and [155], which propose a

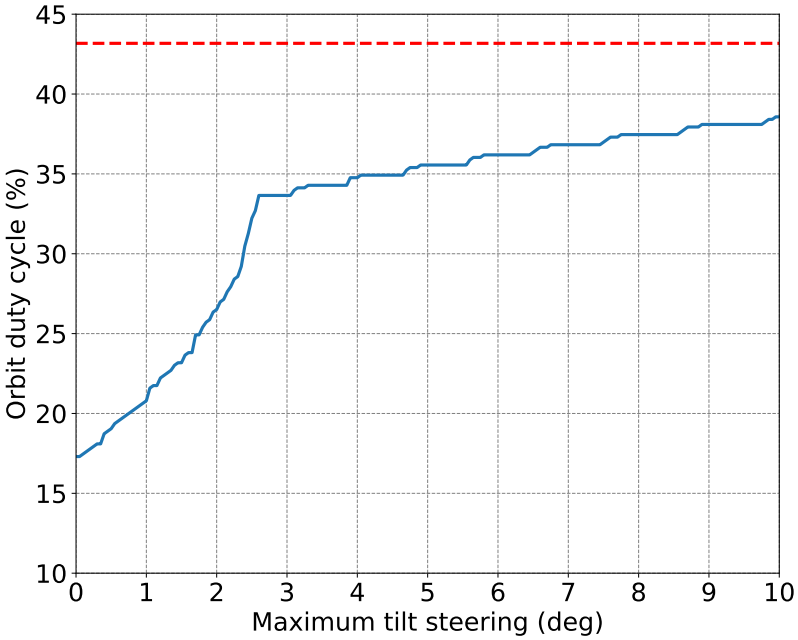

Figure 5.18: Orbit duty cycle of the cross-track multistatic concept with two coverage regions, considering a valid array as having below 5% spacing error, as a function of the maximum allowed tilt steering. The red line indicates the coverage corresponding to the full range of latitudes of interest used as input.

cross-track formation flying system and a system of tethered satellites, respectively. The range of latitudes of interest covers the desert area in North Africa to almost the entirety of the North Pole, which are regions of particular interest for radar sounding. The system parameters are shown in Table 5.6.

System parameters	
Cross-track distance between satellites	33.4 m
Orbital height	500 km
Number of satellites	21
Wavelength	6.66 m
Cross-track resolution	4561.7 m
Bandwidth	10 MHz
Antenna look angle	0° (nadir)
Input coverage latitude range	10° to 82°

Table 5.6: Radar sounder example parameters, reproduced from [155].

The designed formation and array conformance results are shown in Figures 5.19 and 5.20, respectively. The array conformity is excellent across the whole range of latitudes. This formation has the additional advantage of having a separation in the cross-track and radial directions, which adds passive collision safety. Its main limitation, however, is the large along-track separations, which, in distributed radar sounders, can degrade performance due to grating lobes in the synthesized antenna radiation pattern folding within the scene [155]. This deviation could be potentially minimized by offsetting the mean along-track positions to minimize their displacement around the imaging region. The proposed formation offers an almost ideal cross-track separation, but its viability and applicability limits in terms of imaging performance must be further investigated.

5.6 Final Remarks and Conclusions

This chapter presented a novel general algorithm for fitting natural formations of distributed multistatic SAR configurations into arbitrary trajectories in the SAR-appropriate Earth-fixed geometry for limited ranges of argument of latitude. The algorithm was applied to realize baselines for azimuth reconstruction and beamforming in elevation, resulting in formation configurations that achieve high conformance with the required baseline distribution for ranges of latitude as high as 70° and orbit duty cycles above 20%.

This chapter showed that cross-track displacements caused by offsets in the mean argument of latitude can be largely compensated by adjusting the longitude of the ascending node between formation elements, which substantially simplifies along-track reconstruction by reducing sensitivity to topography. For cross-track constellations, it was demonstrated that allowing relative motion in the along-track and line-of-sight directions, while restricting coverage to a portion of the orbit (e.g., 20%), enables the formation of near-uniform arrays with cross-track baseline errors below 1.5%. If the transmitter satellite can adjust its look angle accordingly, the coverage can be extended to two regions separated by 180° in longitude of the ascending node, while still maintaining acceptable conformity to the nominal cross-track displacement. In radar sounder applications, uniform cross-track nadir pointing can be sustained over long orbital arcs, though this comes at the expense of larger along-track and radial separations.

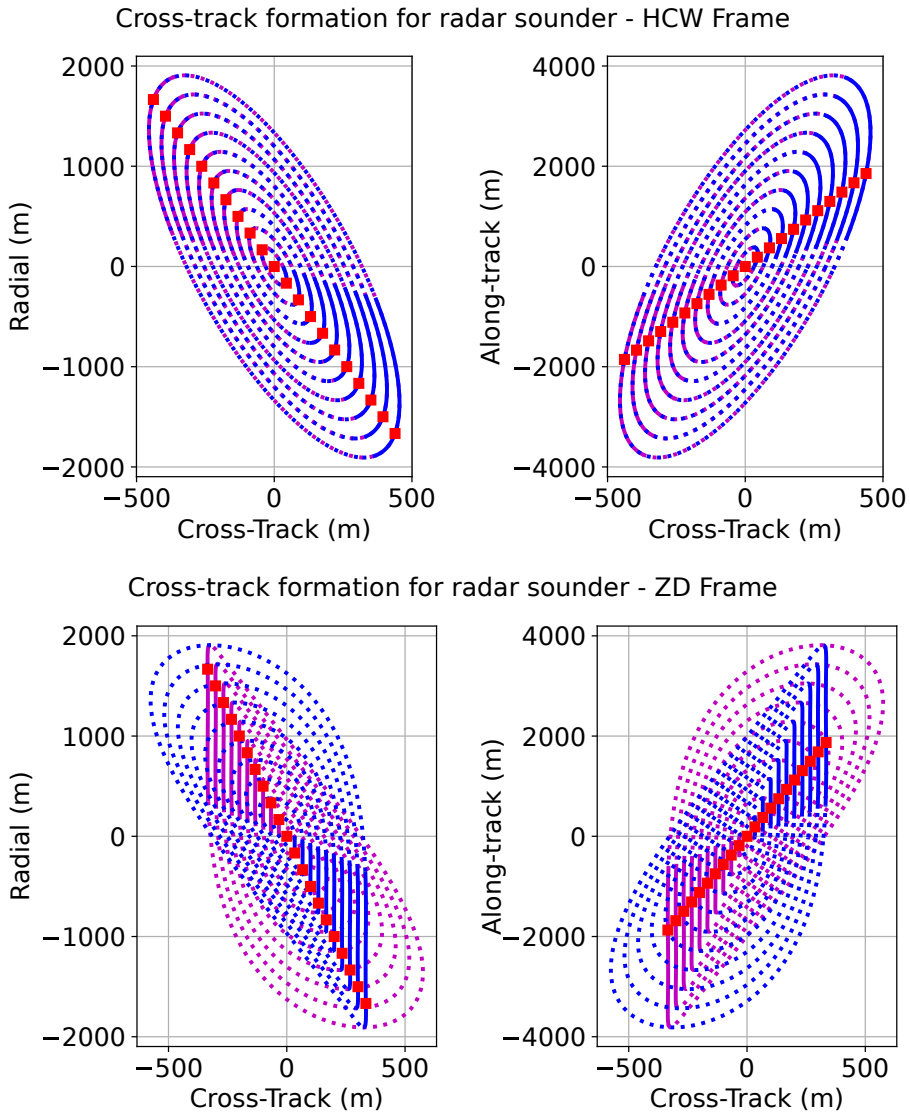

Figure 5.19: Designed trajectories for the radar sounder example. The active imaging region is highlighted with solid lines. The red boxes exemplify the position of the satellites at one common instant. Trajectories behind and ahead of the chief in along-track are represented in magenta and blue, respectively.

The algorithm presented here can be easily generalized to other sets of linear positioning requirements in the ZD plane, making it potentially applicable for formation design and optimization in other contexts, such as interferometry and tomography. While the focus is on non-squinted geometries, the approach could also be extended to squinted geometries. Furthermore, the formation geometries discussed could be incorporated into systems comprising multiple satellites distributed both in along-track and in cross-track.

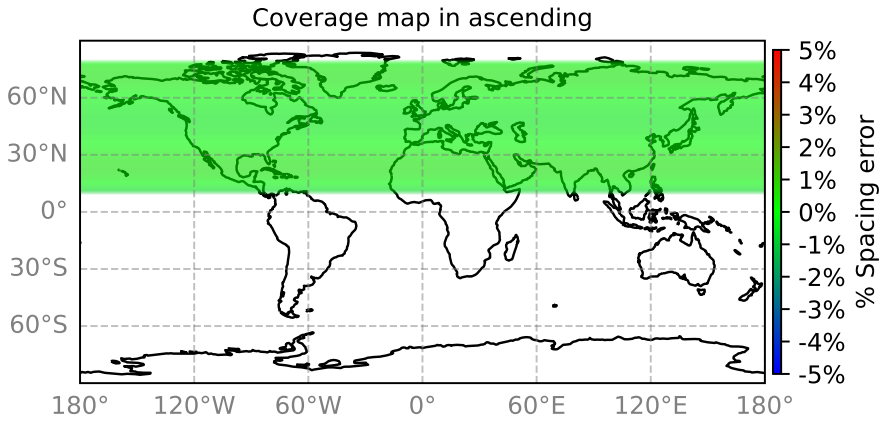

Figure 5.20: Coverage of the cross-track concept for radar sounder in ascending pass. The color code expresses the percentage error of the baselines projected on the direction orthogonal to nadir.

The results presented reveal new formation configurations for SAR imaging concepts using small distributed satellites with precise sub-meter positioning requirements, suitable for high-resolution, wide-swath imaging. This is a significant step towards enabling systems with distributed antennas across different platforms, achieving high-resolution performance and ambiguity suppression using platforms where this would otherwise be impossible due to their small size. Additionally, it opens up possibilities for companion missions using very small passive platforms, such as CubeSats, to enhance the performance of existing small to large-sized platforms.

It should be noted that the scope of this chapter is limited to near-circular Keplerian orbits, which provide a simple model and a reasonable approximation for satellite relative motion in realistic SAR missions in low Earth orbits. Further analysis is required to evaluate the effects of external disturbances, fuel consumption, and the navigation accuracy needed to achieve the sub-meter relative control required for the beamforming concepts analyzed here. These practical considerations are addressed in Chapter 6.

6 Generalized Formation Optimization and Optimal Guidance

6.1 Introduction

The previous chapter demonstrated the general applicability of natural formations for distributed radar systems using a simplified model that captured most of the relative dynamics while allowing for a straightforward analytical description. This chapter generalizes and expands the optimization algorithms presented in Chapter 5 to include: (i) any linear dynamic model for formation flying, which will enable the use of more accurate relative motion descriptions; (ii) thruster actuation, which will expand the formation possibilities to allow local corrections to improve positioning results. Additionally, this chapter introduces a new method to calculate an optimal guidance strategy for natural formations that includes an arbitrarily detailed dynamic model. The model is iterative and incorporates a high-fidelity propagator in the loop. The optimal guidance will make it possible to implement high-precision formation flying control sustainable at low delta-V cost. The chapter concludes with a realistic simulation of constant centimeter-accuracy formation control using the proposed optimal guidance strategy, demonstrating the feasibility of sustained high-precision formation flying—i.e., maintained for long periods, ranging from months to years, on a regular basis—for multistatic SAR applications with low fuel consumption.

The chapter is organized as follows. Section 6.2 introduces generalized formation optimization methods for both natural and unnatural formations, with a focus on distributed SAR imaging concepts. Section 6.3 demonstrates an application of the general algorithm by expanding the coverage range of argument of latitude for cross-track formations while improving positioning performance through active actuation. Building on these foundations, Section 6.4 introduces a fuel-optimal guidance algorithm that accounts for higher gravitational harmonics and small eccentricity in the reference orbit. System examples and simulation results are provided in Section 6.5, illustrating the effectiveness of the described methods. Finally, Section 6.6 concludes the chapter with a summary of key findings.

6.2 Generalized Formation Optimization

This section introduces a generalized version of the optimization algorithm originally presented in Chapter 5. The proposed method leverages the fact that the relative dynamics of satellite motion can be accurately modeled as linear with respect to the relative state variables, even when accounting for orbital perturbations such as Earth's higher-order gravitational harmonics [89]. This linearity enables the formulation of the trajectory planning of the deputy satellite as a convex optimization problem, where the dynamic model is enforced as a constraint, implicitly linking future states to the initial condition.

This formulation provides greater flexibility compared with purely analytical approaches, allowing the inclusion of active control strategies and additional constraints, such as the maximum allowable displacements along each axis. This flexibility makes the algorithm well-suited for practical implementation.

The generalized formation optimization problem for repeating formations consists of determining the initial relative state $\delta\vec{X}_0$ and a sequence of control inputs $\Delta\vec{v}_k$ that minimize a cost function $\mathcal{J}$, while meeting all mission constraints. The objective function typically accounts for both positioning errors and delta-V consumption. Among the constraints, the optimization must enforce the condition that the initial and final states are identical to ensure formation repeatability.

This strategy is similar to that of a Model Predictive Control (MPC) framework [156], with the key difference that in the proposed approach the initial relative state is also an optimization parameter. Another important difference compared to MPCs used in formation flying is that in the context of multistatic SAR missions, the positioning requirements are specified in an Earth-fixed formation geometry, as discussed in Chapter 5.

6.2.1 Dynamic Model and Other Constraints

The most fundamental constraint in satellite formation flying arises from the underlying dynamic model. As introduced in Section 2.4, the state of each deputy satellite in the HCW frame, denoted by $\delta\vec{X}_k$, is defined as

$$\delta\vec{X}_k = \begin{bmatrix} \vec{\rho}_{\text{hcw}}(t_k) \\ \dot{\vec{\rho}}_{\text{hcw}}(t_k) \end{bmatrix}. \tag{6.1}$$

In this formulation, the system is parameterized using Cartesian relative positions and velocities in the HCW frame. Rather than optimizing over a set of ROEs, the algorithm directly searches for the optimal sequence of states $\delta\vec{X}_k$ and active impulsive velocity changes, represented by the control input vector $\Delta\vec{v}_k$.

Although the equations can be expressed in terms of the argument of latitude (u), as in Chapter 5, it is more convenient to use time as the independent variable when applying general solutions of the relative dynamics, because linear models of satellite motion are typically formulated in terms of time.

The orbital period $t \in [0, T]$ is discretized into n_t time steps. The set of discrete time indices is denoted by $\mathcal{P} = \{0, 1, \ldots, n_\mathrm{t} - 1\}$. Each sample time is represented by t_k, with $k \in \mathcal{P}$. A subset $\mathcal{A} \subseteq \mathcal{P}$ identifies the time indices at which control inputs (i.e., delta-V maneuvers) are applied. This subset enables precise scheduling of maneuvers and can be used to enforce control sparsity, manage fuel consumption, or balance accuracy and efficiency.

The state at each time step is determined by the initial conditions, the relative dynamics (which are functions of the chief satellite's orbit), and the applied control inputs. Denoting the state transition matrix between time steps t_k and t_{k+1} as $\Phi(t_k, t_{k+1})$, the dynamic model is enforced through the following constraints

$$\begin{cases} \delta\vec{X}_{k+1} = \Phi(t_k, t_{k+1}) \cdot \delta\vec{X}_k, & t_k \notin \mathcal{A} \\ \delta\vec{X}_{k+1} = \Phi(t_k, t_{k+1}) \cdot \delta\vec{X}_k + B \cdot \Delta\vec{v}_k, & t_k \in \mathcal{A} \end{cases}, \tag{6.2}$$

where $\Delta\vec{v}_k$ is the control input, and B is the control input matrix. The set $\mathcal{A}$ typically corresponds to a time window $[t_{\mathrm{a_i}}, t_{\mathrm{a_f}}] \subseteq [0, T]$ within which actuation is allowed.

The state transition matrix Φ provides a step-wise propagation of the relative motion equations. Multiple models for Φ exist, ranging from the classical HCW equations to more refined models incorporating perturbations such as J2, or the effects of the orbital eccentricity [67]. These models may also use averaged dynamics to filter out short-period variations. The choice of model depends on application requirements, such as the need for real-time computation or high-precision tracking.

To achieve high-accuracy positioning, both short-period disturbances and long-term effects (periodic and secular) should be considered in the relative motion model. Rather than developing or employing a direct analytical formulation of the linear dynamics that includes these effects, an alternative

approach is presented in Section 6.4. In this approach, a simplified Keplerian model is first used to generate an initial estimate, which is then refined through iterative corrections using a high-fidelity propagator. This hybrid method compensates effectively for deviations from the simplified dynamics. In the case of a simple model based on the HCW equations, the state transition matrix can be approximated by (2.44).

In addition to ensuring physical consistency via the dynamic model, another critical constraint is formation repeatability, i.e., the equivalence between the initial and final relative states. This ensures that the formation does not drift due to differences in semi-major axes, and that secular effects are corrected optimally. The repeatability constraint is given by

$$\delta\vec{X}_0 = \delta\vec{X}_{n_t-1}\,. \tag{6.3}$$

As discussed in Section 5.4.1, mean along-track separation can be adjusted to accommodate specific requirements, such as time margin for autonomous collision avoidance or the reduction of plume impingement effects. When using ROE-based parameterization, this is achieved by fixing δl. Assuming circular chief orbits and $\delta a = 0$, this condition can be expressed in the HCW frame as

$$y_0 - \frac{2 \cdot \dot{x}_0}{n} = a \cdot \Delta l\,, \tag{6.4}$$

where Δl is the desired mean longitude separation between satellites, a is the nominal mean semi-major axis, y_0 is the initial y component of the initial position in the HCW frame, and $\dot{x}_0$ is the x component of the velocity in the HCW frame.

Additional constraints can be introduced, provided they preserve the problem's convexity. This flexibility is a major advantage compared to the analytical approach presented in the previous chapter, as it makes the optimization algorithm capable of accommodating various mission constraints. For example, some possible relevant constraints are the maximum along-track displacement or the maximum delta-V, i.e.,

$$y_k \leq y_{\max}\,, \tag{6.5}$$

$$|\Delta v_{x_k}|, |\Delta v_{y_k}|, |\Delta v_{z_k}| \leq \Delta v_{\max}\,, \tag{6.6}$$

where y_k is the cross-track position component, and Δv_{x_k}, Δv_{y_k}, and Δv_{z_k} are the thrust vector components at time t_k, expressed in the HCW frame.

6.2.2 General Cost Function

Before defining the cost function, a subset $\mathcal{I} \subseteq \mathcal{P}$ is introduced to represent the time indices k for which the argument of latitude u_k corresponds to the regions of interest. Formation performance is optimized over this subset $\mathcal{I}$, ensuring that the desired geometric configuration is achieved during imaging. The general cost function is defined as

$$\begin{aligned}\mathcal{J}(\delta\vec{X}_0, \{\vec{u}_k\}_{k\in\mathcal{A}}) = &\sum_{k\in\mathcal{I}} \left(\mathrm{T}_k \cdot \vec{\rho}_{\mathrm{hcw}}(t_k) - \vec{\mathrm{Y}}_k\right)^T \cdot \mathrm{W} \cdot \left(\mathrm{T}_k \cdot \vec{\rho}_{\mathrm{hcw}}(t_k) - \vec{\mathrm{Y}}_k\right) \\ &+ \alpha_v \cdot \sum_{k\in\mathcal{A}} \left(|\Delta v_{x_k}| + |\Delta v_{y_k}| + |\Delta v_{z_k}|\right), \end{aligned} \tag{6.7}$$

where W is a weighting matrix which allows for assigning different weights to components and time steps, T_k and $\vec{\mathrm{Y}}_k$ are arbitrary matrices, respectively, which are not a function of the relative state, and α_v is a weight for the delta-V consumption cost. For the case of multistatic SAR, the positioning requirements are expressed in the ZD frame, and the transformation matrix $T_{\mathrm{hcw}\to\mathrm{zd}}$ must be included in the matrix T_k.

Alternatively, for circular chief orbits, the cost function may be expressed in terms of the ROEs as follows [72]

$$\delta\vec{X}_0 = \begin{bmatrix} 1 & 0 & -a\cdot\mathrm{c}(nt_0) & -a\cdot\mathrm{s}(nt_0) & 0 & 0 \\ 0 & 1 & 2a\cdot\mathrm{s}(nt_0) & -2a\cdot\mathrm{c}(nt_0) & 0 & 0 \\ 0 & 0 & 0 & 0 & a\cdot\mathrm{s}(nt_0) & -a\cdot\mathrm{c}(nt_0) \\ 0 & 0 & na\cdot\mathrm{s}(nt_0) & -na\cdot\mathrm{c}(nt_0) & 0 & 0 \\ -3n/2 & 0 & 2na\cdot\mathrm{c}(nt_0) & 2na\cdot\mathrm{s}(nt_0) & 0 & 0 \\ 0 & 0 & 0 & 0 & na\cdot\mathrm{c}(nt_0) & na\cdot\mathrm{s}(nt_0) \end{bmatrix} \cdot \delta\vec{\alpha}_0 . \tag{6.8}$$

The cost function consists of a convex quadratic term and the ℓ_1-norm (i.e., absolute value) of the control inputs. Although the ℓ_1-norm is non-differentiable at zero, it is still a convex function [157]. The system dynamics are represented by linear equality constraints, which define an affine, and therefore convex, feasible set. Assuming all additional constraints are also convex, the overall problem is a convex optimization problem, ensuring that any local minimum is also a global minimum.

The optimization framework is general and can be applied to any relative positioning objectives that can be expressed as a linear system of equations with respect to the relative position. Notably, the formulation imposes no requirement for the positioning constraints to be time-invariant, allowing for any input shape in the ZD frame.

In cases where a closed-form solution is not available (e.g., the simple closed least-squares fitting presented in the last chapter), a numerical solver is required to obtain the optimal solution. In the examples provided in this thesis, the CVXPY library [158] was employed, with the Embedded Conic Solver (ECOS) used for all numerical searches. This solver converged reliably within a few seconds across all test cases considered.

Finally, it's worth mentioning that passive collision safety and plume impingement avoidance could also be included in the optimization framework. These constraints are important for broadening the applicability of the proposed methods beyond the tight formations on which this work is primarily focused. Their inclusion has been explored in [159] within the context of trajectory planning, where they are implemented using Mixed-Integer Linear Programming (MILP), a formulation that also guarantees a global minimum upon convergence.

An implementation of the passive safety condition could be important to make the method applicable to optimize, for example, formations such as the helix-orbits used for interferometry, possibly including in the optimization formation maintenance cost. Although the plume impingement issue could be mitigated through along-track separation, it could become important in case the used propulsion system could cause surface degradation to the neighboring satellites. These possibilities highlight the versatility of the proposed approach, which can draw on widely available literature in motion planning for formation flying. The inclusion of these constraints will be explored in future works.

6.2.3 From General to Analytical Optimization Models

This subsection establishes the connection between the general optimization model and the specific algorithms introduced in the previous chapter. The aim is to bridge the two formulations and highlight the generality of the framework developed in this chapter.

Along-Track Reconstruction

The target geometry is defined in (6.7) through the matrix T_k and vector Y_k. As mentioned previously, the transformation from the HCW to the ZD frame is included in T_k. For the AT reconstruction case, these are given by

$$Y_k = \vec{\rho}_{\mathrm{zd}}\,, \tag{6.9}$$

and

$$\mathrm{T}_k = \mathrm{T}_{\mathrm{hcw}\to\mathrm{zd}}\,. \tag{6.10}$$

The repeatability constraint in (6.3) is also applied to ensure consistency in the relative positioning performance over time.

The closed-form solution for the Keplerian case presented in Section 5.4 can be obtained by adopting the HCW model as the dynamic framework, transforming the initial state X_0—an optimization argument of the cost function $\mathcal{J}$—from Cartesian coordinates in the HCW frame to ROEs, and assuming no actuation (i.e., $\mathcal{A} = \emptyset$). The inclusion of the repeatability constraint removes one degree of freedom from the optimization problem, resulting in five remaining optimization variables: the relative mean longitude (δl), the components of the relative eccentricity vector $(\delta e_x, \delta e_y)$, and the components of the relative inclination vector $(\delta i_x, \delta i_y)$.

Cross-Track Beamforming

For the cross-track beamforming case, the following equations apply

$$\mathrm{Y}_k = r_{\mathrm{zd}}\,, \tag{6.11}$$

and

$$\mathrm{T}_k = \hat{i}_{\mathrm{arr}}^T \cdot \mathrm{T}_{\mathrm{hcw}\to\mathrm{zd}}\,. \tag{6.12}$$

where $\hat{i}_{\mathrm{arr}}$ is the nominal array direction, as defined in (5.11). In this case, in addition to the repeatability constraint in (6.3), the mean δl offset constraint in (6.4) is enforced to ensure an adjustable along-track separation.

Similarly, the closed-form solution for the Keplerian case presented in Section 5.4 is derived by adopting the HCW model as the dynamic basis and expressing the cost function $\mathcal{J}$ in terms of the ROEs, under the assumption of no actuation. The two constraints eliminate two degrees of freedom from the optimization problem, leaving four independent optimization variables: the components of the relative eccentricity vector $(\delta e_x, \delta e_y)$, and the components of the relative inclination vector $(\delta i_x, \delta i_y)$.

6.3 Quasi-Natural Cross-Track Formation System Example

This section presents results for an example application of the generalized method in which actuation is permitted to enhance coverage and positioning performance in the cross-track configuration, in contrast with the purely natural solutions shown in Chapter 5. The solution is referred to as *quasi-natural*, because the applied thrusts induce only small deviations from a natural trajectory—unlike a fully forced solution, which would override the natural dynamics to meet the relative positioning objectives.

To account only for the delta-V associated with forced motion and ensure direct comparability with the results from Chapter 5, the State Transition Matrix (STM) corresponding to the HCW equations is used. In this example, small thrusts are applied to generate an optimal cross-track formation over a large portion of the orbit, covering nearly the entire Northern Hemisphere during both ascending and descending passes.

System parameters	
Number of satellites	5
Antenna look angle	27.8°
Antenna height	0.4 m
u range of region of interest	10° to 170°
Time step and thrust frequency	15 s
Chief's orbital parameters	
Altitude	580 km
Eccentricity	0
Inclination	97.7°
RAAN	0°

Table 6.1: Orbital and system parameters of the chief satellite used for the *quasi-natural* formation example.

The simulation and optimization parameters are summarized in Table 6.1. They match those used in the cross-track example from Section 5.5.2, except for the input latitude range, which is doubled. For completeness, they are repeated here, along with the chief satellite's orbital parameters.

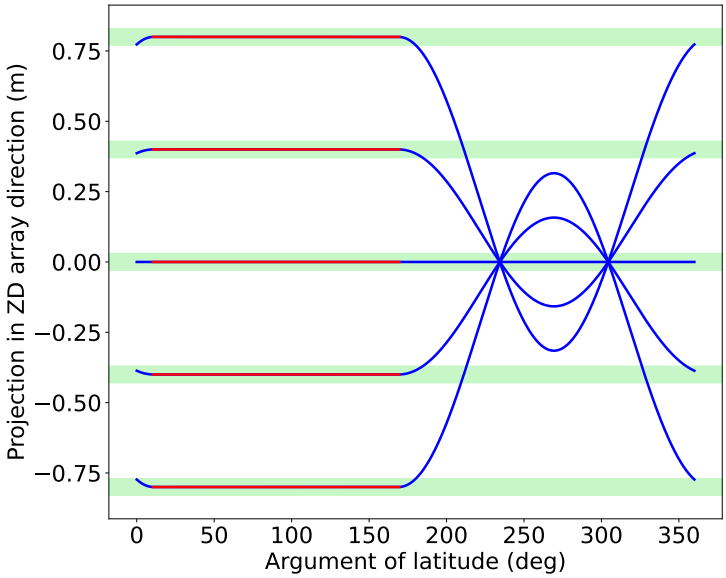

Figure 6.1: Array projection orthogonal to the aperture plane in the cross-track formation concept with a single coverage region and actuation. The regions within ±5% around the nominal positions are highlighted in green. The positions within the input range of arguments of latitude are plotted in red.

The corresponding array projections, compared to the beamforming requirements, are shown in Figure 6.1, while the optimized trajectories in the HCW and ZD frames are shown in Figure 6.2.

The figures show a practically perfect conformance with the nominal relative positioning objectives for the complete input range of arguments of latitude, i.e. from 10° to 170°. Compared with the natural case presented in Section 5.5.2, the revisit time for any specific area within the target region is roughly halved, as the relative geometry meets the requirements during both ascending and descending passes.

The main drawback in this case is the increased fuel consumption. Figure 6.3 presents the delta-V required to achieve the quasi-natural trajectories shown in Figure 6.2, including the components along each axis and the total consumption for formation maintenance. In the figure, the satellites are labeled from S0 to S4 according to their along-track positions, starting with the satellite furthest behind, i.e., with the most negative along-track position, assigned index 0. The chief satellite is labeled with index 2 and is not shown in the figure because it consumes no fuel for formation maintenance.

In the worst cases, the total formation maintenance delta-V consumption reaches approximately 13 m/s per year, which remains compatible with the delta-V budgets of small commercial platforms up to 50 kg, which could potentially accommodate as much as 100 m/s total [160]. Significant

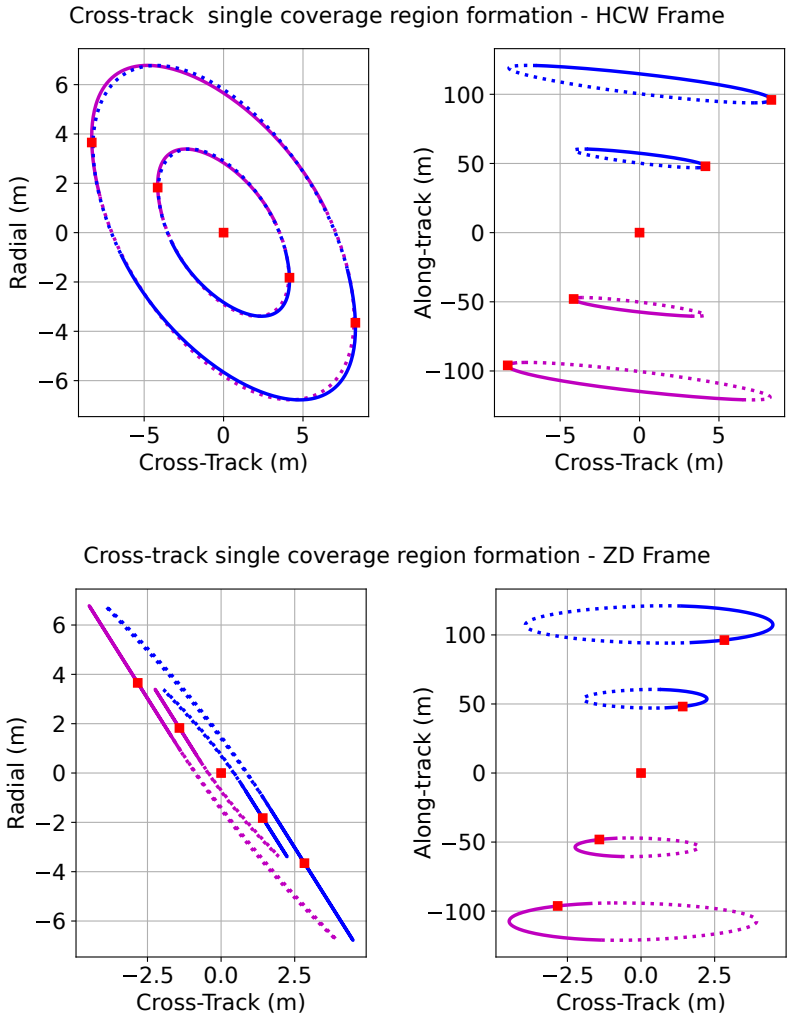

Figure 6.2: Designed quasi-natural trajectories in HCW and ZD frames for cross-track multistatic architectures with one coverage region. The active imaging region is highlighted with solid lines. The red boxes exemplify the position of the satellites at a common instant. Trajectories behind and ahead of the chief in along-track are represented in magenta and blue, respectively.

actuation occurs in both the along-track and cross-track directions, while only minimal actuation is applied in the radial direction, which in practice would be neglected. Most of the control effort is concentrated along the z-axis to counteract oscillations in that direction. The high delta-V consumption in the z-axis indicates that the total fuel consumption could be reduced if control requirements in cross-track were to be relaxed.

Finally, note that, in a practical scenario, the exact profile calculated by the optimizer is limited by the minimum impulse that the thruster can provide. Delta-Vs on the order of tens of micrometers per second every 15 seconds are compatible with small platforms using cold-gas or electric propulsion

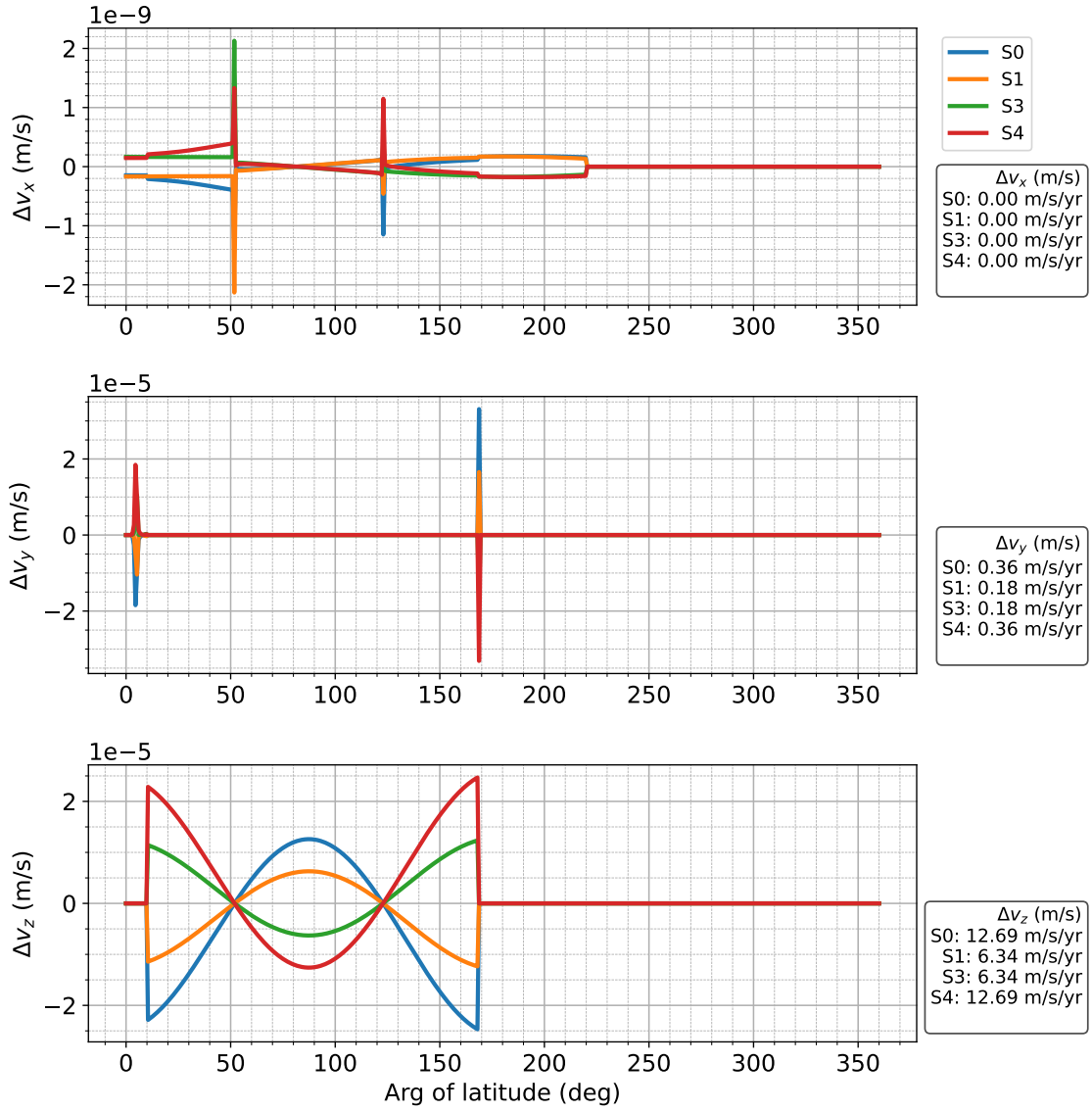

Figure 6.3: Delta-V consumption profile for one orbit of the quasi-natural cross-track formation solution. The annualized delta-V consumption (shown in m/s per year) per axis is displayed on the lower right corners for each of the satellites.

[160], so a velocity profile close to the one depicted in the plot could, in principle, be realized with those platforms.

6.4 Optimal Natural Guidance for Precise Formation Flying

The precision of the general optimization method presented in this chapter is inherently limited by the accuracy of the state transition matrix. This limitation becomes particularly relevant in cases where both secular and short-term periodic perturbations are non-negligible. This section introduces an iterative method to refine the initial state to minimize the positioning error while keeping the delta-V consumption low.

A possible approach to achieve the desired positioning in an operational scenario would be to use the ideal relative trajectories obtained in Chapter 5 as a reference in a feedback controller. If a feedback control loop is used to track this reference trajectory, it will compensate for systematic accelerations that cause deviations from the reference by applying continuous actuation. Although the fuel expenditure per orbit may be negligible for small disturbances when using this approach, the cumulative cost over long-term operations, e.g., spanning several years, can become a driver for the fuel budget.

An alternative approach is to define the reference trajectory as the natural orbit, obtained by propagating the initial state using a high-fidelity dynamical model. In doing so, the systematic perturbations are inherently accounted for, reducing or eliminating the need for continuous correction. However, directly propagating the natural solution obtained using the method described in Chapter 5 may result in degraded positioning accuracy.

Figure 6.4 compares the ideal Keplerian propagation assuming a circular chief orbit with a more realistic propagation that includes J2 perturbations and a slightly eccentric chief orbit. The initial condition corresponds to the optimized along-track configuration presented in Section 5.5.1. While the two trajectories initially coincide, perturbation effects accumulate over time, resulting in deviations of the same order of magnitude as the positioning requirements. Although these errors can be corrected via active control, this comes at the cost of increased delta-V. A more efficient solution is to iteratively adjust the initial conditions to minimize deviations while conserving fuel. This proposed approach is presented in Figure 6.5.

The procedure begins by solving the formation design problem using a simplified model, such as the closed-form method introduced in Chapter 5. The resulting initial state, $\delta\vec{X}_0$, is then propagated using a high-fidelity orbital model. Importantly, the relative motion of the deputy is not propagated directly. Instead, the chief and deputy spacecraft are propagated

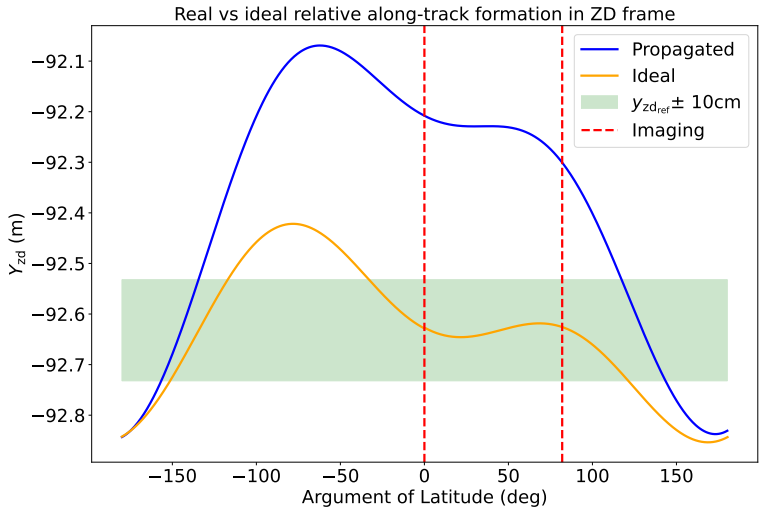

Figure 6.4: Comparison between the along-track component of a train formation propagated using a model including J2 harmonics and a Keplerian model for circular orbits. The required position for which the relative state was designed is highlighted in green, and the target range of arguments of latitude is delimited by the vertical lines.

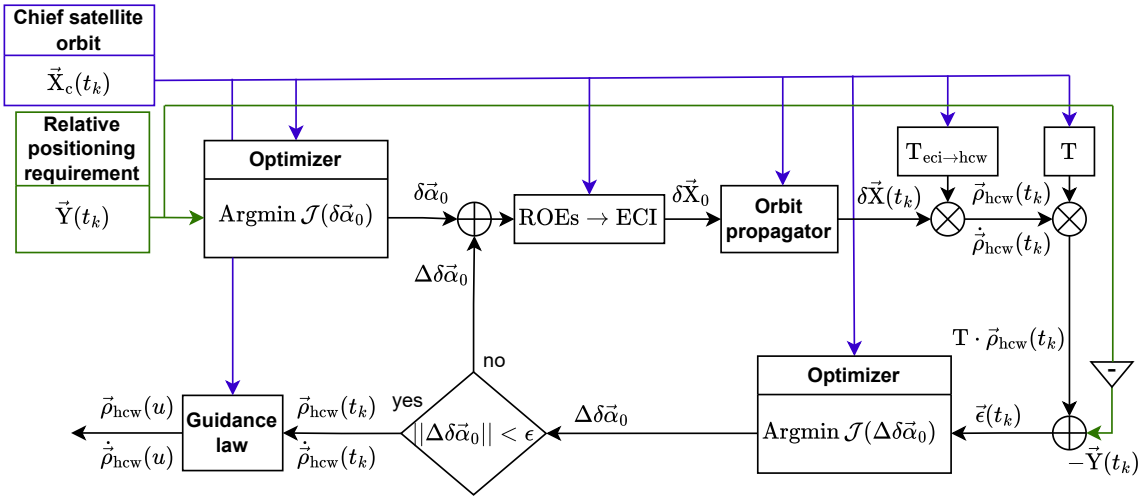

Figure 6.5: Block diagram of guidance optimization algorithm for natural formations. The chief satellite state in an ECI frame is denoted by $\vec{X}_c$; the matrix T denotes the linear transformation from the HCW frame to the design variable space; and $\vec{Y}$ denotes the ideal position in the design space. These, along with an input range of argument of latitude of interest, serve as inputs to the algorithm, which iteratively computes a propagated relative state that minimizes the squared error from the target positions.

independently in an Earth-centered inertial frame, and the deputy's position in the ZD frame is computed subsequently from the definition. This ensures that the relative motion reflects the true dynamics and is not constrained by the assumptions of simplified models.

At each imaging instant t_k, the deviation from the desired state is computed as

$$\vec{\epsilon}_k = \mathrm{T}_k \cdot \vec{\rho}_{\mathrm{hcw}}(u_k) - \vec{\mathrm{Y}}_k,\ k \in \mathcal{I}\,. \tag{6.13}$$

Assuming the system at any time t_k is linear with respect to the initial state, the effect of a modification of the initial state can be propagated directly. In this way, the error can be reduced by compensating with a propagated effect of an alteration in the initial state. Introducing a correction $\Delta\delta\vec{X}_0$ to the initial state in (2.41) leads to

$$\delta\vec{X}_k + \Delta\delta\vec{X}_k = \Phi(t_0, t_k) \cdot \left(\delta\vec{X}_0 + \Delta\delta\vec{X}_0\right), \tag{6.14}$$

Subtracting the nominal propagation from this expression yields

$$\Delta\delta\vec{X}_k = \Phi(t_0, t_k) \cdot \Delta\delta\vec{X}_0\,. \tag{6.15}$$

This relation can be reformulated in terms of the ROEs, assuming no difference in semi-major axis ($\delta a = 0$), as follows

$$\Delta\vec{\rho}_{\mathrm{hcw}}(u) = \mathrm{T}_{\delta l\mathrm{ei}\to\mathrm{hcw}}(u) \cdot \begin{bmatrix} \Delta\delta l \\ \Delta\delta e_x \\ \Delta\delta e_y \\ \Delta\delta i_x \\ \Delta\delta i_y \end{bmatrix}. \tag{6.16}$$

The re-optimization problem aims to determine the optimal adjustment in the initial state which reduces the error of the propagated orbit with respect to the ideal positioning. The cost function for this case, is given by

$$\mathcal{J}(\Delta\delta\vec{\alpha}_0) = \sum_{k\in\mathcal{I}} \left(\mathrm{T}_k \cdot \Delta\vec{\rho}_{\mathrm{hcw}}(t_k) - \vec{\epsilon}_k\right)^T \cdot \mathrm{W} \cdot \left(\mathrm{T}_k \cdot \Delta\vec{\rho}_{\mathrm{hcw}}(t_k) - \vec{\epsilon}_k\right). \tag{6.17}$$

Expressing the initial condition in terms of the ROEs, rather than Cartesian coordinates in the HCW frame, enables the derivation of closed-form expressions for the optimal corrections in both along-track and cross-track formation scenarios. These expressions incorporate all relevant geometric and dynamical constraints. The outcome of the optimization process is a correction to the initial ROEs, which is applied iteratively. After each iteration, the updated initial state is re-propagated, and the optimization is repeated until the resulting correction becomes sufficiently small. The

detailed formulations for both along-track and cross-track formations are presented in the following subsections.

It is important to emphasize that, in general, the repeatability constraint cannot be enforced in realistic scenarios without the use of actuation, due to the presence of secular perturbations. This is illustrated in Figure 6.4, where the final state of the propagated trajectory deviates by a few centimeters from the initial state, differing from the ideal trajectory. A separate strategy to correct for these long-term disturbances, preferably implemented outside the region of interest, is therefore necessary.

Several such strategies have been proposed in the literature [89]. The simplest approach, which will be adopted in the examples presented in Section 6.5, is to allow a discontinuity in the guidance law between $u = 2\pi$ and $u = 0$, and rely on the feedback controller to compensate for the resulting error. In the scenarios considered at the end of this chapter, the differences in relative eccentricity and inclination are sufficiently small that the corresponding secular effects are only on the order of a few centimeters. As a result, this simple approach does not heavily impact the final fuel budget.

Throughout this chapter, the dynamical models are parameterized with respect to time. However, a formulation in terms of the argument of latitude (u) is more appropriate, since optimal positioning is primarily latitude-dependent. A drift in the semi-major axis of the chief satellite leads to along-track dephasing, which can increasingly degrade the formation performance if a time-based parametrization is used. Consequently, a reparameterization from time to argument of latitude after optimization is necessary to maintain the accuracy of the solution.

Finally, while the guidance law is initially derived at discrete values of u, practical implementation requires a continuous representation, as there is no guarantee that control updates will align precisely with those sampled points. Interpolation, such as using cubic splines, is therefore required to construct a smooth and continuous guidance profile suitable for real-time execution.

6.4.1 Optimal Along-Track Formations

The approach adopted to compute the optimal correction to the initial state is analogous to that described in Section 5.4.1, with the main difference being that, instead of fitting a relative trajectory directly to meet the formation requirements, the correction is obtained by fitting the propagated trajectory's deviation from the requirements.

First, the following matrices must be defined

$$\mathrm{A_{at}} = \left[\mathrm{T_{hcw\to zd}}(u_k) \cdot \mathrm{T}_{\delta lei\to \mathrm{hcw}}(u_k)\right]_{k\in\mathcal{I}}, \tag{6.18}$$

and

$$\mathrm{E_{at}} = \left[\mathrm{T_{hcw\to zd}}(u_k) \cdot \vec{\rho}_{\mathrm{hcw}}(u_k) - \vec{\rho}_{\mathrm{zd}}\right]_{k\in\mathcal{I}}, \tag{6.19}$$

where, $[M_k]_k$ denote a matrix formed by vertically stacking the matrices M_k for all indices k, $u_k = u(t_k)$, and the term $\vec{\rho}_{\mathrm{hcw}}(u_k)$ is obtained using the orbital propagator with the disturbance components to be considered in the optimization. The optimal adjustment in the initial state to minimize the deviations from the ideal positioning can be calculated through the least-squares solution

$$\begin{bmatrix} \Delta\delta l \\ \Delta\delta e_x \\ \Delta\delta e_y \\ \Delta\delta i_x \\ \Delta\delta i_y \end{bmatrix} = \left(\mathrm{A_{at}^T} \cdot \mathrm{W} \cdot \mathrm{A_{at}}\right)^{-1} \cdot \mathrm{A_{at}^T} \cdot \mathrm{W} \cdot \mathrm{E_{at}}. \tag{6.20}$$

6.4.2 Optimal Cross-Track Formations

Similarly, the cross-track natural guidance correction algorithm is analogous to the one presented in Section 5.5.2. Defining

$$\mathrm{A_{xt}} = \left[\hat{i}_{\mathrm{arr}}^T \cdot \mathrm{T_{hcw\to zd}}(u_k) \cdot \mathrm{T}_{\delta ei\to \mathrm{hcw}}(u_k)\right]_{k\in\mathcal{I}}, \tag{6.21}$$

and

$$\mathrm{E_{xt}} = \left[r_{\mathrm{zd}} - \hat{i}_{\mathrm{arr}}^T \cdot \mathrm{T_{hcw\to zd}}(u_k) \cdot \vec{\rho}_{\mathrm{hcw}}(u_k)\right]_{k\in\mathcal{I}}, \tag{6.22}$$

the optimal solution can be calculated through the least-squares solution

$$\begin{bmatrix} \Delta\delta e_x \\ \Delta\delta e_y \\ \Delta\delta i_x \\ \Delta\delta i_y \end{bmatrix} = \left(\mathrm{A_{xt}^T} \cdot \mathrm{W} \cdot \mathrm{A_{xt}}\right)^{-1} \cdot \mathrm{A_{xt}^T} \cdot \mathrm{W} \cdot \mathrm{E_{xt}}. \tag{6.23}$$

Both the along-track and cross-track correction algorithms are simple to implement if a propagator is available. The algorithms are almost identical to the ones presented in Chapter 5.

6.5 Optimal Guidance Algorithm Evaluation

This section evaluates the proposed optimal guidance algorithm through two precision formation flying scenarios for distributed multistatic SAR imaging: one employing along-track formations and the other cross-track formations, similar to the cases presented in Section 5.5. In this analysis, however, a high-fidelity simulator is used to assess the impact of the proposed algorithm on the overall fuel budget. A Discrete Linear Quadratic Regulator (DLQR) controller, as described in Section 2.4.3, is implemented for the formation maintenance to counter the effects of disturbances and uncertainties.

6.5.1 Simulation Framework

This subsection describes the satellite formation flying simulator used to evaluate the optimal guidance technique proposed in this chapter. It also provides a first estimate of the delta-V budget required for formation maintenance in the two primary distributed imaging concepts analyzed in this and the previous chapter. The simulator is designed to assess the feasibility of implementing natural formations in an environment including a wide range of error sources typically encountered in real-world scenarios.

The formation flying simulator is composed of four major components: (i) orbit propagator, (ii) real-time absolute and relative navigation simulator, (iii) formation controller, and (iv) thrust simulator. An overview of the simulation framework is shown in Figure 6.6.

The simulation parameters are summarized in Table 6.2. The selected values emulate a typical small-satellite mission scenario. The drag and reflectivity coefficients correspond to commonly reported values in the literature [102]. The considerably larger area projected toward the Sun emulates the effective area of the solar panels and SAR antenna, whose surfaces are mostly orthogonal to the flight direction in a sun-synchronous orbit. The navigation errors are consistent with the state-of-the-art differential GNSS performance planned for the VISORS mission [152]. The thrust direction error of one degree accounts for possible attitude errors and is based on values assumed in the CanX-45 simulations, along with the 10% thrust magnitude error [161]. Finally, the DLQR controller weights were manually tuned, starting from reference values reported for the CanX-45 mission [104].

The core of the simulator is the orbit propagator. In this case, Orekit [162] is used as the primary orbit propagation tool. This open-source software library is widely adopted in mission analysis and design by several space institutions, including the *Centre National d'Études Spatiales* (CNES) and the European Organisation for the Exploitation of Meteorological Satellites (EUMETSAT) [163].

The simulator takes as input: (i) the orbit of the chief satellite, consisting of the absolute state for the whole duration of the simulation period; (ii) the initial position of the deputy satellite; (iii) a guidance law, giving a sequence of relative positions and velocities of the deputy satellite in the HCW frame. This trajectory is tracked by the feedback controller to maintain the formation, based on prior optimization considering multistatic SAR performance requirements.

The real-time navigation simulation module generates the navigation solution. This includes both coarse absolute and more precise relative positioning solutions. The errors are modeled as smoothed zero-mean Gaussian noise, reflecting typical differential GNSS accuracy for both position and velocity estimates. The smoothed errors were simulated by applying Kalman filters to the absolute and relative positions and velocities measurements affected by Gaussian errors.

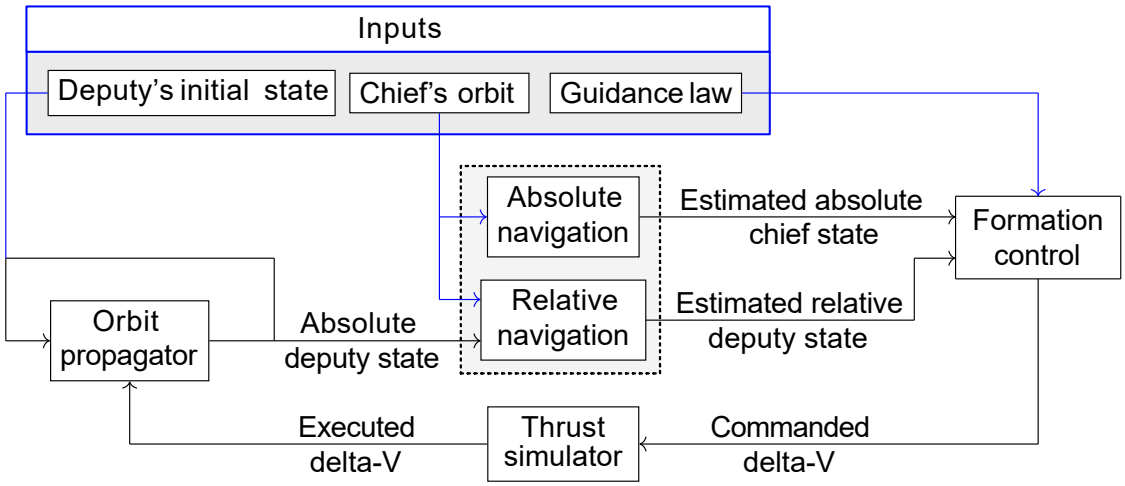

Figure 6.6: Block diagram of the simulation framework for testing formation control. The simulator includes a high-fidelity orbit propagator, navigation simulation, thrust uncertainty simulation, and a DLQR implementation for formation control.

Orbit propagator		
Perturbation	**Model**	**Value**
Earth's asphericity	EGM-2008	120 x 120
Atmospheric drag	NRLMSISE00	$c_{\mathrm{d}} = 2.3$, $A_{\mathrm{cs}} = 0.12$ m^2
Luni-solar perturbations	Point Mass JPL DE	-
Solar radiation pressure	Cannon ball	$c_{\mathrm{r}} = 1.1$, $A_{\odot} = 1$ m^2
Solid tides	IERS 2010 Convention	-
Ocean tides	IERS 2010 Convention	FES-2014
Mass		70 kg
Chief satellite's initial orbital elements		
Semi-major axis		6958.1366 km
Eccentricity		0.0010654427
Inclination		97.7°
RAAN		58.8228°
Argument of perigee		356.2622°
Argument of latitude		0°
Navigation errors (x,y, and z)		
Relative position	Zero-mean Gaussian	1 cm (1 σ)
Relative velocity	Zero-mean Gaussian	0.1 mm/s (1 σ)
Absolute position	Zero-mean Gaussian	1 m (1 σ)
Formation control		
Controller		DLQR
Impulses per orbit		300
Position cost		n
Velocity cost		1
Control input cost		$1/n^2$
Thrust errors		
Magnitude (δF_z)	Zero-mean Gaussian	10% (3 σ)
Cone angle (α)	Zero-mean Gaussian	1° (1 σ)
Azimuth angle (β)	Uniform	$\mathcal{U}(0,\ 360°)$

Table 6.2: Simulation parameters. All simulated random errors are zero-mean. The off-diagonal values of all the error covariance matrices and control weight matrices are zero, and the diagonal values are the same for x, y and z directions. The chief's mean anomaly is denoted by n.

The feedback control module receives the reference trajectory as a function of the chief's argument of latitude and computes the command signal necessary to follow it, based on the measured current state. A Discrete-Time Linear Quadratic Regulator (DLQR) controller is implemented in this module.

Finally, the maneuver execution module simulates the application of thrust commands. It incorporates realistic actuation errors, including misalignment due to structural or attitude errors, pressure fluctuations, and other imperfections. Thrust errors are modeled using a conical misalignment representation (see Figure 6.7), defined by a cone angle α, an azimuthal distribution angle β, and a thrust magnitude error δF_z relative to the nominal thrust command. In this case, the minimum thruster impulse limitation was not applied, and it is therefore assumed to be sufficiently low so as not to significantly impact the control accuracy. This low minimum impulse can realistically be achieved using electric propulsion or cold gas thrusters.

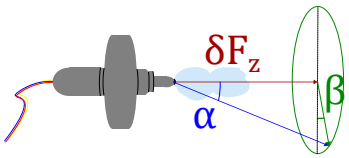

Figure 6.7: Thrusting misalignment errors. Due to imperfections in the thruster and attitude errors, the magnitude of the thrust (δF_z) and its orientation (α and β) vary relative to the commanded nominal.

The next subsections present simulation results for the two formation configurations introduced in Chapter 5: a cross-track and an along-track formation, both with highly stringent relative positioning requirements. For each case, two guidance laws are evaluated: one based on the ideal Keplerian solution assuming a circular chief orbit, as presented in Chapter 5, and another based on the optimal natural guidance method as proposed in Section 6.4. The relative positioning deviation with respect to the ideal and the fuel consumption are evaluated and compared to assess the effectiveness of the optimization procedure proposed in Section 6.4. Additionally, the simulations aims to preliminarily assess the feasibility of distributed SAR systems that rely on very high relative positioning accuracy. Finally, they also aim to assess the representativeness of the simplified models presented in Chapter 5.

6.5.2 Case 1: Along-Track Multistatic Formation

The input parameters for the along-track formation scenario are shown in Table 6.3. These parameters are the same presented in Table 5.2, and repeated for the sake of completeness.

Along-track system parameters	
Number of satellites	5
Wavelength	3.11 cm
Antenna look angle	27.8°
Antenna length	1.3 m
Pulse repetition frequency (PRF)	2.68 kHz
Input coverage latitude range	0° to 82°

Table 6.3: System parameters of the multistatic system example for azimuth reconstruction imaging.

The positioning results in the ZD frame are shown in Figures 6.8 and 6.9, for the guidance laws optimized for the HCW model and complete model, respectively. The mean and standard deviation of the positioning deviation from the objective are also provided in the figures, calculated only within the region of interest, highlighted in blue. The satellites maintain an average along-track separation of approximately 50 m, and comply with the sampling complementarity criteria defined in (5.7). For visualization purposes, the results are shown relative to the ideal positioning. The simulation spans five orbits, corresponding to approximately eight hours.

The results demonstrate that in both cases, the system successfully meets the positioning requirements despite the presence of disturbances, with positioning errors generally below 2 cm in along-track and below 15 cm in radial and cross-track directions. The results are compliant to the 3-cm standard deviation in along-track, which indicated successful azimuth reconstruction. The optimized solution shows a slight improvement in positioning precision in along-track, which can be explained by the fact that the major orbital perturbations are already included in the reference, and therefore do not act as systematic external disturbances anymore, being instead

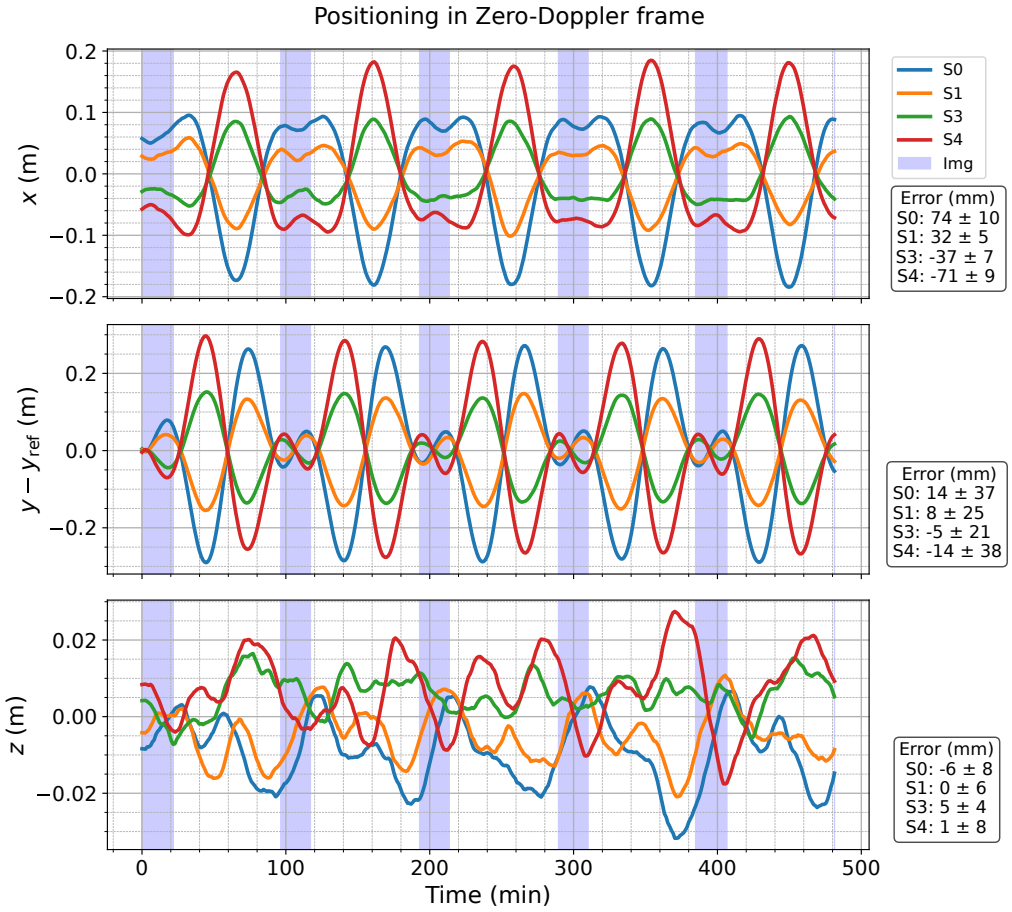

Figure 6.8: Formation keeping results for the along-track formation using a HCW solution as a guidance law. In blue are indicated the passes over the region for which the formation is optimized.

included in the nominal dynamics (see Figure 2.14). Despite the slight improvement, the relative trajectories for the two cases, specially in the along-track direction, are very similar. This shows that the results obtained with the simple models presented in Chapter 5 are already representative.

This reduction in the external disturbance is made clearer when looking at the delta-V profile for each case, shown in Figures 6.10 and 6.11 in the HCW frame. Like in the positioning requirement, the region of interest is highlighted in blue. The total delta-V consumption is expressed in meters per second per year, obtained by scaling the total consumption over the five orbits to an annual rate. This is a reasonable assumption in this case because the satellites are assumed identical and the major disturbances that vary over periods of months or years—mainly solar radiation pressure, third body perturbations and drag—are approximately the same for all spacecraft and therefore cancel out.

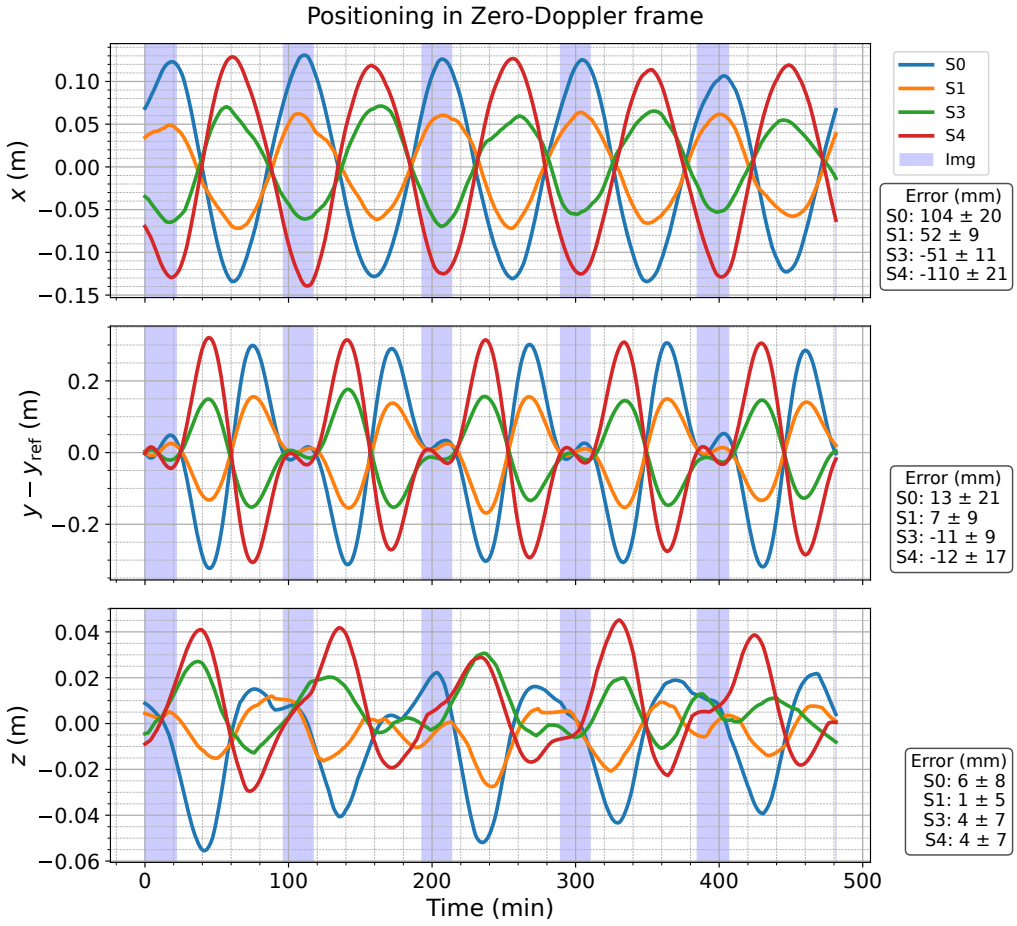

Figure 6.9: Formation keeping results for the along-track formation, using optimal tracking solution as a guidance law. In blue are indicated the passes over the region for which the formation is optimized.

It is important to note that the delta-V values refer only to formation-keeping maneuvers. The chief satellites absolute orbit is left uncorrected over the eight-hour simulation. In an operational context, absolute orbit control would also contribute to the overall delta-V budget.

The results show a remarkable reduction in the delta-V budget almost by one order of magnitude when applying the guidance optimization procedure. The total delta-V budget for satellite S0, the costliest to maintain of the formation, followed closely by S4 in the opposite extremity of the array, is reduced from a maximum of 21.7 m/s/yr to 2.7 m/s/yr. The case optimized for a HCW model exhibits a clear periodic pattern in its delta-V profile, which can be explained by the compensation of the Earth's harmonics, primarily the J2, which repeat at each period. As mentioned before, the unaccounted perturbations count as a systematic external disturbance for the feedback controller, which affects positioning precision and drives fuel consumption.

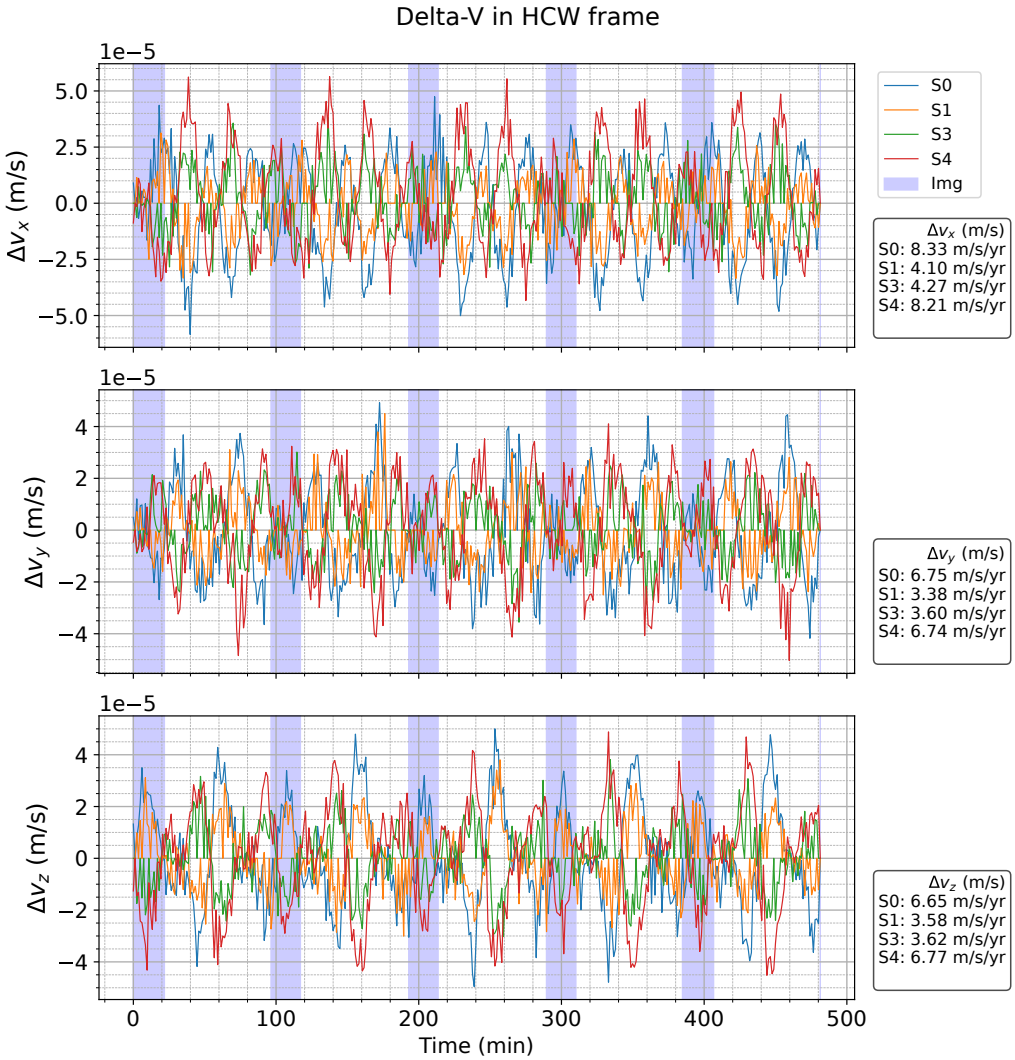

Figure 6.10: Formation keeping delta-V results for the along-track formation, using a HCW solution as a guidance law. In blue are indicated the passes over the region for which the formation is optimized.

The fuel reduction enabled by the optimization has major implications on the class of platforms and propulsion technologies required to implement the distributed SAR imaging concept. For prolonged operations, a fuel consumption of around 20 m/s/yr could rapidly consume the budget, and would likely require either larger platforms which can accommodate more fuel, or the use of more efficient electric propulsion technology. The latter has the major drawback of the high power consumption required, which could compete for the limited available power, especially in small platforms, where the SAR payload is generally also power hungry. This would likely exclude many options of small platforms, possibly outright eliminating the options of using CubeSats.

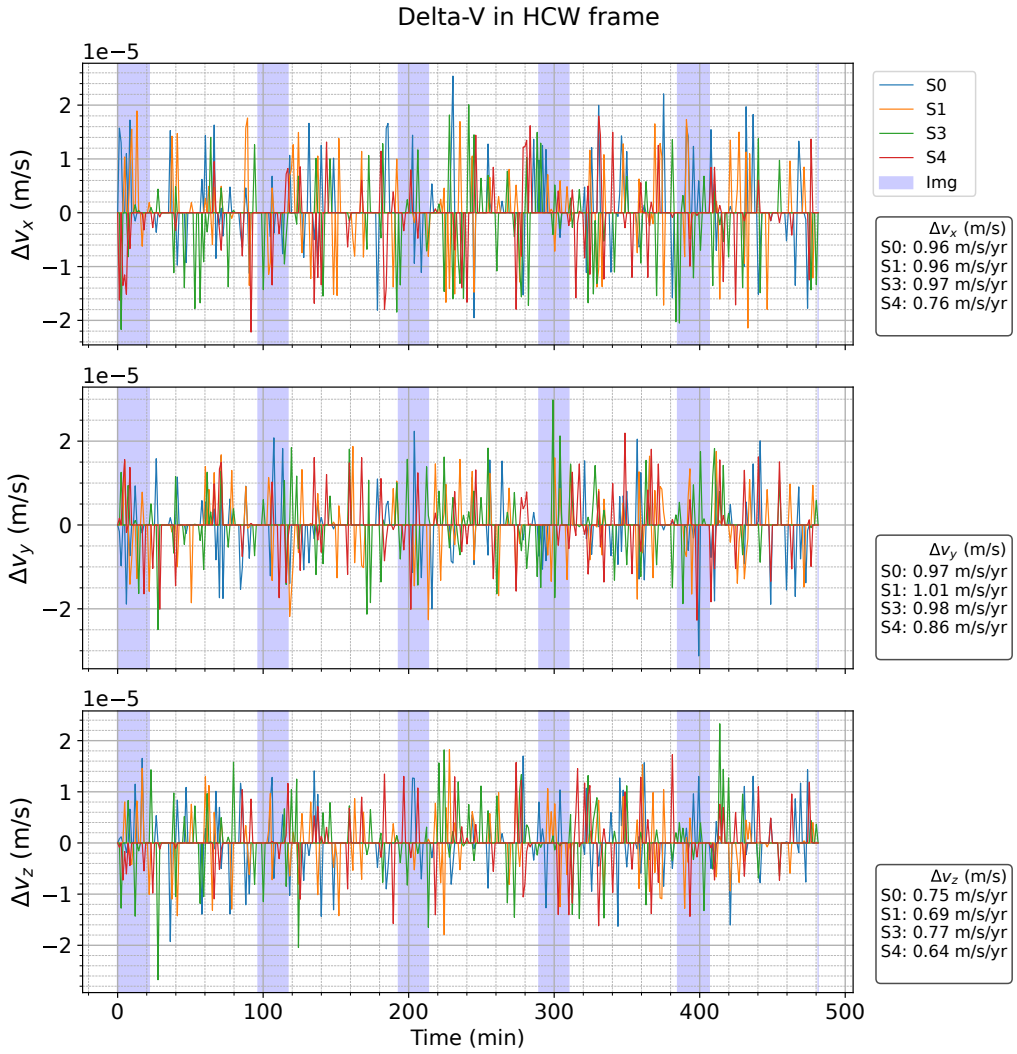

Figure 6.11: Formation keeping dV results for the along-track formation, using optimal tracking solution as a guidance law. In blue are indicated the passes over the region for which the formation is optimized.

A fuel budget of 2.7 m/s/yr, in contrast, would allow for a much broader range of platforms. This budget is particularly manageable with chemical propulsion technologies, which offer the advantage of low power consumption and higher maneuverability due to their higher thrust. This makes it easier for the platforms to comply with both strict relative positioning for the multistatic concepts proposed—on the order of a few centimeters—as well as the strict absolute positioning in the form of an orbital tube—on the order of tens to a couple hundreds of meters. Strict absolute positioning is a common requirement for SAR for its importance in time series analysis, repeat pass interferometry, and tomography.

Finally, it is important to highlight that in the example presented the chief satellite orbit is drifting, which means the optimal guidance is not strictly

optimized for the chief satellite orbit from the first period on. Nonetheless, there is no notable degradation in the positioning nor in the fuel consumption performance, which underscores the robustness of the proposed guidance optimization strategy presented in this chapter. This is enabled by the parametrization of the guidance law in terms of the argument of latitude of the chief satellite instead of explicitly in time, which confers a certain degree of adaptability to it.

6.5.3 Case 2: Cross-Track Multistatic Formation

The input parameters for the cross-track formation case are shown in Table 6.4. These are the same as the ones presented in Section 5.5.2, and are repeated here for completeness as well. Only the case with one range of latitude is covered in this Subsection.

Cross-track system parameters	
Number of satellites	5
Antenna look angle	27.8°
Antenna height	0.4 m
Pulse repetition frequency (PRF)	2.68 kHz
Input coverage latitude range	10° to 82°

Table 6.4: Positioning input requirements of the cross-track multistatic system example for beamforming in elevation.

Figures 6.12 and 6.13 show the results for the cross-track configuration using the HCW and optimized guidance laws, respectively. The figures include the trajectory plots in the ZD frame as well as the projection along the array direction, which is used to evaluate the cross-track positioning requirement. Summary statistics are provided, calculated only over the region of interest highlighted in blue. As in the previous case, adjacent satellites maintain an average along-track separation of approximately 50 m.

The positioning results follow a similar pattern to those of the previous case. The positioning error for the optimized case with a complete model improves compared to the one considering the HCW solution due to the lower external disturbance acting on the feedback controller. For both

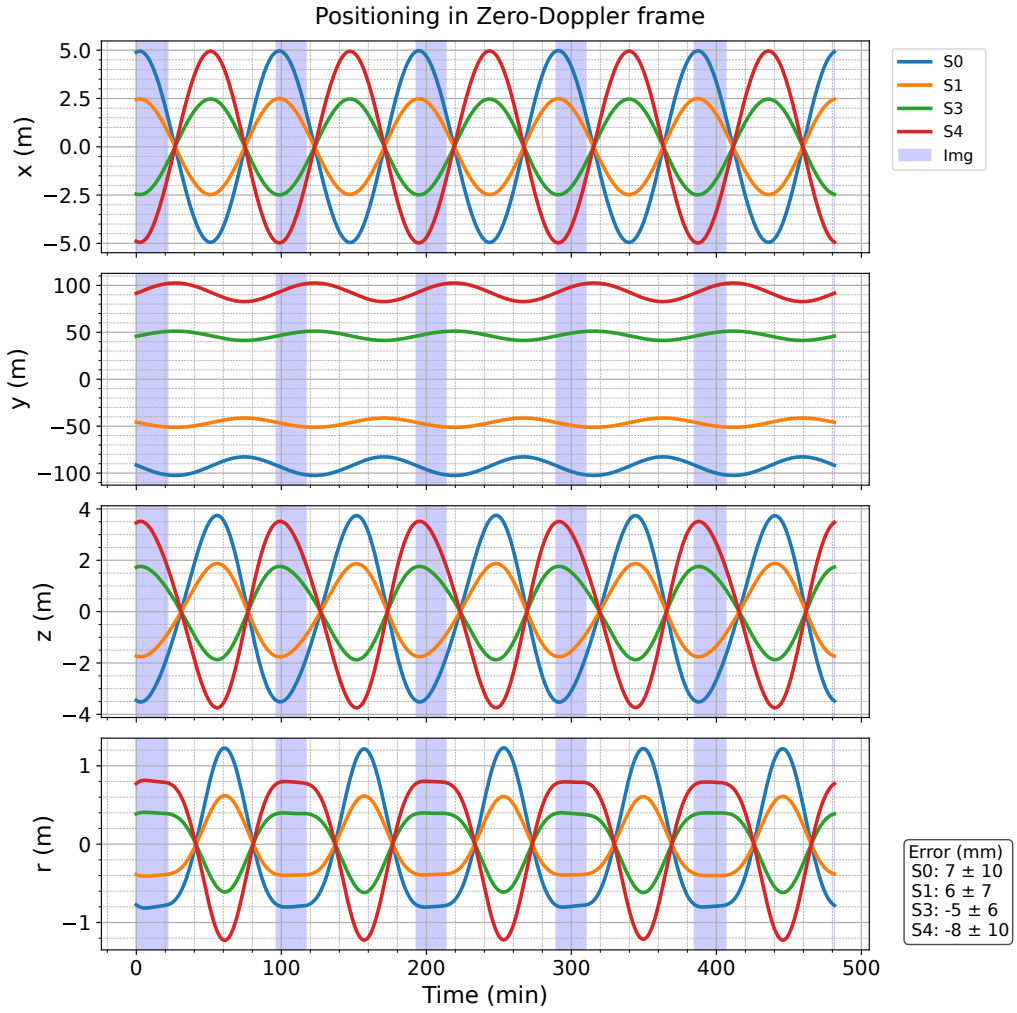

Figure 6.12: Formation keeping results for the cross-track formation, using a HCW solution as a guidance law. In blue are indicated the passes over the region for which the formation is optimized.

cases, the errors exhibit a standard deviation lower than 3 cm, which is sufficient for effective beamforming, according to the simulations performed in Section 5.5.2. The resulting relative trajectories are also very similar and, as in the along-track case, further corroborate the validity of the simplified models introduced in Chapter 5.

The delta-V consumption for the guidance based on the HCW model and the complete model are shown in Figures 6.14 and 6.15, respectively. The region of interest, for which the formation is optimized, is highlighted in blue. The figures also include the annualized delta-V consumption for each axis.

As with the along-track formation, a substantial reduction in delta-V is achieved using the optimized guidance law. For the highest-consuming satellite (S3), the annual delta-V drops from 27.83 m/s to 4.15 m/s. The

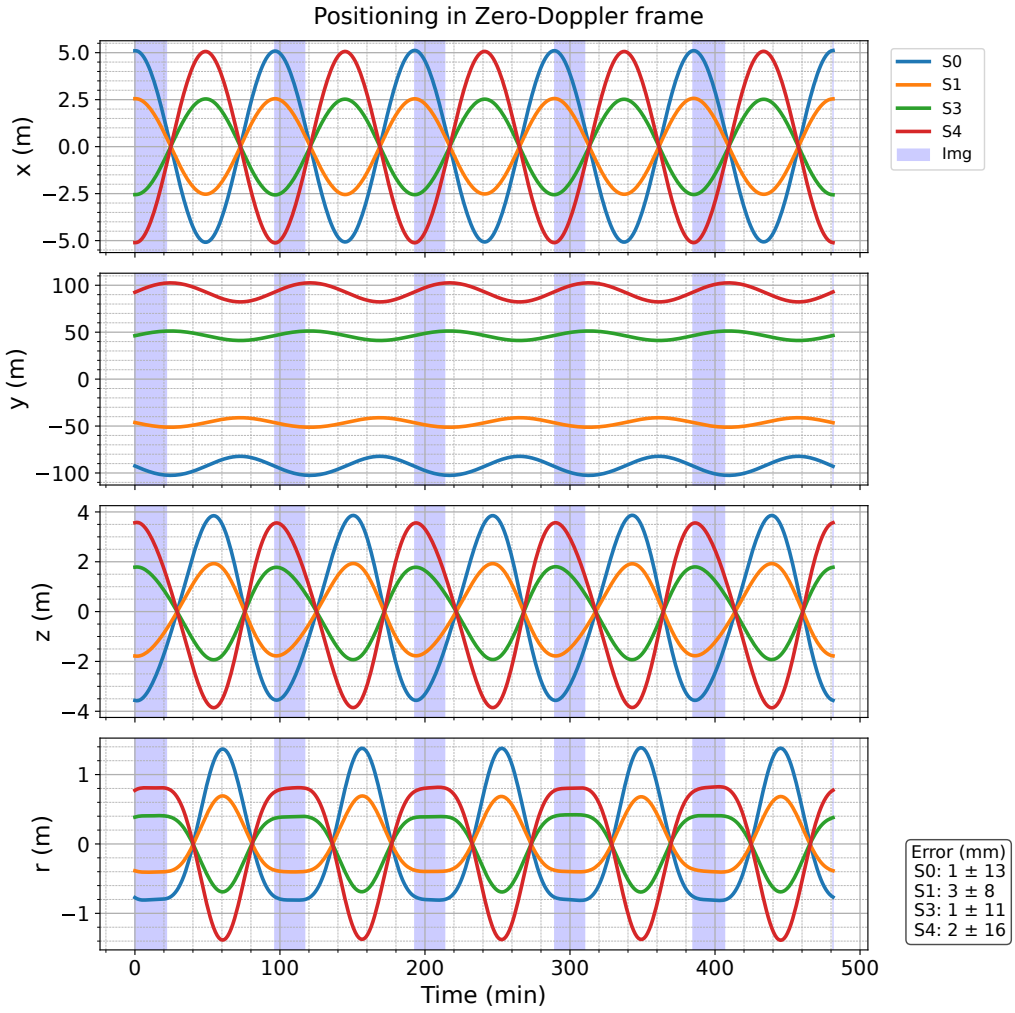

Figure 6.13: Formation keeping results for the cross-track formation, using tracking optimal tracking solution as a guidance law. In blue are indicated the passes over the region for which the formation is optimized.

results are similar to those obtained in the along-track case, with a slight increase in delta-V consumption. The similarity between the results is attributed to the fact that the formations are very similar, with a predominant along-track separation and reduced cross-track and radial separation in the cross-track case. This increase is partially attributed to the higher secular drift in this formation due to higher difference in relative eccentricity and inclination vectors, which drive the secular effects of the J2 perturbation. Despite this small increase, the budget is still compatible with small platforms.

It is also worth noting that the controller corrects for secular drift only at the end of each orbit, which typically results in a drift of a few centimeters between periods. The guidance law does not include a long-term correction for this drift, and this could be contributing to an increased delta-V. Future

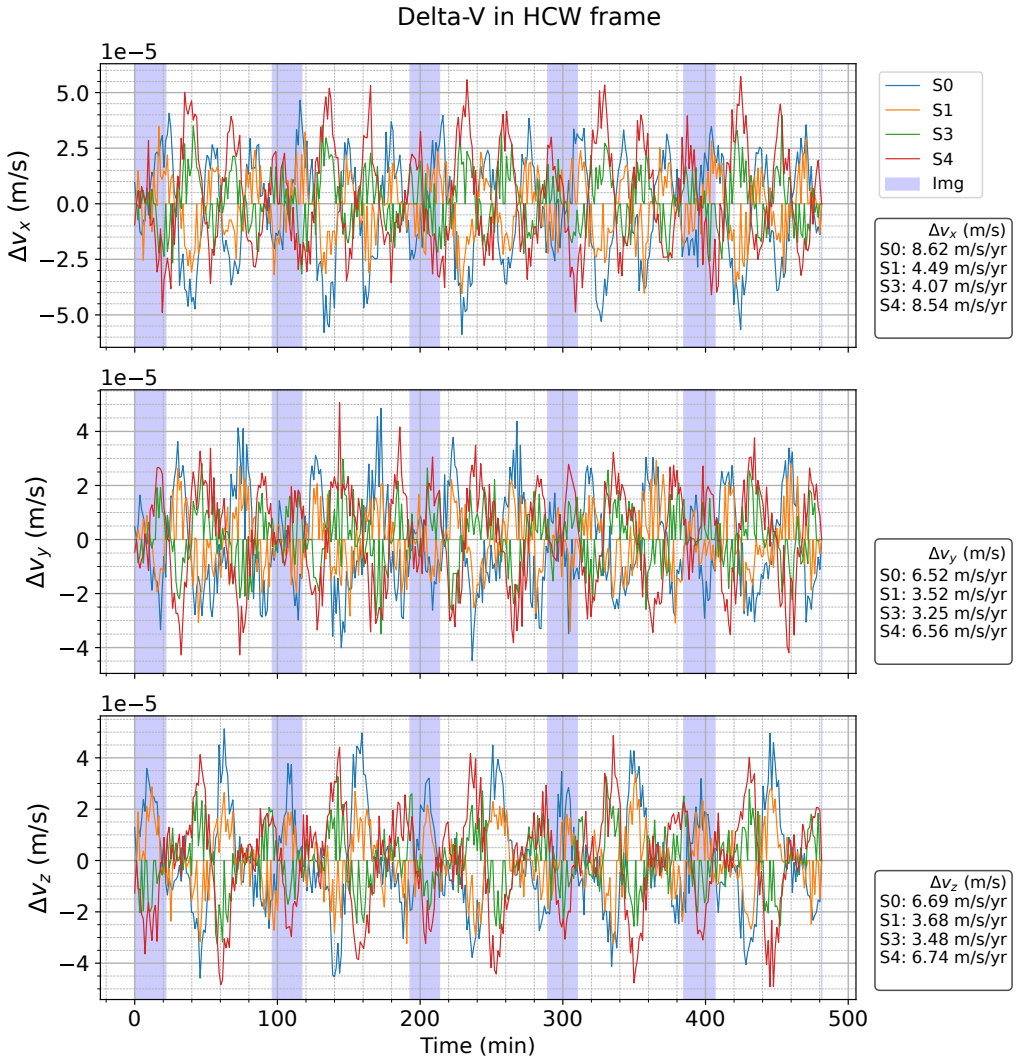

Figure 6.14: Formation keeping delta-V results for the cross-track formation, using a HCW solution as a guidance law. In blue are indicated the passes over the region for which the formation is optimized.

work could incorporate routine correction maneuvers outside the region of interest to optimize performance further. This will become increasingly important in applications involving larger cross-track baselines, such as radar sounders or single-pass tomography, as tight control will be more challenging because the differential disturbances scale with the baseline. This also applies to the along-track formation presented previously.

Still concerning platform complexity, both the along-track and cross-track formation configurations require full three-degree-of-freedom control. This imposes significant demands on the spacecraft design, as thrusters would be needed on six faces of the platform to enable actuation in all translational axes simultaneously, potentially including redundancy for fault tolerance. This required additional hardware increases the complexity, mass,

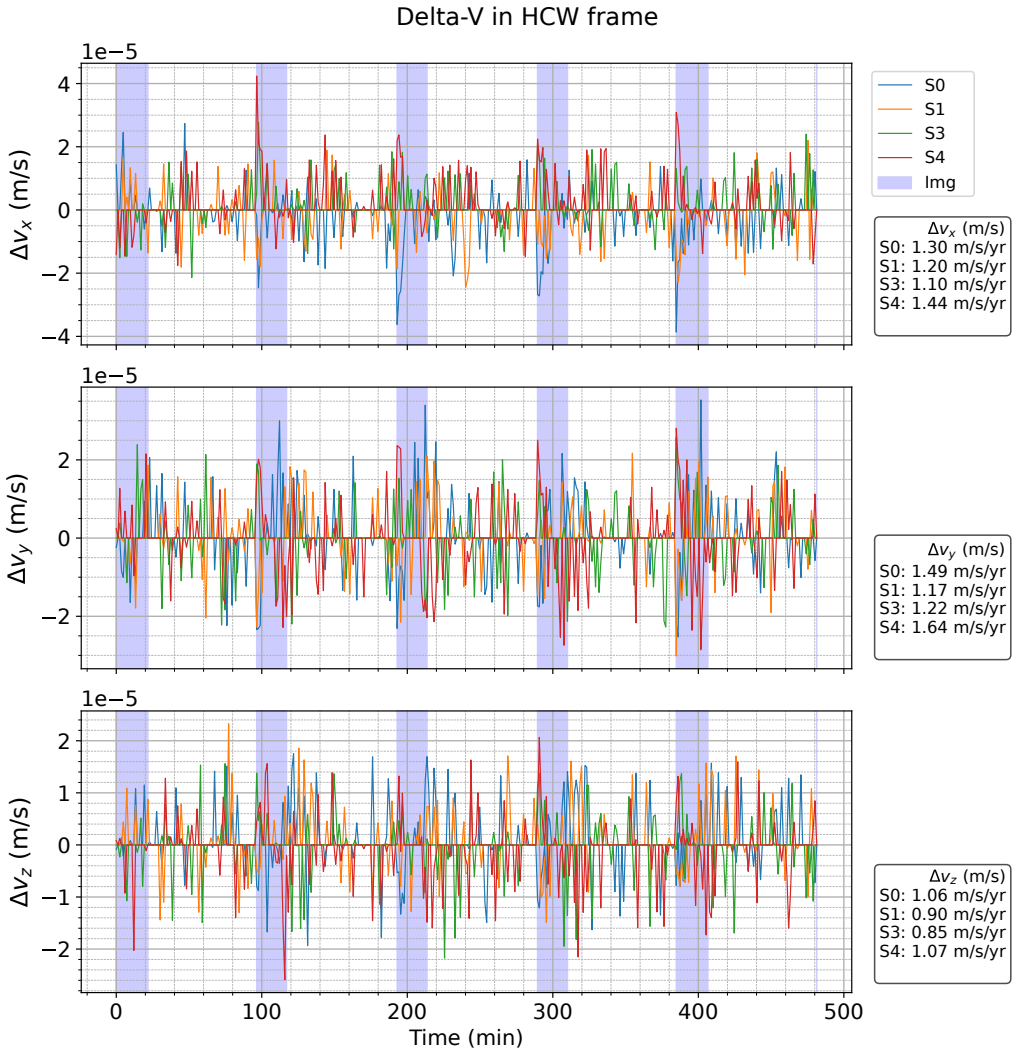

Figure 6.15: Formation keeping delta-V results for the cross-track formation, using tracking optimal tracking solution as a guidance law. In blue are indicated the passes over the region for which the formation is optimized.

and cost of the spacecraft. This is a key reason why many small spacecraft, particularly CubeSats, are typically designed with fewer degrees of freedom, sometimes limited to one thruster in a face opposite to flight direction. Limiting the actuation freedom generally implies accepting degradation in positioning accuracy as a trade-off. This approach, however, could potentially enable the implementation of these concepts with smaller platforms while still achieving acceptable performance.

Finally, for both the along-track and cross-track cases examined in this chapter, there is potential for further reducing the delta-V consumption by employing more efficient control strategies. For example, since the stringent positioning accuracy requirements are only applicable within a limited fraction of the orbit, the control effort could be relaxed outside these

intervals, leading to a reduction in fuel consumption. Additionally, alternative control schemes or the optimization of control gains could result in further improvements in fuel efficiency and control accuracy. These considerations will be explored in future work.

6.6 Conclusions

This chapter addressed the problem of formation design for multistatic SAR under non-ideal relative dynamics and common mission constraints. To this end, it generalized and expanded the previously introduced algorithm by incorporating active control through thruster actuation. In addition, an algorithm for deriving fuel-optimal guidance laws was developed, explicitly accounting for major orbital perturbations and the effects of small eccentricities in the chief satellites orbit. A detailed formation-keeping simulation was used to assess the following: the overall feasibility of tight control for distributed SAR using natural formations under the most relevant disturbances; the effectiveness of the proposed guidance algorithms; the impact of optimizing for dominant orbital perturbations on positioning conformance and delta-V budget; and the applicability of the approach introduced in Chapter 5 in terms of the representativeness of the resulting trajectories.

The simulations produced formation-keeping fuel budgets of only a few meters per second per year for tight, short-baseline distributed SAR formations in both along-track and cross-track directions, which is compatible with small-platform capabilities. The results show that the relative motion can remain conformant to the ideal SAR geometry even in the presence of major perturbations. A comparison between guidance laws optimized using the simplified and complete models reveals a substantial improvement in fuel efficiency, by a factor of seven to ten, without any degradation in positioning performance. This demonstrates that the proposed approach is not merely an incremental enhancement but a fundamental development for enabling such missions. Finally, the simulations indicate that the simplified model already produces representative geometries and could therefore be used for preliminary design or future analytical studies.

The methodology developed in this work can be adapted to a wider range of constraints, including limited thrust directions, restrictions on maximum along-track displacement, upper bounds on thrust magnitude (e.g., to simulate the characteristics of electric propulsion systems), and passive safety. The work therefore provides a basis for a more systematic and optimized design process for relative orbits, supporting effective formation design for

a broader range of positioning requirements and mission scenarios, such as distributed sounders, single-pass interferometry, and single-pass tomography.

7 Conclusions and Outlook

7.1 Summary and Discussion of the Achieved Results

This work proposes novel general and effective solutions to the problems of synchronization and formation flying, which are inherent to most multistatic SAR systems. By addressing these challenges, the work contributes to bringing distributed SAR concepts to practical realization.

7.1.1 Results on Synchronization

This thesis proposes a GNSS-based phase synchronization technique based on common-view differential carrier phase measurements (Chapter 3). The technique is fully non-cooperative, requiring no direct communication between satellites, and is independent of the imaged scene, making it particularly scalable and guaranteeing compatibility between systems developed independently and at different times. This makes it also well-suited for passive companion missions. A comprehensive analytical error model for the proposed technique was developed. The most relevant error contributions identified were the baseline determination error, the thermal noise on the carrier phase measurements, internal loss of coherence within the GNSS receiver, and external factors of which the most important is multipath (Chapter 3). The performance of the proposed technique was evaluated through a combination of simulations and experiments with real hardware.

Simulations were first conducted to assess the impact of GNSS satellite and receiver positioning uncertainties, based on PBD results reported in the literature (Chapter 3). The simulations concluded that precise baseline determination—necessary for applications requiring high-accuracy synchronization—provides the necessary accuracy for the technique. The experiments demonstrated potential for the technique to achieve sufficient accuracy for bistatic or multistatic SAR missions (Chapter 4) up to X-band. A phase synchronization error as low as 0.8 degrees at C-band (or 1.45 degrees at X-band) was achieved in a short-baseline experiment involving

two independent oscillators. The receiver-induced phase contamination was experimentally characterized, and the results showed that measuring this contribution is essential for determining the achievable synchronization accuracy and improving the results through appropriate weighting. Finally, a proof-of-concept for an orbital scenario using a high-end GNSS signal simulator confirmed that realistic baselines and differential Doppler effects do not degrade synchronization performance. Part of the experiments was conducted in support of ESA within the frame of the Harmony mission.

Due to its seamless implementation, it is likely that future systems will rely on GNSS observables as a common standard for the accurate time and phase synchronization according to the scheme postulated in this work. This avoids the need for development of dedicated synchronization subsystems and its associated characterization and calibration.

7.1.2 Results on Formation Flying for Distributed SAR

This work analyzed the feasibility of very stringent SAR formations for SAR cross-imaging based on natural relative motion, which opens the door to the development of fuel-efficient formation flying strategies for bistatic and multistatic radars. To that end, it proposes an optimization method for identifying optimal natural formations that minimize the squared distance to a desired configuration in the Earth-fixed ZD frame across a range of latitudes (Chapter 5). This method is then extended to include active actuation and arbitrary linear relative formation models through convex optimization algorithms (Chapter 6).

The developed method was first applied to along-track formations, where satellites must maintain approximately the same trajectory relative to Earth. The optimization algorithm identifies natural along-track formations in the ZD frame that reduce cross-track baselines to below one decimeter, mitigating their negative impact due to sensitivity to topography and substantially enhancing the feasibility of this distributed imaging concept.

The optimization approach was also applied to cross-track formations, which require the satellites to be evenly distributed with constant cross-track separations for optimal performance. This configuration is relevant, for example, for applications such as beamforming in elevation for ambiguity suppression, clutter suppression in radar sounding, and single-pass SAR tomography. Maintaining consistent cross-track baselines over extended periods is generally viewed as infeasible under the constraints of natural relative motion. However, the optimizer developed in this thesis

found relative trajectories with near-constant cross-track baselines, deviating less than 1.5% from the ideal value, sustained over more than 20% of the orbit duty cycle. This performance was achieved by leveraging the Earth's rotation effect on the formation geometry and relaxing the requirements in the radial and along-track directions. Additionally, the solutions obtained indicate that shapes allowed by the classical HCW equations can be replicated in the ZD frame by compensating for effects of the Earth's rotation with an initial state offset. These cross-track formations can accommodate baselines ranging from a few meters to several tens of meters, significantly improving spatial coverage for many innovative concepts (Chapter 5).

Finally, this thesis expands the analysis on the applicability of natural formations for stringent SAR positioning requirements to a realistic scenario, where the major orbital perturbations are considered (Chapter 6). Highly efficient distributed SAR beamforming, both in along-track and cross-track, could demand tight relative control, on the order of centimeters to decimeters, maintained over long durations, often spanning years. To address this challenge, a method to find an optimal guidance law is proposed that minimizes fuel usage while accounting for deviations from circular Keplerian motion, primarily due to slight eccentricities in frozen orbits and Earth's oblateness.

The method is validated through simulation accounting for major disturbances, which showed fuel consumption of only a few meters per second per year, while maintaining sub-decimeter accuracy in relative positioning for both along-track and cross-track beamforming configurations. Compared to simpler guidance methods that force tracking of ideal relative positions, the proposed guidance law achieves over 80% reduction in delta-V without compromising positioning accuracy. The optimized fuel budgets for along-track and cross-track formations with baselines of a few meters remained below 5 m/s/year, indicating the viability of these distributed imaging concepts with a broad range of platforms and propulsion technologies. Finally, the high similarity between the obtained trajectories under disturbance-free dynamics and considering major perturbations validates the representativeness of the simplified analytical models presented.

7.2 Outlook

The following research topics are suggested as follow-up work to the investigations presented in this thesis:

- **Data fusion of GNSS-based and Autosynch techniques:** The proposed GNSS-based phase synchronization method could be complemented with data-based techniques such as Autosynch [53]. Autosynch provides high-accuracy estimates of the instantaneous differential frequency, which must be integrated in time to obtain the differential phase estimates. This integration leads to phase errors which increase in time within one data take. On the other hand, GNSS-based synchronization offers direct phase estimates, although potentially noisier depending on the GNSS receiver used. Fusing both approaches could yield a hybrid synchronization technique with better and more uniform performance, and improved robustness.
- **Common-mode characterization:** To enable improving the performance of the GNSS-based synchronization method presented in this thesis, it is important to investigate the root causes of the common-mode error, i.e., the error component correlated across carrier phase observables. While thermal noise is highly reduced through averaging, the common-mode error remains, therefore representing a fundamental limitation of the technique. There is a possibility that this error originates from the receiver design itself, so that substantial performance improvement is achievable through modifications in the receiver. Conducting such an investigation would require tracing phase accuracy degradation across the receiver's hardware and signal processing chain. Given the stringent time-transfer accuracy requirements, and the potential for phase noise contamination due to environmental influences, the experimental setup must be meticulously designed. Although this work would be demanding, the potential to develop a time-transfer receiver capable of consistently achieving the accuracies required for interferometric applications at high frequencies (X-band or above) may well justify the effort.
- **Quantitative analysis of the impact of ionospheric turbulences and multipath:** In this thesis, these two factors were analyzed only qualitatively, partly due to the difficulty of achieving a representative models given their context dependency. Multipath, in particular, is strongly dependent on the satellite geometry. A detailed mathematical model is needed for both effects. In the case of multipath, a mathematical foundation could enable mitigation through signal processing, which, if successful, could further improve the robustness of the technique.
- **Safety considerations in tight formations:** The methods developed in this work meet tight positioning requirements for SAR, but the safety aspects were not addressed in detail. The available degree of

freedom after optimization for distributed imaging allows only for separation in the along-track direction, which is unstable and subject to short-term drifts. This suggests that active collision avoidance mechanisms will be necessary, and a robust strategy must be defined. Additionally, the conventional approach of separation via relative eccentricity and inclination vectors may prove too conservative, and one can consider a safety criterion based on probabilistic calculations instead. Moreover, for the low relative velocities involved in distributed SAR, it may be feasible to design spacecraft to withstand minor collisions without critical damage and debris release, thus relaxing some safety constraints. An extensive safety evaluation and the definition of a collision avoidance strategy are recommended for practical implementation of the proposed formations.

- **Integrated formation and orbit control strategy:** Although this work is mainly focused on relative formation control, absolute orbit maintenance is also important. To enable time-series analysis, the orbit control of SAR missions is often constrained to narrow orbital tubes. Managing both relative and absolute control independently may become complex and inefficient. Therefore, a unified strategy that integrates both formation and orbit control should be developed to support the implementation of future distributed SAR mission.
- **Practical considerations in other relevant scenarios:** The simulated formations presented in this work assume a zero-Doppler reference geometry and thruster characteristics akin to cold-gas propulsion. The practical implications on the positioning performance of non-zero-Doppler geometries and the use of electric propulsion should be analyzed in future work. These scenarios can still be accommodated in the general framework proposed, requiring only minor adaptations relative to the examples presented.

Bibliography

[1] J. C. Maxwell, "A dynamical theory of the electromagnetic field," *Philosophical transactions of the Royal Society of London*, no. 155, pp. 459–512, 1865.

[2] D. J. Cichon and W. Wiesbeck, "The Heinrich Hertz wireless experiments at Karlsruhe in the view of modern communication," in *Proceedings of the 1995 International Conference on 100 Years of Radio*. IET, 1995, pp. 1–6.

[3] C. Hülsmeyer, "Verfahren, um entfernte metallische Gegenstände mittels elektrischer Wellen einem Beobachter zu melden," German Patent DE165 546C, 1904.

[4] C. A. Wiley, "Pulsed Doppler radar methods and apparatus," US Patent US3 122 741A, 1965.

[5] ——, "Synthetic aperture radars," *IEEE Transactions on Aerospace and Electronic Systems*, no. 3, pp. 440–443, 1985.

[6] W. M. Brown, "Synthetic aperture radar," *IEEE Transactions on Aerospace and Electronic Systems*, vol. AES-3, no. 2, pp. 217–229, 1967.

[7] K. Tomiyasu, "Tutorial review of synthetic-aperture radar (SAR) with applications to imaging of the ocean surface," *Proceedings of the IEEE*, vol. 66, no. 5, pp. 563–583, 1978.

[8] D. L. Evans, W. Alpers, A. Cazenave, C. Elachi, T. Farr, D. Glackin, B. Holt, L. Jones, W. T. Liu, W. McCandless, Y. Menard, R. Moore, and E. Njoku, "Seasat-A 25-year legacy of success," *Remote Sensing of Environment*, vol. 94, no. 3, pp. 384–404, 2005.

[9] P. Rosen, S. Hensley, I. Joughin, F. Li, S. Madsen, E. Rodriguez, and R. Goldstein, "Synthetic aperture radar interferometry," *Proceedings of the IEEE*, vol. 88, no. 3, pp. 333–382, 2000.

[10] J.-S. Lee and E. Pottier, *Polarimetric radar imaging: from basics to applications*. CRC press, 2017.

[11] J. C. Curlander and R. N. McDonough, *Synthetic Aperture Radar*. Wiley, New York, 1991, vol. 11.

[12] D. Massonnet, M. Rossi, C. Carmona, F. Adragna, G. Peltzer, K. Feigl, and T. Rabaute, "The displacement field of the landers earthquake mapped by radar interferometry," *Nature*, vol. 364, no. 6433, pp. 138–142, 1993.

[13] G. Krieger, I. Hajnsek, K. P. Papathanassiou, M. Younis, and A. Moreira, "Interferometric synthetic aperture radar (SAR) missions employing formation flying," *Proceedings of the IEEE*, vol. 98, no. 5, pp. 816–843, 2010.

[14] I. Seker and M. Lavalle, "Tomographic performance of multi-static radar formations: Theory and simulations," *Remote Sensing*, vol. 13, no. 4, 2021.

[15] G. Krieger and A. Moreira, "Spaceborne bi- and multistatic synthetic aperture radar: potential and challenges," *IEE Proceedings-Radar, Sonar and Navigation*, vol. 153, no. 3, pp. 184–198, Jun. 2006.

[16] G. Krieger, N. Gebert, and A. Moreira, "Unambiguous SAR signal reconstruction from nonuniform displaced phase center sampling," *IEEE Geoscience and Remote Sensing Letters*, vol. 1, no. 4, pp. 260–264, 2004.

[17] G. Krieger and A. Moreira, "Potential of digital beamforming in bi- and multistatic SAR," in *IGARSS 2003. 2003 IEEE International Geoscience and Remote Sensing Symposium. Proceedings (IEEE Cat. No.03CH37477)*, vol. 1, 2003, pp. 527–529 vol.1.

[18] N. Gebert, G. Krieger, and A. Moreira, "Digital beamforming on receive: Techniques and optimization strategies for high-resolution wide-swath SAR imaging," *IEEE Transactions on Aerospace and Electronic Systems*, vol. 45, no. 2, pp. 564–592, 2009.

[19] A. Renga, M. D. Graziano, and A. Moccia, "Formation flying SAR: Analysis of imaging performance by array theory," *IEEE Transactions on Aerospace and Electronic Systems*, vol. 57, no. 3, pp. 1480–1497, 2021.

[20] Y. Chen, Y. Nan, Y. Cai, P. Lu, Z. Chen, R. Wang, and Y. Wu, "An effective range ambiguity suppression scheme for multistatic SAR constellations based on multiechoes coherent processing," *IEEE Transactions on Geoscience and Remote Sensing*, vol. 62, pp. 1–15, 2024.

[21] J. L. Auterman, "Phase stability requirements for bistatic SAR," in *Proc. IEEE Nat. Radar Conf.*, Atlanta, USA, Mar., 1984, pp. 48–52.

[22] N. Willis, *Bistatic radar*. Norwood, USA: Artech House, 1991.

[23] G. Krieger and M. Younis, "Impact of oscillator noise in bistatic and multistatic SAR," *IEEE Geoscience and Remote Sensing Letters*, vol. 3, no. 3, pp. 424–428, 2006.

[24] N. Sakar, M. Rodriguez-Cassola, P. Prats-Iraola, and A. Moreira, "Sampling analysis and processing approach for distributed SAR constellations with along-track baselines," *IEEE Transactions on Geoscience and Remote Sensing*, vol. 60, pp. 1–12, 2022.

[25] B. Wessel, M. Huber, C. Wohlfart, U. Marschalk, D. Kosmann, and A. Roth, "Accuracy assessment of the global TanDEM-X digital elevation model with GPS data," *ISPRS Journal of Photogrammetry and Remote Sensing*, vol. 139, pp. 171–182, 2018.

[26] E. Rodriguez, C. S. Morris, and J. E. Belz, "A global assessment of the SRTM performance," *Photogrammetric Engineering & Remote Sensing*, vol. 72, no. 3, pp. 249–260, 2006.

[27] G. Krieger, A. Moreira, H. Fiedler, I. Hajnsek, M. Werner, M. Younis, and M. Zink, "TanDEM-X: A satellite formation for high-resolution SAR interferometry," *IEEE Transactions on Geoscience and Remote Sensing*, vol. 45, no. 11, pp. 3317–3341, 2007.

[28] M. Zink, A. Moreira, I. Hajnsek, P. Rizzoli, M. Bachmann, R. Kahle, T. Fritz, M. Huber, G. Krieger, M. Lachaise, M. Martone, E. Maurer, and B. Wessel, "TanDEM-X: 10 years of formation flying bistatic SAR interferometry," *IEEE Journal of Selected Topics in Applied Earth Observations and Remote Sensing*, vol. 14, pp. 3546–3565, 2021.

[29] H. Braubach and M. Voelker, "Method for drift compensation with radar measurements with the aid of reference radar signals," US Patent US7 209 072B2, 2007.

[30] M. Zink, M. Bachmann, B. Brautigam, T. Fritz, I. Hajnsek, A. Moreira, B. Wessel, and G. Krieger, "TanDEM-X: The new global DEM takes shape," *IEEE Geoscience and Remote Sensing Magazine*, vol. 2, no. 2, pp. 8–23, 2014.

[31] J. Mittermayer, G. Krieger, A. Bojarski, M. Zonno, M. Villano, M. Pinheiro, M. Bachmann, S. Buckreuss, and A. Moreira, "MirrorSAR: An HRWS add-on for single-pass multi-baseline SAR interferometry," *IEEE Transactions on Geoscience and Remote Sensing*, vol. 60, pp. 1–18, 2022.

[32] R. Wang, K. Liu, Y. Cai, D. Liang, W. Yu, D. Liu, Y. Chen, Q. Yang, J. Li, and L. Liu, "LuTan-1: An innovative L-band spaceborne bistatic interferometric SAR mission," in *EUSAR 2024; 15th European Conference on Synthetic Aperture Radar*. VDE, 2024, pp. 984–988.

[33] U. Wegmüller, C. Magnard, and O. Frey, "Assessment of Hongtu-1 multi-static X-Band SAR constellation interferometry," *Remote Sensing*, vol. 16, no. 19, 2024.

[34] Y. Deng, H. Zhang, K. Liu, W. Wang, N. Ou, H. Han, R. Yang, J. Ren, J. Wang, X. Ren, H. Fan, and S. Guo, "Hongtu-1: The first spaceborne single-pass multibaseline SAR interferometry mission," *IEEE Transactions on Geoscience and Remote Sensing*, vol. 63, pp. 1–18, 2025.

[35] J. Lopez-Dekker, J. Biggs, B. Chapron, A. Hooper, A. Kääb, S. Massina, J. Mouginot, B. Buongiorno Nardelli, C. Pasquero, P. Prats-Iraola *et al.*, "The Harmony mission: Applications and preliminary performance," in *Proceedings of the 6th Workshop on Advanced RF Sensors and Remote Sensing Instruments, ARSI*, vol. 19, 2019.

[36] R. Torres, P. Snoeij, M. Davidson, D. Bibby, and S. Lokas, "The Sentinel-1 mission and its application capabilities," in *2012 IEEE International Geoscience and Remote Sensing Symposium*. IEEE, 2012, pp. 1703–1706.

[37] P. López-Dekker, J. Biggs, B. Chapron, A. Hooper, A. Kääb, S. Masina, J. Mouginot, B. B. Nardelli, C. Pasquero, P. Prats-Iraola, P. Rampal, J. Stroeve, and B. Rommen, "The Harmony mission: End of phase-0 science overview," in *2021 IEEE International Geoscience and Remote Sensing Symposium IGARSS*, 2021, pp. 7752–7755.

[38] P. López-Dekker, H. Rot, S. Solberg, M. Zonno, M. Rodriguez-Cassola, P. Prats-Iraola, and A. Moreira, "Companion SAR constellations for single-pass interferometric applications: The SESAME mission," in *2017 IEEE International Geoscience and Remote Sensing Symposium (IGARSS)*, 2017, pp. 119–122.

[39] A. Renga, A. Gigantino, M. D. Graziano, A. Moccia, A. Fedele, and S. Natalucci, "Design considerations and performance analysis for RODiO distributed SAR mission," *Acta Astronautica*, vol. 210, pp. 474–482, 2023.

[40] A. Gigantino, A. Renga, M. Graziano, A. Moccia, A. Verde, L. Tedesco, G. P. Blasone, S. Zoffoli, D. Tapete, and V. Pulcino, "Bistatic observation opportunities in PLATiNO-1 SAR mission," 01 2024, pp. 544–550.

[41] M. Rodriguez-Cassola, "Bistatic synthetic aperture radar data processing," Ph.D. dissertation, KIT, Karlsruhe, Germany, 2012.

[42] D. Massonnet, "Capabilities and limitations of the interferometric cartwheel," *IEEE Transactions on Geoscience and Remote Sensing*, vol. 39, no. 3, pp. 506–520, 2001.

[43] M. Eineder, "Oscillator clock drift compensation in bistatic interferometric SAR," in *2003 IEEE International Geoscience and Remote Sensing Symposium.* IEEE, 2004.

[44] M. Younis, R. Metzig, and G. Krieger, "Performance prediction of a phase synchronization link for bistatic SAR," *IEEE Geoscience and Remote Sensing Letters*, vol. 3, no. 3, pp. 429–433, Jul. 2006.

[45] M. Pinheiro, M. Rodriguez-Cassola, P. Prats-Iraola, A. Reigber, G. Krieger, and A. Moreira, "Reconstruction of coherent pairs of synthetic aperture radar data acquired in interrupted mode," *IEEE Transactions on Geoscience and Remote Sensing*, vol. 53, no. 4, pp. 1876–1893, Apr. 2015.

[46] G. Jin, K. Liu, D. Liu, D. Liang, H. Zhang, N. Ou, Y. Zhang, Y. Deng, C. Li, and R. Wang, "An advanced phase synchronization scheme for LT-1," *IEEE Transactions on Geoscience and Remote Sensing*, vol. 58, no. 3, pp. 1735–1746, 2020.

[47] D. Liang, K. Liu, H. Zhang, Y. Chen, H. Yue, D. Liu, Y. Deng, H. Lin, T. Fang, C. Li, and R. Wang, "The processing framework and experimental verification for the noninterrupted synchronization scheme of LuTan-1," *IEEE Transactions on Geoscience and Remote Sensing*, vol. 59, no. 7, pp. 5740–5750, 2021.

[48] D. Liang, K. Liu, H. Zhang, Y. Deng, D. Liu, Y. Chen, C. Li, H. Yue, and R. Wang, "A high-accuracy synchronization phase-compensation method based on Kalman filter for bistatic synthetic aperture radar," *IEEE Geoscience and Remote Sensing Letters*, vol. 17, no. 10, pp. 1722–1726, 2020.

[49] M. Rodriguez-Cassola, P. Prats-Iraola, M. Zonno, M. Nannini, P. López-Dekker, B. Carnicero-Dominguez, B. Rommen, and A. Moreira, "End-to-end performance analysis of companion SAR missions," in *2017 IEEE International Geoscience and Remote Sensing Symposium (IGARSS).* Fort Worth, USA: IEEE, Jul. 2017, pp. 153–156.

[50] W. D. Brown and D. C. Ghiglia, "Some methods for reducing propagation-induced phase errors in coherent imaging systems. I.

formalism," *Journal of the Optical Society of America A*, vol. 5, no. 6, pp. 924–941, Jun 1988.

[51] D. Wahl, P. Eichel, D. Ghiglia, and C. Jakowatz, "Phase gradient autofocus-a robust tool for high resolution SAR phase correction," *IEEE Transactions on Aerospace and Electronic Systems*, vol. 30, no. 3, pp. 827–835, 1994.

[52] M. Rodriguez-Cassola, P. Prats, L. Marotti, M. Naninni, M. Younis, G. Krieger, and A. Reigber, "A versatile processing chain for experimental TanDEM-X product evaluation," in *8th European Conference on Synthetic Aperture Radar*, 2010, pp. 1–4.

[53] M. Rodriguez-Cassola, P. Prats, D. Schulze, N. Tous-Ramon, U. Steinbrecher, L. Marotti, M. Nannini, M. Younis, P. Lopez-Dekker, M. Zink, A. Reigber, G. Krieger, and A. Moreira, "First bistatic spaceborne SAR experiments with TanDEM-X," *IEEE Geoscience and Remote Sensing Letters*, vol. 9, no. 1, pp. 33–37, 2012.

[54] M. Rodriguez-Cassola, P. Prats-Iraola, M. Nannini, P. Lopez-Dekker, A. Moreira, and B. Carnicero Dominguez, "Calibration concept for weakly-synchronised SAR companion missions: ESA's SAOCOM/CS case," in *Proceedings of EUSAR 2016: 11th European Conference on Synthetic Aperture Radar*, 2016, pp. 1–4.

[55] N. Cao, H. Lee, E. Zaugg, R. Shrestha, W. E. Carter, C. Glennie, Z. Lu, and H. Yu, "Estimation of residual motion errors in airborne SAR interferometry based on time-domain backprojection and multisquint techniques," *IEEE Transactions on Geoscience and Remote Sensing*, vol. 56, no. 4, pp. 2397–2407, 2018.

[56] W. Wang, D. An, Y. Luo, Z. Zhou, and X. Huang, "A modified map-drift algorithm for SAR autofocusing," in *2018 Asia-Pacific Microwave Conference (APMC)*, 2018, pp. 815–817.

[57] W.-Q. Wang, "GPS-based time & phase synchronization processing for distributed SAR," *IEEE Transactions on Aerospace and Electronic Systems*, vol. 45, no. 3, pp. 1040–1051, 2009.

[58] G. Krieger, M. Zonno, J. Mittermayer, A. Moreira, S. Huber, and M. Rodriguez-Cassola, "MirrorSAR: A fractionated space transponder concept for the implementation of low-cost multistatic SAR missions," in *EUSAR 2018; 12th European Conference on Synthetic Aperture Radar*. Aachen, Germany: VDE, 2018, pp. 1–6.

[59] N. Ustalli, G. Krieger, J. Mittermayer, M. Villano, and C. Waldschmidt, "MirrorSAR concept: Phase synchronization analysis," in *2022 Kleinheubach Conference*, 2022, pp. 1–4.

[60] R. Kahle, B. Schlepp, F. Meissner, M. Kirschner, and R. Kiehling, "The TerraSAR-X/TanDEM-X formation acquisition–from planning to realization," *The Journal of the Astronautical Sciences*, vol. 59, pp. 564–584, 2012.

[61] J.-S. Ardaens, R. Kahle, and D. Schulze, "In-flight performance validation of the TanDEM-X autonomous formation flying system," *International Journal of Space Science and Engineering 5*, vol. 2, no. 2, pp. 157–170, 2014.

[62] G. Fasano, A. Renga, and M. D'Errico, "Formation geometries for multistatic SAR tomography," *Acta Astronautica*, vol. 96, pp. 11–22, 2014.

[63] F. Scala, G. Gaias, C. Colombo, and M. Martín-Neira, "Design of optimal low-thrust manoeuvres for remote sensing multi-satellite formation flying in low earth orbit," *Advances in Space Research*, vol. 68, no. 11, pp. 4359–4378, 2021.

[64] S. Lee, S.-Y. Park, J. Kim, M.-H. Ka, and Y. Song, "Mission design and orbit-attitude control algorithms development of multistatic SAR satellites for very-high-resolution stripmap imaging," *Aerospace*, vol. 10, no. 1, 2023.

[65] J. Wang and C. Liu, "The J2 relative perturbation analysis of satellite formation under the requirement of relative position maintenance with millimeter-level accuracy," *International Journal of Aerospace Engineering*, vol. 2021, no. 1, p. 6687468, 2021.

[66] K. T. Alfriend and H. Yan, "Evaluation and comparison of relative motion theories," *Journal of Guidance, Control, and Dynamics*, vol. 28, no. 2, pp. 254–261, 2005.

[67] J. Sullivan, S. Grimberg, and S. DAmico, "Comprehensive survey and assessment of spacecraft relative motion dynamics models," *Journal of Guidance, Control, and Dynamics*, vol. 40, no. 8, pp. 1837–1859, 2017.

[68] G. W. Hill, "Researches in the lunar theory," *American Journal of Mathematics*, vol. 1, no. 1, pp. 5–26, 1878.

[69] W. H. Clohessy and R. S. Wiltshire, "Terminal guidance system for satellite rendezvous," *Journal of the Aerospace Sciences*, vol. 27, no. 9, pp. 653–658, 1960.

[70] S. A. Schweighart and R. J. Sedwick, "High-fidelity linearized j model for satellite formation flight," *Journal of Guidance, Control, and Dynamics*, vol. 25, no. 6, pp. 1073–1080, 2002.

[71] D.-W. Gim and K. T. Alfriend, "State transition matrix of relative motion for the perturbed noncircular reference orbit," *Journal of Guidance, Control, and Dynamics*, vol. 26, no. 6, pp. 956–971, 2003.

[72] S. D'Amico, "Autonomous formation flying in low earth orbit," Ph.D. dissertation, TU Delft, Delft, Netherlands, 2010.

[73] A. J. Sinclair, R. E. Sherrill, and T. A. Lovell, "Calibration of linearized solutions for satellite relative motion," *Journal of Guidance, Control, and Dynamics*, vol. 37, no. 4, pp. 1362–1367, 2014.

[74] P. Sengupta and S. R. Vadali, "Relative motion and the geometry of formations in Keplerian elliptic orbits with arbitrary eccentricity," *Journal of Guidance, Control, and Dynamics*, vol. 30, no. 4, pp. 953–964, 2007.

[75] A. Mahfouz, G. Gaias, F. D. Vedova, and H. Voos, "Fuel-optimal formation reconfiguration by means of unidirectional low-thrust propulsion system," *Journal of Guidance, Control, and Dynamics*, pp. 1–10, 2024.

[76] A. Mahfouz, G. Gaias, F. Dalla Vedova, and H. Voos, "Delta-V-optimal centralized guidance strategy for under-actuated N-satellite formations," *Acta Astronautica*, vol. 228, pp. 69–87, 2025.

[77] G. Gaias, S. D'Amico, and J.-S. Ardaens, "Generalised multi-impulsive manoeuvres for optimum spacecraft rendezvous in near-circular orbit," *International Journal of Space Science and Engineering*, vol. 3, no. 1, pp. 68–88, 2015.

[78] E. Belloni, S. Silvestrini, J. Prinetto, and M. Lavagna, "Relative and absolute on-board optimal formation acquisition and keeping for scientific activities in high-drag low-orbit environment," *Advances in Space Research*, vol. 73, no. 11, pp. 5595–5613, 2024.

[79] T. Guffanti, T. Bell, S. Y. Low, M. Murray-Cooper, and S. D'Amico, "Autonomous guidance navigation and control of the VISORS formation-flying mission," *arXiv preprint arXiv:2309.16698*, 2023.

[80] E. Rodrigues-Silva, M. Rodriguez-Cassola, G. Krieger, and A. Moreira, "GNSS-based phase synchronization for bistatic and multistatic synthetic aperture radar," *IEEE Transactions on Geoscience and Remote Sensing*, vol. 62, pp. 1–14, 2024.

[81] E. Rodrigues-Silva, M. Rodriguez-Cassola, A. Moreira, and G. Krieger, "Experimental validation and calibration of GNSS-based phase synchronization for bistatic and multistatic SAR missions," *IEEE Transactions on Geoscience and Remote Sensing*, vol. 63, pp. 1–13, 2025.

[82] E. Rodrigues-Silva, J. Matar, M. Rodriguez-Cassola, N. Sakar, R. Katz, R. Kahle, and A. Moreira, "Relative orbit design and optimization for distributed SAR formations," *IEEE Transactions on Geoscience and Remote Sensing*, vol. 63, pp. 1–14, 2025.

[83] E. Rodrigues-Silva and M. Rodriguez-Cassola, "Analysis of a POD-based approach for phase and time synchronization of bistatic and multistatic SAR systems," in *EUSAR 2021; 13th European Conference on Synthetic Aperture Radar*. VDE, 2021, pp. 1–6.

[84] ——, "Experimental evaluation of GNSS-based frequency synchronization for SAR applications," in *IGARSS 2022 - 2022 IEEE International Geoscience and Remote Sensing Symposium*. IEEE, 2022, pp. 7164–7167.

[85] E. Rodrigues-Silva, M. Rodriguez-Cassola, R. Katz, J. Matar, and A. Moreira, "Fuel-efficient formation strategies for cross-track multistatic SAR constellations," in *IGARSS 2023 - 2023 IEEE International Geoscience and Remote Sensing Symposium*. IEEE, 2023, pp. 4556–4559.

[86] E. Rodrigues-Silva, M. Rodriguez-Cassola, A. Moreira, G. Krieger, and S. Thoelert, "Proof-of-concept of GNSS-based phase synchronization for bistatic and multistatic SAR missions." in *EUSAR 2024; 15th European Conference on Synthetic Aperture Radar*. VDE, 2024, pp. 131–136.

[87] P. Misra and P. Enge, *Global Positioning System: Signals, Measurements, and Performance*. Ganga-Jamuna Press, 2011.

[88] P. J. Teunissen, O. Montenbruck *et al.*, *Springer Handbook of Global Navigation Satellite Systems*. Springer, 2017, vol. 10.

[89] K. Alfriend, S. Vadali, P. Gurfil, J. How, and L. Breger, *Spacecraft formation flying: Dynamics, control and navigation*, 11 2009.

[90] A. Freeman, W. Johnson, B. Huneycutt, R. Jordan, S. Hensley, P. Siqueira, and J. Curlander, "The "Myth" of the minimum SAR antenna area constraint," *IEEE Transactions on Geoscience and Remote Sensing*, vol. 38, no. 1, pp. 320–324, 2000.

[91] F. De Zan and A. M. Guarnieri, "TOPSAR: Terrain observation by progressive scans," *IEEE Transactions on Geoscience and Remote Sensing*, vol. 44, no. 9, pp. 2352–2360, 2006.

[92] R. Song, W. Wang, and W. Yu, "The latest developments in spaceborne high-resolution wide-swath SAR systems and imaging methods," *Sensors*, vol. 24, no. 18, p. 5978, 2024.

[93] G. Krieger, N. Gebert, M. Younis, F. Bordoni, A. Patyuchenko, and A. Moreira, "Advanced concepts for ultra-wide-swath SAR imaging," in *7th European Conference on Synthetic Aperture Radar*. VDE, 2008, pp. 1–4.

[94] M. Lavalle, I. Seker, J. Ragan, E. Loria, R. Ahmed, B. P. Hawkins, S. Prager, D. Clark, R. Beauchamp, M. Haynes, P. Focardi, N. Chahat, M. Anderson, K. Matsuka, V. Capuano, and S.-J. Chung, "Distributed aperture radar tomographic sensors (DARTS) to map surface topography and vegetation structure," in *IGARSS 2021 - 2021 IEEE International Geoscience and Remote Sensing Symposium*, 2021, pp. 1090–1093.

[95] M. Battilana, G. Capuani, F. Boldrini, L. Maioli, M. L. Tampellini, F. Gerace, D. Giudici, P. Guccione, J. Marini, L. DAgristina *et al.*, "SATURN: formation flying SAR minisatellites employing MIMO technique," in *Small Satellites Systems and Services Symposium (4S 2024)*, vol. 13546, 2025, pp. 861–876.

[96] H. D. Griffiths and P. Mancini, "Ambiguity suppression in SARs using adaptive array techniques," in *IGARSS 1991; Proceedings of the 11th Annual International Geoscience and Remote Sensing Symposium*, vol. 2, 1991, pp. 1015–1018.

[97] Y.-Y. Wu and A. Madson, "Error sources of interferometric synthetic aperture radar satellites," *Remote Sensing*, vol. 16, no. 2, 2024.

[98] Q. Lin, S. Li, and W. Yu, "Review on phase synchronization methods for spaceborne multistatic synthetic aperture radar," *Sensors*, vol. 24, no. 10, p. 3122, May 2024.

[99] P. Groves, *Principles of GNSS, Inertial, and Multisensor Integrated Navigation Systems, Second Edition*, ser. GNSS/GPS. Artech House, 2013.

[100] R. Kroes, "Precise relative positioning of formation flying spacecraft using GPS." Ph.D. dissertation, TU Delft, Delft, Netherlands, 2006.

[101] A. W. Koenig and S. D'Amico, "Robust and safe N-spacecraft swarming in perturbed near-circular orbits," *Journal of Guidance, Control, and Dynamics*, vol. 41, no. 8, pp. 1643–1662, 2018.

[102] D. A. Vallado, *Fundamentals of astrodynamics and applications*. Springer Science & Business Media, 2001, vol. 12.

[103] D. Izzo, M. Sabatini, and C. Valente, "A new linear model describing formation flying dynamics under J2 effects," in *Proceedings of the 17th AIDAA National Congress*, vol. 1, 2003, pp. 15–19.

[104] J. K. Eyer, C. J. Damaren, R. E. Zee, and E. Cannon, "A formation flying control algorithm for the CanX-4&5 low earth orbit nanosatellite mission," *Space Technology*, vol. 27, no. 4, p. 147, 2007.

[105] R. Kroes, O. Montenbruck, W. Bertiger, and P. Visser, "Precise GRACE baseline determination using GPS," *GPS Solutions*, vol. 9, pp. 21–31, 2005.

[106] J. H. González, J. M. W. Antony, M. Bachmann, G. Krieger, M. Zink, D. Schrank, and M. Schwerdt, "Bistatic system and baseline calibration in TanDEM-X to ensure the global digital elevation model quality," *ISPRS Journal of Photogrammetry and Remote Sensing*, vol. 73, pp. 3–11, 2012.

[107] J.-S. Ardaens, S. D'Amico, and O. Montenbruck, "Flight results from the PRISMA GPS-based navigation," in *5th ESA Workshop on Satellite Navigation Technologies, NAVITEC*, Noordwijk, Netherlands, Jan. 2010.

[108] G. Krieger and F. De Zan, "Relativistic effects in bistatic SAR processing and system synchronization," in *EUSAR 2012; 9th European Conference on Synthetic Aperture Radar*, 2012, pp. 231–234.

[109] P. van Barneveld, "Orbit determination of satellite formations." Ph.D. dissertation, TU Delft, Delft, Netherlands, 2012.

[110] H. Peter, T. Springer, F. Zangerl, and H. Reichinger, "Beyond gravity PODRIX GNSS receiver on Sentinel-6 Michael Freilich– receiver performance and POD analysis," in *Proceedings of the 35th International Technical Meeting of the Satellite Division of The Institute of Navigation (ION GNSS+ 2022)*, 2022, pp. 589–601.

[111] S. J. Setty, P. J. Cefola, H. Fiedler, and J. F. S. J. Diaz, "Attributes affecting the accuracy of a batch least square orbit determination using semi-analytical satellite theory," in *Proceedings of the Maui Optical and Space Surveillance Technologies Conference*, Sep. 2016.

[112] S. Sun, H. Chai, M. Wang, C. Liu, Y. Zhou, Q. Zhang, and Y. Liu, "POD performance of LEO satellites with Galileo high accuracy service (HAS) of initial service phase," *Advances in Space Research*, 2024.

[113] O. Montenbruck and C. Renaudie, "Phoenix-S/-XNS performance validation," German Space Operations Center (GSOC), DLR, Tech. Rep. GTN-TST-0120, Apr 2007.

[114] U. Weinbach, S. Schon, and T. Feldmann, "Evaluation of state-of-the-art geodetic GPS receivers for frequency comparisons," in *2009 IEEE International Frequency Control Symposium Joint with the 22nd European Frequency and Time forum*. IEEE, 2009, pp. 263–268.

[115] O. Montenbruck, L. van Barneveld, Y. Yoon, and P. Visser, "GPS-based precision baseline reconstruction for the TanDEM-X SAR-formation," in *19th International Symposium on Space Flight Dynamics*, Annapolis, USA, Sep. 2007.

[116] O. Montenbruck, M. Garcia-Fernandez, Y. Yoon, S. Schön, and A. Jäggi, "Antenna phase center calibration for precise positioning of LEO satellites," *GPS solutions*, vol. 13, no. 1, p. 23, 2009.

[117] A. Jäggi, R. Dach, O. Montenbruck, U. Hugentobler, H. Bock, and G. Beutler, "Phase center modeling for LEO GPS receiver antennas and its impact on precise orbit determination," *Journal of Geodesy*, vol. 83, no. 12, pp. 1145–1162, 2009.

[118] B. Hofmann-Wellenhof, H. Lichtenegger, and J. Collins, *GPS, Theory and Practice*. New York: Springer-Verlag Wien, 1997.

[119] L. Lau and P. Cross, "Development and testing of a new ray-tracing approach to GNSS carrier-phase multipath modelling," *Journal of Geodesy*, vol. 81, pp. 713–732, 2007.

[120] M. L. Psiaki and S. Mohiuddin, "Modeling, analysis, and simulation of GPS carrier phase for spacecraft relative navigation," *Journal of Guidance, Control, and Dynamics*, vol. 30, no. 6, pp. 1628–1639, 2007.

[121] J.-T. Wu, S. C. Wu, G. A. Hajj, W. I. Bertiger, and S. M. Lichten, "Effects of antenna orientation on GPS carrier phase," *Manuscripta geodaetica*, vol. 18, no. 2, pp. 91–98, 1993.

[122] X. Guo and Q. Zhao, "M-estimation-based robust and precise baseline determination for formation-flying satellites," *GPS Solutions*, vol. 25, pp. 1–12, 2021.

[123] General mission analysis tool (GMAT) project page. Accessed: October 2020. [Online]. Available: https://opensource.gsfc.nasa.gov/projects/GMAT/index.php

[124] W. Lear, "GPS navigation for low-earth orbiting vehicles," *NASA Lyndon B. Johnson Space Center, Mission planning and analysis division, 1st revision, NASA*, 1987.

[125] H. Cantalloube, M. Wendler, V. Giroux, P. Dubois-Fernandez, and G. Krieger, "Challenges in SAR processing for airborne bistatic acquisitions," in *Proc. EUSAR*, 2004, pp. 577–580.

[126] H. Cantalloube, P. Dubois-Fernandez, V. Giroux, and G. Krieger, "Bistatic moving target indication using across-track and along-track interferometry," in *Proc. EUSAR*, 2006, pp. 1–4.

[127] A. Theodosiou and P. López-Dekker, "Data-driven phase synchronization of harmonys ocean surface topography product," *IEEE Transactions on Geoscience and Remote Sensing*, vol. 63, pp. 1–16, 2025.

[128] O. Montenbruck, P. Steigenberger, and A. Hauschild, "Broadcast versus precise ephemerides: a multi-GNSS perspective," *GPS solutions*, vol. 19, pp. 321–333, 2015.

[129] NovAtel, "OEM729 product sheet," [Online]. Available: https://hexagondownloads.blob.core.windows.net/public/Novatel/assets/Documents/Papers/OEM729-Product-Sheet/OEM729-Product-Sheet.pdf, July 2023.

[130] Septentrio, "PolaRx5TR product sheet," [Online]. Available: https://www.septentrio.com/en/products/gnss-receivers/gnss-reference-receivers/polarx-5tr#resources, August 2024.

[131] D. Calliess, O. Montenbruck, M. Wermuth, and H. Reichinger, "Long-term analysis of Sentinel-6A orbit determination: Insights from three years of flight data," *Advances in Space Research*, vol. 74, no. 7, pp. 3011–3027, 2024.

[132] F. Kunzi and O. Montenbruck, "Precise onboard time synchronization for LEO satellites," *NAVIGATION: Journal of the Institute of Navigation*, vol. 69, no. 3, 2022.

[133] F. S. Prol, R. M. Ferre, Z. Saleem, P. Välisuo, C. Pinell, E. S. Lohan, M. Elsanhoury, M. Elmusrati, S. Islam, K. Çelikbilek, K. Selvan, J. Yliaho, K. Rutledge, A. Ojala, L. Ferranti, J. Praks, M. Z. H. Bhuiyan, S. Kaasalainen, and H. Kuusniemi, "Position, navigation, and timing (PNT) through low earth orbit (LEO) satellites: A survey on current status, challenges, and opportunities," *IEEE Access*, vol. 10, pp. 83 971–84 002, 2022.

[134] M. Kihara, S. Ono, and P. Eskelinen, *Digital Clocks for Synchronization and Communications*, ser. Artech House Telecommunications Library. Artech House, 2002.

[135] H. Cui and S. Zhang, "Satellite availability and service performance evaluation for next-generation GNSS, RNSS and LEO augmentation constellation," *Remote Sensing*, vol. 13, no. 18, 2021.

[136] M. Rodriguez-Cassola, P. Prats-Iraola, P. López-Dekker, A. Reigber, G. Krieger, and A. Moreira, "Autonomous time and phase calibration of spaceborne bistatic SAR systems," in *EUSAR 2014; 10th European Conference on Synthetic Aperture Radar*, 2014, pp. 1–4.

[137] J. Rutman, "Characterization of phase and frequency instabilities in precision frequency sources: Fifteen years of progress," *Proceedings of the IEEE*, vol. 66, no. 9, pp. 1048–1075, 1978.

[138] E. Loria, S. Prager, I. Seker, R. Ahmed, B. Hawkins, and M. Lavalle, "Modeling the effects of oscillator phase noise and synchronization on multistatic SAR tomography," *IEEE Transactions on Geoscience and Remote Sensing*, vol. 61, pp. 1–12, 2023.

[139] H. Fiedler, E. Boerner, J. Mittermayer, and G. Krieger, "Total zero Doppler steering-a new method for minimizing the Doppler centroid," *IEEE Geoscience and Remote Sensing Letters*, vol. 2, no. 2, pp. 141–145, 2005.

[140] R. K. Raney, "Doppler properties of radars in circular orbits," *International Journal of Remote Sensing*, vol. 7, no. 9, pp. 1153–1162, 1986.

[141] A. Currie and M. A. Brown, "Wide-swath SAR," in *IEE Proceedings F (Radar and Signal Processing)*, vol. 139, no. 2. IET, 1992, pp. 122–135.

[142] J. Aguttes, "The SAR train concept: required antenna area distributed over N smaller satellites, increase of performance by N," in *IGARSS 2003 - 2003 IEEE International Geoscience and Remote Sensing Symposium*, vol. 1, 2003, pp. 542–544 vol.1.

[143] A. Renga, A. Gigantino, and M. D. Graziano, "Multiplatform image synthesis for distributed synthetic aperture radar in long baseline bistatic configurations," *IEEE Transactions on Aerospace and Electronic Systems*, vol. 59, no. 6, pp. 9267–9284, 2023.

[144] H. Lin, Y. Deng, H. Zhang, D. Liang, and X. Jia, "An imaging method for spaceborne cooperative multistatic SAR formations with nonzero cross-track baselines," *IEEE Journal of Selected Topics in Applied Earth Observations and Remote Sensing*, vol. 15, pp. 8541–8551, 2022.

[145] O. Dogan, F. Uysal, and P. L. Dekker, "Unambiguous recovery of multistatic SAR data for nonzero cross track baseline case," *IEEE Geoscience and Remote Sensing Letters*, vol. 19, pp. 1–5, 2022.

[146] N. Petrushevsky, A. Monti-Guarnieri, and A. Rosario Persico, "Unambiguous imaging by a distributed SAR system with cross-track baselines," *IEEE Transactions on Geoscience and Remote Sensing*, vol. 62, pp. 1–11, 2024.

[147] F. deBruijn, E. Gill, and J. How, "Comparative analysis of cartesian and curvilinear Clohessy-Wiltshire equations," *Journal of Aerospace Engineering*, vol. 3, no. 2, p. 1, 2011.

[148] M. Suess, B. Grafmueller, and R. Zahn, "A novel high resolution, wide swath SAR system," in *IGARSS 2001. Scanning the Present and Resolving the Future. Proceedings. IEEE 2001 International Geoscience and Remote Sensing Symposium (Cat. No.01CH37217)*, vol. 3, 2001, pp. 1013–1015 vol.3.

[149] L. Carrer, C. Gerekos, F. Bovolo, and L. Bruzzone, "Distributed radar sounder: A novel concept for subsurface investigations using sensors in formation flight," *IEEE Transactions on Geoscience and Remote Sensing*, vol. 57, no. 12, pp. 9791–9809, 2019.

[150] H. Fiedler, G. Krieger, F. Jochim, M. Kirschner, and A. Moreira, "Analysis of bistatic configurations for spaceborne SAR interferometry," *Proceedings EUSAR 2002*, pp. 29–32, 2002.

[151] M. Delpech, J.-C. Berges, T. Karlsson, and F. Malbet, "Results of PRISMA/FFIORD extended mission and applicability to future formation flying and active debris removal missions," *International Journal of Space Science and Engineering 5*, vol. 1, no. 4, pp. 382–409, 2013.

[152] A. W. Koenig, S. DAmico, and E. G. Lightsey, "Formation flying orbit and control concept for virtual super optics reconfigurable swarm mission," *Journal of Guidance, Control, and Dynamics*, vol. 46, no. 9, pp. 1657–1670, 2023.

[153] M. Doyon, J. Smyth, G. Kroupnik, C. Carrie, M. Sauvageau, J.-F. Levesque, F. Babiker, V. Abbasi, C. Giguere, S. Côté *et al.*, "RADARSAT constellation mission: Toward launch and operations," in *2018 SpaceOps Conference*, 2018, p. 2605.

[154] M. Rodriguez-Cassola, P. M. N. Thi, G. Krieger, J. Matar, N. Sakar, E. R. S. Filho, and A. Moreira, "On the performance of swath reconstruction algorithms for multistatic SAR constellations: a sensitivity

analysis," in *IGARSS 2023 - 2023 IEEE International Geoscience and Remote Sensing Symposium*, 2023, pp. 7914–7917.

[155] S. Aliberti, M. B. Quadrelli, and M. Romano, "A distributed space radar sounder using a cross-track flying tethered satellite system," *Acta Astronautica*, vol. 221, pp. 266–282, 2024.

[156] A. Weiss, M. Baldwin, R. S. Erwin, and I. Kolmanovsky, "Model predictive control for spacecraft rendezvous and docking: Strategies for handling constraints and case studies," *IEEE Transactions on Control Systems Technology*, vol. 23, no. 4, pp. 1638–1647, 2015.

[157] S. P. Boyd and L. Vandenberghe, *Convex optimization*. Cambridge university press, 2004.

[158] S. Diamond and S. Boyd, "CVXPY: A python-embedded modeling language for convex optimization," *Journal of Machine Learning Research*, vol. 17, no. 83, pp. 1–5, 2016.

[159] A. Richards, T. Schouwenaars, J. P. How, and E. Feron, "Spacecraft trajectory planning with avoidance constraints using mixed-integer linear programming," *Journal of Guidance, Control, and Dynamics*, vol. 25, no. 4, pp. 755–764, 2002.

[160] B. Yost and S. Weston, "State-of-the-art small spacecraft technology," NASA Ames Research Center, Moffett Field, CA, Tech. Rep. NASA/TP20240001462, 2024, NASA Small Spacecraft Systems Virtual Institute (S3VI), Annual Report. [Online]. Available: https://www.nasa.gov/smallsat-institute/sst-soa/

[161] N. H. Roth, B. Johnston-Lemke, C. J. Damaren, and R. E. Zee, "Formation and attitude control for the CanX-4 and CanX-5 formation flying mission," *IFAC Proceedings Volumes*, vol. 44, no. 1, pp. 3033–3038, 2011, 18th IFAC World Congress.

[162] maisonobe, B. Cazabonne, E. Ward, R. Serra, M. Journot, S. Dinot, G. Bonnefille, T. Neidhart, L. Maisonobe, C. Jonglez, M. Rutten, yjeand, J. Hernanz, lirw1984, V. Cucchietti, A. Goetz, Guiuux, gaetanpierre0, L. N. Christensen, A. Fossà, jvalet, A. Ferrero, gabb5, liscju, C. Schank, T. Mills, plan3d, V. Yadav, S. Iyer, and P. Hyvönen, "CS-SI/Orekit: 12.2," Oct. 2024. [Online]. Available: https://doi.org/10.5281/zenodo.13950582

[163] L. Maisonobe, P. Cefola, N. Frouvelle, S. Herbinière, F. Laffont, S. Lizy-Destrez, and T. Neidhart, "Open governance of the Orekit space flight dynamics library," in *International Conference on Astrodynamics Tools and Techniques*, 2012.